
Memorial Descritivo de Atividades

Solicitação de contratação para o cargo de de **Professor Doutor - MS-3.1**
apresentada ao Instituto de Física "Gleb Wataghin", da Universidade de
Campinas

Solicitante: **André Monteiro Paschoal**

Abril de 2022

Índice Analítico

1 Identificação	5
2 Formação	6
3 Títulos	7
3.1 Diplomas, dignidades universitárias e prêmios de cunho científico e cultural	7
3.2 Participação em congressos, simpósios e outros certames científicos e culturais com apresentação de trabalhos	7
3.3 Obtenção de bolsa de estudo em instituições de renome científico ou cultural	10
4 Produção científica	12
4.1 Trabalhos aceitos em congressos	12
4.2 Artigos Científicos Publicados em Periódicos Nacionais e Internacionais na sua área de atuação	12
4.3 Dissertação de Mestrado	13
4.4 Tese de doutorado	13
5 Experiências Didáticas Universitárias	14
5.1 Monitorias para disciplinas de graduação	14
5.2 Membro de comissão avaliadora	14
6 Coordenação de Eventos e Conferencista	15
6.1 Comissão Organizadora de Eventos Internacional, Nacional, Regional ou Local	15
A Documentos comprobatórios	16
Documentos comprobatórios	16
1 Diploma de Graduação em Ciências Físicas e Biomoleculares, junto ao Instituto de Física de São Carlos (IFSC - USP)	17
2 Diploma de Mestre em Ciências, junto ao Instituto de Física de São Carlos (IFSC - USP)	20
3 Diploma de Doutor em Ciências, junto ao Departamento de Física da Faculdade de Filosofia, Ciências e Letras de Ribeirão Preto (FFCLRP) da Universidade de São Paulo (USP)	22
4 Certificado de Pós Doutorado, junto à Faculdade de Medicina de Ribeirão Preto (FMRP) da Universidade de São Paulo (USP)	25
5 Prêmios de mérito científico	28
6 Prêmios de mérito científico - Prêmio CAPES de Teses	30
7 Participação em Eventos Científicos (com apresentação de trabalho ou oferecimento de cursos, palestras ou debates)	32
8 Participação em Eventos Científicos (com apresentação de trabalho ou oferecimento de cursos, palestras ou debates)	34
9 Participação em Eventos Científicos (com apresentação de trabalho ou oferecimento de cursos, palestras ou debates)	36
10 Participação em Eventos Científicos (com apresentação de trabalho ou oferecimento de cursos, palestras ou debates)	39
11 Participação em Eventos Científicos (com apresentação de trabalho ou oferecimento de cursos, palestras ou debates)	41
12 Participação em Eventos Científicos (com apresentação de trabalho ou oferecimento de cursos, palestras ou debates)	43
13 Participação em Eventos Científicos (com apresentação de trabalho ou oferecimento de cursos, palestras ou debates)	45

14	Participação em Eventos Científicos (com apresentação de trabalho ou oferecimento de cursos, palestras ou debates	47
15	Participação em Eventos Científicos (com apresentação de trabalho ou oferecimento de cursos, palestras ou debates	49
16	Participação em Eventos Científicos (com apresentação de trabalho ou oferecimento de cursos, palestras ou debates	51
17	Participação em Eventos Científicos (com apresentação de trabalho ou oferecimento de cursos, palestras ou debates	57
18	Participação em Eventos Científicos (com apresentação de trabalho ou oferecimento de cursos, palestras ou debates	59
19	Participação em Eventos Científicos (com apresentação de trabalho ou oferecimento de cursos, palestras ou debates	61
20	Participação em Eventos Científicos (com apresentação de trabalho ou oferecimento de cursos, palestras ou debates	68
21	Participação em Eventos Científicos (com apresentação de trabalho ou oferecimento de cursos, palestras ou debates	70
22	Participação em Eventos Científicos (com apresentação de trabalho ou oferecimento de cursos, palestras ou debates	72
23	Participação em Eventos Científicos (com apresentação de trabalho ou oferecimento de cursos, palestras ou debates	74
24	Participação em Eventos Científicos (com apresentação de trabalho ou oferecimento de cursos, palestras ou debates	76
25	Participação em Eventos Científicos (com apresentação de trabalho ou oferecimento de cursos, palestras ou debates	80
26	Participação em Eventos Científicos (com apresentação de trabalho ou oferecimento de cursos, palestras ou debates	82
27	Participação em Eventos Científicos (com apresentação de trabalho ou oferecimento de cursos, palestras ou debates	84
28	Participação em Eventos Científicos (com apresentação de trabalho ou oferecimento de cursos, palestras ou debates	86
29	Participação em Eventos Científicos (com apresentação de trabalho ou oferecimento de cursos, palestras ou debates	88
30	Participação em Eventos Científicos (com apresentação de trabalho ou oferecimento de cursos, palestras ou debates	91
31	Participação em Eventos Científicos (com apresentação de trabalho ou oferecimento de cursos, palestras ou debates	97
32	Participação em Eventos Científicos (com apresentação de trabalho ou oferecimento de cursos, palestras ou debates	100
33	Obtenção de bolsa de estudo em instituições de renome científico ou cultural	104
34	Obtenção de bolsa de estudo em instituições de renome científico ou cultural	106
35	Obtenção de bolsa de estudo em instituições de renome científico ou cultural	109
36	Obtenção de bolsa de estudo em instituições de renome científico ou cultural	112
37	Autoria de artigos completos publicados em anais de congresso, em jornais e revistas de circulação nacional e internacional na sua área	114
38	Autoria de artigos completos publicados em anais de congresso, em jornais e revistas de circulação nacional e internacional na sua área	117
39	Autoria de artigos completos publicados em anais de congresso, em jornais e revistas de circulação nacional e internacional na sua área	119
40	Autoria de artigos completos publicados em jornais e revistas de circulação nacional e internacional na sua área	122
41	Autoria de artigos completos publicados em jornais e revistas de circulação nacional e internacional na sua área	127
42	Autoria de artigos completos publicados em jornais e revistas de circulação nacional e internacional na sua área	135

43	Autoria de artigos completos publicados em jornais e revistas de circulação nacional e internacional na sua área	146
44	Autoria de artigos completos publicados em jornais e revistas de circulação nacional e internacional na sua área	155
45	Autoria de artigos completos publicados em jornais e revistas de circulação nacional e internacional na sua área	169
46	Autoria de artigos completos publicados em jornais e revistas de circulação nacional e internacional na sua área	179
47	Autoria de artigos completos publicados em jornais e revistas de circulação nacional e internacional na sua área	195
48	Autoria de artigos completos publicados em jornais e revistas de circulação nacional e internacional na sua área	198
49	Monitorias para disciplinas de graduação	210
50	Monitorias para disciplinas de graduação	212
51	Monitorias para disciplinas de graduação	214
52	Monitorias para disciplinas de graduação	216
53	Membro de Comissão Avaliadora	218
54	Membro de Comissão Avaliadora	220
55	Comissão Organizadora de Eventos Internacional, Nacional, Regional ou Local	222
56	Comissão Organizadora de Eventos Internacional, Nacional, Regional ou Local	224

Apresentação

Memorial apresentado por **André Monteiro Paschoal**, para concurso de Professor Temporário junto ao Instituto de Física da Universidade de São Paulo (IFUSP), para avaliação de desempenho acadêmico.

O presente memorial relata as atividades desempenhadas no período de **Fevereiro de 2013 até Setembro de 2020**. Os documentos comprobatórios referenciados neste memorial estão organizados em volumes anexos devidamente numerados. Por fim, os Anexos que se referem a artigos publicados em conferências e periódicos contém apenas a primeira página do trabalho e o email informando a aceitação do trabalho para publicação (quando pertinente).

1 Identificação

- **André Monteiro Paschoal.**
- Filiação:
Pai: Oswaldo Luiz Fortes Paschoal.
Mãe: Ana Célia Navajas Monteiro Paschoal.
- Nascido em 04 de agosto de 1988 na cidade de Santa Cruz do Rio Pardo - SP.
- Cargo atual na carreira universitária: bolsista de Pós-Doutorado junto ao Instituto de Radiologia, Departamento de Radiologia e Oncologia do Hospital das Clínicas da Faculdade de Medicina da Universidade de São Paulo, sendo bolsista da Fundação de Amparo à Pesquisa do Estado de São Paulo (FAPESP).
- Residente na Avenida Santa Marina, (apartamento 171, torre 3) no bairro Água Branca no município de São Paulo - SP.
- Telefone para contato: (11) 98911-0265.
- E-mail para contato: ampaschoal@hmail.com
- Membro das Seguintes Sociedades:
 - International Society of Magnetic Resonance in Medicine (ISMRM).
 - European Society of Magnetic Resonance in Medicine and Biology (ESMRMB).
 - Membro colaborador da *Open Science Iniciative for Perfusion Imaging* (OSIPI), líder da *Task Force 6.1 - ASL Challenges*.

2 Formação

2.1. Graduação:

- Graduação em **Ciências Físicas e Biomoleculares**, obtida junto ao Instituto de Física de São Carlos (IFSC - USP) no ano de 2012. [**Doc. 1**]

2.2. Pós-graduação:

- Mestre em Ciências com grau obtido no programa de Física Aplicada: opção biomolecular, junto ao Instituto de Física de São Carlos (IFSC - USP) no ano de 2015. [**Doc. 2**]
- Doutor em Ciências com grau obtido no programa de Física Aplicada à Medicina e Biologia (FAMB), junto ao Departamento de Física da Faculdade de Filosofia, Ciências e Letras de Ribeirão Preto (FFCLRP) da Universidade de São Paulo (USP) no ano de 2020. [**Doc. 3**]
- Pós-doutorando junto à Faculdade de Medicina de Ribeirão Preto (FMRP-USP) desde Fevereiro de 2020. [**Doc. 4**]

2.3. Idiomas:

- Inglês: comprehende bem; lê bem; escreve bem; fala bem.
- Português: comprehende bem; lê bem; escreve bem; fala bem.

3 Títulos

3.1 Diplomas, dignidades universitárias e prêmios de cunho científico e cultural.

3.1. Prêmios de mérito científico:

- OHBM Travel Awards. [Doc. 5]
- Menção Honrosa no Prêmio CAPES de Teses 2021 [Doc. 6]

3.2 Participação em congressos, simpósios e outros certames científicos e culturais com apresentação de trabalhos

1. **Evento:** III Semana Integrada do Instituto de Física de São Carlos. [Doc. 7]

Propósito: Participante

Propósito (i): Apresentação do resumo “Otimização do Contraste em ASL Multifase”

Ano: 2013

Local: São Carlos - SP, Brasil.

2. **Evento:** IV Semana Integrada do Instituto de Física de São Carlos [Doc. 8]

Propósito (i): Participante

Propósito (ii): Apresentação do resumo “Otimização do Contraste em ASL Multifase”

Ano: 2014

Local: São Carlos - SP, Brasil.

3. **Evento:** I Transatlantic Workshop on Methods for Multimodal Neurosciences Studies. [Doc. 9]

Propósito (i): Participante

Propósito (ii): Apresentação do resumo “Contrast Optimization in Multiphase ASL.”

Ano: 2014

Local: São Pedro - SP, Brasil.

4. **Evento:** V Semana Integrada do Instituto de Física de São Carlos. [Doc. 10]

Propósito (i): Participante

Propósito (ii): Apresentação do resumo “Desenvolvimento de uma plataforma multimodal para o estudo da hemodinâmica cerebral: uma abordagem combinando ASL e NIRS.”

Ano: 2015

Local: São Carlos - SP, Brasil.

5. **Evento:** XV Semana da Física Médica. [Doc. 11]

Propósito (i): Participante

Propósito (ii): Apresentação do resumo “Desenvolvimento de métodos para o estudo de funções e conectividade cerebral usando Arterial Spin Labeling.”

Ano: 2016

Local: Ribeirão Preto - SP, Brasil.

6. **Evento:** XXII Congresso Brasileiro de Física Médica. [Doc. 12]

Propósito (i): Participante

Propósito (ii): Apresentação do resumo “Arterial Transit Time Maps Utilizing Arterial Spin Labeling.”

Ano: 2017

Local: Ribeirão Preto - SP, Brasil.

7. **Evento:** Seminário semanal do programa de Física Aplicada à Medicina e Biologia.

[Doc. 13]

Propósito (i): Palestrante

Propósito (ii): Apresentação da palestra “Improving Arterial Spin Labeling Acquisition to Reduce the Effect of Delayed Arrival Time.”

Ano: 2017

Local: Ribeirão Preto - SP, Brasil.

8. **Evento:** O Cérebro estatístico: desafios científicos do CEPID NeuroMat. [Doc. 14]

Propósito (i): Ouvinte

Ano: 2017

Local: Ribeirão Preto - SP, Brasil.

9. **Evento:** O 8º Simpósio de Instrumentação e Imagens Médicas (SIIM) e o 7º Simpósio de Processamento de Sinais (SPS). [Doc. 15]

Propósito (i): Participante

Propósito (ii): Apresentação do resumo “Evaluation of removing residual motion artifacts and global signal fluctuations in functional ASL data.”

Ano: 2017

Local: São Bernardo do Campo - SP, Brasil.

10. **Evento:** ISMRM 25th Annual Meeting & Exhibition. [Doc. 16]

Propósito (i): Participante

Propósito (ii): Apresentação do resumo “Improving Arterial Spin Labeling Acquisition to Reduce the Effect of Delayed Arrival Time.”

Ano: 2017

Local: Honolulu - Hawaii, EUA.

11. **Evento:** 4th BRAINN Congress [Doc. 17]

Propósito (i): Ouvinte

Ano: 2017

Local: Campinas - SP, Brasil.

12. **Evento:** XVI Semana da Física Médica. **Propósito (i):** Participante

Propósito (ii): Apresentação do resumo “Brain Functional Analysis with Arterial Spin Labeling.” [Doc. 20]

Propósito (iii): Ministrante do Minicurso “Processamento de Imagens Médicas” [Doc. 21]

Ano: 2017

Local: Ribeirão Preto - SP, Brasil.

13. Evento: 5th BRAINN Congress [Doc. 18]**Propósito (i):** Participante**Propósito (ii):** Apresentação do resumo “Simultaneous assessment of CBF and brain function through Dual-Echo Arterial Spin Labeling.”**Ano:** 2018**Local:** Campinas - SP, Brasil.**14. Evento:** Joint Annual Meeting ISMRM-ESMRMB. [Doc. 19]**Propósito (i):** Participante**Propósito (ii):** Apresentação do resumo “Regularized nonnegative least-square fitting for intravoxel incoherent motion data processing: a simulation study.”**Propósito (iii):** Apresentação do resumo “Brain connectivity assessment between rest condition and verbal fluency task through Arterial Spin Labeling.”**Ano:** 2018**Local:** Paris, France.**15. Evento:** XVII Semana da Física Médica. [Doc. 22]**Propósito (i):** Participante**Propósito (ii):** Apresentação do resumo “A novel approach to delineate brain function and physiology under a semantic verbal fluency condition by a dual-echo ASL sequence.”**Ano:** 2018**Local:** Ribeirão Preto - SP, Brasil.**16. Evento:** ISMRM Benelux Chapter. [Doc. 23]**Propósito (i):** Ouvinte**Ano:** 2019**Local:** Leiden, the Netherlands.**17. Evento:** Organization for Human Brain Mapping Annual Meeting. [Doc. 24]**Propósito (i):** Participante**Propósito (ii):** Apresentação do resumo “Organization Of Semantic Verbal Fluency Brain Network Assessed By Dual-Echo Arterial Spin Labeling.”**Ano:** 2019**Local:** Rome, Italy.**18. Evento:** XVIII Semana da Física Médica. [Doc. 25]**Propósito (i):** Participante**Propósito (ii):** Apresentação do resumo “Diffuse Glioma assessed by non-negative least square fitting for IVIM-MRI.”**Ano:** 2019**Local:** Ribeirão Preto - SP, Brasil.**19. Evento:** MRTrax3 Workshop. [Doc. 26]**Propósito (i):** Ouvinte**Ano:** 2020**Local:** Ribeirão Preto - SP, Brasil.**20. Evento:** InBrain Workshop 2020: Advanced Brain Imaging. [Doc. 27]**Propósito (i):** Palestrante

Ano: 2020

Local: Ribeirão Preto - SP, Brasil.

- 21. Evento:** ISMRM 28th Annual Meeting & Exhibition. [Doc. 28]

Propósito (i): Participante

Ano: 2020

Local: Virtual.

- 22. Evento:** ESMRMB 37th Annual Meeting & Exhibition. [Doc. 29]

Propósito (i): Participante

Propósito (ii): Apresentação do resumo “Evaluation of IVIM-MRI acquisition parameters for clinical protocol optimization in high-grade glioma patients.”

Ano: 2020

Local: Virtual.

- 23. Evento:** ISMRM 29th Annual Meeting & Exhibition. [Doc. 30]

Propósito (i): Participante

Propósito (ii): Apresentação do resumo “The utility of IVIM maps in the assessment of microvascular perfusion of brain glioma.”

Propósito (iii): Apresentação do resumo “The Open Source Initiative for Perfusion Imaging (OSIPI) ASL MRI Challenge. In: Annual Meeting of the International Society of Magnetic Resonance in Medicine.”

Propósito (iv): Apresentação do resumo “Gaussian Mixture for Peak Identification in Non-Negative Least Squares Fitting of the IVIM Signal.”

Ano: 2021

Local: Virtual.

- 24. Evento:** Jornada Paulista de Radiologia 2021. [Doc. 31]

Propósito (i): Palestrante

Propósito (ii): Apresentação da aula “ASL: Física, Técnica, Sequências e Aplicações.”

Ano: 2021

Local: São Paulo - SP, Brasil.

- 25. Evento:** ISMRM Perfusion Workshop: from head to toe. [Doc. 32]

Propósito (i): Palestrante e Participante

Propósito (ii): Apresentação da palestra “Results of the OSIPI Challenges (ASL).”

Propósito (iii): Apresentação do resumo “Feasibility of Arterial Spin Labeling to Assess Blood-Brain Barrier Permeability in Clinical Environment: Application to Multiple Sclerosis Patients.”

Ano: 2022

Local: Los Angeles - CA, USA.

3.3 Obtenção de bolsa de estudo em instituições de renome científico ou cultural

- 1. Nível:** Mestrado. [Doc. 33]

Agência de Fomento: CAPES

Período: Março de 2013 à Junho de 2015

Local: Instituto de Física de São Carlos - SP, Brasil.

2. **Nível:** Doutorado [[Doc. 34](#)]

Agência de Fomento CNPq

Período: Fevereiro de 2016 à Janeiro de 2020

Local: Departamento de Física - Faculdade de Filosofia Ciências e Letras de Ribeirão Preto (FFCLRP - USP), Ribeirão Preto - SP, Brasil.

3. **Nível:** Doutorado Sanduíche [[Doc. 35](#)]

Agência de Fomento: PDSE - CAPES

Período: Novembro de 2018 à Abril de 2019

Local: Leiden University Medical Center, Leiden - the Netherlands.

4. **Nível:** Pós-Doutorado [[Doc. 36](#)]

Agência de Fomento: PDJ - CNPq

Período: Fevereiro de 2020 à Dezembro de 2020

Local: Faculdade de Medicina de Ribeirão Preto (FMRP - USP), Ribeirão Preto - SP.

4 Produção científica

4.1 Trabalhos aceitos em congressos

1. PASCHOAL, A. M.; LEONI, R. ; SANTOS, A. ; FOERSTER, B. U. ; PAIVA, F. F. **ASL Contrast Optimization in Multiphase STAR Labeling using Variable Flip Angle.** Organization for Human Brain Mapping, 2015, Honolulu. Proceedings of the Organization for Human Brain Mapping, 2015. v. 1. [Doc. 37]
2. Paschoal, A.M.; dos Santos, A.C.; Paiva, F.F.; Leoni, R.F. **Non-negative Least Squares Fitting for IVIM-MRI in Diffuse Glioma.** Congresso Brasileiro de Física Médica, 2019. [Doc. 38]
3. PASCHOAL, A.M.; SCHMID, S.; FRANKLIN, S.L.; LEONI, R.F.; OSCH, M.J.P.V. **3D GRASE readout optimization for time-encoded pCASL.** ESMRMB 2019, 36th Annual Scientific Meeting, 2019, Rotterdam, NL. October 3-5: Abstracts, Friday, 2019. v. 32. p. S152-S153. [Doc. 39]

4.2 Artigos Científicos Publicados em Periódicos Nacionais e Internacionais na sua área de atuação

1. PAIVA, F.F. ; FOERSTER, B.U. ; PASCHOAL, A.M. ; MOLL, F.F.T. ; MOLL NETO, J.N. **Otimização do Contraste em ASL Multi-fase.** Revista Brasileira de Física Médica (Online), v. 7, p. 41-44, 2013. [Doc. 40]
2. Silva, J.P.S.; Monaco, L.M.; Paschoal, A.M.; Oliveira, I.A; Leoni, R.F. **Effects of global signal regression and subtraction methods on resting-state functional connectivity using arterial spin labeling data.** Magnetic Resonance Imaging, v 51, p 151-157, 2018. doi: 10.1016/j.mri.2018.05.006 (Qualis A2) [Doc. 41]
3. Paschoal, A.M.; Leoni, R.F.; dos Santos, A.C.; Paiva, F.F. **Intravoxel incoherent motion MRI in neurological and cerebrovascular diseases.** NeuroImage-Clinical, v. 20, p. 705-714, 2018. doi: 10.1016/j.nicl.2018.08.030 (Qualis A1) [Doc. 42]
4. Paschoal, A.M.; Paiva, F.F.; Leoni, R.F. **Dual-Echo Arterial Spin Labeling for Brain Perfusion Quantification and Functional Analysis.** CONCEPTS IN MAGNETIC RESONANCE PART A, v. 2019, p. 1-7, 2019. doi: 10.1155/2019/5040465 [Doc. 43]
5. Paschoal, A.M.; Leoni, R.F.; Foerster, B.U.; dos Santos, A.C.; Pontes Neto, O.M.; Paiva, F.F. **Contrast optimization in arterial spin labeling with multiple post-labeling delays for cerebrovascular assessment.** Magnetic Resonance Materials in Physics, Biology and Medicine (MAGMA) v. online, 2020. doi: 10.1007/s10334-020-00883-z (Qualis A2) [Doc. 44]
6. PASCHOAL, A.M.; LEONI, R.F.; PASTORELLO, B.F.; OSCH, M.J.P.; **Three-dimensional gradient and spin-echo readout for time-encoded**

pseudo-continuous arterial spin labeling: Influence of segmentation factor and flow compensation. Magnetic Resonance in Medicine, v. 86, p. 1454-1462, 2021. doi: 10.1002/mrm.28807 (Qualis A1) [Doc. 45]

7. PASCHOAL, A.M.; SILVA, P.H.R.; RONDINONI, C.; ARRIGO, I.V.; PAIVA, F.F.; LEONI, R.F.; **Semantic verbal fluency brain network: delineating a physiological basis for the functional hubs using dual-echo ASL and graph theory approach.** Journal of Neural Engineering, v. 18, p. 1-15, 2021. doi:10.1088/1741-2552/ac0864 (Qualis A1) [Doc. 46]
8. PASCHOAL, A.M.; **Editorial for -Diffusion Tensor Imaging Reveals Altered Topological Efficiency of Structural Networks in Type-2 Diabetes Patients With and Without Mild Cognitive Impairment.** Journal of Magnetic Resonance Imaging, v.55, p. 928-929, 2021. doi:10.1002/jmri.27899 (Qualis A1) [Doc. 47]
9. Paschoal, A.M.; Zotin, M.C.Z.; COSTA, L.M.; Santos, A.C.; Leoni, R.F.; **Feasibility of intravoxel incoherent motion in the assessment of tumor microvasculature and blood-brain barrier integrity: a case-based evaluation of gliomas.** Magnetic Resonance Materials in Physics, Biology and Medicine (MAGMA) v.35, p. 17-27, 2020. doi: 10.1007/s10334-021-00987-0 (Qualis A2) [Doc. 48]

4.3 Dissertação de Mestrado

1. PASCHOAL, André Monteiro. Otimização do contraste em Arterial Spin Labeling multifase. 2015. Dissertação (Mestrado em Física Aplicada) - Instituto de Física de São Carlos, University of São Paulo, São Carlos, 2015. doi:10.11606/D.76.2015.tde-29092015-101918. Acesso em: 2020-09-15. Disponível online em: <https://teses.usp.br/teses/disponiveis/76/76132/tde-29092015-101918/pt-br.php>

4.4 Tese de doutorado

1. PASCHOAL, André Monteiro. Optimization and application of quantitative magnetic resonance imaging methods to analyze brain perfusion and function. 2019. Tese (Doutorado em Física Aplicada à Medicina e Biologia) - Faculdade de Filosofia, Ciências e Letras de Ribeirão Preto, University of São Paulo, Ribeirão Preto, 2020. doi:10.11606/T.59.2020.tde-19032020-104417. Acesso em: 2020-09-15. Disponível online em: <https://www.teses.usp.br/teses/disponiveis/59/59135/tde-19032020-104417/pt-br.php>

5 Experiências Didáticas Universitárias

5.1 Monitorias para disciplinas de graduação

1. **Disciplina:** Laboratório de Física Geral II [Doc. 49]

Departamento: Instituto de Física de São Carlos - IFSC - USP

Ano: 2015

Programa: Monitoria Institucional do IFSC.

Bolsa: Bolsa do IFSC

2. **Disciplina:** Processamento de imagens médicas [Doc. 50]

Departamento: Instituto de Física de São Carlos - IFSC - USP

Ano: 2015

Programa: Monitoria Institucional do IFSC.

Bolsa: Bolsa do IFSC

3. **Disciplina:** Imagens por Ressonância Magnética Nuclear em Biomedicina [Doc. 51]

Departamento: Departamento de Física - Faculdade de Filosofia, Ciências e Letras de Ribeirão Preto - FFCLRP - USP

Ano: 2017

Programa: Monitor do Programa de Aperfeiçoamento ao Ensino (PAE).

Bolsa: Sem bolsa

4. **Disciplina:** Física I (teórica vinculada)

Departamento: Departamento de Física - Faculdade de Filosofia, Ciências e Letras de Ribeirão Preto - FFCLRP - USP [Doc. 52]

Ano: 2019

Programa: Monitor do Programa de Aperfeiçoamento ao Ensino (PAE).

Bolsa: Bolsista PAE

5.2 Membro de comissão avaliadora

1. **Evento:** Simpósio Internacional de Iniciação Científica e Tecnológica da USP - SIICUSP. [Doc. 53]

Departamento: Departamento de Física - Faculdade de Filosofia, Ciências e Letras de Ribeirão Preto - FFCLRP - USP

Ano: 2019

2. **Evento:** XVIII Semana da Física Médica, 2019 [Doc. 54]

Departamento: Departamento de Física - Faculdade de Filosofia, Ciências e Letras de Ribeirão Preto - FFCLRP - USP

Ano: 2019

6 Coordenação de Eventos e Conferencista

6.1 Comissão Organizadora de Eventos Internacional, Nacional, Regional ou Local

1. Program Committee Member of the InBrain Workshop 2020: Advanced Brain Imaging [Doc. [55](#)]
2. III Escola de Inverno em Física Aplicada à Medicina e Biologia (III EIFAMB). [Doc. [56](#)]

A Documentos comprobatórios

Esta seção contém os documentos comprobatórios referentes às atividades listadas neste memorial.

1 Diploma de Graduação em Ciências Físicas e Biomoleculares, junto ao Instituto de Física de São Carlos (IFSC - USP)

Esta subseção apresenta o diploma de graduação do candidato.



REPÚBLICA FEDERATIVA DO BRASIL
UNIVERSIDADE DE SÃO PAULO
INSTITUTO DE FÍSICA DE SÃO CARLOS

O REITOR DA UNIVERSIDADE DE SÃO PAULO,
NO USO DE SUAS ATRIBUIÇÕES,
CONFERE A

ANDRÉ MONTEIRO PASCHOAL



DE NACIONALIDADE BRASILEIRA,
PORTADOR DA CÉDULA DE IDENTIDADE
RG Nº 44.813.973-X SP,
NASCIDO EM 4 DE AGOSTO DE 1988
E NATURAL DO ESTADO DE SÃO PAULO,
O GRAU DE



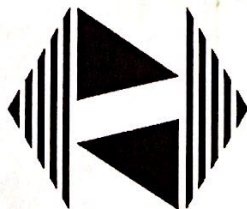
BACHAREL EM CIÊNCIAS FÍSICAS E BIOMOLECULARES

OBTIDO EM 19 DE DEZEMBRO DE 2012,
NO CURSO DE CIÊNCIAS FÍSICAS E BIOMOLECULARES.
E, PARA QUE POSSA GOZAR DE TODOS OS DIREITOS E
PRERROGATIVAS LEGAIS, OUTORGA-LHE O PRESENTE DIPLOMA.

SÃO CARLOS, 17 DE JANEIRO DE 2013.

João Grandino Rodas
REITOR
PROF. DR. JOÃO GRANDINO RODAS

Antônio Carlos Hernandes
DIRETOR DO IFSC
PROF. DR. ANTONIO CARLOS HERNANDES



DIPLOMADO
ANDRÉ MONTEIRO PASCHOAL

RECONHECIDO PELA PORTARIA CEE/GP Nº
558 DE 21/12/2011, D.O.E. DE 22/12/2011

<p>UNIVERSIDADE DE SÃO PAULO SECRETARIA GERAL DIVISÃO DE REGISTROS ACADÉMICOS DIPLOMA REGISTRADO SOB Nº UGR0001223 PROCESSO Nº 2013.1.85.76.0 NOS TERMOS DO ARTIGO 48 DA LEI 9394/96. SÃO PAULO, 24 DE JANEIRO DE 2013.</p> <p></p> <p>FERNANDA LOPEZ TONON TÉCNICA PARA ASSUNTOS ADMINISTRATIVOS</p> <p>DE ACORDO.</p> <p></p> <p>PROF. DR. RUBENS BEÇAK SECRETÁRIO GERAL</p>

SECRETARIA GERAL
DIVISÃO DE REGISTROS ACADÉMICOS
O PRESENTE DOCUMENTO, EXPEDIDO PELA
UNIVERSIDADE DE SÃO PAULO É AUTÊNTICO.
SÃO PAULO, 24 DE JANEIRO DE 2013.



ARIOSVALDO BEZERRA DE SOUSA

Nº 0169538

2 Diploma de Mestre em Ciências, junto ao Instituto de Física de São Carlos (IFSC - USP)

Esta subseção apresenta o diploma de Mestre em Ciências do candidato.



REPÚBLICA FEDERATIVA DO BRASIL
UNIVERSIDADE DE SÃO PAULO
INSTITUTO DE FÍSICA DE SÃO CARLOS

O REITOR DA UNIVERSIDADE DE SÃO PAULO,
NO USO DE SUAS ATRIBUIÇÕES,
CONFERE A

ANDRÉ MONTEIRO PASCHOAL

DE NACIONALIDADE BRASILEIRA,
PORTADOR DA CÉDULA DE IDENTIDADE
RG Nº 44.813.973-X SP,
NASCIDO EM 4 DE AGOSTO DE 1988
E NATURAL DO ESTADO DE SÃO PAULO,

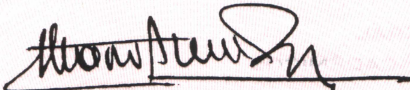


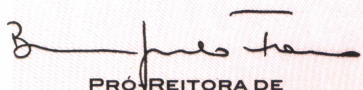
O TÍTULO DE

MESTRE EM CIÊNCIAS

OBTIDO EM 22 DE JULHO DE 2015,
NO PROGRAMA: FÍSICA,
ÁREA DE CONCENTRAÇÃO: FÍSICA APLICADA.
E, PARA QUE POSSA GOZAR DE TODOS OS DIREITOS E
PRERROGATIVAS LEGAIS, OUTORGA-LHE O PRESENTE DIPLOMA.

SÃO CARLOS, 21 DE AGOSTO DE 2015.


REITOR
PROF. DR. MARCO ANTONIO ZAGO


PRÓ-REITORA DE
PÓS-GRADUAÇÃO

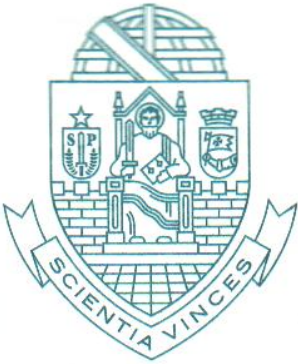
PROFA. DRA. BERNADETTE
DORA GOMBOSSY DE MELO
FRANCO



DIPLOMADO
ANDRÉ MONTEIRO PASCHOAL

3 Diploma de Doutor em Ciências, junto ao Departamento de Física da Faculdade de Filosofia, Ciências e Letras de Ribeirão Preto (FFCLRP) da Universidade de São Paulo (USP)

Esta subseção apresenta o diploma de Doutor em Ciências do candidato.



REPÚBLICA FEDERATIVA DO BRASIL
UNIVERSIDADE DE SÃO PAULO
FACULDADE DE FILOSOFIA, CIÊNCIAS E LETRAS DE
RIBEIRÃO PRETO

O REITOR DA UNIVERSIDADE DE SÃO PAULO,
NO USO DE SUAS ATRIBUIÇÕES,
CONFERE A

ANDRÉ MONTEIRO PASCHOAL

DE NACIONALIDADE BRASILEIRA,
PORTADOR DA CÉDULA DE IDENTIDADE
RG Nº 44.813.973-X SP,
NASCIDO EM 04 DE AGOSTO DE 1988
E NATURAL DO ESTADO DE SÃO PAULO,

O TÍTULO DE

DOUTOR EM CIÊNCIAS

OBTIDO EM 23 DE JANEIRO DE 2020,
NO PROGRAMA: FÍSICA APlicada à MEDICINA E BIOLOGIA.
E, PARA QUE POSSA GOZAR DE TODOS OS DIREITOS E
PRERROGATIVAS LEGAIS, OUTORGA-LHE O PRESENTE DIPLOMA.

RIBEIRÃO PRETO, 11 DE FEVEREIRO DE 2020.

PROF. DR. VAHAN AGOPYAN

PRÓ-REITOR DE PÓS-
GRADUAÇÃO
PROF. DR. CARLOS GILBERTO
CARLOTTI JUNIOR

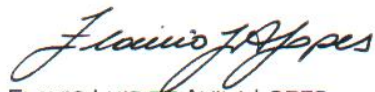


DIPLOMADO
ANDRÉ MONTEIRO PASCHOAL

PROGRAMA RECONHECIDO DE ACORDO COM O
DISPOSTO NA PORTARIA MEC Nº 609 DE
14/03/2019, DOU DE 18/03/2019.

UNIVERSIDADE DE SÃO PAULO
SECRETARIA GERAL
DIVISÃO DE REGISTROS ACADÉMICOS

DIPLOMA REGISTRADO SOB N° UPG039477
PROCESSON° 2020.5.72.59.0
NOS TERMOS DO ARTIGO 48 DA LEI 9394/96.
SÃO PAULO, 11 DE FEVEREIRO DE 2020.



FLÁVIO LUIS DE ÁVILA LOPES
TÉCNICO ACADÉMICO

DE ACORDO.



PROF. DR. PEDRO VITORIANO DE OLIVEIRA
SECRETÁRIO GERAL

SECRETARIA GERAL
DIVISÃO DE REGISTROS ACADÉMICOS

O PRESENTE DOCUMENTO, EXPEDIDO PELA
UNIVERSIDADE DE SÃO PAULO É AUTÊNTICO.

SÃO PAULO, 11 DE FEVEREIRO DE 2020.



ARIOSVALDO BEZERRA DE SOUSA

Nº 0385719

4 Certificado de Pós Doutorado, junto à Faculdade de Medicina de Ribeirão Preto (FMRP) da Universidade de São Paulo (USP)

Esta subseção apresenta o certificado de conclusão do pós doutorado junto à FMRP do candidato.

ATESTADO DE CONCLUSÃO

O Pró-Reitor de Pesquisa da Universidade de São Paulo, no uso de suas atribuições, atesta que ANDRÉ MONTEIRO PASCHOAL, de nacionalidade BRASILEIRA, portador(a) do documento tipo RG número 44813973X, nascido(a) em 4 de AGOSTO de 1988 e natural do Estado de São Paulo, concluiu o PROGRAMA DE PÓS-DOUTORADO, realizado no Departamento de Imagens Médicas, Hematologia e Oncologia Clínica da Faculdade de Medicina de Ribeirão Preto.

PROJETO: DESENVOLVIMENTO DE MÉTODOS QUANTITATIVOS E NÃO INVASIVOS DE IMAGEM POR RESSONÂNCIA MAGNÉTICA PARA OBTENÇÃO DE MEDIDAS DE PERMEABILIDADE DA BARREIRA HEMATO-ENCEFÁLICA E SUA APLICAÇÃO EM PACIENTES COM GLIOMA DIFUSO

SUPERVISOR: PROF. DR. ANTONIO CARLOS DOS SANTOS

PERÍODO: 01/02/2020 a 31/01/2021

CARGA HORÁRIA: 1580 HORAS

CNPq - Conselho Nacional de Desenvolvimento Científico e Tecnológico

Sylvio Roberto Accioly Canuto

PRÓ-REITOR DE PESQUISA

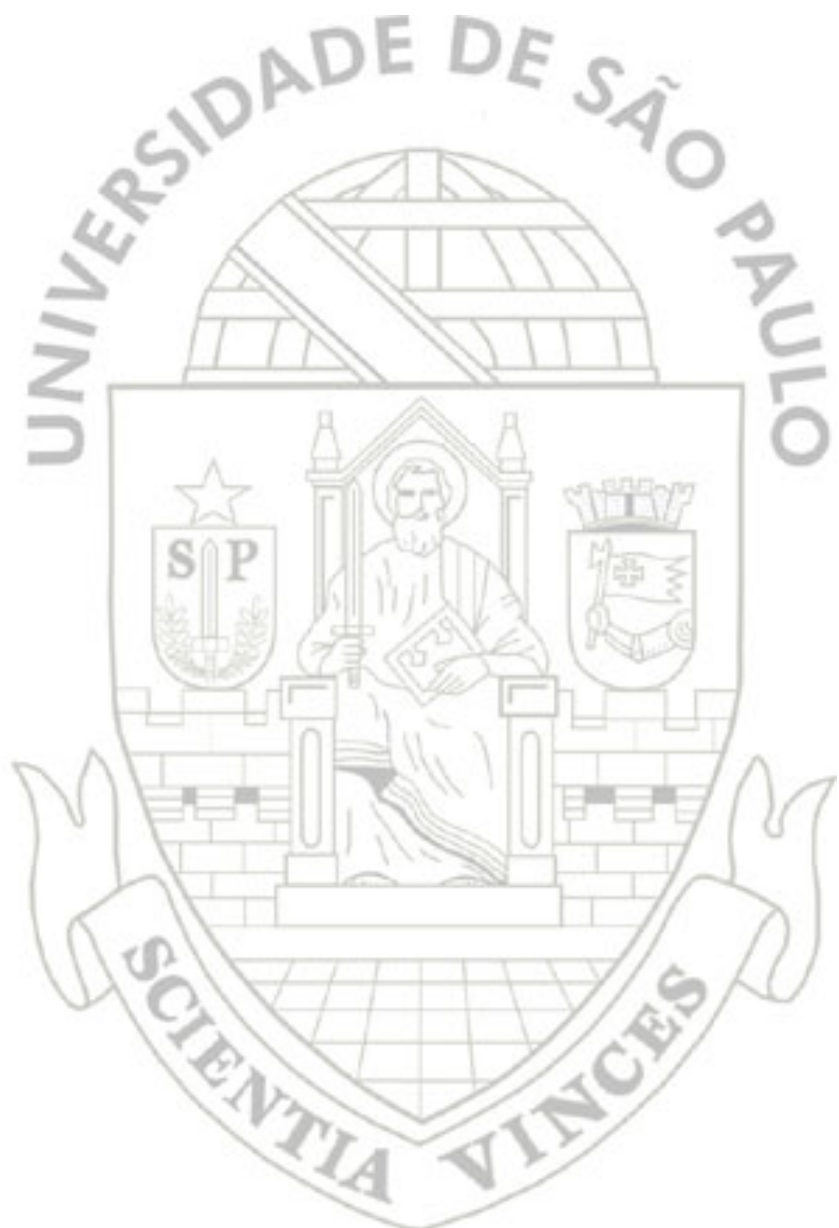
Documento emitido às 16:35:22 horas do dia 17/08/2021 (hora e data de Brasília).

Código de Controle: BJT2-7PXC-NTH8-GXLF

A autenticidade deste documento pode ser verificada na página da Universidade de São Paulo
<https://uspdigital.usp.br/webdoc/>

Atividades Desenvolvidas

Desenvolvimento de projeto de pesquisa, orientação de alunos de iniciação científica e de pós-graduação (1580 horas)



5 Prêmios de mérito científico

Esta subseção apresenta o certificado de obtenção do Prêmio **OHBM Travel Award**, concedido no Encontro Anual da *Organization for Human Brain Mapping* no ano de 2019, realizado em Roma - Itália.



Organization for
Human Brain Mapping
Advancing Understanding of the Human Brain

In recognition of a top rated abstract,
the Program Committee of the Organization for Human Brain Mapping presents

Andre Monteiro Paschoal

with a

Travel Stipend Award

"Organization of semantic verbal fluency brain network assessed by dual-echo arterial spin labeling"

25th Annual Meeting of the Organization of Human Brain Mapping
Rome, Italy / June 2019

Vin
D.C.

Vince Calhoun, 2019 Council Chair

Lucina Q. Uddin

Lucina Uddin, 2019 Program Committee Chair

6 Prêmios de mérito científico - Prêmio CAPES de Teses

Esta subseção apresenta o certificado de obtenção da Menção Honrosa no **Prêmio CAPES de Teses 2021**, concedido pela CAPES no ano de 2021.



A Coordenação de Aperfeiçoamento de Pessoal de Nível Superior - CAPES outorga a

ANDRE MONTEIRO PASCHOAL

a Menção Honrosa no Prêmio CAPES de Tese – Edição 2021, da área de MEDICINA II , pela tese “OPTIMIZAÇÃO E APLICAÇÃO DE MÉTODOS QUANTITATIVOS DE IMAGEM POR RESSONÂNCIA MAGNÉTICA PARA ANALISAR PERFUSÃO SANGUÍNEA E FUNÇÕES CEREBRAIS” defendida sob orientação de RENATA FERRANTI LEONI e coorientação de FERNANDO FERNANDES PAIVA, do Programa de Pós-Graduação em FÍSICA APLICADA À MEDICINA E BIOLOGIA, da UNIVERSIDADE DE SÃO PAULO (RIBEIRÃO PRETO) - USP/RP.

3 de setembro de 2021

Claudia Mansani Queda de Toledo

Presidente da CAPES



MINISTÉRIO DA
EDUCAÇÃO



7 Participação em Eventos Científicos (com apresentação de trabalho ou oferecimento de cursos, palestras ou debates)

Esta subseção apresenta o comprovante da participação na III Semana Integrada do Instituto de Física de São Carlos com seus respectivos propósitos.

CERTIFICADO

Certificamos que

André Monteiro Paschoal

apresentou o trabalho intitulado “Implementação de metodologias de imagens por ressonância magnética para medidas não invasivas de perfusão sanguínea cerebral” na sessão de pôsteres do Workshop de Pós-Graduação e Iniciação Científica da III Semana Integrada do Instituto de Física de São Carlos - SIFSC 3 ocorrida no período de 30 de Setembro a 04 de Outubro de 2013.



Prof. Dr. Antonio Carlos Hernandes
Diretor IFSC - USP



8 Participação em Eventos Científicos (com apresentação de trabalho ou oferecimento de cursos, palestras ou debates)

Esta subseção apresenta o comprovante da participação na IV Semana Integrada do Instituto de Física de São Carlos com seus respectivos propósitos.

CERTIFICADO

Certificamos que

André Monteiro Paschoal

apresentou o trabalho intitulado “Maximização do contraste ASL em sequências multi-fase com a introdução de uma modulação no ângulo de flip” na sessão de pôsteres do Workshop de Pós-Graduação e Iniciação Científica da IV Semana Integrada do Instituto de Física de São Carlos - SIFSC 4 ocorrida no período de 6 a 9 de Outubro de 2014.

PROF. DR. OTÁVIO HENRIQUE THIEMANN
PRESIDENTE DA COMISSÃO DE PÓS-GRADUAÇÃO
IFSC - USP

PROF. DR. TITO JOSÉ BONAGAMBA
DIRETOR
IFSC - USP

9 Participação em Eventos Científicos (com apresentação de trabalho ou oferecimento de cursos, palestras ou debates)

Esta subseção apresenta o comprovante da participação no I Transatlantic Workshop on Methods for Multimodal Neurosciences Studies com seus respectivos propósitos.

I Transatlantic Workshop on methods for multimodal neuroscience studies

São Pedro, SP, Brazil

Certificate of Participation

This is to certify that

André Monteiro Paschoal

has participated in the I Transatlantic Workshop on Methods for Multimodal Neuroscience Studies held in São Pedro, SP, Brazil, March 12-14, 2014.



Prof. Dr. Fernando Fernandes Paiva
Chair - CIERMag - IFSC / USP

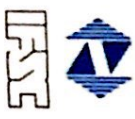


Prof. Dr. Alberto Tannus
CIERMag - IFSC / USP

 The University of
Nottingham

 FAPESP

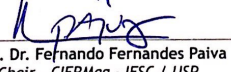
 CNPq





Certificate

This is to certify that the poster entitled **CONTRAST OPTIMIZATION IN MULTIPHASE ASL** by **Paschoal, A.M.; Paiva, F.F.** has been presented in the **I Transatlantic Workshop on Methods for Multimodal Neuroscience Studies** held in São Pedro, SP, Brazil, March 12-14, 2014.


Prof. Dr. Fernando Fernandes Paiva
Chair - CIERMag - IFSC / USP


Prof. Dr. Alberto Tannús
CIERMAG-IFSC, / USP



Scanned with CamScanner

10 Participação em Eventos Científicos (com apresentação de trabalho ou oferecimento de cursos, palestras ou debates)

Esta subseção apresenta o comprovante da participação na V Semana Integrada do Instituto de Física de São Carlos com seus respectivos propósitos.



CERTIFICADO

V Semana Integrada do Instituto de Física de São Carlos



Certificamos que

André Monteiro Paschoal

apresentou o trabalho intitulado “Desenvolvimento de uma plataforma multimodal para o estudo da hemodinâmica cerebral: uma abordagem combinando ASL e NIRS” na sessão de pôsteres do Workshop de Pós-Graduação e Iniciação Científica da V Semana Integrada do Instituto de Física de São Carlos - SIFSC 5 ocorrida no período de 28 de Setembro a 02 de Outubro de 2015.

Tito J. Bonagamba

Prof. Dr. TITO JOSÉ BONAGAMBA
Diretor
IFSC-USP

11 Participação em Eventos Científicos (com apresentação de trabalho ou oferecimento de cursos, palestras ou debates)

Esta subseção apresenta o comprovante da participação na XV Semana da Física Médica com seus respectivos propósitos.



Universidade de São Paulo
Departamento de Física da Faculdade de Filosofia, Ciências e
Letras de Ribeirão Preto



Certificamos que **André Monteiro Paschoal** participou da XV Semana de Física Médica e 1º Simpósio de Física Médica, organizada pelo Departamento de Física da Faculdade de Filosofia, Ciências e Letras de Ribeirão Preto, realizado de 07 a 11 de Novembro de 2016. Carga horária adquirida: 1 hora e 30 minutos.

Prof. Dr. Nelson Alves

Prof. Dr. Alessandro Martins

12 Participação em Eventos Científicos (com apresentação de trabalho ou oferecimento de cursos, palestras ou debates)

Esta subseção apresenta o comprovante da participação no XXII Congresso Brasileiro de Física Médica com seus respectivos propósitos.



CERTIFICADO DE APRESENTAÇÃO DE TRABALHO

Certificamos que trabalho intitulado,

MAPAS DE TEMPO DE TRANSITO ARTERIAL UTILIZANDO ARTERIAL SPIN LABELING

de autoria de: André Monteiro Paschoal; Fernando Fernandes Paiva; Renata Ferranti Leoni; foi apresentado na forma **Poster**, no **XXII Congresso Brasileiro de Física Médica**, realizado no Centro de Convenções de Ribeirão Preto, Ribeirão Preto, SP, Brasil, de 06 a 09 de setembro de 2017.

Ribeirão Preto, 09 de setembro de 2017

Comitê Científico
XXII Congresso Brasileiro de Física Médica

Autenticação: 877869423192034090000000

A autenticidade deste documento pode ser confirmada em: <http://www.sisconevedev.com.br/AutenticaCertificados2.aspx>

www.cbfm2017.com.br

13 Participação em Eventos Científicos (com apresentação de trabalho ou oferecimento de cursos, palestras ou debates)

Esta subseção apresenta o comprovante da participação no Seminário semanal do programa de Física Aplicada à Medicina e Biologia com seus respectivos propósitos.



UNIVERSIDADE DE SÃO PAULO

Faculdade de Filosofia, Ciências e Letras – Departamento de Física.

Programa de Pós-Graduação em Física Aplicada à Medicina e Biologia

DECLARAÇÃO

Declaro que o Doutorando **André Monteiro Paschoal** ministrou o seminário "**Improving Arterial Spin Labeling Acquisition to Reduce the Effect of Delayed Arrival Time**" para os alunos do Programa de Pós-Graduação em Física Aplicada à Medicina e Biologia da Faculdade de Filosofia, Ciências e Letras de Ribeirão Preto da Universidade de São Paulo, no dia 08 de março de 2017.

Ribeirão Preto, 08 de março de 2017.


Antonio Carlos Roque da Silva Filho
Vice-Coordenador do Programa de Pós-Graduação
de Física Aplicada à Medicina e Biologia

14 Participação em Eventos Científicos (com apresentação de trabalho ou oferecimento de cursos, palestras ou debates)

Esta subseção apresenta o comprovante da participação na palestra “O Cérebro estatístico: desafios científicos do CEPID NeuroMat” com seus respectivos propósitos.

CERTIFICADO

Certifico para os devidos fins que **André Monteiro Paschoal** participou, como ouvinte, da conferência "**O Cérebro estatístico: desafios científicos do CEPIID NeuroMat**", organizada pelo Instituto de Estudos Avançados da USP, Polo Ribeirão Preto, no dia 9 de junho de 2017, com carga horária de duas horas.

Por ser verdade, firmo o presente.

Prof. Dr. Fernando Queiroz Cunha
Coordenador do Instituto de Estudos Avançados
Polo Ribeirão Preto

15 Participação em Eventos Científicos (com apresentação de trabalho ou oferecimento de cursos, palestras ou debates)

Esta subseção apresenta o comprovante da participação no 8º Simpósio de Instrumentação e Imagens Médicas (SIIM) e 7º Simpósio de Processamento de Sinais (SPS) com seus respectivos propósitos.



8º Simpósio de Instrumentação e Imagens Médicas
7º Simpósio de Processamento de Sinais

CERTIFICADO DE PARTICIPAÇÃO

Certificamos que **André Monteiro Paschoal** participou do VIII Simpósio de Instrumentação e Imagens Médicas (SIIM) / VII Simpósio de Processamento de Sinais (SPS), realizado nos dias 29, 30 de novembro e 01 de dezembro de 2017, em São Bernardo do Campo, na Universidade Federal do ABC (UFABC).

A handwritten signature in blue ink.

Prof. Diogo Coutinho Soriano

Coordenador geral do Oitavo Simpósio de Instrumentação e Imagens Médicas

A handwritten signature in blue ink.

Prof. Ricardo Suyama

Coordenador geral do Sétimo Simpósio de Processamento de Sinais

16 Participação em Eventos Científicos (com apresentação de trabalho ou oferecimento de cursos, palestras ou debates)

Esta subseção apresenta o comprovante da participação no ISMRM 25th Annual Meeting & Exhibition com seus respectivos propósitos.

Obs: Ese congresso não emite certificado de apresentação de trabalhos, apenas de participação no evento.



Certificate of Participation

*The International Society
for Magnetic Resonance in Medicine*

Certifies that

Andre M. Paschoal, M.Sc.

has participated at the live event

ISMRM 25th Annual Meeting & Exhibition

22-27 April 2017, Honolulu

and has attended 34.75 hours.

A handwritten signature in cursive script that reads "Candace Spradley".

Candace Spradley
Director of Education

The International Society for Magnetic Resonance in Medicine designates this live activity for a maximum of 46.00 AMA PRA Category 1 Credits™. Physicians should claim only the credit commensurate with the extent of their participation in the activity.

The International Society for Magnetic Resonance in Medicine is accredited by the Accreditation Council for Continuing Medical Education to provide continuing medical education for physicians.

Session Name	Session Date	Hours
Physics for Physicists - Morning	Saturday, 22 April 2017 (8:15 AM - 12:15 PM)	4.00
The Basics of Perfusion & Permeability Imaging	Saturday, 22 April 2017 (1:15 PM - 4:45 PM)	3.50
Image Acquisition & Reconstruction	Sunday, 23 April 2017 (8:30 AM - 12:00 PM)	3.50
Recent Advances in Diffusion, Perfusion & fMRI	Sunday, 23 April 2017 (1:15 PM - 4:45 PM)	3.50
fMRI: Best Practices & Cautionary Tales: Acquisition & Pathology	Monday, 24 April 2017 (7:00 AM - 7:50 AM)	0.75
Combining fMRI with Advanced Neurotechniques	Monday, 24 April 2017 (8:15 AM - 10:15 AM)	2.00
Cerebrovascular Disease: Intracranial & Extracranial	Monday, 24 April 2017 (1:45 PM - 3:45 PM)	2.00
fMRI: Best Practices & Cautionary Tales: Analysis & Resting-State Indices	Tuesday, 25 April 2017 (7:00 AM - 7:50 AM)	0.75
From Aging Brain to Alzheimer's Disease	Tuesday, 25 April 2017 (8:15 AM - 10:15 AM)	2.00
fMRI: Mechanisms & Physiology	Tuesday, 25 April 2017 (1:45 PM - 3:45 PM)	2.00
Dynamic Functional Connectivity MRI: Approaches & Mechanisms	Wednesday, 26 April 2017 (7:00 AM - 7:50 AM)	0.75
Arterial Spin Labeling: Making it More Robust & Informative	Wednesday, 26 April 2017 (8:15 AM - 10:15 AM)	2.00
fMRI Connectivity	Wednesday, 26 April 2017 (4:15 PM - 6:15 PM)	2.00
Combining Structural and Functional Brain Connectivity	Thursday, 27 April 2017 (8:15 AM - 10:15 AM)	2.00
fMRI: Multimodal & Neuromodulation	Thursday, 27 April 2017 (1:00 PM - 3:00 PM)	2.00
fMRI Clinical & Neuroscience Applications	Thursday, 27 April 2017 (3:30 PM - 5:30 PM)	2.00

Subject: ISMRM 2017 Annual Meeting Notification for Abstract Tracking
Number 6117
From: <ISMRM2017@mirasmart.com>
Date: 30/01/2017 20:58
To: <andre.paschoal@usp.br>

Re: "Improving Arterial Spin Labeling Acquisition to Reduce the Effect of Delayed Arrival Time"

Dear Colleague:

Thank you for submitting an abstract to be considered for presentation at the scientific sessions of the ISMRM 25th Annual Meeting in Hawaii. I am pleased to inform you that your abstract (title above), has been selected for presentation as a traditional poster at this year's Scientific Meeting.

A poster presentation is 60 minutes in length. To maximize opportunities for discussion, one half of the posters will be presented at a time by authors at each of the poster sessions. Your poster is tentatively assigned to be presented during the following session:

Session: Pulse Sequences
Day/Date: Monday, April 24, 2017
Session Time: 08:15

Program numbers will be assigned later in February. When you arrive at the meeting, however, please verify the time of your session in the official program in case there have been last-minute changes.

The Annual Meeting has now moved to a 6-day schedule. The educational program will begin on the morning of Saturday April 22 and the meeting will end with the closing ceremony and party on the evening of Thursday, April 27. Unlike previous years, there will be no scientific sessions held on Friday morning.

The opening ceremonies, which will include gold medal presentations and the Lauterbur lecture, will take place on Sunday evening immediately prior to the opening party.

Please be sure to note the change from the usual 6.5-day schedule when making your travel arrangements.

The tentative schedule has been posted on the ISMRM website at ismrm.org/17/.

Educational, Clinical, New Entrant, and E.K. Zavoisky Stipend Applicants

should NOT register for the meeting until they have been notified of the status of their stipend application.

Each presenter is assigned a poster surface which measures 36 inches (91.44 cm) wide and 36 inches (91.44 cm) high. For your convenience, helpful information regarding poster presentations is available at our website (coming soon.) Be sure to monitor the website for current news.

You will be informed of your program number before the meeting. When you arrive at the meeting please verify your program number in the Program in case there have been last minute changes.

The meeting Proceedings will be published online only, with the full text of all accepted abstracts available to advance registrants on 7 April, 2017. Submission of your work constituted a commitment by the author(s) to present if invited. Unexcused failure to present will jeopardize participation in future ISMRM programs.

Please note that, while every effort has been made to honor authors' choices of traditional or e-poster formats, because of thematic or space considerations, some abstracts were not assigned the preferred format. Authors who submitted more than one paper will receive a separate letter indicating the committee's decision on each.

For a list of all abstracts accepted for presentation at the Annual Meeting, please go to http://www.ismrm.org/17/accepted_abstracts.pdf

The deadline for early registration is 14 March 2017, and the deadline for housing is 21 March 2017. Please visit <http://www.ismrm.org/2017-annual-meeting-exhibition/> for information.

On behalf of the Annual Meeting Program Committee, I thank you in advance for your participation in this year's meeting. Our members and attendees look forward to learning about your work.

Best regards,

Scott Reeder, Chair
ISMRM 25th Annual Meeting

Disclaimer

The information contained in this communication from the sender is confidential. It is intended solely for use by the recipient and others authorized to receive it. If you are not the recipient, you are hereby notified that any disclosure, copying, distribution or taking action in relation of the contents of this information is strictly prohibited and may be unlawful.

This email has been scanned for viruses and malware, and may have been automatically archived by **Mimecast Ltd**,

an innovator in Software as a Service (SaaS) for business. Providing a **safer** and **more useful** place for your human generated data. Specializing in; Security, archiving and compliance. To find out more [Click Here](#).

17 Participação em Eventos Científicos (com apresentação de trabalho ou oferecimento de cursos, palestras ou debates)

Esta subseção apresenta o comprovante da participação no 4º BRAINN Congress com seus respectivos propósitos.

4th BRAINN Congress - 2017

CERTIFICADO

Declaro que André Monteiro Paschoal participou do evento
4th BRAINN Congress, realizado em 27 a 29 de Março de 2017,
no Auditório da Faculdade de Ciências Médicas da UNICAMP.

Prof. Dr. Li Li Min
Coordenador de Educação e
Difusão do Conhecimento

Prof. Dr. Fernando Cendes
Coordenador Geral do Programa
CEPID BRAINN

Prof. Dr. Roberto Covolan
Coordenador de Transferência de
Tecnologia



18 Participação em Eventos Científicos (com apresentação de trabalho ou oferecimento de cursos, palestras ou debates)

Esta subseção apresenta o comprovante da participação no 5º BRAINN Congress com seus respectivos propósitos.

5th BRAINN Congress - 2018

CERTIFICADO

Certificamos que o trabalho intitulado “**Simultaneous assessment of CBF and brain function through Dual-Echo Arterial Spin Labeling**”, de autoria de André Paschoal, Fernando Paiva, Renata Leoni, foi apresentado na modalidade oral durante o **5th BRAINN Congress**, realizado de 09 a 11 de abril de 2018, no Auditório da Faculdade de Ciências Médicas da UNICAMP.

Prof. Dr. Li Li Min
Coordenador de Educação e
Difusão do Conhecimento

Prof. Dr. Fernando Cendes
Coordenador Geral do Programa
CEPID BRAINN

Prof. Dr. Roberto Covolan
Coordenador de Transferência de
Tecnologia

19 Participação em Eventos Científicos (com apresentação de trabalho ou oferecimento de cursos, palestras ou debates)

Esta subseção apresenta o comprovante da participação no Joint Annual Meeting ISMRM-ESMRMB com seus respectivos propósitos.

Obs: Ese congresso não emite certificado de apresentação de trabalhos, apenas de participação no evento.



Certificate of Participation

*The International Society
for Magnetic Resonance in Medicine*

Certifies that

Andre M. Paschoal, M.Sc.

has participated at the live event

Joint Annual Meeting ISMRM-ESMRMB

16 - 21 June 2018

and has attended 25.5 hours.

A handwritten signature in black ink, appearing to read "Melissa Simcox".

Melissa Simcox
Director of Education

The International Society for Magnetic Resonance in Medicine designates this live activity for a maximum of 46.00 AMA PRA Category 1 Credits™. Physicians should claim only the credit commensurate with the extent of their participation in the activity.

The International Society for Magnetic Resonance in Medicine is accredited by the Accreditation Council for Continuing Medical Education to provide continuing medical education for physicians.

Session Name	Session Date	Hours
Basics of Perfusion Imaging	Sunday, 17 June 2018 (8:00 AM - 11:28 AM)	3.50
Advanced Topics in Perfusion MRI	Sunday, 17 June 2018 (1:15 PM - 4:30 PM)	3.25
Is ASL Ready to Replace Contrast-Agent Perfusion Methods in the Clinic?	Monday, 18 June 2018 (7:00 AM - 7:50 AM)	0.75
fMRI: Physiology & Neurovascular Coupling	Monday, 18 June 2018 (8:15 AM - 10:15 AM)	2.00
Quantitative Neurovascular Imaging Methods	Monday, 18 June 2018 (1:45 PM - 3:45 PM)	2.00
Arterial Spin Labeling	Monday, 18 June 2018 (4:15 PM - 6:15 PM)	2.00
Application of Neurovascular Methods	Tuesday, 19 June 2018 (8:15 AM - 10:15 AM)	2.00
Perfusion & Permeability	Tuesday, 19 June 2018 (1:45 PM - 3:45 PM)	2.00
Diffusion: Validation	Wednesday, 20 June 2018 (8:15 AM - 10:15 AM)	2.00
Quantitative Neuroimaging	Wednesday, 20 June 2018 (1:45 PM - 3:45 PM)	2.00
Diffusion MRI: Applications	Thursday, 21 June 2018 (8:00 AM - 10:00 AM)	2.00
Diffusion MRI: Acquisition & Artifact Correction	Thursday, 21 June 2018 (3:30 PM - 5:30 PM)	2.00

Subject: ISMRM 2018 Annual Meeting Notification for Abstract Tracking
Number 8049
From: <ISMRM2018@mirasmart.com>
Date: 02/02/2018 21:03
To: <andre.paschoal@usp.br>

Re: "Regularized nonnegative least-square fitting for intravoxel incoherent motion data processing: a simulation study"

Dear Colleague:

Thank you for submitting an abstract to be considered for presentation at the scientific sessions of the Joint Annual Meeting ISMRM-ESMRMB in Paris, France.

I am pleased to inform you that your abstract (title above), has been selected for presentation as a traditional printed poster at this year's Scientific Meeting.

A poster presentation is 60 minutes in length. To maximize opportunities for discussion, one half of the posters will be presented at a time by authors at each of the poster sessions. Your poster is tentatively assigned to be presented during the following session:

Session: Diffusion MRI: signal reconstruction and representation
Day/Date: Tuesday, 19 June 2018
Session Time: 08:15

The tentative schedule has been posted on the ISMRM website at www.ismrm.org/18m/. Note that the meeting will run from Saturday through Thursday, with the same broad format as the 2017 Annual Meeting.

Program numbers will be assigned later in March. When you arrive at the meeting, however, please verify the time of your session in the official program in case there have been last-minute changes.

Authors who submitted more than one abstract will receive a separate letter indicating the outcome for each submission.

Educational, Clinical, New Entrant, and E. K. Zavoisky Stipend Applicants should NOT register for the meeting until they have been notified of the status of their stipend application. Notifications of stipend awards will be sent out by 16 February 2018.

Each presenter is assigned a poster surface which measures 36 inches (91.44 cm) wide and 36 inches (91.44 cm) high. For your convenience, helpful information regarding poster presentations is available at our website (coming

soon). Be sure to monitor the website for current news.

You will be informed of your program number before the meeting. When you arrive at the meeting, please verify your program number in the Program-at-a-Glance in case there have been last-minute changes.

The meeting Proceedings will be published online only, with the full text of all accepted abstracts available to advance registrants on 01 June 2018.

Submission of your work constituted a commitment by the author(s) to present if invited. Unexcused failure to present will jeopardize participation in future ISMRM programs.

Please note that while every effort has been made to honor authors' choices of traditional or e-poster formats, because of thematic or space considerations, some abstracts were not assigned the preferred format.

For a list of all abstracts accepted for presentation at the Annual Meeting, please go to https://www.ismrm.org/18/accepted_abstracts.pdf.

The deadline for early registration is 12 April 2018, and the deadline for housing is 12 March 2018. Please visit <https://www.ismrm.org/18m/> for more information.

On behalf of the Annual Meeting Program Committee, I thank you in advance for your participation in this year's meeting. Our members and attendees look forward to learning about your work.

Best regards,

Karla Miller, Chair
Joint Annual Meeting ISMRM-ESMRMB

Disclaimer

The information contained in this communication from the sender is confidential. It is intended solely for use by the recipient and others authorized to receive it. If you are not the recipient, you are hereby notified that any disclosure, copying, distribution or taking action in relation of the contents of this information is strictly prohibited and may be unlawful.

This email has been scanned for viruses and malware, and may have been automatically archived by **Mimecast Ltd**, an innovator in Software as a Service (SaaS) for business. Providing a **safer** and **more useful** place for your human generated data. Specializing in; Security, archiving and compliance. To find out more [Click Here](#).

Subject: ISMRM 2018 Annual Meeting Notification for Abstract Tracking
Number 8330
From: <ISMRM2018@mirasmart.com>
Date: 02/02/2018 21:03
To: <andre.paschoal@usp.br>

Re: "Brain connectivity assessment between rest condition and verbal fluency task through Arterial Spin Labeling"

Dear Colleague:

Thank you for submitting an abstract to be considered for presentation at the scientific sessions of the Joint Annual Meeting ISMRM-ESMRMB in Paris, France.

I am pleased to inform you that your abstract (title above), has been selected for presentation as a traditional printed poster at this year's Scientific Meeting.

A poster presentation is 60 minutes in length. To maximize opportunities for discussion, one half of the posters will be presented at a time by authors at each of the poster sessions. Your poster is tentatively assigned to be presented during the following session:

Session: Perfusion methods

Day/Date: Wednesday, 20 June 2018

Session Time: 08:15

The tentative schedule has been posted on the ISMRM website at www.ismrm.org/18m/. Note that the meeting will run from Saturday through Thursday, with the same broad format as the 2017 Annual Meeting.

Program numbers will be assigned later in March. When you arrive at the meeting, however, please verify the time of your session in the official program in case there have been last-minute changes.

Authors who submitted more than one abstract will receive a separate letter indicating the outcome for each submission.

Educational, Clinical, New Entrant, and E. K. Zavoisky Stipend Applicants should NOT register for the meeting until they have been notified of the status of their stipend application. Notifications of stipend awards will be sent out by 16 February 2018.

Each presenter is assigned a poster surface which measures 36 inches (91.44 cm) wide and 36 inches (91.44 cm) high. For your convenience, helpful information regarding poster presentations is available at our website (coming

soon). Be sure to monitor the website for current news.

You will be informed of your program number before the meeting. When you arrive at the meeting, please verify your program number in the Program-at-a-Glance in case there have been last-minute changes.

The meeting Proceedings will be published online only, with the full text of all accepted abstracts available to advance registrants on 01 June 2018.

Submission of your work constituted a commitment by the author(s) to present if invited. Unexcused failure to present will jeopardize participation in future ISMRM programs.

Please note that while every effort has been made to honor authors' choices of traditional or e-poster formats, because of thematic or space considerations, some abstracts were not assigned the preferred format.

For a list of all abstracts accepted for presentation at the Annual Meeting, please go to https://www.ismrm.org/18/accepted_abstracts.pdf.

The deadline for early registration is 12 April 2018, and the deadline for housing is 12 March 2018. Please visit <https://www.ismrm.org/18m/> for more information.

On behalf of the Annual Meeting Program Committee, I thank you in advance for your participation in this year's meeting. Our members and attendees look forward to learning about your work.

Best regards,

Karla Miller, Chair
Joint Annual Meeting ISMRM-ESMRMB

Disclaimer

The information contained in this communication from the sender is confidential. It is intended solely for use by the recipient and others authorized to receive it. If you are not the recipient, you are hereby notified that any disclosure, copying, distribution or taking action in relation of the contents of this information is strictly prohibited and may be unlawful.

This email has been scanned for viruses and malware, and may have been automatically archived by **Mimecast Ltd**, an innovator in Software as a Service (SaaS) for business. Providing a **safer** and **more useful** place for your human generated data. Specializing in; Security, archiving and compliance. To find out more [Click Here](#).

20 Participação em Eventos Científicos (com apresentação de trabalho ou oferecimento de cursos, palestras ou debates)

Esta subseção apresenta o comprovante da participação na XV Semana da Física Médica com seus respectivos propósitos.

Universidade de São Paulo
Departamento de Física da Faculdade de Filosofia, Ciências e Letras de Ribeirão Preto



Certificamos que o trabalho “**Brain Functional Analysis with Arterial Spin Labeling**” foi apresentado na modalidade Pôster, por **André Monteiro Paschoal**, na XVI Semana de Física Médica, organizada pelo Departamento de Física da Faculdade de Filosofia, Ciências e Letras de Ribeirão Preto, no período de 23 a 27 de Outubro de 2017.

XVI Semana de Física Médica
23 a 27 de outubro



Nelson Alves

Prof. Dr. Nelson Augusto Alves

Alessandro Martins da Costa

Prof. Dr. Alessandro Martins da Costa

21 Participação em Eventos Científicos (com apresentação de trabalho ou oferecimento de cursos, palestras ou debates)

Esta subseção apresenta o comprovante da participação na XV Semana da Física Médica com seus respectivos propósitos.

Universidade de São Paulo
Departamento de Física da Faculdade de Filosofia, Ciências e Letras de Ribeirão Preto

Certificamos que **André Monteiro Paschoal** ministrou o minicurso “Processamento de Imagens Médicas” durante a XVI Semana de Física Médica, organizada pelo Departamento de Física da Faculdade de Filosofia, Ciências e Letras de Ribeirão Preto, em 26 de Outubro de 2017.

23 de outubro

Foto: Prof. Dr. Nelson Augusto Alves

Nelson Augusto Alves

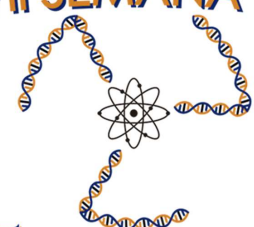
Prof. Dr. Nelson Augusto Alves

Prof. Dr. Alessandro Martins da Costa

22 Participação em Eventos Científicos (com apresentação de trabalho ou oferecimento de cursos, palestras ou debates)

Esta subseção apresenta o comprovante da participação na XV Semana da Física Médica com seus respectivos propósitos.

XVII SEMANA DA Física Médica



Certificamos que o trabalho: “*A novel approach to delineate brain function and physiology under a semantic verbal fluency condition by a dual-echo ASL sequence*” foi apresentado na modalidade Pôster, por **André Monteiro Paschoal**, na **XVII Semana Da Física Médica** no período de 05 a 09 de Novembro de 2018 que ocorreu no Departamento de Física da Faculdade de Filosofia Ciências e Letras de Ribeirão Preto da Universidade de São Paulo.

A handwritten signature in blue ink, appearing to read "Alessandro Martins da Costa".

Prof. Dr. Alessandro Martins da Costa

A handwritten signature in blue ink, appearing to read "Antonio José da Costa Filho".

Prof. Dr. Antonio José da Costa Filho

23 Participação em Eventos Científicos (com apresentação de trabalho ou oferecimento de cursos, palestras ou debates)

Esta subseção apresenta o comprovante da participação no ISMRM Benelux Chapter com seus respectivos propósitos.

Certificate of Attendance

The ISMRM Benelux Chapter

certifies that

André Monteiro Paschoal

has attended the

11th Annual Meeting of the ISMRM Benelux Chapter

on Thursday, January 17, 2019 in Leiden, the Netherlands.

On behalf of the organizing committee,



Stephan Missault

24 Participação em Eventos Científicos (com apresentação de trabalho ou oferecimento de cursos, palestras ou debates)

Esta subseção apresenta o comprovante da participação no Organization for Human Brain Mapping Annual Meeting com seus respectivos propósitos.

Obs: Ese congresso não emite certificado de apresentação de trabalhos, apenas de participação no evento.



OHBM 2019 Certificate of Attendance

The Organization for Human Brain Mapping Administration hereby certifies that

Name of Participant: André Monteiro Paschoal

From

Name of Institution: InBrain Lab - University of Sao Paulo

Attended the 25th Annual Meeting of the Organization for Human Brain Mapping

Date from: 9th June 2019 **until** 13th June 2019

Location: Auditorium Parco Della Musica, Rome, Italy

Certificate Authorized by:

JoAnn Taie, OHBM Executive Director

jtaie@humanbrainmapping.org

Organization for Human Brain Mapping

5841 Cedar Lake Road, Suite 204

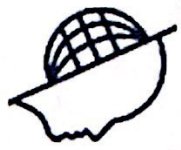
Minneapolis, MN, USA

Phone: 1 952-646-2029

Fax: 1 952-545-6073

info@humanbrainmapping.org

www.humanbrainmapping.org



Organization for
Human Brain Mapping
Advancing Understanding of the Human Brain

In recognition of a top rated abstract,
the Program Committee of the Organization for Human Brain Mapping presents

Andre Monteiro Paschoal

with a

Travel Stipend Award

"Organization of semantic verbal fluency brain network assessed by dual-echo arterial spin labeling"

25th Annual Meeting of the Organization of Human Brain Mapping
Rome, Italy / June 2019

Vin
D.C.

Vince Calhoun, 2019 Council Chair

Lucina Q. Uddin

Lucina Uddin, 2019 Program Committee Chair

Subject: 2019 OHBM Abstract Acceptance
From: info@humanbrainmapping.org
Date: 01/03/2019 11:49
To: andre.paschoal@usp.br

Dear Andre Monteiro Paschoal:

3327 - Organization of semantic verbal fluency brain network assessed by dual-echo arterial spin labeling

Congratulations! The OHBM Program Committee has completed their review of all submitted abstracts, and we are pleased to inform you that your abstract has been accepted for a poster presentation during the 2019 OHBM Annual Meeting in Rome, Italy. In 2019, posters will be displayed for 1 day each, over a 4 day period, June 10-13. There will be a poster reception each evening. You will receive a separate email in April with your poster number, poster session stand-by time, poster guidelines, and instructions for uploading an E-poster (an electronic version of the poster as a pdf).

As a poster presenter, you must register for the meeting and make your own travel and hotel arrangements. Having an accepted poster is not equivalent to a conference registration. Please visit the OHBM conference website: <https://www.humanbrainmapping.org/i4a/pages/index.cfm?pageid=3905> for more information on how to register. The Early Registration deadline for the meeting is March 20, 2019. Register now and save on registration fees!

You will notice an increase in registration fees for the 2019 conference. Please note that this includes a mandatory 22% VAT which has already been added to the registration fees. For any questions pertaining to VAT in Italy, please contact: vat@taxport-switzerland.com

Any author on the abstract is eligible to present at the meeting. If another author will be presenting at the meeting, please forward this email to them. If your poster cannot be presented at the conference, please notify the OHBM Executive Office as soon as possible at info@humanbrainmapping.org.

Congratulations again on your poster acceptance. See you in Rome!

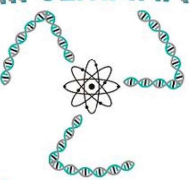
Sincerely,

OHBM Program Committee

25 Participação em Eventos Científicos (com apresentação de trabalho ou oferecimento de cursos, palestras ou debates)

Esta subseção apresenta o comprovante da participação na XV Semana da Física Médica com seus respectivos propósitos.

XVIII SEMANA DA Física Médica



Certificamos que **André Monteiro Paschoal** apresentou pôster com projeto intitulado “*Diffuse Glioma assessed by non-negative least square fitting for IVIM-MRI*” na **XVIII Semana da Física Médica** no dia 4 de Novembro de 2019, que ocorreu no Departamento de Física da Faculdade de Filosofia, Ciências e Letras de Ribeirão Preto da Universidade de São Paulo.



USP
Ribeirão Preto



Profº Dr. Antônio José da Costa Filho



Profº Dr. Ubiraci Pereira da Costa Neves

26 Participação em Eventos Científicos (com apresentação de trabalho ou oferecimento de cursos, palestras ou debates)

Esta subseção apresenta o comprovante da participação no 3rd MRTrax 3 Workshop com seus respectivos propósitos.



The **InBrain Lab** hereby certifies that **André Monteiro Paschoal**, from *University of São Paulo* attended the **3rd MRtrix3 Workshop**, held at Ribeirão Preto - São Paulo, Brazil, from February 8th to 12th, 2020, with a workload of 22h.

A handwritten signature of Donald Tournier in black ink.

Donald Tournier
Lecturer

A handwritten signature of Robert Smith in black ink.

Robert Smith
Lecturer

A handwritten signature of Carlos Ernesto Garrido Salmon in black ink.

Carlos Ernesto Garrido Salmon
Local organizer



FFCLRP - University of São Paulo
Building B3 - Room 103
Bandeirantes Avenue, 3900
Ribeirão Preto, SP

E-mail: inbrain@usp.br
Tel: +55 16 3315-3721

27 Participação em Eventos Científicos (com apresentação de trabalho ou oferecimento de cursos, palestras ou debates)

Esta subseção apresenta o comprovante da participação no InBrain Workshop 2020: Advanced Brain Imaging com seus respectivos propósitos.

INBRAIN WORKSHOP

Advanced  Imaging

• 2 0 2 0 •

The **InBrain Lab** hereby certifies that **Dr. André Paschoal**, conducted the session "*Intravoxel Incoherent Motion in neurological diseases*" at the **InBrain Workshop: Advanced Brain Imaging 2020**, held at Ribeirão Preto - São Paulo, Brazil, from February 13th to 15th, 2020.



Carlos Ernesto Garrido Salmon
Organizing Committee



Renata Ferranti Leoni
Organizing Committee



FFCLRP - University of São Paulo
Building B3 - Room 103
Bandeirantes Avenue, 3900
Ribeirão Preto, SP

E-mail: inbrain@usp.br
Tel: +55 16 3315-3721

28 Participação em Eventos Científicos (com apresentação de trabalho ou oferecimento de cursos, palestras ou debates)

Esta subseção apresenta o comprovante da participação no ISMRM 28th Annual Meeting & Exhibition com seus respectivos propósitos.



Certificate of Attendance

The International Society for Magnetic Resonance in Medicine
and
Society for MR Radiographers & Technologists
certifies that

Andre Monteiro Paschoal

has attended the
2020 ISMRM & SMRT Virtual Conference & Exhibition

A handwritten signature in black ink, appearing to read "Melissa Simcox".

Melissa Simcox
Director of Education

2020-08-24 19:37:06 UTC

Today's Date

International Society for Magnetic Resonance in Medicine
Society for MR Radiographers & Technologists
One Concord Center, 2300 Clayton Road, Suite 620
Concord, CA 94520

Telephone: +1 (510) 841-1899 | Fax: +1 (510) 841-2340
E-mail: info@ismrm.org | Website: <http://www.ismrm.org>
The International Society for Magnetic Resonance in Medicine is accredited by the Accreditation Council for Continuing Medical Education to provide continuing medical education for physicians.

29 Participação em Eventos Científicos (com apresentação de trabalho ou oferecimento de cursos, palestras ou debates)

Esta subseção apresenta o comprovante da participação no ESMRMB 37th Annual Meeting & Exhibition com seus respectivos propósitos.

Obs: Esse congresso não emite certificado de apresentação de trabalhos, apenas de participação no evento.

Andre M Paschoal
andre.paschoal@usp.br

CONFIRMATION OF ATTENDANCE

ESMRMB 2020 | Online Event

First Name: Andre
Last Name: M Paschoal

This document confirms that the individual designated above has participated in the 37th Annual Scientific Meeting of the ESMRMB – Online Meeting, September 30-October 2.

Yours sincerely,

ESMRMB Congress Office Vienna



It is the responsibility of the individual to correct any errors printed on this document by contacting the ESMRMB Office by mail. This confirmation of attendance is available only to the designated individual and will not be supplied to accrediting agencies and other organisations/health authorities.

Subject: ESMRMB Congress 2020 ONLINE - Your Abstract Notification
From: ESMRMB Office <office@esmrmb.org>
Date: 12/08/2020 07:00
To: andre.paschoal@usp.br



Dear Dr Paschoal,

On behalf of the Congress Planning Committee of the European Society for Magnetic Resonance in Medicine and Biology (ESMRMB) it is our great pleasure to inform you that your submitted abstract (see details below) has been accepted as a **Lightning Talk presentation** at the ESMRMB 2020 ONLINE to be held from September 30 - October 2, 2020.

1) Lightning talk:

Presentation number: L01.30

Abstract ID: A-1420

Abstract title: Evaluation of IVIM-MRI acquisition parameters for clinical protocol optimization in high-grade glioma patients

Talk duration: 2 minutes

Presenter: Andre M Paschoal

Please prepare a brief PowerPoint Presentation (max. 3 slides, including the title slide) for a 2-minute presentation and **record yourself presenting your talk**.

You will receive the detailed 'Guidelines for Lightning Talk Presentations', including a quick how to and which format to use for your recording very soon.

The deadline to hand in pre-recorded presentations still has to be coordinated with our technical provider. Please be prepared for a relatively short deadline - so we suggest starting to work on your presentations now. However, please await further instructions for handing in/uploading your presentations.

Please note that the **upload of your pre-recorded talk and a valid congress registration is required in order for your work to be displayed at the ESMRMB 2020**.

Please confirm your participation by August 31, 2020 by answering this email, stating your presentation number. In case we do not receive any feedback by August 31, your abstract will be withdrawn.

REGISTRATION

A valid registration for the presenting author is mandatory. Registration will be available soon, please regularly check our website at www.esmrmb.org for updates!

Should you have any questions, please do not hesitate to contact the ESMRMB Office.

We are looking forward to your contribution to the Rotterdam meeting.

Yours sincerely,

ESMRMB Office

30 Participação em Eventos Científicos (com apresentação de trabalho ou oferecimento de cursos, palestras ou debates)

Esta subseção apresenta o comprovante da participação no ISMRM 29th Annual Meeting & Exhibition com seus respectivos propósitos.

Obs: Ese congresso não emite certificado de apresentação de trabalhos, apenas de participação no evento.



Certificate of Attendance

The International Society for Magnetic Resonance in Medicine
and
Society for MR Radiographers & Technologists
certifies that

Andre Monteiro Paschoal

has attended the
2021 ISMRM & SMRT Annual Meeting & Exhibition

A handwritten signature in black ink, appearing to read "Melissa Simcox".

Melissa Simcox
Director of Education

2022-03-16 15:59:38 UTC

Today's Date

International Society for Magnetic Resonance in Medicine
Society for MR Radiographers & Technologists
One Concord Center, 2300 Clayton Road, Suite 620
Concord, CA 94520

Telephone: +1 (510) 841-1899 | Fax: +1 (510) 841-2340
E-mail: info@ismrm.org | Website: <http://www.ismrm.org>
The International Society for Magnetic Resonance in Medicine is accredited by the Accreditation Council for Continuing Medical Education to provide continuing medical education for physicians.

Subject: ISMRM 2021 Annual Meeting Notification for Abstract Tracking Number 5577
From: <ISMRM2021@mirasmart.com>
Date: 24/02/2021 19:40
To: <ampaschoal@gmail.com>

Re: "The utility of IVIM maps in the assessment of microvascular perfusion of brain glioma"

Dear Colleague:

Thank you for submitting an abstract to be considered for presentation at the scientific sessions of the upcoming **ISMRM & SMRT Annual Meeting & Exhibition - An Online Experience**, to be held virtually from 15-20 May 2021.

I am pleased to inform you that your abstract (title above) has been selected for presentation as a **digital poster** at the Scientific Meeting. Your presentation will be in the form of either a pre-recorded 5-minute video or a PDF file, which should be uploaded by 15 April 2021. This presentation will be available for on-demand viewing prior to the Annual Meeting. In the live portion of the Annual Meeting, authors will be assigned to small-group Q&A sessions where attendees can discuss the content of the posters and pose questions face-to-face. If possible, you should plan to join in this session live to participate. Additional session guidelines and detailed presentation instructions will be sent at a later time. Digital poster presentation guidelines will be available shortly at the meeting website.

Formal presentations of digital poster sessions will be one hour in length. Your digital poster is tentatively assigned to be presented during the following session:

Session: Diffusion Applications: Cancer

The tentative schedule will be posted on the ISMRM website at <https://www.ismrm.org/21m/>. Program numbers will be assigned in March. When the meeting commences, however, please verify the time of your session in the official program in case there have been last-minute changes. Please check the Program-at-a-Glance closer to the meeting in order to see the time slot you've been allotted.

Authors who submitted more than one abstract will receive a separate letter indicating the outcome for each submission.

Stipend Notifications

Educational, Clinical, New Entrant, and E.K. Zavoisky Stipend Applicants should NOT register for the meeting until they have been notified of the status of their stipend application. Notifications of stipend awards will be sent out within the next week.

The meeting Proceedings will be published online only, with the full text of all accepted abstracts available to advance registrants on 30 April 2021. Submission of your work constituted a commitment by the author(s) to present if invited. Unexcused failure to present will jeopardize participation in future ISMRM programs.

For a list of all abstracts accepted for presentation at the Annual Meeting, please go to https://www.ismrm.org/21/accepted_abstracts.pdf.

The deadline for early registration is 14 April 2021. Please visit <https://www.ismrm.org/21m/> for more information.

On behalf of the Annual Meeting Program Committee, I thank you in advance for your participation in this year's meeting. Our members and attendees look forward to learning about your work.

Best regards,

Nicole Seiberlich, Program Chair
ISMRM & SMRT Annual Meeting & Exhibition - An Online Experience

Disclaimer

The information contained in this communication from the sender is confidential. It is intended solely for use by the recipient and others authorized to receive it. If you are not the recipient, you are hereby notified that any disclosure, copying, distribution or taking action in relation of the contents of this information is strictly prohibited and may be unlawful.

This email has been scanned for viruses and malware, and may have been automatically archived by **Mimecast Ltd**, an innovator in Software as a Service (SaaS) for business. Providing a **safer** and **more useful** place for your human generated data. Specializing in; Security, archiving and compliance. To find out more [Click Here](#).

Subject: Fwd: ISMRM 2021 Annual Meeting Notification for Abstract Tracking Number 5033

From: Lucas da Costa <lucasdacosta@usp.br>

Date: 24/02/2021 20:54

To: Renata Ferranti Leoni <leonirf@usp.br>, André Monteiro Paschoal <andre.paschoal@usp.br>, bruno.hebling.vieira@usp.br

----- Forwarded message -----

De: <ISMRM2021@mirassmart.com>

Date: qua., 24 de fev. de 2021 às 19:41

Subject: ISMRM 2021 Annual Meeting Notification for Abstract Tracking Number 5033

To: <lucasdacosta@usp.br>

Re: "Gaussian Mixture for Peak Identification in Non-Negative Least Squares Fitting of the IVIM Signal"

Dear Colleague:

Thank you for submitting an abstract to be considered for presentation at the scientific sessions of the upcoming **ISMRM & SMRT Annual Meeting & Exhibition - An Online Experience**, to be held virtually from 15-20 May 2021.

I am pleased to inform you that your abstract (title above) has been selected for presentation as a **digital poster** at the Scientific Meeting. Your presentation will be in the form of either a pre-recorded 5-minute video or a PDF file, which should be uploaded by 15 April 2021. This presentation will be available for on-demand viewing prior to the Annual Meeting. In the live portion of the Annual Meeting, authors will be assigned to small-group Q&A sessions where attendees can discuss the content of the posters and pose questions face-to-face. If possible, you should plan to join in this session live to participate. Additional session guidelines and detailed presentation instructions will be sent at a later time. Digital poster presentation guidelines will be available shortly at the meeting website.

Formal presentations of digital poster sessions will be one hour in length. Your digital poster is tentatively assigned to be presented during the following session:

Session: Multicomponent models of diffusion, perfusion and relaxation

The tentative schedule will be posted on the ISMRM website at <https://www.ismrm.org/21m/>. Program numbers will be assigned in March. When the meeting commences, however, please verify the time of your session in the official program in case there have been last-minute changes. Please check the Program-at-a-Glance closer to the meeting in order to see the time slot you've been allotted.

Authors who submitted more than one abstract will receive a separate letter indicating the outcome for each submission.

Stipend Notifications

Educational, Clinical, New Entrant, and E.K. Zavoisky Stipend Applicants should NOT register for the meeting until they have been notified of the status of their stipend application. Notifications of stipend awards will be sent out within the next week.

The meeting Proceedings will be published online only, with the full text of all accepted abstracts available to advance registrants on 30 April 2021. Submission of your work constituted a commitment by the author(s) to present if invited. Unexcused failure to present will jeopardize participation in future ISMRM programs.

For a list of all abstracts accepted for presentation at the Annual Meeting, please go to https://www.ismrm.org/21/accepted_abstracts.pdf.

The deadline for early registration is 14 April 2021. Please visit <https://www.ismrm.org/21m/> for more information.

On behalf of the Annual Meeting Program Committee, I thank you in advance for your participation in this year's meeting. Our members and attendees look forward to learning about your work.

Best regards,

Nicole Seiberlich, Program Chair
ISMRM & SMRT Annual Meeting & Exhibition - An Online Experience

Disclaimer

The information contained in this communication from the sender is confidential. It is intended solely for use by the recipient and others authorized to receive it. If you are not the recipient, you are hereby notified that any disclosure, copying, distribution or taking action in relation of the contents of this information is strictly prohibited and may be unlawful.

This email has been scanned for viruses and malware, and may have been automatically archived by **Mimecast Ltd**, an innovator in Software as a Service (SaaS) for business. Providing a **safer** and **more useful** place for your human generated data. Specializing in; Security, archiving and compliance. To find out more [Click Here](#).

31 Participação em Eventos Científicos (com apresentação de trabalho ou oferecimento de cursos, palestras ou debates)

Esta subseção apresenta o comprovante da participação no Jornada Paulista de Radiologia 2021 com seus respectivos propósitos.



22 a 25 de setembro • Transamerica Expo Center • São Paulo, Brasil

**RADIOLOGIA
SEM FRONTEIRAS**
BRASILEIROS PELO MUNDO



Certificado

Certificamos que

ANDRÉ MONTEIRO PASCHOAL

participou como congressista da

51ª Jornada Paulista de Radiologia (JPR 2021), evento realizado nos dias 22 a 25 de setembro de 2021, no Transamerica Expo Center (TEC), em São Paulo - Brasil e por meio de uma plataforma de eventos virtuais.

Carga horária total: 25 horas.

São Paulo, 25 de setembro de 2021.


Dr. Cesar Higa Nomura
Presidente


Dr. Douglas Jorge Racy
Secretário Geral

jpr2021.org.br

Programação



Organização



Apoio





22 a 25 de setembro • Transamerica Expo Center • São Paulo, Brasil

**RADIOLOGIA
SEM FRONTEIRAS**
BRASILEIROS PELO MUNDO



Certificado

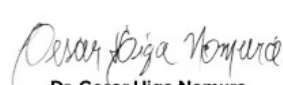
Certificamos que

ANDRÉ MONTEIRO PASCHOAL

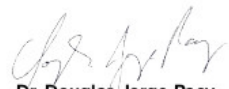
participou como Conferencista da

51ª Jornada Paulista de Radiologia (JPR 2021), evento realizado nos dias 22 a 25 de setembro de 2021, no Transamerica Expo Center (TEC), em São Paulo - Brasil, e por meio de uma plataforma de eventos virtuais, no módulo de Física em Radiodiagnóstico, apresentando o tema **ASL: Física, Técnica, Sequências e Aplicações**.

São Paulo, 25 de setembro de 2021.



Dr. Cesar Higa Nomura
Presidente



Dr. Douglas Jorge Racy
Secretário Geral

jpr2021.org.br

Programação



Organização



Apoio



32 Participação em Eventos Científicos (com apresentação de trabalho ou oferecimento de cursos, palestras ou debates)

Esta subseção apresenta o comprovante da participação no ISMRM Perfusion Workshop: from head to toe com seus respectivos propósitos.

Obs: Esse congresso não emite certificado de apresentação de trabalhos, apenas de participação no evento.



Certificate of Participation

The International Society
for Magnetic Resonance in Medicine

Certifies that

Andre M. Paschoal, Ph.D

has participated in the educational live activity entitled

ISMRM Workshop on Perfusion MRI: From Head to Toe

04-07 March 2022

and has attended 10.25 hour(s).

The International Society for Magnetic Resonance in Medicine is accredited by the Accreditation Council for Continuing Medical Education to provide continuing medical education for physicians.

A handwritten signature in black ink, appearing to read "Melissa Simcox".

Melissa Simcox
Director of Education

Subject: ISMRM Workshop on Perfusion MRI -- Abstract Results

From: Gerardo Mopera <gerardo@ismrm.org>

Date: 02/12/2021 20:09

To: ampaschoal@gmail.com



1 December 2021

RE: ABSTRACT ENTITLED: Feasibility of Arterial Spin Labeling to Assess Blood-Brain Barrier Permeability in Clinical Environment: Application to Multiple Sclerosis Patients

To: Andre M. Paschoal, Ph.D.,

It is a pleasure to inform you that the abstract that you submitted (title above) has been accepted for the ISMRM Workshop on Perfusion MRI: From Head to Toe in Los Angeles, CA, USA.

The organizing committee is in the process of finalizing the program, and before the presentation format of your abstract can be decided, we need to know if you will be able to attend the meeting **in person** or will need to present **virtually**. A virtual presentation involves submitting a recorded talk available for on-demand viewing, as well as having access to the chat feature where attendees can ask questions.

In considering how you will attend the meeting, we ask that you decide based on the information you have now, knowing that as the date approaches, travel situations may change. We will need to know how you plan to attend by **9 December 2021**. Please fill out the [online form here](#).

- **Registration:** Registration is now OPEN and is required to participate live or virtually. If you have not yet done so, please register for the workshop at this link: <https://www.ismrm.org/workshops/2022/Perfusion/reg.htm>.

PLEASE NOTE: MASKS AND PROOF OF VACCINATION ARE REQUIRED AT THE WORKSHOP VENUE.

Please note: if you applied for a stipend, you will receive a separate email regarding the status of that application next week.

The preliminary program and other information for the workshop are available at our website: <https://www.ismrm.org/workshops/2022/Perfusion/>.

The organizers are very happy to have you participate in this workshop and are looking forward to your presentation. If you have any questions, please do not hesitate to contact me.

Sincerely,

Gerardo

Gerardo Mopera, Education Coordinator

International Society for Magnetic Resonance in Medicine (ISMRM)

International Society for MR Radiographers & Technologists (ISMRT - a section of the ISMRM)

One Concord Center
2300 Clayton Road, Suite 620
Concord, CA 94520
T: +1 510 841 1899 • F: +1 510 841 2340 • E: Gerardo@ismrm.org
www.ismrm.org • www.facebook.com/ismrm • www.twitter.com/ismrm

Help us cultivate the MR leaders of tomorrow! Give to the [ISMRM Research & Education Fund](#).

SAVE THE DATE FOR 2022!

Joint Annual Meeting ISMRM-ESMRMB • 07-12 May 2022 • London, England, UK
SMRT 31st Annual Meeting • 06-09 May 2022 • London, England, UK

33 Obtenção de bolsa de estudo em instituições de renome científico ou cultural

Esta subseção apresenta o comprovante de concessão da bolsa de mestrado CAPES/PROEX.



DECLARAÇÃO

Declaro, para os devidos fins e de acordo com os assentamentos existentes neste Serviço de Pós-Graduação, que o senhor **André Monteiro Paschoal**, RG: 44.813.973-X - SP, foi bolsista de mestrado da CAPES/PROEX, no período de NOV/2013 a JUL/2015, junto ao Programa de Pós-Graduação em Física, do Instituto de Física de São Carlos - IFSC, da Universidade de São Paulo - USP.

Serviço de Pós-Graduação, do Instituto de Física de São Carlos, Universidade de São Paulo, aos 15 dias do mês de setembro de 2020.



Silvio César Athayde
Chefe Administrativo de Serviço
SVPGRAD / IFSC / USP
Nº USP 2022162

34 Obtenção de bolsa de estudo em instituições de renome científico ou cultural

Esta subseção apresenta o comprovante de concessão da bolsa de doutorado CNPq, processo número: 140110/2016-0.

TERMO DE ACEITAÇÃO DE INDICAÇÃO DE BOLSISTA DOUTORADO - GD PROGRAMA DE POS GRADUAÇÃO

PROJETO:
870324/1997-7 -

COORDENADOR:
Antonio Jose da Costa Filho
CPF: 44778651391

ORIENTADOR:
Antonio Jose da Costa Filho
CPF: 44778651391

Eu, **André Monteiro Paschoal**, CPF número **38330271854**, declaro conhecer e atender integralmente às exigências do edital/chamada **Cotas do Programa de Pós-Graduação** e às normas específicas do CNPq que regem a concessão da bolsa especificada abaixo:

BOLSA:
Processo: 140110/2016-0
Modalidade - Categoria: Doutorado - GD -
Vigência: De 01/02/2016 a 31/01/2020
Valor mensal da bolsa: R\$ 2.200,00

Declaro ainda que me comprometo a cumpri-las, não podendo, em nenhuma hipótese, delas alegar desconhecimento.

DATA:
05 de Fevereiro de 2016

ACEITE:

Ao enviá-lo ao CNPq, o BENEFICIÁRIO declara que leu e aceitou integralmente os termos deste documento.

BENEFICIÁRIO:

André Monteiro Paschoal
CPF: 38330271854

Termo de indicação registrado eletronicamente por meio da internet junto ao CNPq, pelo agente receptor 10.0.2.20(srv256.cnpq.br), mediante uso de senha pessoal do Beneficiário em 05/02/2016, originário do número IP 200.130.33.73(200.130.33.73) e número de controle 6097666360976663:2727436558-2235883124.

Para visualizar este documento novamente ou o PDF assinado digitalmente, acesse: <http://efomento.cnpq.br/efomento/termo?numeroAcesso=4160964726156139>.

Formação Acadêmica e Atuação profissional extraídas do Curriculum Vitae - CNPq

Última atualização: 04/02/2016 17:13:34

Geração: 05/02/2016 09:22:00

Dados Pessoais

Nome André Monteiro Paschoal
Filiação Oswaldo Luiz Fortes Paschoal e Ana Célia Navajas Monteiro Paschoal
Nascimento 04/08/1988 - Santa Cruz do Rio Pardo/SP - Brasil
Carteira de 44813973X SSP - SP - 18/06/2008
Identidade
CPF 38330271854

Formação Acadêmica/Titulação

2016 Doutorado em Física Aplicada à Medicina e Biologia.
Universidade de São Paulo, USP, Sao Paulo, Brasil
Título: DESENVOLVIMENTO DE MÉTODOS PARA ESTUDO DE FUNÇÃO E CONECTIVIDADE CEREBRAL UTILIZANDO ARTERIAL SPIN LABELING
Orientador: Renata Ferranti Leoni

2013 - 2015 Mestrado em Física.
Universidade de São Paulo, USP, Sao Paulo, Brasil
Título: Otimização do contraste em Arterial Spin Labeling multifase, Ano de obtenção: 2015
Orientador: Fernando Fernandes Paiva
Bolsista do(a): Coordenação de Aperfeiçoamento de Pessoal de Nível Superior

2008 - 2012 Graduação em Ciências Físicas e Biomoleculares.
Universidade de São Paulo, USP, Sao Paulo, Brasil
Título: Avaliação Biológica de Novos Candidatos a Agentes Anticâncer
Orientador: Adriano Defini Andricopulo

Atuação Profissional

1. Serviço de Assessoria e Proteção Radiológica - SAPRA

Vínculo institucional

2011 - 2012 Vínculo: Funcionário Privado , Enquadramento funcional: Estagiário , Carga horária: 30, Regime : Dedicação Exclusiva

35 Obtenção de bolsa de estudo em instituições de renome científico ou cultural

Esta subseção apresenta o comprovante de concessão da bolsa de doutorado sanduíche PDSE-CAPES, processo número: 88881.188976/2018-01.

Ilmo(a). Sr(a).

ANDRE MONTEIRO PASCHOAL

Benedicta Rodrigues Domingos - 889 - Bloco Danubio, apartamento 32
 Parque Industrial Lagoinha
 Ribeirão Preto - São Paulo
 Brasil
 14.095-050

Brasília, 27/07/2018

Processo: Programa de Doutorado Sanduíche no Exterior -88881.188976/2018-01

Prezado(a) Senhor(a),

A CAPES informa a aprovação de sua bolsa para o nível de formação doutorado, modalidade Doutorado Sanduícheno Exterior, na Instituição **UNIVERSITEIT LEIDEN , Holanda**.

Os benefícios associados à sua bolsa são:

Rubrica	Valor Unitário	Parcelas (Até)	Valor Total
Auxílio instalação	€ 1.300,00	1	€ 1.300,00
Auxílio Seguro Saúde	€ 90,00	6	€ 540,00
Mensalidade	€ 1.300,00	6	€ 7.800,00

. Período de bolsa:**11/2018 a 04/2019.**

· A Capes pagará, em conta corrente no Brasil, a primeira remessa de mensalidades e, quando for o caso, adicional localidade ao(à) bolsista que resida no país no momento da concessão da bolsa.

· A primeira remessa de mensalidades no exterior será realizada em sua integralidade. No entanto, a segunda remessa poderá sofrer ajustes em função do dia de chegada, nos termos da Portaria Capes nº 186, de 29 de setembro de 2017, ou atos normativos subsequentes que disciplinem a matéria. O valor referente aos dias descontados no início da bolsa não será compensado ao término da concessão.

.O pagamento do(s) auxílio(s) que lhe foi(foram) concedido(s) será(ão) realizado(s) no Brasil, em parcela única, conforme Portaria Capes nº 125, de 29 de maio de 2018, ou atos normativos subsequentes que disciplinem a matéria.

· Ficam automaticamente suprimidos o pagamento do auxílio instalação e a **concessão da passagem de ida**, caso o bolsista viaje com mais de 30 dias de antecedência ao início da vigência da bolsa, com exceção àqueles que se afastarem com autorização formal da Capes.

. A Capes somente efetuará o pagamento da primeira remessa de mensalidades após o envio da cópia do comprovante de suspensão ou de cancelamento da bolsa no país, emitido pela instituição que a concedeu, via Linha Direta. Essa suspensão ou cancelamento vigorará a partir do mês de início de sua bolsa no exterior.

. Para o pagamento dos benefícios iniciais é necessário que o(a) bolsista realize a implementação da bolsa no sistema SCBA (<http://scba.capes.gov.br>), preencha e envie à Capes o Termo de Compromisso datado, assinado e digitalizado, via sistema Linha Direta (<http://linhadireta.capes.gov.br>), bem como realize o aceite eletrônico da bolsa, além de preencher os dados de conta bancária no Brasil na forma e no prazo estipulado nos regulamentos dos programas ou instrumentos de seleção.

. Não será permitido o acúmulo de benefícios para a mesma finalidade e o mesmo nível, devendo o(a) bolsista(a) declarar a recepção de outras bolsas concedidas por órgãos ou entidades da Administração Pública federal, estadual ou municipal e requerer sua suspensão ou cancelamento, de modo que não haja acúmulo de bolsas durante o período de estudos no exterior.

. O período máximo de financiamento do doutorado no Brasil por agência pública de fomento é de 48 meses. A apuração do limite total da bolsa leva em consideração: o programa matriculado atualmente, os programas que porventura tenha feito anteriormente no mesmo nível doutorado e o período de bolsa no exterior, nos termos da Portaria Capes nº 23, de 30 de janeiro de 2017, nº 186, de 29 de setembro de 2017, e nº 125, de 29 de maio de 2018, ou atos normativos subsequentes que disciplinem a matéria.

. Os benefícios concedidos estão vinculados ao tempo da efetiva permanência no exterior, dentro do período de vigência da bolsa.

. A Capes realizará a aquisição de passagem, em classe econômica e tarifa promocional, para o deslocamento de ida e volta do bolsista, entre o país de origem e o país de destino, conforme Portaria Capes nº 125, de 29 de maio de 2018, ou atos normativos subsequentes que disciplinem a matéria.

. A Capes não se responsabiliza por despesas relacionadas ao pagamento de taxas acadêmicas e de pesquisa no nível de formação doutorado, modalidade Doutorado Sanduíche.

. À respeito do cumprimento dos pré-requisitos básicos para a realização da viagem (como a validade do passaporte, do visto e da vacinação - caso seja obrigatório), é de inteira responsabilidade do(a) beneficiário(a).

. No caso de servidor público, o procedimento para obtenção da **autorização de afastamento do país** junto à instituição com a qual mantém vínculo empregatício é de sua responsabilidade. Comunique à sua Instituição que o ato de autorização para seu afastamento deve constar o **ônus para a CAPES**, conforme **Decreto 91.800 de 18/10/1985**. A Capes poderá solicitar a comprovação do afastamento publicado em Diário Oficial a qualquer momento.

Em anexo, encaminhamos os documentos relacionados abaixo:

- Carta de concessão da bolsa em língua estrangeira;
- Termo de compromisso, que deve ser assinado e devolvido uma cópia pelo sistema “Linha Direta”, no link para acesso: <http://linhadireta.capes.gov.br>.

. O Formulário para a solicitação das passagens internacionais, bem como as orientações de preenchimento, será enviado, via Linha Direta.

Atenciosamente,



Vanessa Fernandes de Araújo

Coordenadora de Candidaturas a Bolsas e Auxílios no Exterior

Esta assinatura independe de reconhecimento de firma, por se tratar de documento público
- Art. 19, Inciso II - Constituição Federal do Brasil.

36 Obtenção de bolsa de estudo em instituições de renome científico ou cultural

Esta subseção apresenta o comprovante de concessão da bolsa de pós-doutorado junior PDJ-CNPq, processo número: 151245/2019-3 .



7009713275203136

TERMO DE ACEITAÇÃO DE BOLSA NO PAÍS

Eu, André Monteiro Paschoal, CPF nº 383.302.718-54, declaro conhecer e atender integralmente às normas geral e específica que regulamentam a modalidade de bolsa descrita abaixo e, se houver, às exigências da Chamada específica (normas e/ou Chamada disponíveis na página eletrônica do CNPq):

Bolsa

Processo: 151245/2019-3

Demandado/Chamada: Pós-doutorado Júnior - PDJ

Modalidade: PDJ

Categoria/Nível:

Instituição de Execução

Nome: Faculdade de Medicina de Ribeirão Preto

Cidade/Estado: Ribeirão Preto / SP

Este termo vigerá pelo prazo total de até 12 (doze) meses, a contar do mês de início da bolsa, a qual deverá ser implementada de acordo com o prazo estipulado no Calendário de Solicitação de Bolsas e Auxílios do CNPq ou em Chamada específica. Sabedor de que a bolsa concedida pelo CNPq constitui doação com encargos em prol do desenvolvimento científico e tecnológico e considerando a necessidade de prestar contas do recurso público utilizado, declaro:

a) que tenho ciência de que o não cumprimento das normas aplicáveis a esta modalidade de bolsa ensejará o ressarcimento integral ao CNPq de todas as despesas realizadas, atualizadas monetariamente de acordo com a correção dos débitos para com a Fazenda Nacional, sob pena de ter meu nome inscrito no Cadastro Informativo de Créditos Não Quitados do Setor Público Federal - CADIN, de submeter-me à Tomada de Contas Especial pelo CNPq, ao julgamento do Tribunal de Contas da União, à inscrição do débito decorrente na Dívida Ativa da União e, como consequência, à execução judicial, com a respectiva penhora de bens;

b) que tenho ciência de que esta declaração é feita sob pena da incidência nos artigos 297-299 do [Código Penal Brasileiro](#) sobre a falsificação de documento público e falsidade ideológica, respectivamente.

Declaro, ainda, que li e aceitei integralmente os termos deste documento, comprometendo-me a cumpri-los fielmente, não podendo, em nenhuma hipótese, deles alegar desconhecimento.

Termo de aceitação registrado eletronicamente por meio da internet junto ao CNPq, pelo agente receptor 10.0.2.22(srv258.cnpq.br), mediante uso de senha pessoal do Beneficiário em 13/11/2019, originário do número IP 200.130.33.73(200.130.33.73) e número de controle 6120430761204307:1766938564-3878138025.

Para visualizar este documento novamente ou o PDF assinado digitalmente, acesse: <http://efomento.cnpq.br/efomento/termo?numeroAcesso=7009713275203136>.

37 Autoria de artigos completos publicados em anais de congresso, em jornais e revistas de circulação nacional e internacional na sua área

Esta subseção apresenta o comprovante da autoria do resumo publicado em anais do congresso Organization for Human Brain Mapping, 2015.

Subject: OHBM 2015 Oral Session Invitation

From: OHBM <info@humanbrainmapping.org>

Date: 04/03/2015 18:57

To: "ampaschoal@gmail.com" <ampaschoal@gmail.com>

Dear Andre Paschoal,

Congratulations! The OHBM Program Committee has completed their review of all submitted abstracts, and we are pleased to inform you that your abstract has been selected for a traditional Poster Presentation **AND** an Oral Session presentation at the OHBM Annual Meeting being held June 14-18, 2015 in Honolulu, Hawaii. Information regarding the Oral Session presentation is as follows:

Oral Session: MRI Acquisition

Abstract Title: 7257 ASL Contrast Optimization in Multiphase STAR Labeling using Variable Flip Angle

Presentation Date and Time: Wednesday, June 17 from 11:00-11:15

Oral Session presentations are allotted 15 minutes (10 minute presentation and 5 minute question and answer). Your oral presentation must be in an electronic format (PowerPoint or Apple Keynote). Speaker Guidelines, as well as instructions for uploading your electronic presentation, and the location of your presentation will be forwarded to you closer to the conference.

Responsibilities as an Oral Session Presenter:

1. Please go to <http://www.humanbrainmapping.org/2015speakerconf> to confirm that you will participate in the Oral Session by **Friday, March 27, 2015**. If you are unable to present but would like a co-author to present in your place, please indicate so on the Speaker Confirmation Form. For ACCME purposes, all Oral Session presenters are required to complete the Financial Disclosure form found within the Speaker Confirmation Form.
2. Your selection as a presenter during an Oral Session is in addition to a poster presentation. You are still required to present a traditional poster at the meeting. You will receive an email in April with your poster number, poster session stand-by time, poster guidelines, and instructions for uploading an E-poster (an electronic version of your poster as a pdf).
3. Registration: You must pre-register for the meeting and you will need to make your own travel and hotel arrangements. Please visit the OHBM conference website at www.humanbrainmapping.org/OHBM2015 for more information. The Early Registration deadline for the meeting is **March 23, 2015**. Register now and save on registration fees!

If you have any questions, please contact the OHBM Executive Office at info@humanbrainmapping.org. We look forward to seeing you in Hawaii!

Sincerely,

John Darrell Van Horn
OHB M 2015 Program Committee Chair

38 Autoria de artigos completos publicados em anais de congresso, em jornais e revistas de circulação nacional e internacional na sua área

Esta subseção apresenta o comprovante da autoria do resumo publicado em anais do congresso Brasileiro de Física Médica, 2019.



XXIV CONGRESSO BRASILEIRO DE FÍSICA MÉDICA | 2019

21-24
AGOSTO
SANTOS

RESULTADO DA AVALIAÇÃO

Comunicamos que o seu trabalho **ID: 838: Non-negative least square fitting for IVIM-MRI in diffuse glioma** foi **Aceito** para apresentação no XXIV Congresso Brasileiro de Física Médica. Pedimos que compartilhe-a com seus coautores.

Em breve faremos a escolha da forma de apresentação dos trabalhos (pôster ou oral).

Comentários dos avaliadores:

Avaliador 1: Não se faz referência aos resultados do trabalho.

Avaliador 2:

Avaliador 3:

Santos, 21 de junho de 2019

Paulo Roberto Costa
Presidente do XXIV CBFM

Elisabeth M. Yoshimura
Comitê Científico

39 Autoria de artigos completos publicados em anais de congresso, em jornais e revistas de circulação nacional e internacional na sua área

Esta subseção apresenta o comprovante da autoria do resumo publicado em anais do congresso Brasileiro de Física Médica, 2019.

Subject: ESMRMB Congress 2019 in Rotterdam/NL - Your Abstract Notification
From: ESMRMB Office <office@esmrmb.org>
Date: 24/06/2019 09:40
To: andre.paschoal@usp.br

ESMRMB 2019 OCT. 3 – OCT. 5 ROTTERDAM/NL

36TH ANNUAL SCIENTIFIC MEETING



Dear Mr. Paschoal,

On behalf of the Scientific Programme Committee of the European Society for Magnetic Resonance in Medicine and Biology (ESMRMB) it is our great pleasure to inform you that your submitted abstract (see details below) has been accepted as an **electronic poster presentation including an oral presentation** in a lightning talk session at the ESMRMB 2019 to be held in Rotterdam/NL from October 3 - October 5, 2019.

1) Lightning talk:

Presentation number: L03.23

Abstract ID: A-1225

Abstract title: 3D GRASE readout optimization for time-encoded pCASL

Session type: Lightning Talks

Session title: Diffusion, Perfusion & CEST

Session day: 04.10.19

Session time: 10:50-11:50

Presentation within session: 23

Talk duration: 2 minutes

Room: The Stage

Presenter*: André M Paschoal

Please prepare a brief PowerPoint Presentation (max. 3 slides, including the title slide) for a 2-minute presentation, without discussion. You will receive the detailed 'Guidelines for Lightning Talk Presentations' at a later stage.

2) Meet-the-Author slot:

A 30-minutes "Meet-the-Author" slot in the electronic poster area will follow directly after the session. All presenters are asked to present their work to the audience and answer potential questions at a designated workstation.

Your "Meet the Author" timeslot for the above listed electronic poster presentation is on:

04.10.19, 11:50-12:20

Your PC number is**: 13

Presenter*: André M Paschoal

* Note that this information is sent to the submitting author, who is responsible for passing on any relevant information to the presenting author. Please kindly inform us at your earliest convenience in case the presenting author has changed.

** All PCs in the electronic poster area at the ESMRMB 2019 are numbered and easy to find. We recommend to check your programme and workstation number prior to your Meet-the-Author slot (and Lightning Talk).

Please note that attendance at the Lightning Talk Session as well as the Meet-the-Author slot is mandatory.

3) Submission of your electronic poster presentation

The electronic poster submission system will be online soon and as you have been assigned an electronic poster presentation you have to submit your poster by **September 17, 2019**. Detailed information on the submission process will follow shortly.

4) Poster Awards

At the ESMRMB 2019, the Scientific Programme Committee will again present a number of posters with awards! If you wish to participate in this award competition, you are kindly asked to submit your electronic poster until **August 22, 2019**.

Please note that the presence of the presenting author and a valid congress registration is required in order for your work to be displayed in the electronic poster system of the ESMRMB 2019.

Please confirm your participation by August 12, 2019 by answering this email, stating your presentation number
In case we do not receive any feedback by August 12, your abstract will be withdrawn.

REGISTRATION

A valid registration for the presenting author is mandatory. In case you have not yet registered for the meeting, please note that the early registration deadline is on **July 10, 2019**. [Click here](#) for further information on the ESMRMB 2019 registration fees and conditions or [go directly to our online registration tool](#) for the congress.

TRAVEL & ACCOMMODATION

A number of rooms have been reserved in different hotels in Rotterdam for delegates, [which you can book here](#). Bookings are subject to availability. This is a third party service provided by an external company. In case of any questions and inquiries kindly contact Preferred Hotel Reservations directly.

Should you have any questions, please do not hesitate to contact the ESMRMB Office.

We are looking forward to your contribution to the Rotterdam meeting.

Yours sincerely,

ESMRMB Office

ESMRMB Office
European Society for Magnetic Resonance in Medicine and Biology - ESMRMB
Am Gestade 1, AT-1010 Vienna
+43 1 533 40 64 915
office@esmrmb.org
www.esmrmb.org

40 Autoria de artigos completos publicados em jornais e revistas de circulação nacional e internacional na sua área

Esta subseção apresenta o comprovante da autoria do resumo publicado em anais do congresso Brasileiro de Física Médica, 2019.

Otimização do Contraste em ASL Multi-Fase

Contrast Optimization in Multiphase Arterial Spin Labeling

Fernando F. Paiva¹, Bernd U. Foerster², André M. Paschoal¹, Fernanda Tovar-Moll³ e Jorge Moll³

¹Instituto de Física de São Carlos, Universidade de São Paulo (USP) – São Carlos (SP), Brasil.

²Philips Medical Systems LatAm – São Paulo (SP), Brasil.

³Instituto D'Or de Pesquisa e Ensino – Rio de Janeiro (RJ), Brasil.

Resumo

ASL multi-fase é uma maneira eficaz para evitar o problema originado pela variação regional do tempo de trânsito, o que dificulta a estimativa dos valores de perfusão. No entanto, nas implementações convencionais das técnicas mutli-fase, o contraste ASL em fases tardia é prejudicado devido à aplicação repetida de pulsos de excitação e da relação longitudinal da magnetização, tornando difícil a avaliação da perfusão tecidual em regiões onde o tempo de trânsito é mais longo. No presente estudo, apresentamos uma melhoria do esquema de aquisição, explorando a modulação do ângulo de *flip* utilizado durante a aquisição das imagens de forma a manter o contraste ASL constante ao longo das várias fases.

Palavras-chave: imagem por ressonância magnética, cérebro, imagem de perfusão.

Abstract

Multiphase ASL is an effective way to overcome the regional variation of the transit time that difficult the estimation of perfusion values. However, with conventional multiple phases ASL techniques, the ASL contrast at later phases is impaired due to repeated application of excitation pulses and longitudinal relaxation making it difficult to evaluate the tissue perfusion in regions where the transit time is longer. In the present study, we show an improvement of the acquisition scheme by exploring a modulation on the *flip* angle of the MR acquisition to keep the ASL contrast constant over multiple phases.

Keywords: magnetic resonance imaging, brain, perfusion imaging.

Introdução

Arterial spin labeling^{1,2} (ASL) é um método bem estabelecido para obtenção de mapas quantitativos de perfusão sanguínea cerebral de forma não invasiva. Na maioria das implementações de ASL, um único tempo de inversão (TI) é usado para estimar os valores de fluxo sanguíneo cerebral (CBF). Neste caso, os efeitos provocados pelas diferenças regionais no tempo de trânsito arterial são difíceis de estimar e podem potencialmente introduzir erros no cálculo dos valores de perfusão³. Isto é particularmente crítico para os pacientes com doenças relacionadas à perfusão sanguínea cerebral, tais como acidente vascular cerebral e estenose de carótida. Uma abordagem possível para superar este problema relacionado ao tempo de trânsito se baseia na utilização de diferentes TIs entre a marcação e a aquisição das imagens⁴. No entanto, com estas técnicas convencionais multi-fases, o contraste ASL em fases tardias é prejudicado devido à aplicação repetida de pulsos de excitação e à relaxação longitudinal, tornando difícil a avaliação da perfusão tecidual em regiões onde o tempo de trânsito é mais longo. No presente estudo,

apresentamos uma otimização do esquema de aquisição, explorando a modulação do ângulo de *flip* utilizado para aquisição das imagens de modo a manter o contraste ASL constante ao longo das múltiplas fases.

Material e Métodos

Foi realizada uma simulação baseada na magnetização longitudinal e transversal durante uma aquisição ASL para as condições de controle e marcação. Ao aplicar a condição de contorno de que a diferença de sinal entre as imagens de controle e de marcação devem se manter constantes para todas as fases da aquisição ASL, o ângulo de *flip* para a *i*-ésima fase é dado pela equação 1.

$$FA_i = \arctan \left[\frac{\sin(FA_{\max}) * \exp\left(-\frac{(m-i)\tau}{T_1}\right)}{\sqrt{1 + \sum_{k=1}^{m-i-1} \sin^2(FA_{\max}) * \exp\left(-\frac{2k\tau}{T_1}\right)}} \right] \quad (1)$$

Autor correspondente: Fernando Fernandes Paiva – Instituto de Física de São Carlos, Universidade de São Paulo (USP) – Avenida Trabalhador São-Carlense, 400 – Pq. Arnold Schmidt – CEP: 13566-590 – São Carlos (SP), Brasil – E-mail: paiva@fsc.usp.br

onde:

F_{Amax} é o ângulo de flip máximo a ser utilizado, o que tem que ser especificado com base no tempo de repetição, uma vez que o estado de equilíbrio não foi levado em conta para efeito das simulações;

m é o número total de fases;

t é o intervalo entre as fases e T_1 é o tempo de relaxação longitudinal do sangue.

Voluntários adultos saudáveis ($n=10$, idade média= 25 ± 5) foram escaneados como parte de um protocolo aprovado pelo Comitê de Ética do Instituto D'Or de Pesquisa e Ensino, em um sistema de Ressonância Magnética Achieva 3T (Philips Medical Systems, Holanda), equipado com gradientes capazes de gerar amplitudes de 80 mT/m e 200 mT/m/ms de tempo de subida. Uma bobina transmissora de corpo foi utilizada em conjunto com uma bobina receptora de cabeça de 8 canais. As imagens foram adquiridas utilizando uma sequência GE-EPI com

os seguintes parâmetros: TR/TE=5000/14 ms, FOV=240 x 240mm², matriz=128x128, espessura de corte=5 mm e 8 fases adquiridas com TIs que variam de 750 a 2500 ms ($t=250$ ms). Um conjunto de 25 aquisições ASL foi feito para cálculo da média do sinal.

Resultados

A Figura 1A mostra a evolução típica da magnetização transversal durante o controle (linha vermelha) e durante a marcação (linha verde) em um experimento de ASL multifásico. Como o ângulo de flip (linha azul) é mantido constante para todas as fases, o sinal da diferença entre ambas as condições evolui para zero, o que torna impossível avaliar com precisão as regiões onde o tempo de trânsito é maior do que 1,3 s, por exemplo.

A Figura 1B revela como a diferença de sinal entre as imagens de marcação e de controle pode ser constante

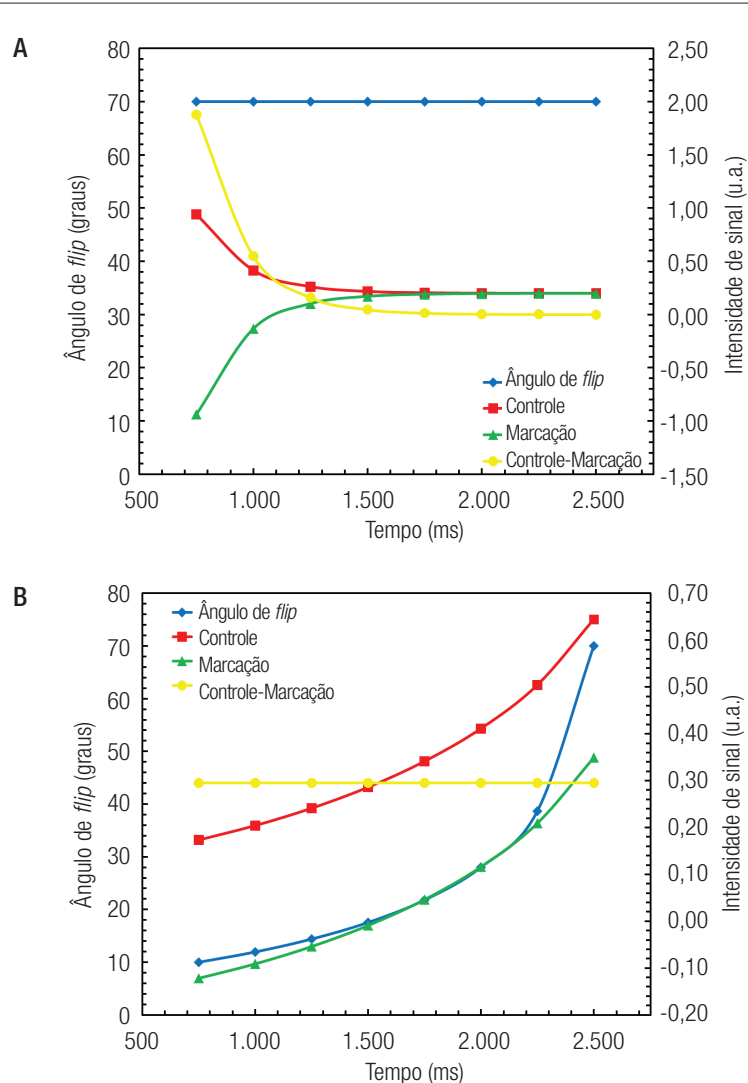


Figura 1. Simulação da intensidade do sinal para um experimento de ASL multi-fase usando um ângulo de flip constante (A) e com modulação no ângulo de flip (B).

se o ângulo de *flip* utilizado para a aquisição das imagens for modulado.

A Figura 2A mostra imagens anatômicas dos três cortes representativos escolhidos para ilustrar o efeito da modulação do ângulo de *flip* nos mapas de perfusão. A Figura 2B mostra imagens de perfusão representativas obtidas em um voluntário utilizando a metodologia ASL multi-fase convencional com um ângulo de *flip* constante de 30 graus. Pode-se notar claramente o contraste ASL comprometido nas fases posteriores, o que está de acordo com o esperado a partir da simulação. A Figura 2C mostra os dados obtidos a partir do mesmo voluntário utilizando a modulação do ângulo de *flip*. Neste caso, mesmo quando as fases mais tardias são adquiridas, um contraste de perfusão razoável ainda pode ser notado.

Discussão e Conclusões

No presente estudo, a combinação da modulação do ângulo de *flip* com uma metodologia multi-fase ASL

mostrou suas vantagens para avaliar a perfusão de tecidos, mesmo em regiões onde os tempos de trânsito longos geralmente comprometem a análise. Embora de acordo com as simulações da intensidade do sinal da imagem ponderada por perfusão em aquisição multi-fase possa atingir valores maiores para algumas fases quando se utiliza a abordagem convencional, isso normalmente ocorre para os tempos em que os spins do sangue dos vasos maiores ainda têm sinal alto, o que compromete a precisão da estimativa de CBF. Por outro lado, se pode apreciar na Figura 2C a melhora do contraste de perfusão nas fases posteriores, inclusive na matéria branca, por exemplo, onde se sabe que o tempo de trânsito é intrinsecamente mais longo quando comparado com as regiões de matéria cinzenta. Em resumo, a modulação do ângulo de *flip* pode ser uma alternativa promissora para implementações multi-fase da técnica ASL. Além disso, a otimização do modelo provavelmente irá permitir uma análise quantitativa do CBF, bem como possibilitar a quantificação do tempo de trânsito.

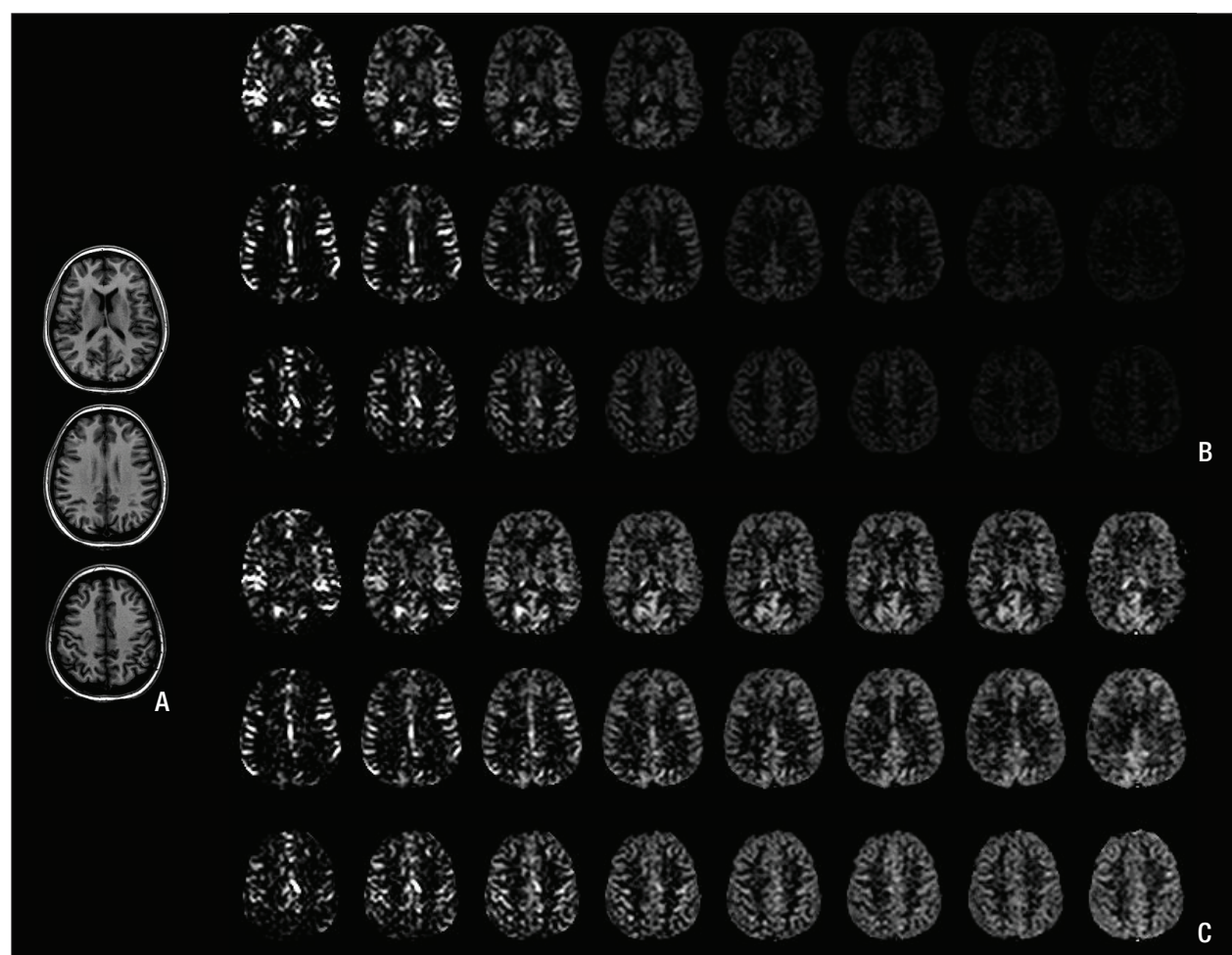


Figura 2. (A) Imagens anatômicas ponderadas por T1 de um voluntário representativo; (B) Respectivas imagens de perfusão obtidas usando um esquema de aquisição ASL multi-fase convencional (com ângulo de *flip* constante) e (C) usando uma modulação do ângulo de *flip* de acordo com o proposto no presente trabalho.

Referências

1. Detre JA, Zhang W, Roberts DA, Silva AC, Williams DS, Grandis DJ, et al. Tissue specific perfusion imaging using arterial spin labeling. *NMR Biomed.* 1994;7:75-82.
2. Golay X, Hendrikse J, Lim TC. Perfusion imaging using arterial spin labeling. *Top Magn Reson Imaging.* 2004;15:10-27.
3. Calamante F, Williams SR, van Bruggen N, Kwong KK, Turner R. A model for quantification of perfusion in pulsed labelling techniques. *NMR Biomed.* 1996;9:79-83.
4. Buxton RB, Frank LR, Wong EC, Siewert B, Warach S, Edelman RR. A general kinetic model for quantitative perfusion imaging with arterial spin labeling. *Magn Reson Med.* 1998;40:383-96.

41 Autoria de artigos completos publicados em jornais e revistas de circulação nacional e internacional na sua área

Esta subseção apresenta o comprovante da autoria do artigo publicado na revista nacional *Revista Brasileira de Física Médica* no ano de 2013.



Original contribution

Effects of global signal regression and subtraction methods on resting-state functional connectivity using arterial spin labeling data



João Paulo Santos Silva¹, Luciana da Mata Mônaco¹, André Monteiro Paschoal¹,
Ícaro Agenor Ferreira de Oliveira¹, Renata Ferranti Leoni^{*,1}

Inbrain Lab, Department of Physics, FFCLRP, University of São Paulo, Ribeirão Preto, Brazil

ARTICLE INFO

Keywords:

Functional arterial spin labeling
Artifact removal
Pairwise subtraction
Functional connectivity
Cerebral blood flow

ABSTRACT

Background: Arterial spin labeling (ASL) is an established magnetic resonance imaging (MRI) technique that is finding broader applications in functional studies of the healthy and diseased brain. To promote improvement in cerebral blood flow (CBF) signal specificity, many algorithms and imaging procedures, such as subtraction methods, were proposed to eliminate or, at least, minimize noise sources. Therefore, this study addressed the main considerations of how CBF functional connectivity (FC) is changed, regarding resting brain network (RBN) identification and correlations between regions of interest (ROI), by different subtraction methods and removal of residual motion artifacts and global signal fluctuations (RMAGSF).

Methods: Twenty young healthy participants (13 M/7F, mean age = 25 ± 3 years) underwent an MRI protocol with a pseudo-continuous ASL (pCASL) sequence. Perfusion-based images were obtained using simple, sinc and running subtraction. RMAGSF removal was applied to all CBF time series. Independent Component Analysis (ICA) was used for RBN identification, while Pearson's correlation was performed for ROI-based FC analysis.

Results: Temporal signal-to-noise ratio (TSNR) was higher in CBF maps obtained by sinc subtraction, although RMAGSF removal had a significant effect on maps obtained with simple and running subtractions. Neither the subtraction method nor the RMAGSF removal directly affected the identification of RBNs. However, the number of correlated and anti-correlated voxels varied for different subtraction and filtering methods. In an ROI-to-ROI level, changes were prominent in FC values and their statistical significance.

Conclusions: Our study showed that both RMAGSF filtering and subtraction method might influence resting-state FC results, especially in an ROI level, consequently affecting FC analysis and its interpretation. Taking our results and the whole discussion together, we understand that for an exploratory assessment of the brain, one could avoid removing RMAGSF to not bias FC measures, but could use sinc subtraction to minimize low-frequency contamination. However, CBF signal specificity and frequency range for filtering purposes still need to be assessed in future studies.

1. Introduction

Arterial spin labeling (ASL) is a noninvasive magnetic resonance imaging (MRI) technique for cerebral blood flow (CBF) quantification that has been recently used to investigate resting-state brain networks (RBNs) [1–3]. The specificity of ASL signal intrinsically related to cerebral metabolism and then neuronal activity turns the technique very interesting to obtain CBF time-series, allowing the assessment of an isolated hemodynamic parameter with a relatively simple experimental design [1,4,5]. However, because of low signal-to-noise ratio (SNR), spatial and temporal resolutions of ASL images, studying functional connectivity with CBF fluctuations is still at development regarding

image acquisition and processing [3,6–11].

In ASL, the amount of signal related to blood perfusion is assumed to be proportional to the difference between control and label images. Then, CBF maps are calculated using the perfusion images and mathematical approaches [12,13]. However, different methods of subtraction have been used. The first one, simple subtraction, calculates the signal difference between one control-label pair to obtain one perfusion-based image. Although simple and widely used, it does not filter physiological noise [5,14]. Therefore, other methods have been proposed: (1) surround subtraction, which uses a mean control (or label) image averaged from two images acquired just before and after the label (or control) image, attenuating high frequency noise, such as the

* Corresponding author at: Department of Physics, FFCLRP, University of São Paulo, Av. Bandeirantes, 3900, 14040-901 Ribeirão Preto, São Paulo, Brazil.

E-mail address: leoniri@usp.br (R.F. Leonir).

¹ All authors equally contributed.

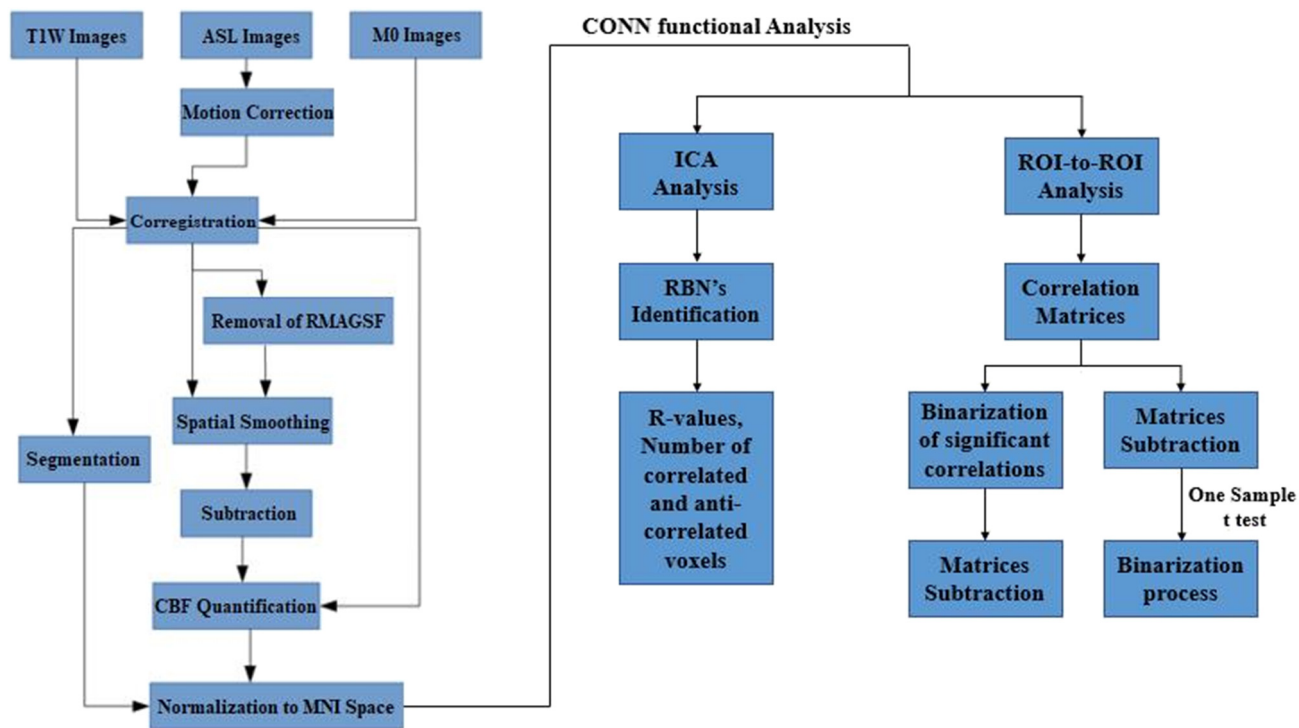


Fig. 1. Pipeline and analyzing image processing. RMAGSF: residual motion artifacts and global signal fluctuations.

cardiac one [5,14,15]; (2) sinc subtraction that consists of a temporal shifting correction for the delay time between control and label image acquisitions, acting like a band-pass filter [14–17]; and (3) running subtraction that increases the number of time points in CBF time series and improves temporal SNR [14,16].

Moreover, ASL images are affected by the blood oxygenation level dependent (BOLD) contamination. It is known that ASL images acquired with fast readouts, such as echo planar imaging (EPI), undergo a signal attenuation due to $T2^*$ effects [16,17], which are comparable to those observed in BOLD images and reflects other physiological parameters than CBF. This BOLD contamination is minimized when images are acquired with a reduced echo time (TE) [11]; however, reducing TE is limited due to consequent reduction of signal intensity [10,18]. Therefore, besides choosing an optimal TE (generally 8–15 ms), one may use a temporal filter to reduce signal with frequencies at the noise range (up to 0.02 Hz) or obtain perfusion-based images using a specific method of subtraction with sinc interpolation that acts like temporal filtering [14,19].

When analyzing brain functional connectivity, another issue to deal with is the baseline global signal inherent to the image acquisition and subject physiology, such as thermal noise [20]. Considered a noise that supposedly perturbs the fluctuations of interest, the global signal is generally removed in a preprocessing step, improving temporal SNR and test-retest reliability of CBF time series [20–22]. On the other hand, studies have reported that global signal is strongly coupled to low-frequency fluctuations and therefore it may be associated with the synchronism of all neurons, independently of their specific functions [23–25]. Therefore, it may contribute to the study of the brain at rest instead of being noise. So far, there is still no consensus about removing or not the global signal during image preprocessing.

Therefore, in the present study, we aimed to assess the effect of different methods of subtraction and the impact of residual motion artifact and global signal removal on the identification of RBNs and evaluation of functional connectivity using CBF time series of healthy young volunteers.

2. Methods

2.1. Subjects

Twenty healthy subjects (13 M/7F, [mean \pm SD] = 25 \pm 3 years old) participated in this study after reading and signing an informed consent approved by the Ethics in Research Committee of the Clinical Hospital, School of Medicine of Ribeirão Preto (HCFMRP). Exclusion criteria included the presence of pacemaker or prosthesis incompatible with the magnetic resonance environment; claustrophobia; dementia or cognitive impairment; diabetes, hypertension and neurological diseases; pregnancy; and not signing the consent form.

2.2. Image acquisition

Images were acquired on a 3T MRI system (Philips Achieva, The Netherlands) at the HCFMRP, using a 32-channel head coil for reception and a body coil for transmission. Resting-state pseudo-continuous ASL images were acquired using a 2D single-shot EPI sequence (TR/TE = 4000/14 ms, matrix = 80 \times 80, FOV = 240 \times 240 mm 2 , number of slices = 20, slice thickness = 5 mm, gap = 0.5 mm, slice time (ST) = 36.25 ms, labeling time (LT) = 1650 ms, post-labeling delay (PLD) = 1525 ms, number of control/label pairs = 75, and scan duration = 10 min). For CBF quantification, a proton density image was acquired using the same sequence and positioning of ASL images, but with no labeling (TR/TE = 15,000/14 ms, matrix = 80 \times 80, FOV = 240 \times 240 mm 2 , number of slices = 20, slice thickness = 5 mm, gap = 0.5 mm, number of repetitions = 5, and scan duration = 1 min and 30 s). In addition, for anatomical reference, a high-resolution 3D T1-weighted image was acquired (TR/TE = 7/3.1 ms, excitation angle = 8°, matrix = 240 \times 240, FOV = 240 \times 240 mm 2 , number of slices = 160, slice thickness = 1 mm, and scan duration = 5 min and 30 s).

2.3. Image processing

Image processing was performed using SPM12 (<http://www.fil.ion>.

ucl.ac.uk/spm/), an open-source toolbox for ASL images (ASLtbx), and routines developed by our group in Matlab (TheMathWorks, Inc., USA). Statistical analyses were performed using R project for Statistical Computing (<https://www.R-project.org>). The processing pipeline was applied to each subject separately (Fig. 1). First, raw ASL images were head-motion corrected with a separate realignment for control and label images [14]. Image volumes in which the realignment caused a displacement of > 1 mm in any translational direction or > 1° in any rotational orientation were excluded. After the realignment, a coregistration with the anatomical reference was applied followed by the segmentation to obtain masks of gray matter (GM), white matter (WM) and cerebrospinal fluid (CSF).

Although the first step was a correction for head motion, residual motion effect may remain [26]. It mainly affects the CBF quantification since it is obtained by the subtraction between two images acquired at different times. So, to our purpose of studying functional connectivity, where fluctuations due to neuronal activity can be easily overwritten by noise, removing residual motion artifacts is relevant. Therefore, we evaluated the effect of removing residual motion artifacts and global signal fluctuations (RMAGSF) together, as proposed by Wang [20]: (1) all label and control images in the original acquisition order were input to the standard motion correction procedure and 3 translational and 3 rotational motion time courses were estimated for the entire ASL image series; (2) the zig-zagged label-control patterns were removed from those motion time courses through simple regressions; (3) cleaned motion parameters were used for denoising; (4) temporal filtering was done using a high-pass Butterworth filter (cut-off frequency = 0.04 Hz). Finally, a spatial smoothing with a Gaussian filter (FWHM = 4 mm) was performed.

The subtraction of control and label images was done to obtain perfusion-weighted maps using three different methods: simple, sinc and running [17] (Fig. 2). Then, CBF time series were calculated using a General Kinetic Model described by Buxton [13], considering the labeling efficiency 0.85, blood-brain water coefficient partition 0.9 g/ml, T_1 of tissue 1020 ms for GM and 770 ms for WM, and T_{1app} of blood 1650 ms.

All anatomical masks (GM, WM, CSF) and CBF time-series obtained with different filters and subtraction methods were normalized to MNI Space. Low-Pass temporal filtering (cut-off frequency = 0.07 Hz) was applied to limit the frequency band of signal analysis [27,28]. WM and CSF signals were removed through the COMPCOR algorithm [29], using a standard principal component analysis (PCA).

For all individual CBF data sets obtained from different subtraction

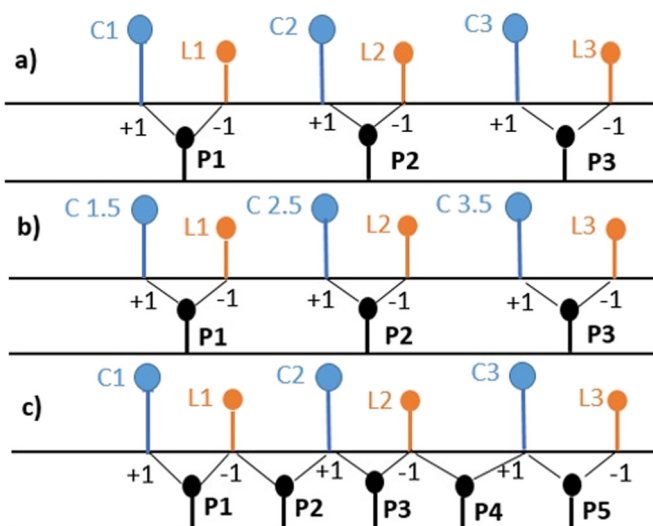


Fig. 2. Illustrative scheme of a) simple, b) sinc and c) running subtractions used to obtain the perfusion time series. C: control, L: label, P: perfusion.

methods, with and without RMAGSF removal process, temporal SNR (tSNR) was calculated by the ratio of the mean GM signal and its standard deviation. Statistical differences were analyzed with a two-way ANOVA test.

2.4. Functional connectivity analysis

Functional connectivity (FC) was analyzed using CONN toolbox [30]. Group-level independent component analysis (ICA) was used to obtain the RBNs from CBF time series [31]. The number of independent components (ICs) was set to 20, and the dataset was analyzed with the fast-ICA algorithm [32] to extract the ICs. The individual temporal series and spatial maps were computed through the reverse reconstruction by the GICA1 algorithm [33]. RBNs were identified from the spatial correlation of the ICs with the CONN functional atlas and final visual verification. After identification, the number of significant correlations and anti-correlations ($p < 0.05$, FDR-corrected) were calculated for all RBNs.

Moreover, Pearson's correlation was calculated between the average time series of regions of interest (ROI), defined from 103 anatomical areas of the Harvard-Oxford atlas (excluding Vermis and Cerebellum areas not covered by our imaging acquisition). Six correlation matrices were obtained: two for each subtraction method, with and without RMAGSF removal. Then, three analyses were performed:

Analysis 1: To evaluate the effect of the subtraction method on FC, matrices obtained without RMAGSF removal were subtracted two by two (simple – sinc, running – sinc, and running - simple). The resulted matrices were thresholded using a one sample t -test ($p < 0.05$, FDR-corrected for multiple comparisons), followed by a binarization process to highlight differences in r-values that survived the test.

Analysis 2: To evaluate the effect of RMAGSF removal on FC, for each subtraction method, matrices obtained with and without RMAGSF removal were subtracted. The resulted matrices were thresholded using a one sample t -test ($p < 0.05$, FDR-corrected for multiple comparisons), followed by a binarization process to highlight differences in r-values that survived the test.

Analysis 3: For each subtraction method, matrices obtained with and without RMAGSF removal were thresholded using a one sample t -test ($p < 0.05$, FDR-corrected for multiple comparisons), followed by a binarization process to highlight significant correlation, and then subtracted to show the correlations that were significant for just one condition (with or without RMAGSF removal).

3. Results

Temporal SNR was obtained for all CBF time series. No statistically significant difference was observed among different subtraction methods; however, tSNR significantly increased after RMAGSF removal for simple and running subtraction ($p < 0.05$).

Our group-level ICA identified three RBNs regardless the subtraction method or RMAGSF removal: default mode (DMN), visual and sensory-motor (SMN) networks (Fig. 3). They all showed similar spatial correlation values with RBNs of the CONN functional atlas.

Compared to the networks obtained from sinc-subtracted images, simple subtraction resulted in networks with an increased number of correlated voxels (DMN – 14%, visual – 7%, SMN – 10%) and decreased number of anti-correlated voxels (DMN – 29%, visual – 26%, SMN – 9%). However, running-subtracted images resulted in networks with an increased number of both correlated (DMN – 38%, visual – 28%, SMN – 27%) and anti-correlated (DMN – 35%, visual – 38%, SMN – 34%) voxels.

The removal of RMAGSF also influenced the size of the networks. For the DMN, the filtering process decreased the number of correlated voxels (simple – 7%, sinc – 1%, running – 31%), but increased the number of anti-correlated voxels (simple – 22%, sinc – 19%, running – 7%). The decreases of correlated voxels were < 20% for both visual

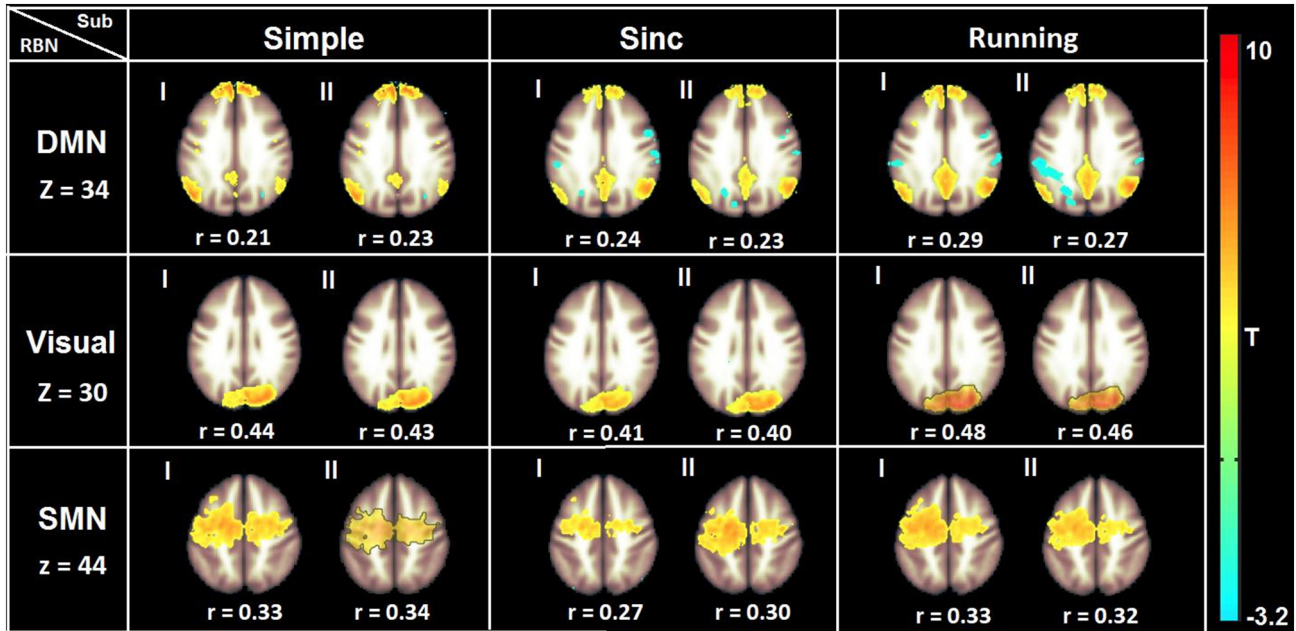


Fig. 3. Resting-state brain networks (default mode network – DMN, visual and sensory-motor – SMN) identified simple, sinc and running subtraction methods without (I) and with (II) removal of residual motion artifacts and global signal fluctuations (RMAGSF). R-values indicate the spatial correlation with Harvard–Oxford functional atlas.

network (simple – 18%, sinc – 9%, running – 5%) and SMN (simple – 4%, sinc – 3%, running – 7%). However, the increases of anti-correlated voxels were more accentuated (visual network: simple – 30%, sinc – 22%, running – 31%; SMN: simple – 20%, sinc – 14%, running – 29%).

Our ROI-to-ROI connectivity analysis showed that the subtraction method also influenced significantly the FC values ($p\text{-FDR} < 0.05$), especially the running subtraction. Approximately one-quarter of the ROI pairs showed a significant difference of r-values between the running subtraction and the other two methods (25%, for running – simple; 26%, for running – sinc) (Fig. 4).

We also evaluated the effect of RMAGSF removal on the FC values. Fig. 5 shows binarized matrices that highlight ROI pairs with statistically significant differences in r-values when comparing data obtained with and without RMAGSF removal ($p\text{-FDR} < 0.05$). Approximately one-quarter of the correlations significantly changed when using the RMAGSF removal for data obtained by sinc subtraction (24%) and one-third for running (33%) subtraction.

Moreover, Fig. 6 shows binarized matrices that highlight ROI pairs with statistically significant correlation only for data processed without (in blue) or with (in red) RMAGSF removal. If we only consider the number of significant correlations, the increase after RMAGSF removal was < 10% (simple – 2%, sinc – 0.2%, running – 10%), because the number of correlations that became significant after global signal regression was similar to the number that became not significant when applying it. However, as shown in Fig. 6, after RMAGSF removal, 8%, 31% and 32% of the correlations changed their status (significant or not) for simple, sinc and running subtraction, respectively.

4. Discussion

In the present study, we investigated the effects of subtraction methods and RMAGSF removal on tSNR values, identification of RBNs using ICA and ROI-based analysis of functional connectivity.

Regarding tSNR, higher values were observed after RMAGSF removal for CBF times series obtained with simple and running subtraction, as expected and previously reported [20,42]. However, RMAGSF removal did not affect the tSNR obtained with sinc subtraction, which may be related to the filtering role of sinc interpolation, which not only

minimizes unrelated blood perfusion signals but also improves image quality [14,19]. Moreover, our results showed that the use of running subtraction does not provide significant higher tSNR compared to simple subtraction as occurred in previous studies [10,20].

Regardless the subtraction method or filtering choice, default mode, visual and sensory-motor networks were identified by ICA with similar spatial correlation to the functional templates. These networks are the ones that appear mostly in the literature, due to individual behavior in resting state, with eyes open, related to mind-wandering, visual cortex activity and movements due to fatigue during the image acquisition [34]. However, other common RBNs were not obtained, such as the left and right executive control networks previously shown using pCASL with 3D background suppressed GRASE readout [10]. One possible explanation is related to the 2D pCASL images that usually show intrinsic low SNR, spatial resolution, and sensitivity to CBF value differentiation in a voxel level [35]. These characteristics may affect ICA results, which is performed voxel-wisely and is very sensitive to spatial-temporal conditions of the acquired image. Moreover, many tools used for RBN identification, such as the mathematical processes involved with group ICA, group-level back reconstruction algorithm and number of ICs can act directly in the final results [36].

Regarding the number of correlated and anti-correlated voxels, we observed that there was an increase in anti-correlations when the removal of RMAGSF was applied, as commented in a previous study [23], especially for the running subtraction. However, due to many aspects, some researchers have discussed that global signal regression may show a two-sided influence. While some reported a specificity of positive correlations with an improvement in anatomical connectivity correspondence [37], another speculated a potentially spurious “artefactual” correlation in the modeled data [38]. Then, all these factors influence FC results and should be considered in the analysis [39].

In an ROI-to-ROI level, running subtraction seems to introduce more correlations in the results. The correlation matrix obtained by running subtraction, when compared to other methods, showed more changes after RMAGSF use, which suggests more presence of potential noise that can interfere with FC analysis. One possible reason that can explain this result is related to the increase in CBF time series length. By definition, Pearson's correlation is directly influenced by sample characteristics as

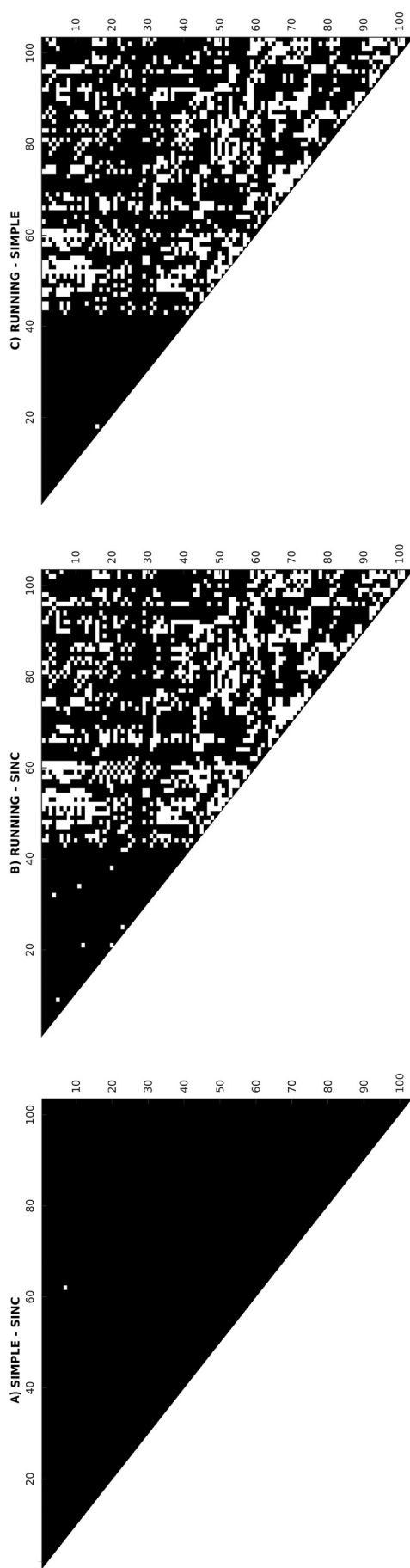


Fig. 4. Binarized matrices that highlight (in white) ROI pairs with statistically significant differences in r-values ($p < 0.05$, FDR-corrected for multiple comparisons) when comparing data obtained with different subtraction methods, without RMAGSF removal, two by two: A) simple – sinc, B) running – sinc, and C) running - simple. These are the results of Analysis 1, [Section 2.4](#).

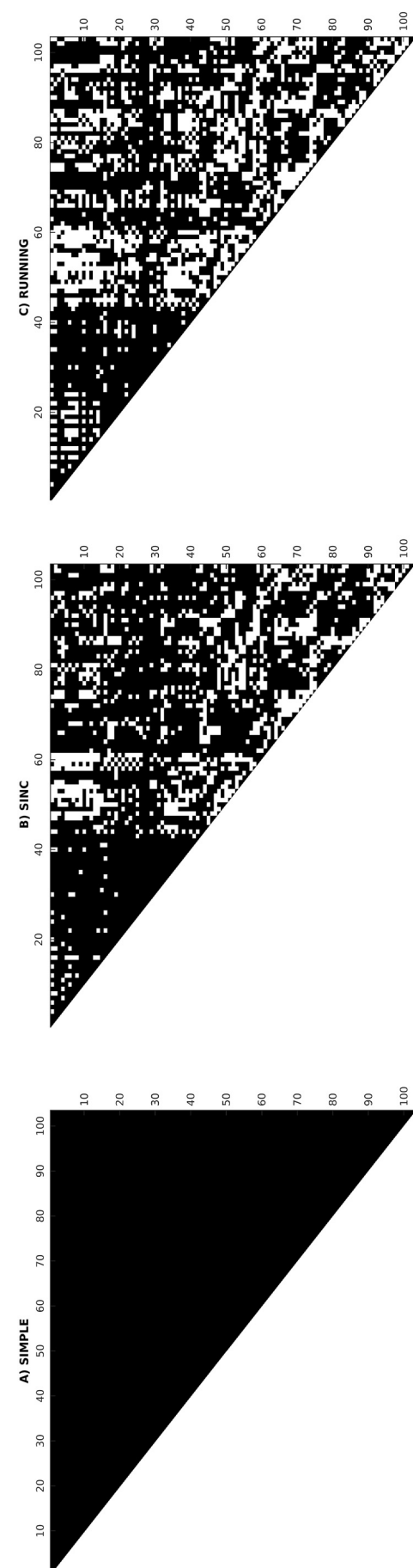


Fig. 5. Binarized matrices that highlight (in white) ROI pairs with statistically significant differences in r-values ($p < 0.05$, FDR-corrected for multiple comparisons) when comparing data obtained with and without RMAGSF removal, for each subtraction method: A) simple, B) sinc, and C) running. These are the results of Analysis 2, [Section 2.4](#).

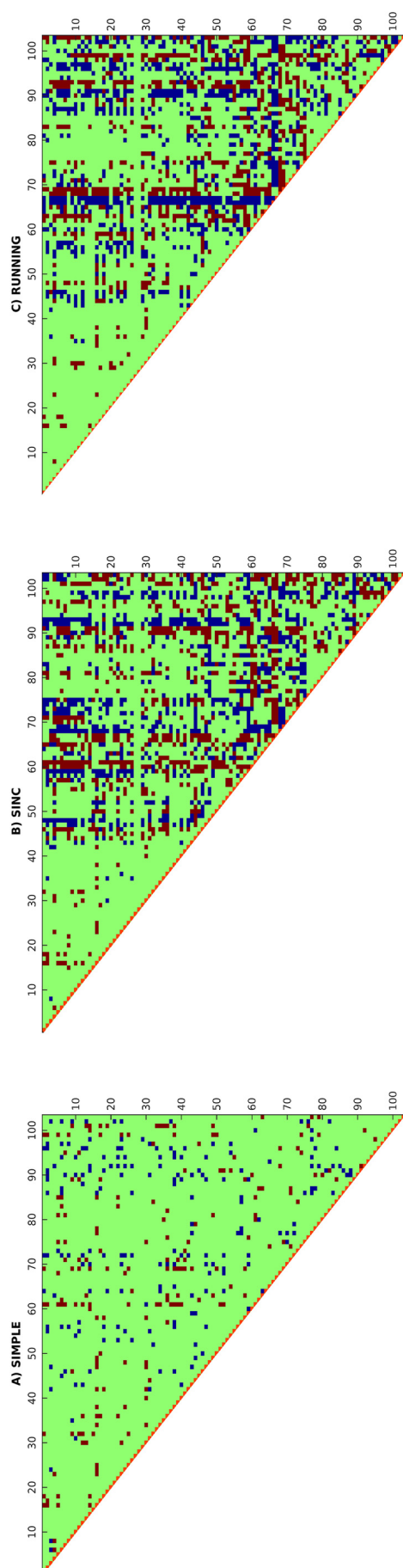


Fig. 6. Binarized matrices that highlight correlations statistically significant only for data without (in blue) or with (in red) RMAGSF removal ($p < 0.05$, FDR-corrected for multiple comparisons), for each subtraction method: A) simple, B) sinc and C) running. These are the results of Analysis 3, Section 2.4. (For interpretation of the references to colour in this figure legend, the reader is referred to the web version of this article.)

standard deviation and covariance between two datasets [40]. In the context of functional ASL analysis, the increase of CBF time points not only changes the CBF time evolution pattern but also can change its statistical parameters and directly impact its properties like statistical significance and FC calculation. Beyond that, the use of running subtraction may result in bigger contamination of other signals and effects that are not necessarily related to blood perfusion, like BOLD contamination [10,41].

Our results also showed that there is a difference in connectivity pattern since there are new significant correlations and loss of others after the RMAGSF removal. For all analysis performed considering the results obtained by three subtraction methods, the number of significant correlations always increased, but not in the same proportion. Running subtraction was the method that suffered more with the introduction of correlations and changes in their statistical values. In contrast, r-values of data obtained with simple subtraction seemed to be less affected by RMAGSF removal. In addition, although the absolute number of significant correlations increased $< 10\%$ after RMAGSF removal, up to 32% of the correlations changed their status of significance, which might interfere with data interpretation.

It is important to note that the above ROI-based results may be affected by the r-value thresholding. Here we used a p -value approach considering the FDR-correction for multiple comparisons which may lead to different results when comparing to other studies on FC analysis. Moreover, in more heterogeneous groups, such as elderly or patients, the result of RMAGSF removal could be even more accentuated due to their physiological conditions and head movement during the exam [39].

5. Conclusion

This study evaluated the effects of different subtractions and RMAGSF removal on the identification of RBNs and functional connectivity analysis. Our results showed no significant impact on network identification, but the RMAGSF removal increased the anti-correlations for all approaches. For the ROI-based analysis, the results were significantly influenced by the subtraction method and RMAGSF removal, especially for the running subtraction. Therefore, taking our results and the whole discussion together, we understand that for an exploratory assessment of the brain, one could avoid removing RMAGSF to not bias FC measures, but could use sinc subtraction to minimize low-frequency contamination. However, CBF signal specificity, frequency range for filtering purposes, and effects on different subject groups still need to be assessed in future studies.

Conflicts of interest

The authors declare that they have no conflict of interest.

Funding

This work was supported by the CAPES (Coordination for the Improvement of Higher Education Personnel).

References

- [1] Liang X, Connelly A, Calamante F. Graph analysis of resting-state ASL perfusion MRI data: nonlinear correlations among CBF and network metrics. *Neuroimage* 2014;87:265–75. <http://dx.doi.org/10.1016/j.neuroimage.2013.11.013>.
- [2] Jann K, Gee DG, Kilroy E, Schwab S, Smith RX, Cannon TD, et al. Functional connectivity in BOLD and CBF data: SIMILARITY and reliability of resting brain networks. *Neuroimage* 2015;106:111–22. <http://dx.doi.org/10.1016/j.neuroimage.2014.11.028>.
- [3] Mayhew SD, Mullinger KJ, Bagshaw AP, Bowtell R, Francis ST. Investigating intrinsic connectivity networks using simultaneous BOLD and CBF measurements. *Neuroimage* 2014;99:111–21. <http://dx.doi.org/10.1016/j.neuroimage.2014.05.042>.
- [4] Andreotti J, Jann K, Melie-Garcia L, Giezendanner S, Dierks T, Federspiel A.

- Repeatability analysis of global and local metrics of brain structural networks. *Brain Connect* 2014;4:203–20. <http://dx.doi.org/10.1089/brain.2013.0202>.
- [5] Warnock G, Özbay PS, Kuhl FP, Nanz D, Buck A, Boss A, et al. Reduction of BOLD interference in pseudo-continuous arterial spin labeling: towards quantitative fMRI. *J Cereb Blood Flow Metab* 2017;1:1–10. <http://dx.doi.org/10.1177/0271678X17704785>.
- [6] Detre JA, Wang J. Technical aspects and utility of fMRI using BOLD and ASL. *Clin Neurophysiol* 2002;113:621–34. [http://dx.doi.org/10.1016/S1388-2457\(02\)00038-X](http://dx.doi.org/10.1016/S1388-2457(02)00038-X).
- [7] Chuang KH, van Gelderen P, Merkle H, Bodurka J, Ikonomidou VN, Koretsky AP, et al. Mapping resting-state functional connectivity using perfusion MRI. *Neuroimage* 2008;40:1595–605. <http://dx.doi.org/10.1016/j.neuroimage.2008.01.006>.
- [8] Steketee RME, Mutsaerts HJMM, Bron EE, Van Osch MJP, Majoe CBLM, Van Der Lugt A, et al. Quantitative functional arterial spin labeling (fASL) MRI - sensitivity and reproducibility of regional CBF changes using pseudo-continuous ASL product sequences. *PLoS One* 2015;10:1:17. <http://dx.doi.org/10.1371/journal.pone.0132929>.
- [9] Zhu S, Fang Z, Hu S, Wang Z, Rao H. Resting state brain function analysis using concurrent BOLD in ASL perfusion fMRI. *PLoS One* 2013;8:4:13. <http://dx.doi.org/10.1371/journal.pone.0065584>.
- [10] Chen J, Jann K, Wang DJ. Characterizing resting-state brain function using arterial-spin labeling. *Brain Connect* 2015;5:527–42. <http://dx.doi.org/10.1089/brain.2015.0344>.
- [11] Liu TT, Wong EC. A signal processing model for arterial spin labeling functional MRI. *Neuroimage* 2005;24:207–15. <http://dx.doi.org/10.1016/j.neuroimage.2004.09.047>.
- [12] Buxton RB, Frank LR, Wong EC, Siewert B, Warach S, Edelman RR. A general kinetic model for quantitative perfusion imaging with arterial spin labeling. *Magn Reson Med* 1998;40:383–96. <http://dx.doi.org/10.1002/mrm.1910400308>.
- [13] Buxton RB. Quantifying CBF with arterial spin labeling. *J Magn Reson Imaging* 2005;22(6):723. <http://dx.doi.org/10.1002/jmri.20462>.
- [14] Wang Z, Aguirre GK, Rao H, Wang J, Fernández-Seara MA, Childress AR, et al. Empirical optimization of ASL data analysis using an ASL data processing toolbox: ASLtbox. *Magn Reson Imaging* 2008;26:261–9. <http://dx.doi.org/10.1016/j.mri.2007.07.003>.
- [15] Aguirre GK, Detre JA, Zarahn E, Alsop DC. Experimental design and the relative sensitivity of BOLD and perfusion fMRI. *Neuroimage* 2002;15:488–500. <http://dx.doi.org/10.1006/nimg.2001.0990>.
- [16] Li H, Donahue MJ, Van Zijl PCM. Detrimental effects of BOLD signal in arterial spin labeling fMRI at high field strength. *Magn Reson Med* 2006;56:546–52. <http://dx.doi.org/10.1002/mrm.20976>.
- [17] Alsop DC, Detre JA, Golay X, Gunther M, Hendrikse J, Hernandez-Garcia L, et al. Recommended implementation of arterial spin-labeled perfusion MRI for clinical applications: a consensus of the ISMRM perfusion study group and the European consortium for ASL in dementia. *Magn Reson Med* 2015;73:102–16. <http://dx.doi.org/10.1002/mrm.25197>.
- [18] Jahanian H, Peltier S, Noll DC, Garcia LH. Arterial cerebral blood volume-weighted functional MRI using pseudocontinuous arterial spin tagging (AVAST). *Magn Reson Med* 2015;73:1053–64. <http://dx.doi.org/10.1002/mrm.25220>.
- [19] Aguirre GK, Detre JA. Experimental design and the relative sensitivity of BOLD and Perfusion fMRI. 15. 2002. p. 488–500. <http://dx.doi.org/10.1006/nimg.2001.0990>.
- [20] Wang Z. Improving cerebral blood flow quantification for arterial spin labeled perfusion MRI by removing residual motion artifacts and global signal fluctuations. *Magn Reson Imaging* 2012;30:1409–15. <http://dx.doi.org/10.1016/j.mri.2012.05.004>.
- [21] Dai W, Varma G, Scheidegger R, Alsop DC. Quantifying fluctuations of resting state networks using arterial spin labeling perfusion MRI. *J Cereb Blood Flow Metab* 2015;36:463–73. <http://dx.doi.org/10.1177/0271678X15615339>.
- [22] Aguirre GK, Zarahn E, D'Esposito M. Empirical analyses of BOLD fMRI statistics. *Neuroimage* 1997;5:199–212. <http://dx.doi.org/10.1006/nimg.1997.0264>.
- [23] Murphy K, Birn RM, Handwerker DA, Jones TB, Bandettini PA. The impact of global signal regression on resting state correlations: are anti-correlated networks introduced? *Neuroimage* 2009;44:893–905. <http://dx.doi.org/10.1016/j.neuroimage.2008.09.036>.
- [24] Bright MG, Murphy K. Is fMRI “noise” really noise? Resting state nuisance regressors remove variance with network structure. *Neuroimage* 2015;114:158–69. <http://dx.doi.org/10.1016/j.neuroimage.2015.03.070>.
- [25] Leopold DA, Maier A. Ongoing physiological processes in the cerebral cortex. *Neuroimage* 2012;62:2190–200. <http://dx.doi.org/10.1016/j.neuroimage.2011.10.059>.
- [26] Friston KJ, Williams S, Howard R, Frackowiak RSJ, Turner R. Movement-related effects in fMRI time-series. *Magn Reson Med* 1996;35:346–55. <http://dx.doi.org/10.1002/mrm.1910350312>.
- [27] Mengual E, Vidorreta M, Castellanos G, Irigoyen J, Erro E. Resting state functional connectivity of the subthalamic nucleus in Parkinson's disease assessed using arterial spin-labeled perfusion fMRI. *Hum Brain Mapp* 2015;36:1937–50. <http://dx.doi.org/10.1002/hbm.22747>.
- [28] Boissonneault J, Letzen J, Lai S, O'Shea A, Craggs J, Robinson ME, et al. Abnormal resting state functional connectivity in patients with chronic fatigue syndrome: an arterial spin-labeling fMRI study. *Magn Reson Imaging* 2016;34:603–8. <http://dx.doi.org/10.1016/j.mri.2015.12.008>.
- [29] Behzadi Y, Restom K, Liu J, Liu TT. A component based noise correction method (CompCor) for BOLD and perfusion based fMRI. *Neuroimage* 2007;37:90–101. <http://dx.doi.org/10.1016/j.neuroimage.2007.04.042>.
- [30] Whitfield-Gabrieli S, Nieto-Castanon A. Conn: a functional connectivity toolbox for correlated and Anticorrelated brain networks. *Brain Connect* 2012;2:125–41. <http://dx.doi.org/10.1089/brain.2012.0073>.
- [31] Beckmann CF, DeLuca M, Devlin JT, Smith SM. Investigations into resting-state connectivity using independent component analysis. *Philos Trans R Soc B Biol Sci* 2005;360:1001–13. <http://dx.doi.org/10.1098/rstb.2005.1634>.
- [32] Hyvärinen A, Oja E. A fast fixed-point algorithm for independent component analysis. *Neural Comput* 1997;9:1483–92. <http://dx.doi.org/10.1162/neco.1997.9.7.1483>.
- [33] Calhoun VD, Adali T, Pearlson GD, Pekar JJ. A method for making group inferences from functional MRI data using independent component analysis. *Hum Brain Mapp* 2001;14:140–51. <http://dx.doi.org/10.1002/hbm>.
- [34] Zou Q, Yuan BK, Gu H, Liu D, Wang DJJ, Gao JH, et al. Detecting static and dynamic differences between eyes-closed and eyes-open resting states using ASL and BOLD fMRI. *PLoS One* 2015;10:1:12. <http://dx.doi.org/10.1371/journal.pone.0121757>.
- [35] Borogovac A, Asllani I. Arterial spin labeling (ASL) fMRI: advantages, theoretical constraints and experimental challenges in neurosciences. *Int J Biomed Imaging* 2012;2012:1–13. <http://dx.doi.org/10.1155/2012/818456>.
- [36] Cole DM, Smith SM, Beckmann CF. Advances and pitfalls in the analysis and interpretation of resting-state fMRI data. *Front Syst Neurosci* 2010;4:1–15. <http://dx.doi.org/10.3389/fnsys.2010.00008>.
- [37] Fox M, Zhang D. The global signal and observed anticorrelated resting state brain networks. *J Neurophysiol* 2009;101:3270–83. <http://dx.doi.org/10.1152/jn.90777.2008>.
- [38] Anderson JS, Druzgal TJ, Lopez-Larson M, Jeong EK, Krishnaji D, Yurgelun-Todd D. Network anticorrelations, global regression, and phase-shifted soft tissue correction (PSTCor). *Hum Brain Mapp* 2011;32:919–34. <http://dx.doi.org/10.1002/hbm.21079.Network>.
- [39] Murphy K, Fox MD. Towards a consensus regarding global signal regression for resting state functional connectivity MRI. *Neuroimage* 2017;154:169–73. <http://dx.doi.org/10.1016/j.neuroimage.2016.11.052>.
- [40] Lee MH, Smyser CD, Shimony JS. Resting-state fMRI: a review of methods and clinical applications. *Am J Neuroradiol* 2013;34:1866–72. <http://dx.doi.org/10.3174/ajnr.A3263>.
- [41] Rogers BP, Morgan VL, Newton AT, Gore JC. Assessing functional connectivity in the human brain by fMRI. *Magn Reson Imaging* 2007;25:1347–57. <http://dx.doi.org/10.1016/j.mri.2007.03.007>.
- [42] Jann K, Smith RX, Piedra EAR, Dapretto M, Wang DJJ. Noise reduction in arterial spin labeling based functional connectivity using nuisance variables. *Front Neurosci* 2016;10:1–13. <http://dx.doi.org/10.3389/fnins.2016.00371>.

42 Autoria de artigos completos publicados em jornais e revistas de circulação nacional e internacional na sua área

Esta subseção apresenta o comprovante da autoria do artigo publicado na revista internacional *Neuroimage: clinical* no ano de 2018.



Intravoxel incoherent motion MRI in neurological and cerebrovascular diseases*



André M. Paschoal^a, Renata F. Leoni^a, Antonio C. dos Santos^b, Fernando F. Paiva^{c,*}

^a Inbrain Lab, Departamento de Física, FFCLRP, Universidade de São Paulo, São Carlos, SP, Brazil

^b Departamento de Clínica Médica, FMERP, Universidade de São Paulo, São Carlos, SP, Brazil

^c Instituto de Física de São Carlos, Universidade de São Paulo, São Carlos, SP, Brazil

A B S T R A C T

Intravoxel Incoherent Motion (IVIM) is a recently rediscovered noninvasive magnetic resonance imaging (MRI) method based on diffusion-weighted imaging. It enables the separation of the intravoxel signal into diffusion due to Brownian motion and perfusion-related contributions and provides important information on microperfusion in the tissue and therefore it is a promising tool for applications in neurological and neurovascular diseases. This review focuses on the basic principles and outputs of IVIM and details its major applications in the brain, such as stroke, tumor, and cerebral small vessel disease. A bi-exponential model that considers two different compartments, namely capillaries, and medium-sized vessels, has been frequently used for the description of the IVIM signal and may be important in those clinical applications cited before. Moreover, the combination of IVIM and arterial spin labeling MRI enables the estimation of water permeability across the blood-brain barrier (BBB), suggesting a potential imaging biomarker for disrupted-BBB diseases.

1. Introduction

Perfusion refers to the passage of blood delivering nutrients and oxygen to the tissue in the capillary bed (Krogh, 1922). It is an important mechanism of the brain metabolism and plays a crucial role in its normal operation. It is directly involved with regulatory mechanisms (e.g. autoregulation of blood flow, vascular reactivity, and hyperemia) that once unregulated result in cerebral disorders (Hall and Guyton, 2011), such as stroke, dementia and cognitive deficits.

In the brain, perfusion is classically quantified as cerebral blood flow (CBF) which consists of blood volume per unit of brain tissue per unit of time, usually given in mL/100 g/min (Le Bihan, 1992). However, other metrics can be estimated depending on the imaging method. Among several methods, intravoxel incoherent motion (IVIM) estimates brain perfusion based on magnetic resonance imaging (MRI) (Le Bihan et al., 1986). Other approaches are also based on MRI, nuclear medicine and optics (Obregón, 2014; Wintermark et al., 2005).

MRI-based perfusion methods include dynamic contrast enhancement (DCE), dynamic susceptibility contrast (DSC), arterial spin labeling (ASL) (Wintermark et al., 2005), and IVIM. The former two techniques are based on the concept of a bolus of blood volume transiting through the tissue. DCE provides information about K_{trans} (volumetric transfer constant between blood plasma and extracellular extravascular space (EES)) (Sourbron and Buckley, 2013b), permeability-

surface area product, and cerebral blood volume (CBV) (Heye et al., 2016; Paldino and Barboriak, 2009). However, the latter is not usually assessed. DSC, the best choice for brain evaluation in clinical settings, provides a relative measurement of CBV, mean transit time (MTT), time to peak (TTP) and an estimation of CBF. ASL is a noninvasive alternative that assesses perfusion through quantification of CBF, which takes advantage of the hydrogen in the arterial blood as an endogenous tracer (Detre et al., 1992; Ferre et al., 2013; Williams et al., 1992).

In the late 1980's, Le Bihan designed IVIM, another approach that measures perfusion-related parameters using MRI noninvasively (Le Bihan et al., 1986). Multiple diffusion-weighted images (DWI) were acquired varying the diffusion gradient weighting. The amplitude of the resulted signal decays exponentially as the diffusion weighting increases. This decay is fitted to a theoretical model to separate diffusion and perfusion contributions of the signal (Le Bihan et al., 1988). A detailed explanation is provided in section 2.

Initially, IVIM drew interest for applications in liver and kidney. Several studies proved its usefulness (Hu et al., 2017; Li et al., 2017; Luciani et al., 2008; Meeus et al., 2018; Yamada et al., 1999). Despite having been initially tested for cerebral imaging, due to its high fractional anisotropy, the existence of several other established imaging methods, and the lack of a consensus about the best fitting method to adjust the signal to a physiological model, IVIM was not very well explored a priori. However, a better physiological description of IVIM

* Grant Support: This work was supported by São Paulo Research Foundation (FAPESP) (grant # 2013/23740-0) and National Council for Scientific and Technological Development (CNPq) (grant # 140110/2016-0).

* Corresponding author at: Instituto de Física de São Carlos, Universidade de São Paulo, CP 369, 13560-970, São Carlos, SP, Brazil.

E-mail address: fernando.paiva@usp.br (F.F. Paiva).

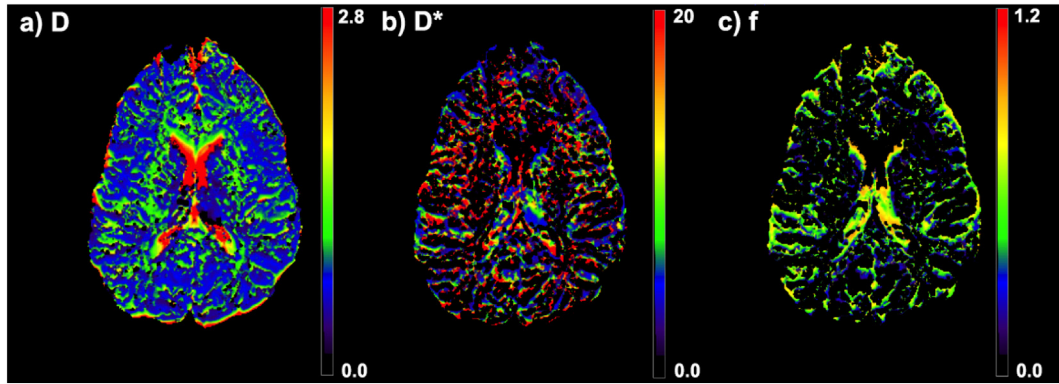


Fig. 1. Examples of D, f and D* maps.

signal and emergence of optimized fitting approaches have increased the application of IVIM in the brain over the past years.

This review provides an overview of the IVIM technique and addresses its main applications in the brain and future directions regarding its use for the study and evaluation of neurological and neurovascular diseases. The combination of IVIM with ASL and their complementarity are also discussed.

2. Theoretical considerations

2.1. The concept of the IVIM signal

Water molecules in a fluid exhibit microscopic random translational motion, called Brownian motion (Einstein, 1956), which results in molecular diffusion. The mean square distance traveled by a molecule is proportional to time and diffusion coefficient D. The latter coefficient depends on diffusing molecules, fluid viscosity, and temperature. At the capillary bed, besides the free water diffusion, the water molecules also flow (Budinger et al., 1985), due to the blood flow. Therefore, in the vascular compartment, the molecular diffusion path is limited by the vessel wall and influenced by the fluid viscosity and blood flow, which results in another diffusion contribution, modulated by a different coefficient, D*, one order of magnitude greater than coefficient D and first described by Le Bihan in 1986 (Le Bihan et al., 1986).

Restrictions imposed on diffusion motion (Tanner and Stejskal, 1968) are measured by MR experiments through the application of magnetic field gradients and result in diffusion-weighted images (Carr and Purcell, 1954; Hahn, 1950). After the use of those gradients, the MR signal decays exponentially according to the diffusion coefficient and the b-value, introduced by Stejskal and Tanner in 1965 (Stejskal and Tanner, 1965) and refers to the weighting of the diffusion pulse sequence. The b-value, expressed in s/mm², depends on the diffusion gradient waveform, the time duration of the gradients and the interval between them, according to the following equations:

$$b = (2\pi)^2 \int_0^{TE} \vec{K}_{(t)} * \vec{K}_{(t)} dt \quad (1)$$

$$\vec{K}_{(t)} = \frac{\gamma}{2\pi} \int_0^t \vec{G}_{(t')} dt' \quad (2)$$

where γ is the gyromagnetic ratio, G is the diffusion gradient magnitude in mT/m and t is the time duration of the application of the gradient pulse.

If the signal is measured in a pure solution, where the only source of motion is Brownian due to thermal diffusion, the MR signal can be expressed by a single exponential equation:

$$\frac{S(b)}{S_0} = e^{-bD} \quad (3)$$

where S(b) represents the signal acquired at a specific b-value and S₀ is

the signal with no application of diffusion gradients.

When the signal comes from a biological tissue, some factors reduce the diffusion motion, such that it decays according to a different diffusion coefficient, called apparent diffusion coefficient (ADC) (Le Bihan et al., 1986) which is the sum of contribution of all diffusion coefficients related to the resulting motion. Under such a condition, diffusion MR signal can be expressed by:

$$\frac{S(b)}{S_0} = e^{-bADC} \quad (4)$$

which is the representation of the diffusion mono-exponential model.

Several components account for the total ADC under biological conditions. However, in comparison to contributions of thermal diffusion and flowing effects, other sources can be neglected, and the signal can be modeled through a bi-exponential model (Eq. (5)), in which each exponential amplitude depends on the blood volume perfusion fraction (f) in a way the sum of those amplitudes must be one.

$$\frac{S(b)}{S_0} = fe^{-bD^*} + (1 - f)e^{-bD} \quad (5)$$

Eq. (5) describes the IVIM signal where D is the diffusion coefficient of free water, D* is the pseudo-diffusion coefficient, f is the perfusion fraction and b is the b-value. The idea beyond the IVIM method is to separate those contributions through the mapping of D, D* and f (Fig. 1). Each map contributes with different information, which, combined, helps the understanding of the water movement. Perfusion fraction f represents the volume of blood flowing into the capillary, whose water movement has the contribution of the blood flow and the diffusion motion within a single voxel. All such motions are summarized into pseudo-diffusion coefficient D*. Thus, with the parameters f and D*, IVIM provides the perfusion contribution to the MR signal. Although D* maps are noisier than the others (Fig. 1b), studies in the literature have shown their utility, as discussed in section 2.1. The omission of D* maps might result in the loss of useful information. On the other hand, D is the pure water diffusion coefficient and represents a voxel diffusion contribution to the signal in the extra-vascular pool.

Since D* is one order of magnitude higher than D, the exponential decay with the pseudo-diffusion coefficient vanishes faster, and its contribution to the total signal is distinguishable only at low b-values. At higher b-values, the contribution of the exponential with D models the signal. Multiple b-values are necessary to estimate from which b-value there is only diffusion contribution and consequently to estimate D, D* and f precisely (Fig. 2). Le Bihan proposed acquisition with only three b-values, which are theoretically enough for the obtaining of IVIM outputs. However, more points are necessary especially for the brain due to noise contamination and low D/f ratio, i.e., 0.5%, in comparison to 3.5% in the liver, for example (Le Bihan, 2017). Such a small percentage of perfusion contribution requires oversampling of low b-

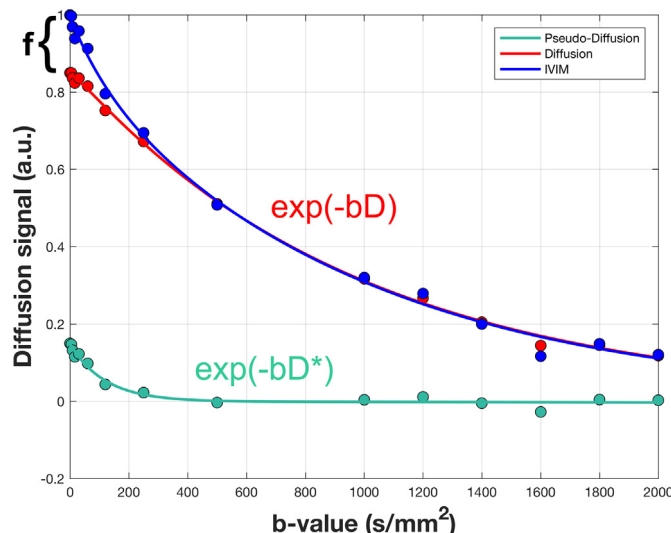


Fig. 2. Example of Pseudo-Diffusion (green) and Diffusion (red) contributions to IVIM signal (blue). Pseudo-diffusion (D^*) and diffusion coefficients (D) are extracted from the exponential decay of green and red curves, respectively. Perfusion fraction f is obtained from the difference of the intercept of blue and red curves. (For interpretation of the references to color in this figure legend, the reader is referred to the online version of this chapter.)

values. Therefore, between 10 and 30 b-values are usually employed, and the maximum b-value ranges from 1000 to 2000 s/mm² (Lemke et al., 2011).

The IVIM signal represents approximately 5% of the total diffusion signal, which motivated Neil et al. to develop strategies for suppressing the diffusion contribution and better understanding the IVIM signal (Neil et al., 1991). The approach used was the injection of a contrast agent for decreasing T1 and selectively suppressing the signal of non-flowing components. Once the diffusion contribution had been suppressed, the authors expected to fit the resulted signal by a mono-exponential model. However, they observed the signal was better adjusted through a bi-exponential approach. Other studies also investigated that behavior towards explaining the results (Henkelman et al., 1994; Neil and Ackerman, 1992; Neil et al., 1994).

Fournet et al. described a more specific bi-exponential model (Fournet et al., 2017) that considers two different compartments, namely capillaries, and medium-sized vessels. The authors hypothesized the bi-exponential behavior reflected the contribution of flow through two different vascular pools. The slow and fast pools represent capillaries and medium-sized vessels, respectively. That differs from classical IVIM models that consider a single compartment: the intravascular. At high b-values, both models converge to the mono-exponential decay, however, at low b-values, the signal is better fitted considering two pools. Such information helps the understanding of the IVIM signal and can also be useful for clinical applications.

2.2. Physiological models and fitting approaches

Since IVIM was proposed in 1986, several models were developed to explain the physiology related to the IVIM signal (physiological models) and others to fit better the acquired signal resulting in more trustful output maps (fitting models/approaches). However, there is some confusion in the literature about the terminology employed to classify all these models, especially about the bi-exponential terminology that is recurrently used to refer to both physiological and fitting models.

2.2.1. Physiological models

Physiological models aim to explain the nature of the measured IVIM signal. Le Bihan et al. (1988) introduced the two first models, the

mono-exponential and sinc models. Part of the confusion on terminology is related to the mono-exponential model since it is described by an equation of two exponential terms (Eq. (5)). It is referred to as mono-exponential because only one compartment (the intravascular one) is used for explaining the pseudo-diffusion contribution to a single exponential term. On the other hand, Fournet's bi-exponential IVIM model considers two compartments, namely capillaries and medium-sized vessels, to explain the pseudo-diffusion and perfusion related information (Fournet et al., 2017). Therefore, the use of mono- and bi-compartment models may help to end the confusion.

2.2.2. Fitting models

The main step of the IVIM data analysis consists of fitting the measured signal to a theoretical model and, consequently, researchers have focused on the optimization of the fitting approaches. Classically, the IVIM signal is fitted through a two-step mono-exponential analysis. First, the diffusion coefficient (D) is obtained from the mono-exponential fitting of the exponential decay for high b-values (usually higher than 200 s/mm²). Then, a mono-exponential fitting of the exponential decay for low b-values is applied towards estimating the pseudo-diffusion coefficient (D^*) and perfusion fraction (f). The other usual fitting model is the bi-exponential, which tries to adjust the entire curve including all b-values to obtain D , D^* and f . The approach is commonly used for the mono-exponential physiological model.

Several studies have implemented more robust models for fitting the IVIM signal, e.g. kurtosis model, non-negative least squares (NNLS), models that use artificial neural network and Bayesian approaches. Details can be found in (Bertleff et al., 2017; Gustafsson et al., 2018; Keil et al., 2017).

2.3. IVIM and classical perfusion measurements

IVIM emerged as a different approach for the obtaining of perfusion information and studies have aimed to correlate IVIM outputs with standard perfusion-related measures, as CBF and CBV (Bisdas et al., 2014; Henkelman, 1990; Le Bihan and Turner, 1992).

Conventional perfusion can be assessed by nuclear medicine techniques, as positron emission tomography (PET) and single photon emission computed tomography (SPECT). In both techniques, a bolus of exogenous tracer is intravenously injected for tagging the arterial blood with radioisotopes. Emissions from radioisotopes enable the estimation of the delivery of nutrients, as oxygen, glucose and tracer injected in the tissues, which results in the measurement of CBF in physiological units, mL/100 g of tissue/min (Le Bihan, 1992).

MRI-based DSC and DCE are well established methods applied in clinical routine for the assessment of perfusion (Sourbron and Buckley, 2013a). DSC uses T2*-weighted images of high temporal resolution to calculate perfusion-related metrics (CBV, MTT and TTP), towards CBF estimation. On the other hand, DCE – originally a technique to assess permeability of blood-brain barrier (BBB) – estimates CBF and CBV according to dynamic T1-weighted images and classic permeability parameters, as volume transfer constant (K_{trans}) and plasma volume (V_p). It is the best option for the study of neck, breast, and abdomen, which are regions of high field inhomogeneities due to fat, bone and air interfaces that suffer from susceptibility artifacts in T2*-weighted images. However, both methods require an intravenous injection of gadolinium. Besides concerns regarding its deposition in the brain, some factors hamper the quantification of perfusion-related parameters – e.g. gauge of the venous access that limits injection velocity; physical characteristics of the contrast agent, as temperature and viscosity; characteristics of the injection bomb; the injection protocol, and characteristics of patients, as arterial blood pressure and atherosclerosis.

In ASL, labeled blood flows through capillaries, delivers nutrients and oxygen to the brain tissue, and exchanges magnetization. The approach consists in the magnetic labeling of the arterial blood through the application of radiofrequency pulses. After the labeled blood has

reached the slices of interest, the image is acquired and then subtracted from a label-free image acquired at the same position, which results in a perfusion map proportional to the CBF (Buxton, 2005; Buxton et al., 1998) that takes into account some physiological and acquisition parameters (Alsop et al., 2015).

On the other hand, IVIM perfusion measures all water motion contributions to the intravoxel signal, as the Brownian motion of free water at perivascular space, the microperfusion signal of water flowing in randomly distributed microvasculature and flowing blood inside arteries. Since f represents the volume fraction of the intravascular blood and D^* refers to pseudo-diffusion motions related to blood flow, these measurements can be connected to those of classical methods. The first hypothesis proposed by Le Bihan and colleagues (Le Bihan, 2017; Le Bihan and Turner, 1992) suggests the link is related to capillary network geometry, as described by:

$$f_{IVIM} = \frac{CBV}{f_w} \quad (6)$$

$$MTT = \frac{L}{v} = \frac{Ll}{6D^*} \quad (7)$$

$$CBF = \left(\frac{6f_w}{Ll} \right) f_{IVIM} D^* \quad (8)$$

where f_w is the MRI-visible water content fraction, L is the total capillary length, l is the mean capillary segment length and v is the average blood velocity. Therefore, CBF is related to IVIM perfusion through product fD^* .

Recent studies have compared the blood flow measured with ASL and fD^* measured with IVIM. Yao and colleagues showed the correlation between fD^* and ASL-CBF was fair to good for stroke patients (Yao et al., 2016). Liang and colleagues also obtained a good correlation with the renal cortex, but weak correlation when the whole kidney was considered (Liang et al., 2016). Wu and colleagues did not achieve the same good correlation for the brain (Wu et al., 2015). Therefore, the comparison between IVIM parameters and ASL-CBF is still inconclusive and must be clarified. However, more than comparing IVIM parameters with standard ones, it is important to understand their physiological meaning, since they may provide complementary and useful information.

3. Neurological and Neurovascular applications

The analysis of neurological and neurovascular diseases revealed that measures of perfusion provide essential information for the patient's diagnosis and the disease characterization and monitoring. IVIM is an imaging tool that represents a new insight in perfusion measurements combined with simultaneously acquired diffusion information. Since its development, some applications for IVIM such as glioma grading, tumor diagnosis, stroke and cerebral death have been reported (Federau et al., 2014b), and once the results have proven positive, their range has been extended over the past few years.

3.1. Cerebrovascular diseases

3.1.1. Stroke

Stroke is the second leading cause of death worldwide (World Health Organization, 2017), therefore, it has been the subject of extensive studies regarding its characterization, diagnosis, and tissue lesion progression. Besides structural sequences, as T2W, T1W and T2-FLAIR (fluid attenuation inversion recovery), the standard protocols used for stroke evaluation include DWI and perfusion-weighted imaging. The current perfusion mapping is mostly performed by DSC, DCE and, more recently ASL methods (Heye et al., 2014; Huang et al., 2013; Zhang et al., 2015). Measurements of perfusion in stroke aim to assess the reduction of regional blood flow, volume and transit time through

maps of CBF, CBV, and MTT, respectively. However, DSC and DCE use gadolinium-based contrast injected in peripheral veins and are highly dependent on hemodynamics impairment, stenosis of proximal large arteries and velocity of contrast injection. Moreover, they provide information mainly from large vessels rather than the microvasculature (Jahng et al., 2014). On the other hand, the use of ASL, the classic non-contrast-agent technique, strongly depends on changes in the arterial arrival time and may provide underestimated CBF values (MacIntosh et al., 2010).

IVIM provides intrinsically local information, and nondependent on the regional effects of big arteries and peripheral hemodynamic impairment or problems related to gadolinium injection. It also provides absolute perfusion and diffusion information with a single three-minute sequence. According to IVIM-based maps, information from D or ADC enables the anatomical determination of stroke lesions since it indicates the degree of diffusion restriction of water molecules (Muir et al., 2006). Simultaneously, due to incoherent motion, perfusion information is also available (f map) making it possible to determine if it is from intra- or extravascular medium.

The assessment of stroke by IVIM was first reported by Wiestam et al. (Wiestam et al., 1997). Perfusion fraction f was reduced in affected areas in comparison to the respective contralateral region. After that study, stroke evaluation by IVIM was not reported until 2014, when Federau et al. revisited (Federau et al., 2014c). In agreement with the previous study (Wiestam et al., 1997), the authors also reported a reduction in perfusion fraction f in 14 out of 17 patients. The novelty was the combined analysis of quantitative maps of ADC and f (Fig. 3b and c), which provided information about the penumbra region.

Other studies reported the possible use of different IVIM outputs, as maps of D, ADC, D^* , f , and fD^* for analysis of affected regions (Hu et al., 2015; Yao et al., 2016). The authors concluded f and fD^* are more sensitive to detect changes during the stroke process, as these parameters are more related to CBF, with similar results to those obtained using ASL. In a different analysis, Suo et al. evaluated the correlation between ADC and IVIM-derived parameters and showed that for stroke lesions this correlation is different in comparison to normal tissue. Such a difference is clear in the analysis of the scatter plot of the correlations, where stroke areas can be distinguished, especially for the ADC- f correlation (Suo et al., 2016).

3.1.2. Cerebral small vessel disease

A novel application of IVIM refers to the assessment of patients with cerebral small vessel disease (CSVD), a common microvascular pathology that can progress to complications such as lacunar stroke, leukoaraiosis and vascular dementia (Wardlaw, 2010; Wardlaw et al., 2013a). Such patients have reported alterations in the parenchyma, lacunes, enlarged perivascular spaces (PVS) and atrophy, which result in structural MRI abnormalities, as hyperintensities and microbleeds (Cordonnier et al., 2007; Ewers et al., 2006; Jovicich et al., 2009; Kruggel et al., 2010; Reig et al., 2009; Roob et al., 1999; Schnack et al., 2004; Wardlaw et al., 2013c; Wonderlick et al., 2009). Although the identification of CSVD through conventional MRI is relatively easy, finding indications of normal appearing white matter (NAWM) that can advance to CSVD is still a challenge.

Perfusion images have shown a reduction in white matter CBF for CSVD patients (Markus et al., 2000; O'Sullivan et al., 2002), while DWI has also shown abnormalities (Wardlaw et al., 2013b).

Wong et al. used FLAIR image to localize affected areas (Fig. 4a) and IVIM to estimate perfusion fraction f (Fig. 4b) (Wong et al., 2017). They observed an increase in f values for both affected areas and in regions of FLAIR-NAWM, which is contrary to previous perfusion-based studies in CSVD. The results may be an evidence of vasodilation to increase the blood flow in those regions to suppress the cognition loss effects. Other possible explanations include deregulation in blood-brain barrier (BBB) and effects of increased vessel tortuosity. Even though the authors showed that IVIM might be useful to indicate affected regions before

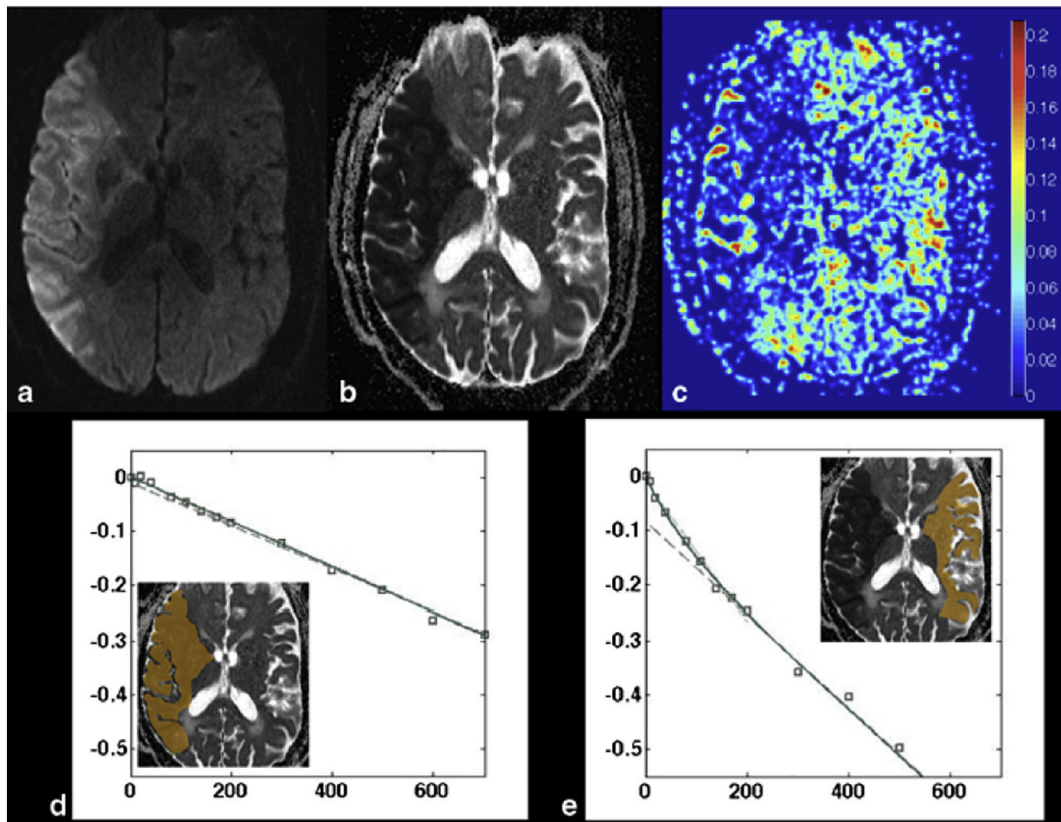


Fig. 3. Example of a patient with a stroke in the middle cerebral artery territory. a) Raw image ($b = 900 \text{ s/mm}^2$). b) ADC map. c) Perfusion fraction map. d) IVIM fitting in the stroke area. e) IVIM fitting in the contralateral hemisphere (Federau et al., 2014c).

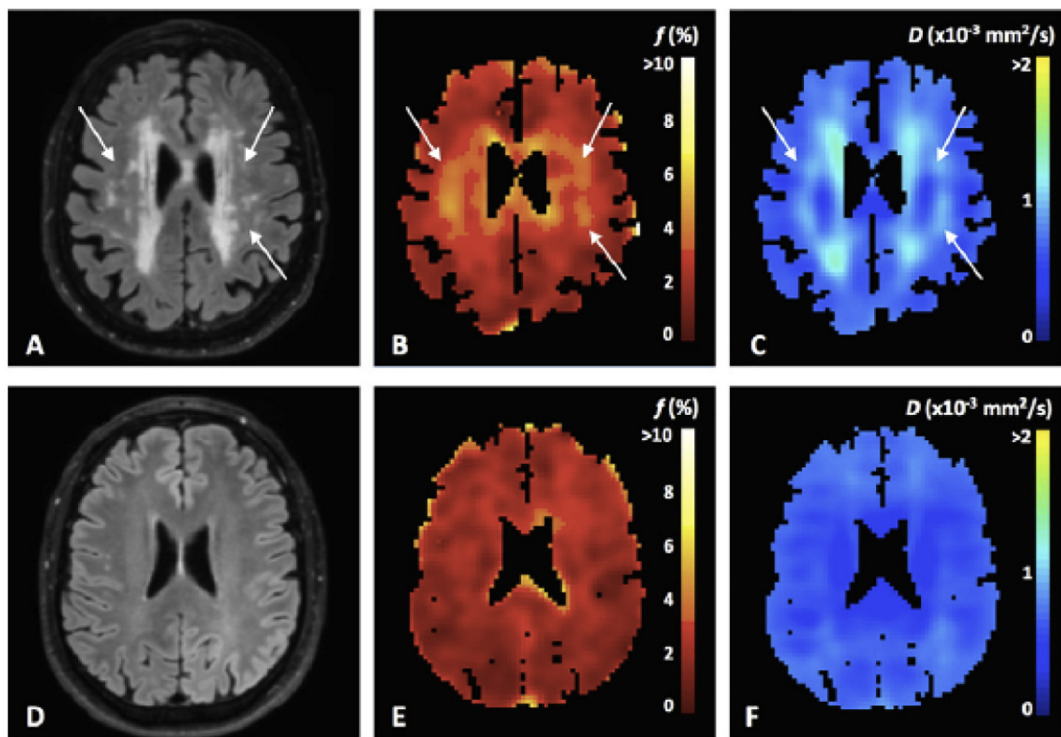


Fig. 4. Example of FLAIR images (A, D), perfusion fraction f maps (B, E) and parenchymal diffusivity D (C, F) for a small vessel disease patient (top row) and a healthy subject (bottom row) (Wong et al., 2017).

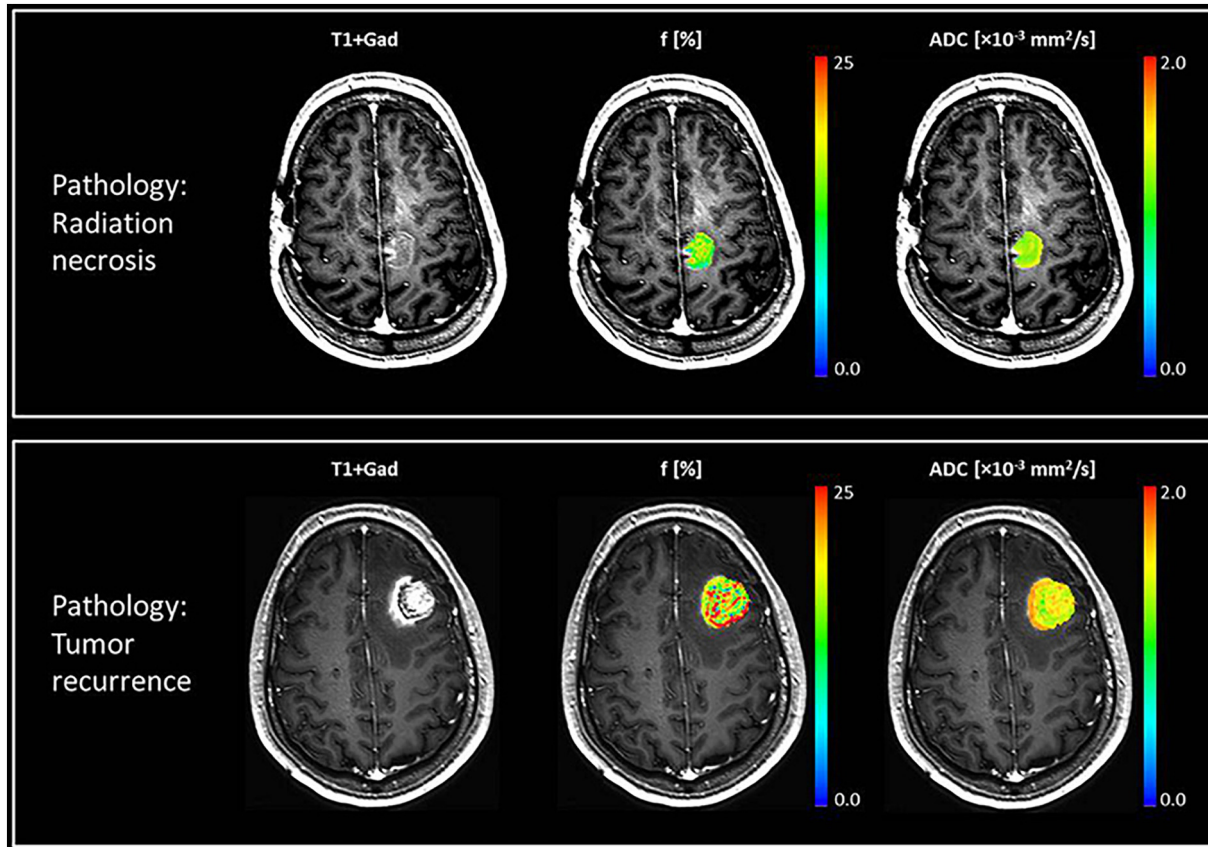


Fig. 5. Example of IVIM parameter maps for a patient with radiation necrosis (top row) and another with tumor recurrence (bottom row) (Detsky et al., 2017).

structural MRI, future studies must investigate the mechanism more carefully.

3.2. Tumor

Brain tumors deriving from cells of the central nervous system (CNS) are classified into benign and malignant. The most common malignant brain tumors are diffuse gliomas, mainly astrocytomas, and glioblastomas (de Robles et al., 2015). Due to their high mortality rate, early diagnosis and precise characterization are crucial to the treatment prospectus. Clinically, DSC and DWI are commonly used to help the diagnosis in case of tumor suspicion (Mullen and Huang, 2017). Therefore, tumors have quickly become an important target of application for IVIM that provides perfusion and diffusion information (Federau et al., 2014b).

3.2.1. Glioma

Gliomas represent over 50% of primary brain neoplasms and approximately 80% of all malignant brain tumors (Goodenberger and Jenkins, 2012). Term glioma refers to all glial tumors, however diffuse gliomas (grades II to IV) are more critical than low proliferative and well-delimited gliomas (grade I), which enable complete surgical resection. Diffuse gliomas are divided into low grade (LGG, grade II), high grade (HGG, grade III), and glioblastoma (GBM, grade IV), according to the World Health Organization (WHO) (Louis et al., 2016). Histologically, grade II gliomas have well-differentiated cells, and patients have an average survival of 5 to 10 years after diagnosis. Grade III anaplastic oligodendroglomas or astrocytomas show anaplasia and mitotic activity and patients usually survive less than 5 years. Grade IV GBM shows further microvascular proliferation and necrosis and is associated with less than two-year average survival. Because of such differences, therapeutic strategies are different, and the grading of diffuse gliomas is

crucial.

Bisdas showed the first evidence that IVIM could provide useful information in grading gliomas (Bisdas et al., 2013). They reported both D^* and f could be used to differentiate gliomas since these parameters were higher in HGG in comparison to LGG, which is consistent with the pathophysiology of the disease. Other researchers have reported similar results and emphasized IVIM-derived parameters could be used as markers for the diagnosis of glioma (Federau et al., 2014a; Togao et al., 2016).

According to Hu et al. ADC and D were significantly lower in HGG in comparison to LGG and, similarly to previous studies, D^* at tumor site showed higher values for HGG (Hu et al., 2014). However, the authors found lower f values for HGG, possibly due to the use of different b -values, especially for lower ones, and to ROI selection that, in contrast to other studies, included the solid tumor with the highest signal intensity on DWI. Moreover, the highest cellularity density, nuclear-cytoplasmic ratio, and relatively fewer mesenchymal components are present in anaplastic gliomas and glioblastomas (Plate et al., 1992), which are possible sources of reduction in perfusion fraction (Bisdas et al., 2013; Federau et al., 2014a).

There are also reports on IVIM to differentiate between glioblastoma, metastasis and primary central nervous system lymphoma (PCNSL) (Shim et al., 2015; Suh et al., 2014; Yamashita et al., 2016). Other researchers reported ADC obtained from a mono-exponential model of DWI could differentiate glioblastoma from PCNSL (Calli et al., 2006; Guo et al., 2002; Toh et al., 2008; Yamasaki et al., 2005). However, there is evidence that perfusion effects enhance this difference in ADC within the affected region. Suh et al. used the bi-exponential model to separate perfusion and diffusion information on the IVIM signal and found no significant difference in the D coefficient comparing PCNSL and glioblastoma. They suggested the difference in ADC was related to perfusion (Suh et al., 2014), which was confirmed

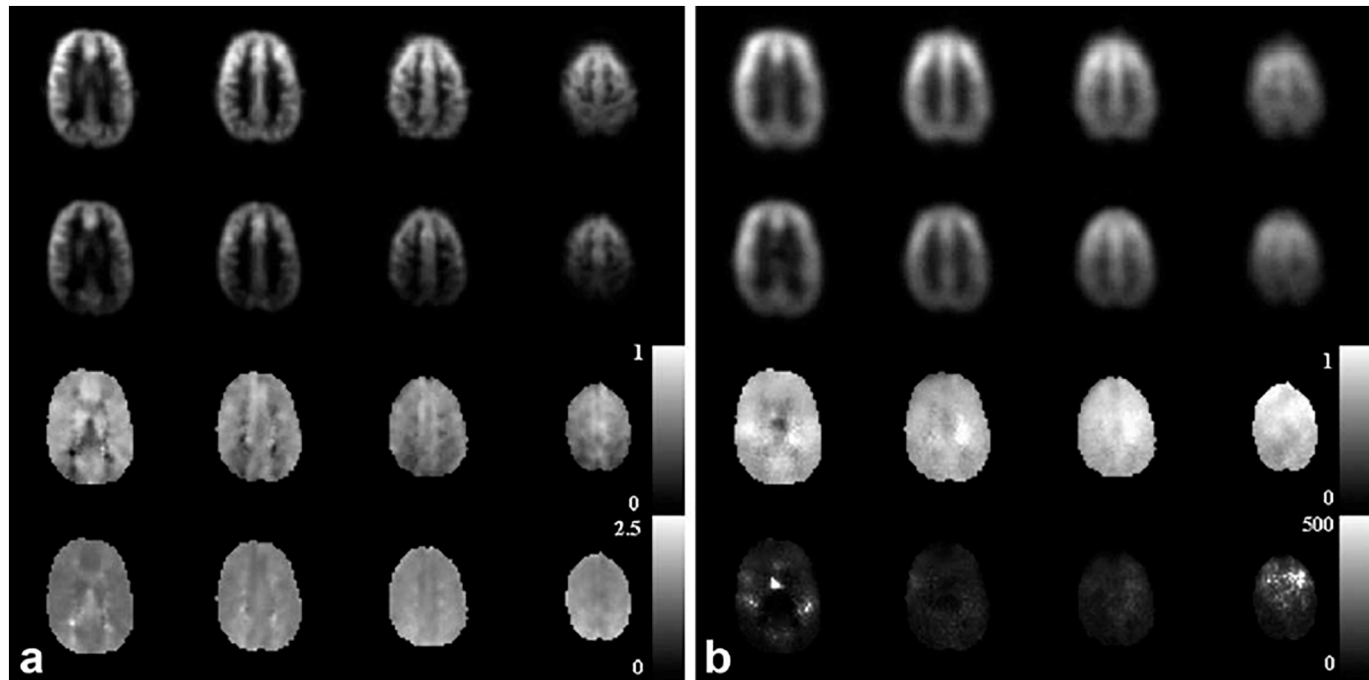


Fig. 6. Examples of ASL-DWI images. For both figures a and b, first row shows the average diffusion-weighted (ΔM) maps for b_0 ; second row shows ΔM including diffusion weighting (b_{dw}); third row shows the ratio $\Delta M(b_{dw})/\Delta M(b_0)$. In fourth row, in figure a it is shown the Transit time to the capillary-tissue compartment (τ_a) while in figure b it is presented the exchange rate of water from blood to tissue (k_w) (Lawrence et al., 2012)

through the analysis of the perfusion fraction f higher in glioblastoma than in PNSCL, such a result is in agreement with histological examination, once the level of cellularity in tumors is higher in comparison to normal tissue (Guo et al., 2002; Toh et al., 2008; Yamasaki et al., 2005).

3.2.2. Tumor monitoring

IVIM parameters have been used in the monitoring of tumors in patients treated with drugs, as antiangiogenic and vascular target agents applied outside the brain (Cui et al., 2015; Joo et al., 2016; Joo et al., 2014; Marzi et al., 2015; Yang et al., 2017).

Detsky and colleagues used IVIM imaging to investigate patients subjected to stereotactic radiotherapy (Detsky et al., 2017), and differentiate radiation necrosis from tumor progression. This differentiation is crucial for the continuation of or changes in the treatment. A signal enhancement in conventional MRI for both tumor progression and radiation necrosis hampers differentiation, although occurring in different scales. Detsky et al. showed perfusion fraction f might be useful for that differentiation (Fig. 5). The perfusion fraction map is uniformly low in the affected region for the radiation necrosis (top row of Fig. 5), whereas for tumor recurrence, it is more heterogeneous and shows higher perfusion fraction values (bottom row of Fig. 5). However, such findings must be validated in a larger cohort.

4. Combination of IVIM and ASL

Recent studies have documented gadolinium deposits in the brain and adverse effects in several subjects (Costa et al., 2018; Fitzgerald et al., 2018; Pullicino et al., 2018; Rahatli et al., 2018). As addressed in section 1, an accurate estimation of perfusion parameters based on DSC and DCE depends on different factors, including injection protocol and patients' anatomical vascularization. Therefore, a combination of ASL and IVIM may render a possible diagnostic benefit without the use of gadolinium.

Early ASL models assumed the labeled arterial blood could be classified as a freely diffusible tracer (Detre et al., 1992). However, other studies have reported the assumption is not completely valid, due

to regulatory mechanisms of BBB that reduce water permeability according to the tissue necessity (Eichling et al., 1974; Li et al., 2005; Parkes and Tofts, 2002; Zhou et al., 2001). Researchers started to assess the ASL signal through a two-compartment model that considers BBB permeability. ASL images acquired at multiple inflow times, which is known as multi-TI/PLD ASL, are an alternative for the obtaining of the BBB permeability resulted from a fitting model. However, the origin of ASL signal must be investigated through its splitting into intravascular and extravascular contributions, which can be done with IVIM. Therefore, a combination of ASL and IVIM started to be considered.

The combination of ASL and diffusion gradients was first described by Wang et al. (Wang et al., 2007), who used a hybrid sequence of continuous ASL and the twice-refocused spin-echo method for acquiring images with different b -values at three different post-labeling delays (PLDs). They estimated the BBB permeability to water through the bi-exponential model. Lawrence et al. reported a similar study but using a two-stage approach (Lawrence et al., 2012). First, the hybrid ASL-DWI sequence was used in the estimation of b -values necessary for the separation of extra and intravascular components of the ASL signal. Using only the chosen b -values and varying the PLD, the authors acquired images that enabled the calculation of each contribution to the signal (Fig. 6).

Other studies have aimed at better results of BBB permeability and understanding of the origin of the MRI perfusion signal (Hales and Clark, 2013; Zhang et al., 2018). The results of the combination of ASL and IVIM methods are promising and suggest a possible new imaging tool for the assessment of water exchange across BBB, providing important information about diseases as tumor and CSVD, and neurodegeneration.

5. Conclusions

IVIM method is a diffusion-weighted MRI sequence for the estimation of perfusion parameters that offers several advantages in comparison to commonly used approaches. First, it is a noninvasive alternative for the measurement of perfusion with no intravenous injection of exogenous contrast agents, as gadolinium, and provides information on

perfusion and diffusion simultaneously through a single image sequence, which shortens the exam. Third, its signal has high spatial specificity since it comes primarily from where the measure is achieved independently of the arterial blood path before arriving there. Finally, it provides complementary information in comparison to ASL and the combination of both methods can be useful for the assessment of neurological diseases.

However, for being a recently rediscovered method, especially for brain applications, IVIM is in development in almost every stage, such as acquisition, analysis, and applications. There is still discussion on how many b-values are necessary to obtain a reliable signal fitting, the maximum b-value to be acquired and the cutoff value where diffusion dominates the signal. Regarding analysis, physiological models and fitting strategies are still under investigation.

Conflict of interest

The author(s) declare(s) that there is no conflict of interest regarding the publication of this paper.

Acknowledgments

The authors would like to acknowledge Angela Cristina Pregnolato Giampedro for editing the manuscript for language and style.

References

- Alsop, D.C., Detre, J.A., Golay, X., Gunther, M., Hendrikse, J., Hernandez-Garcia, L., Lu, H., MacIntosh, B.J., Parkes, L.M., Smits, M., van Osch, M.J., Wang, D.J., Wong, E.C., Zaharchuk, G., 2015. Recommended implementation of arterial spin-labeled perfusion MRI for clinical applications: a consensus of the ISMRM perfusion study group and the European consortium for ASL in dementia. *Magn. Reson. Med.* 73, 102–116.
- Bertleff, M., Domsch, S., Weingartner, S., Zapp, J., O'Brien, K., Barth, M., Schad, L.R., 2017. Diffusion parameter mapping with the combined intravoxel incoherent motion and kurtosis model using artificial neural networks at 3 T. *NMR Biomed.* 30.
- Bisdas, S., Koh, T.S., Roder, C., Braun, C., Schittenhelm, J., Ernemann, U., Klose, U., 2013. Intravoxel incoherent motion diffusion-weighted MR imaging of gliomas: feasibility of the method and initial results. *Neuroradiology* 55, 1189–1196.
- Bisdas, S., Braun, C., Skardelly, M., Schittenhelm, J., Teo, T.H., Thng, C.H., Klose, U., Koh, T.S., 2014. Correlative assessment of tumor microcirculation using contrast-enhanced perfusion MRI and intravoxel incoherent motion diffusion-weighted MRI: is there a link between them? *NMR Biomed.* 27, 1184–1191.
- Budinger, T.F., Knittel, B.L., Bruner, P., Harrison, C., 1985. Tissue perfusion phantom for magnetic resonance flow studies. In: 4th Annual Meeting of Society of Magnetic Resonance in Medicine, Berkley, California, pp. 577–588.
- Buxton, R.B., 2005. Quantifying CBF with arterial spin labeling. *J. Magn. Reson. Imaging* 22, 723–726.
- Buxton, R.B., Frank, L.R., Wong, E.C., Siewert, B., Warach, S., Edelman, R.R., 1998. A general kinetic model for quantitative perfusion imaging with arterial spin labeling. *Magn. Reson. Med.* 40, 383–396.
- Calli, C., Kitis, O., Yunteen, N., Yurtseven, T., Islekeli, S., Akalin, T., 2006. Perfusion and diffusion MR imaging in enhancing malignant cerebral tumors. *Eur. J. Radiol.* 58, 394–403.
- Carr, H.Y., Purcell, E.M., 1954. Effects of diffusion on free precession in nuclear magnetic resonance experiments. *Phys. Rev.* 94, 630–638.
- Cordonnier, C., Al-Shahi Salman, R., Wardlaw, J., 2007. Spontaneous brain microbleeds: systematic review, subgroup analyses and standards for study design and reporting. *Brain* 130, 1988–2003.
- Costa, A., Ronchi, A., Pigatto, P.D., Guzzi, G., 2018. Brain gadolinium deposition, hypointense MRI signals, and resonance contrast agents. *Magn. Reson. Imaging* 137–138.
- Cui, Y., Zhang, C., Li, X., Liu, H., Yin, B., Xu, T., Zhang, Y., Wang, D., 2015. Intravoxel incoherent motion diffusion-weighted magnetic resonance imaging for monitoring the early response to ZD6474 from nasopharyngeal carcinoma in Nude Mouse. *Sci. Rep.* 5, 16389.
- de Robles, P., Fiest, K.M., Frolkis, A.D., Pringsheim, T., Atta, C., St Germaine-Smith, C., Day, L., Lam, D., Jette, N., 2015. The worldwide incidence and prevalence of primary brain tumors: a systematic review and meta-analysis. *Neuro-Oncology* 17, 776–783.
- Detre, J.A., Leigh, J.S., Williams, D.S., Koretsky, A.P., 1992. Perfusion imaging. *Magn. Reson. Med.* 23, 37–45.
- Detsky, J.S., Keith, J., Conklin, J., Symons, S., Myrehaug, S., Sahgal, A., Heyn, C.C., Soliman, H., 2017. Differentiating radiation necrosis from tumor progression in brain metastases treated with stereotactic radiotherapy: utility of intravoxel incoherent motion perfusion MRI and correlation with histopathology. *J. Neuro-Oncol.* 134, 433–441.
- Eichling, J.O., Raichle, M.E., Grubb Jr., R.L., Ter-Pogossian, M.M., 1974. Evidence of the limitations of water as a freely diffusible tracer in brain of the rhesus monkey. *Circ. Res.* 35, 358–364.
- Einstein, A., 1956. *Investigations on the Theory of the Brownian Movement*. Dover Publications, New York.
- Ewers, M., Teipel, S.J., Dietrich, O., Schonberg, S.O., Jessen, F., Heun, R., Scheltens, P., van de Pol, L., Freymann, N.R., Moeller, H.J., Hampel, H., 2006. Multicenter assessment of reliability of cranial MRI. *Neurobiol. Aging* 27, 1051–1059.
- Federau, C., Meuli, R., O'Brien, K., Maeder, P., Hagmann, P., 2014a. Perfusion measurement in brain gliomas with intravoxel incoherent motion MRI. *Am. J. Neuroradiol.* 35, 256–262.
- Federau, C., O'Brien, K., Meuli, R., Hagmann, P., Maeder, P., 2014b. Measuring brain perfusion with intravoxel incoherent motion (IVIM): initial clinical experience. *J. Magn. Reson. Imaging* 39, 624–632.
- Federau, C., Sumer, S., Beccé, F., Maeder, P., O'Brien, K., Meuli, R., Wintermark, M., 2014c. Intravoxel incoherent motion perfusion imaging in acute stroke: initial clinical experience. *Neuroradiology* 56, 629–635.
- Ferre, J.C., Bannier, E., Raoult, H., Mineura, G., Carsin-Nicol, B., Gauvrit, J.Y., 2013. Arterial spin labeling (ASL) Perfusion: techniques and clinical use. *J. De Radiol. Diag. et Intervent.* 94, 1208–1221.
- Fitzgerald, R.T., Agarwal, V., Hoang, J.K., Gaillard, F., Dixon, A., Kanal, E., 2018. The impact of gadolinium deposition on radiology practice: an international survey of radiologists. *Curr. Probl. Diagn. Radiol.*
- Fournet, G., Li, J.R., Cerjanic, A.M., Sutton, B.P., Ciobanu, L., Le Bihan, D., 2017. A two-pool model to describe the IVIM cerebral perfusion. *J. Cereb. Blood Flow Metab.* 37, 2987–3000.
- Goodenberger, M.L., Jenkins, R.B., 2012. Genetics of adult glioma. *Cancer Genet.* 205, 613–621.
- Guo, A.C., Cummings, T.J., Dash, R.C., Provenzale, J.M., 2002. Lymphomas and high-grade astrocytomas: comparison of water diffusibility and histologic characteristics. *Radiology* 224, 177–183.
- Gustafsson, O., Montelius, M., Starck, G., Ljungberg, M., 2018. Impact of prior distributions and central tendency measures on Bayesian intravoxel incoherent motion model fitting. *Magn. Reson. Med.* 79, 1674–1683.
- Hahn, E.L., 1950. Spin Echoes. *Phys. Rev.* 77, 746.
- Hales, P.W., Clark, C.A., 2013. Combined arterial spin labeling and diffusion-weighted imaging for noninvasive estimation of capillary volume fraction and permeability-surface product in the human brain. *J. Cereb. Blood Flow Metab.* 33, 67–75.
- Hall, J.E., Guyton, A.C., 2011. *Guyton and Hall Textbook of Medical Physiology*, 12th ed. Saunders/Elsevier, Philadelphia, PA.
- Henkelman, R.M., 1990. Does Ivm measure Classical Perfusion. *Magn. Reson. Med.* 16, 470–475.
- Henkelman, R.M., Neil, J.J., Xiang, Q.S., 1994. A quantitative interpretation of Ivm measurements of vascular perfusion in the rat-brain. *Magn. Reson. Med.* 32, 464–469.
- Heye, A.K., Culling, R.D., Valdes Hernandez Mdel, C., Thriplleton, M.J., Wardlaw, J.M., 2014. Assessment of blood-brain barrier disruption using dynamic contrast-enhanced MRI: A systematic review. *Neuroimage Clin.* 6, 262–274.
- Heye, A.K., Thriplleton, M.J., Armitage, P.A., Valdes Hernandez, M.D.C., Makin, S.D., Glatz, A., Sakka, E., Wardlaw, J.M., 2016. Tracer kinetic modelling for DCE-MRI quantification of subtle blood-brain barrier permeability. *NeuroImage* 125, 446–455.
- Hu, Y.C., Yan, L.F., Wu, L., Du, P., Chen, B.Y., Wang, L., Wang, S.M., Han, Y., Tian, Q., Yu, Y., Xu, T.Y., Wang, W., Cui, G.B., 2014. Intravoxel incoherent motion diffusion-weighted MR imaging of gliomas: efficacy in preoperative grading. *Sci. Rep.* 4.
- Hu, L.B., Hong, N., Zhu, W.Z., 2015. Quantitative measurement of cerebral perfusion with intravoxel incoherent motion in acute ischemia stroke: initial clinical experience. *Chin. Med. J.* 128, 2565–2569.
- Hu, F., Yang, R., Huang, Z., Wang, M., Zhang, H., Yan, X., Song, B., 2017. Liver fibrosis: in vivo evaluation using intravoxel incoherent motion-derived histogram metrics with histopathologic findings at 3.0 T. *Abdom. Radiol. (NY)* 42, 2855–2863.
- Huang, Y.C., Liu, H.L., Lee, J.D., Yang, J.T., Weng, H.H., Lee, M., Yeh, M.Y., Tsai, Y.H., 2013. Comparison of arterial spin labeling and dynamic susceptibility contrast perfusion MRI in patients with acute stroke. *PLoS One* 8, e69085.
- Jahng, G.H., Li, K.L., Ostergaard, L., Calamante, F., 2014. Perfusion magnetic resonance imaging: a comprehensive update on principles and techniques. *Korean J. Radiol.* 15, 554–577.
- Joo, I., Lee, J.M., Han, J.K., Choi, B.I., 2014. Intravoxel incoherent motion diffusion-weighted MR imaging for monitoring the therapeutic efficacy of the vascular disrupting agent CKD-516 in rabbit VX2 liver tumors. *Radiology* 272, 417–426.
- Joo, I., Lee, J.M., Grimm, R., Han, J.K., Choi, B.I., 2016. Monitoring vascular disrupting therapy in a rabbit liver tumor model: relationship between tumor perfusion parameters at IVM diffusion-weighted MR imaging and those at dynamic contrast-enhanced MR imaging. *Radiology* 278, 104–113.
- Jovicich, J., Czanner, S., Han, X., Salat, D., van der Kouwe, A., Quinn, B., Pacheco, J., Albert, M., Killiany, R., Blacker, D., Maguire, P., Rosas, D., Makris, N., Gollub, R., Dale, A., Dickerson, B.C., Fischl, B., 2009. MRI-derived measurements of human subcortical, ventricular and intracranial brain volumes: Reliability effects of scan sessions, acquisition sequences, data analyses, scanner upgrade, scanner vendors and field strengths. *NeuroImage* 46, 177–192.
- Keil, V.C., Madler, B., Gielan, G.H., Pinteau, B., Hithethiya, K., Gaspranova, A.R., Gieseke, J., Simon, M., Schild, H.H., Hadizadeh, D.R., 2017. Intravoxel incoherent motion MRI in the brain: Impact of the fitting model on perfusion fraction and lesion differentiability. *J. Magn. Reson. Imaging* 46, 1187–1199.
- Krogh, A., 1922. *The Anatomy and Physiology of Capillaries*. Yale University Press, New Haven, Conn.
- Kruggel, F., Turner, J., Muftuler, L.T., Alzheimer's Disease Neuroimaging, 2010. Impact of scanner hardware and imaging protocol on image quality and compartment volume precision in the ADNI cohort. *NeuroImage* 49, 2123–2133.
- Lawrence, K.S., Owen, D., Wang, D.J.J., 2012. A two-stage approach for measuring

- vascular water exchange and arterial transit time by diffusion-weighted perfusion MRI. *Magn. Reson. Med.* 67, 1275–1284.
- Le Bihan, D., 1992. Theoretical principles of perfusion imaging. Application to magnetic resonance imaging. *Investig. Radiol.* 27 (Suppl. 2), S6–11.
- Le Bihan, D., 2017. What can we see with IVIM MRI? *NeuroImage* 1–12.
- Le Bihan, D., Turner, R., 1992. The capillary network: a link between IVIM and classical perfusion. *Magn. Reson. Med.* 27, 171–178.
- Le Bihan, D., Breton, E., Lallemand, D., Grenier, P., Cabanis, E., Laval-Jeantet, M., 1986. MR imaging of intravoxel incoherent motions: application to diffusion and perfusion in neurologic disorders. *Radiology* 161, 401–407.
- Le Bihan, D., Breton, E., Lallemand, D., Aubin, M.L., Vignaud, J., Laval-Jeantet, M., 1988. Separation of diffusion and perfusion in intravoxel incoherent motion MR imaging. *Radiology* 168, 497–505.
- Lemke, A., Stieljes, B., Schad, L.R., Laun, F.B., 2011. Toward an optimal distribution of b values for intravoxel incoherent motion imaging. *Magn. Reson. Imaging* 29, 766–776.
- Li, K.L., Zhu, X., Hylton, N., Jahng, G.H., Weiner, M.W., Schuff, N., 2005. Four-phase single-capillary stepwise model for kinetics in arterial spin labeling MRI. *Magn. Reson. Med.* 53, 511–518.
- Li, Y.T., Cercueil, J.P., Yuan, J., Chen, W., Loffroy, R., Wang, Y.X., 2017. Liver intravoxel incoherent motion (IVIM) magnetic resonance imaging: a comprehensive review of published data on normal values and applications for fibrosis and tumor evaluation. *Quant. Imaging Med. Surg.* 7, 59–78.
- Liang, L., Chen, W.B., Chan, K.W., Li, Y.G., Zhang, B., Liang, C.H., Liu, G.S., Zhang, S.X., 2016. Using intravoxel incoherent motion MR imaging to study the renal pathophysiological process of contrast-induced acute kidney injury in rats: Comparison with conventional DWI and arterial spin labelling. *Eur. Radiol.* 26, 1597–1605.
- Louis, D.N., Perry, A., Reifenberger, G., von Deimling, A., Figarella-Branger, D., Cavenee, W.K., Ohgaki, H., Wiestler, O.D., Kleihues, P., Ellison, D.W., 2016. The 2016 World Health Organization classification of tumors of the central nervous system: a summary. *Acta Neuropathol.* 131, 803–820.
- Luciani, A., Vignaud, A., Cavet, M., Nhieu, J.T., Mallat, A., Ruel, L., Laurent, A., Deux, J.F., Brugieres, P., Rahmouni, A., 2008. Liver cirrhosis: intravoxel incoherent motion MR imaging—pilot study. *Radiology* 249, 891–899.
- MacIntosh, B.J., Filippini, N., Chappell, M.A., Woolrich, M.W., MacKay, C.E., Jezzard, P., 2010. Assessment of arterial arrival times derived from multiple inversion time pulsed arterial spin labeling MRI. *Magn. Reson. Med.* 63, 641–647.
- Markus, H.S., Lythgoe, D.J., Ostegard, L., O'Sullivan, M., Williams, S.C.R., 2000. Reduced cerebral blood flow in white matter in ischaemic leukoaraiosis demonstrated using quantitative exogenous contrast based perfusion MRI. *J. Neurol. Neurosurg. Psych.* 69, 48–53.
- Marzi, S., Forina, C., Marucci, L., Giovinazzo, G., Giordano, C., Piludu, F., Landoni, V., Spriano, G., Vidiri, A., 2015. Early radiation-induced changes evaluated by intravoxel incoherent motion in the major salivary glands. *J. Magn. Reson. Imaging* 41, 974–982.
- Meeus, E.M., Novak, J., Dehghani, H., Peet, A.C., 2018. Rapid measurement of intravoxel incoherent motion (IVIM) derived perfusion fraction for clinical magnetic resonance imaging. *MAGMA* 31, 269–283.
- Muir, K.W., Buchan, A., von Kummer, R., Rother, J., Baron, J.C., 2006. Imaging of acute stroke. *Lancet Neurol.* 5, 755–768.
- Mullen, K.M., Huang, R.Y., 2017. An update on the approach to the imaging of brain tumors. *Curr. Neurosci. Rep.* 17, 53.
- Neil, J.J., Ackerman, J.J.H., 1992. Detection of pseudodiffusion in rat-brain following blood substitution with perfluorocarbon. *J. Magn. Reson.* 97, 194–201.
- Neil, J.J., Scherer, L.A., Ackerman, J.J.H., 1991. An approach to solving the dynamic-range problem in measurement of the pseudodiffusion coefficient *in vivo* with spin echoes. *J. Magn. Reson.* 95, 607–614.
- Neil, J.J., Bosch, C.S., Ackerman, J.J.H., 1994. An evaluation of the sensitivity of the intravoxel incoherent motion (IVIM) method of blood-flow measurement to changes in cerebral blood-flow. *Magn. Reson. Med.* 32, 60–65.
- Obrig, H., 2014. NIRS in clinical neurology - a 'promising' tool? *NeuroImage* 85, 535–546.
- O'Sullivan, M., Lythgoe, D.J., Pereira, A.C., Summers, P.E., Jarosz, J.M., Williams, S.C.R., Markus, H.S., 2002. Patterns of cerebral blood flow reduction in patients with ischemic leukoaraiosis. *Neurology* 59, 321–326.
- Paldino, M.J., Barboriak, D.P., 2009. Fundamentals of quantitative dynamic contrast-enhanced MR imaging. *Magn. Reson. Imaging Clin. N. Am.* 17, 277–289.
- Parkes, L.M., Tofts, P.S., 2002. Improved accuracy of human cerebral blood perfusion measurements using arterial spin labeling: accounting for capillary water permeability. *Magn. Reson. Med.* 48, 27–41.
- Plate, K.H., Breier, G., Weich, H.A., Risau, W., 1992. Vascular endothelial growth factor is a potential tumour angiogenesis factor in human gliomas *in vivo*. *Nature* 359, 845–848.
- Pullincino, R., Radon, M., Biswas, S., Bhojak, M., Das, K., 2018. A review of the current evidence on gadolinium deposition in the brain. *Clin. Neuroradiol.* 28, 159–169.
- Rahatli, F.K., Donmez, F.Y., Kibaroglu, S., Kesim, C., Haberal, K.M., Turnaoglu, H., Agildere, A.M., 2018. Does renal function affect gadolinium deposition in the brain? *Eur. J. Radiol.* 104, 33–37.
- Reig, S., Sanchez-Gonzalez, J., Arango, C., Castro, J., Gonzalez-Pinto, A., Ortuno, F., Crespo-Facorro, B., Bargallo, N., Desco, M., 2009. Assessment of the increase in variability when combining volumetric data from different scanners. *Hum. Brain Mapp.* 30, 355–368.
- Roob, G., Schmidt, R., Kapeller, P., Lechner, A., Hartung, H.P., Fazekas, F., 1999. MRI evidence of past cerebral microbleeds in a healthy elderly population. *Neurology* 52, 991–994.
- Schnack, H.G., van Haren, N.E., Hulshoff Pol, H.E., Picchioni, M., Weisbrod, M., Sauer, H., Cannon, T., Huttunen, M., Murray, R., Kahn, R.S., 2004. Reliability of brain volumes from multicenter MRI acquisition: a calibration study. *Hum. Brain Mapp.* 22, 312–320.
- Shim, W.H., Kim, H.S., Choi, C.G., Kim, S.J., 2015. Comparison of apparent diffusion coefficient and intravoxel incoherent motion for differentiating among glioblastoma, metastasis, and lymphoma focusing on diffusion-related parameter. *PLoS One* 10.
- Sourbron, S.P., Buckley, D.L., 2013a. Classic models for dynamic contrast-enhanced MRI. *NMR Biomed.* 26, 1004–1027.
- Sourbron, S.P., Buckley, D.L., 2013b. Classic models for dynamic contrast-enhanced MRI. *NMR Biomed.* 26, 1004–1027.
- Stejskal, E.O., Tanner, J.E., 1965. Spin diffusion measurements: spin echoes in the presence of time-dependent field gradient. *J. Chem. Phys.* 42, 288.
- Suh, C.H., Kim, H.S., Lee, S.S., Kim, N., Yoon, H.M., Choi, C.G., Kim, S.J., 2014. Atypical imaging features of primary central nervous system lymphoma that mimics glioblastoma: utility of intravoxel incoherent motion MR imaging. *Radiology* 272, 504–513.
- Suo, S., Cao, M., Zhu, W., Li, L., Li, J., Shen, F., Zu, J., Zhou, Z., Zhuang, Z., Qu, J., Chen, Z., Xu, J., 2016. Stroke assessment with intravoxel incoherent motion diffusion-weighted MRI. *NMR Biomed.* 29, 320–328.
- Tanner, J.E., Stejskal, E.O., 1968. Restricted self-diffusion of protons in colloidal systems by pulsed-gradient spin-echo method. *J. Chem. Phys.* 49, 1768.
- Togao, O., Hiwatashi, A., Yamashita, K., Kikuchi, K., Mizoguchi, M., Yoshimoto, K., Suzuki, S.O., Iwaki, T., Obara, M., Van Cauteren, M., Honda, H., 2016. Differentiation of high-grade and low-grade diffuse gliomas by intravoxel incoherent motion MR imaging. *Neuro-Oncology* 18, 132–141.
- Toh, C.H., Castillo, M., Wong, A.M., Wei, K.C., Wong, H.F., Ng, S.H., Wan, Y.L., 2008. Primary cerebral lymphoma and glioblastoma multiforme: differences in diffusion characteristics evaluated with diffusion tensor imaging. *AJNR Am. J. Neuroradiol.* 29, 471–475.
- Wang, J.J., Fernandez-Seara, M.A., Wang, S.M., St Lawrence, K.S., 2007. When perfusion meets diffusion: *in vivo* measurement of water permeability in human brain. *J. Cereb. Blood Flow Metab.* 27, 839–849.
- Wardlaw, J.M., 2010. Blood-brain barrier and cerebral small vessel disease. *J. Neurol. Sci.* 299, 66–71.
- Wardlaw, J.M., Doubal, F.N., Valdes-Hernandez, M., Wang, X., Chappell, F.M., Shuler, K., Armitage, P.A., Carpenter, T.C., Dennis, M.S., 2013a. Blood-brain barrier permeability and long-term clinical and imaging outcomes in cerebral small vessel disease. *Stroke* 44, 525–527.
- Wardlaw, J.M., Smith, C., Dichgans, M., 2013b. Mechanisms of sporadic cerebral small vessel disease: insights from neuroimaging. *Lancet Neurol.* 12, 483–497.
- Wardlaw, J.M., Smith, E.E., Biessels, G.J., Cordonnier, C., Fazekas, F., Frayne, R., Lindley, R.I., O'Brien, J.T., Barkhof, F., Benavente, O.R., Black, S.E., Brayne, C., Breteler, M., Chabriat, H., Decarli, C., de Leeuw, F.E., Doubal, F., Duering, M., Fox, N.C., Greenberg, S., Hachinski, V., Kilimann, I., Mok, V., Oostenbrugge, R., Pantoni, L., Speck, O., Stephan, B.C., Teipel, S., Viswanathan, A., Werring, D., Chen, C., Smith, G., van Buchem, M., Norrving, B., Gorelick, P.B., Dichgans, M., Neuroimaging, S.T.f.R.V.c.o., 2013c. Neuroimaging standards for research into small vessel disease and its contribution to ageing and neurodegeneration. *Lancet Neurol.* 12, 822–838.
- Williams, D.S., Detre, J.A., Leigh, J.S., Koretsky, A.P., 1992. Magnetic resonance imaging of perfusion using spin inversion of arterial water. *Proc. Natl. Acad. Sci. U S A* 89, 212–216.
- Wintermark, M., Sesay, M., Barbier, E., Borbely, K., Dillon, W.P., Eastwood, J.D., Glenn, T.C., Grandin, C.B., Pedraza, S., Soustiel, J.F., Nariai, T., Zaharchuk, G., Caille, J.M., Dousset, V., Yonas, H., 2005. Comparative overview of brain perfusion imaging techniques. *J. Neuroradiol.* 32, 294–314.
- Wirestam, R., Brockstedt, S., Lindgren, A., Geijer, B., Thomsen, C., Holtas, S., Stahlberg, F., 1997. The perfusion fraction in volunteers and in patients with ischaemic stroke. *Acta Radiol.* 38, 961–964.
- Wonderlick, J.S., Ziegler, D.A., Hosseini-Varnamkhasti, P., Locascio, J.J., Bakkour, A., van der Kouwe, A., Triantafyllou, C., Corkin, S., Dickerson, B.C., 2009. Reliability of MRI-derived cortical and subcortical morphometric measures: effects of pulse sequence, voxel geometry, and parallel imaging. *NeuroImage* 44, 1324–1333.
- Wong, S.M., Zhang, C.E., van Bussel, F.C.G., Staals, J., Jeukens, C.R.L.P.N., Hofman, P.A.M., van Oostenbrugge, R.J., Backes, W.H., Jansen, J.F.A., 2017. Simultaneous investigation of microvasculature and parenchyma in cerebral small vessel disease using intravoxel incoherent motion imaging. *NeuroImage Clin.* 14, 216–221.
- World Health Organization, 2017. The Top 10 Causes of Death.
- Wu, W.C., Chen, Y.F., Tseng, H.M., Yang, S.C., My, P.C., 2015. Caveat of measuring perfusion indexes using intravoxel incoherent motion magnetic resonance imaging in the human brain. *Eur. Radiol.* 25, 2485–2492.
- Yamada, J., Aung, W., Himeno, Y., Nakagawa, T., Shibuya, H., 1999. Diffusion coefficients in abdominal organs and hepatic lesions: evaluation with intravoxel incoherent motion echo-planar MR imaging. *Radiology* 210, 617–623.
- Yamasaki, F., Kurisu, K., Satoh, K., Arita, K., Sugiyama, K., Ohtaki, M., Takaba, J., Tominaga, A., Hanaya, R., Yoshioka, H., Hama, S., Ito, Y., Kajiwara, Y., Yahara, K., Saito, T., Thohar, M.A., 2005. Apparent diffusion coefficient of human brain tumors at MR imaging. *Radiology* 235, 985–991.
- Yamashita, K., Hiwatashi, A., Togao, O., Kikuchi, K., Kitamura, Y., Mizoguchi, M., Yoshimoto, K., Kuga, D., Suzuki, S.O., Baba, S., Isoda, T., Iwaki, T., Ihara, K., Honda, H., 2016. Diagnostic utility of intravoxel incoherent motion mr imaging in differentiating primary central nervous system lymphoma from glioblastoma multiforme. *J. Magn. Reson. Imaging* 44, 1256–1261.
- Yang, S.H., Lin, J., Lu, F., Han, Z.H., Fu, C.X., Lv, P., Liu, H., Gao, D.M., 2017. Evaluation of antiangiogenic and antiproliferative effects of sorafenib by sequential histology and intravoxel incoherent motion diffusion-weighted imaging in an orthotopic hepatocellular carcinoma xenograft model. *J. Magn. Reson. Imaging* 45, 270–280.
- Yao, Y., Zhang, S., Tang, X., Zhang, S., Shi, J., Zhu, W., Zhu, W., 2016. Intravoxel incoherent motion diffusion-weighted imaging in stroke patients: initial clinical

- experience. Clin. Radiol. 71 (938), e911–e936.
- Zhang, S.X., Yao, Y.H., Zhang, S., Zhu, W.J., Tang, X.Y., Qin, Y.Y., Zhao, L.Y., Liu, C.X., Zhu, W.Z., 2015. Comparative study of DSC-PWI and 3D-ASL in ischemic stroke patients. J. Huazhong Univ. Sci. Technol. Med. Sci. 35, 923–927.
- Zhang, X., Ingo, C., Teeuwisse, W.M., Chen, Z., van Osch, M.J.P., 2018. Comparison of perfusion signal acquired by arterial spin labeling-prepared intravoxel incoherent motion (IVIM) MRI and conventional IVIM MRI to unravel the origin of the IVIM signal. Magn. Reson. Med. 79, 723–729.
- Zhou, J., Wilson, D.A., Ulatowski, J.A., Traystman, R.J., van Zijl, P.C., 2001. Two-compartment exchange model for perfusion quantification using arterial spin tagging. J. Cereb. Blood Flow Metab. 21, 440–455.

43 Autoria de artigos completos publicados em jornais e revistas de circulação nacional e internacional na sua área

Esta subseção apresenta o comprovante da autoria do artigo publicado na revista internacional *Concepts in Magnetic Resonance Part A* no ano de 2019.

Research Article

Dual-Echo Arterial Spin Labeling for Brain Perfusion Quantification and Functional Analysis

André Monteiro Paschoal ,¹ Fernando Fernandes Paiva,² and Renata Ferranti Leoni ¹

¹Departamento de Física, FFCLRP, Universidade de São Paulo, Ribeirão Preto, SP, Brazil

²Instituto de Física de São Carlos, Universidade de São Paulo, São Carlos, SP, Brazil

Correspondence should be addressed to Renata Ferranti Leoni; leonirf@usp.br

Received 28 March 2019; Accepted 19 June 2019; Published 1 August 2019

Academic Editor: Claudio Luchinat

Copyright © 2019 André Monteiro Paschoal et al. This is an open access article distributed under the Creative Commons Attribution License, which permits unrestricted use, distribution, and reproduction in any medium, provided the original work is properly cited.

Arterial Spin Labeling (ASL) is a noninvasive MRI-based method to measure cerebral blood flow (CBF). Recently, the study of ASL as a functional tool has emerged once CBF fluctuation comes from capillaries in brain tissue, giving a more spatially specific response when compared to the standard functional MRI method, based on the blood oxygenation level-dependent (BOLD) contrast. Although the BOLD effect could be desirable to study brain function, if one aims to quantify CBF, such effect is considered contamination that can be more attenuated if short TE value is used in the image acquisition. An approach that provides both CBF and function information in a simultaneous acquisition is the use of a dual-echo ASL (DE-ASL) readout. Our purpose was to evaluate the information provided by DE-ASL regarding CBF quantification and functional connectivity with a motor task. Pseudocontinuous ASL of twenty healthy subjects (age: 32.4 ± 10.2 years, 13 male) was acquired at a 3T scanner. We analyzed the influence of TE on CBF values and brain connectivity provided by CBF and concurrent BOLD (cc-BOLD) time series. Brain networks were obtained by the general linear model and independent component analysis. Connectivity matrices were generated using a bivariate correlation (Fisher Z values). No effect of the sequence readout, but significant effect of the TE value, was observed on gray matter CBF values. Motor networks with reduced extension and more connections with important regions for brain integration were observed for CBF data acquired with short TE, proving its higher spatial specificity. Therefore, it was possible to use a dual-echo readout provided by a standard commercial ASL pulse sequence to obtain reliable quantitative CBF values and functional information simultaneously.

1. Introduction

Arterial Spin Labeling (ASL) is a magnetic resonance (MR) perfusion-weighted technique with the advantage of not using an exogenous contrast agent. It is achieved by using the arterial blood as an endogenous tracer, which is magnetically labeled (label image) through the application of radiofrequency (RF) pulses. Such pulses are applied in a strategic position (labeling plane) so that the magnetization in the region of interest (ROI) is changed compared to a non-label situation (control image) [1, 2]. With this set of images, cerebral blood flow (CBF) is estimated from the subtraction between control and label images. Due to the ASL intrinsic low signal-to-noise ratio (SNR), there is the necessity of

acquiring multiple control-label pairs, and the CBF map is the mean of all subtractions executed [3]. On the other hand, the temporal series of ASL images allows the evaluation of CBF fluctuations over time, from which functional information can be estimated [4–6].

Although in functional magnetic resonance imaging (fMRI) the blood oxygen level-dependent (BOLD) contrast is mainly used, applications of ASL in functional studies have increased over the last years mainly because of two reasons. First, while BOLD contrast depends on a complex combination of blood oxygenation, cerebral blood volume (CBV), CBF, and metabolic rate of oxygen (CMRO₂), ASL provides quantitative information of one physiologic parameter (CBF) [7, 8]. Second, ASL has a better spatial specificity to neuronal

activity when compared to BOLD [9–13]. Moreover, ASL combined with dual-echo readout (DE-ASL) is an interesting approach to optimize the acquisition aimed at both CBF quantification and functional analysis [14]. Images acquired using short echo time (TE) are more weighted in perfusion, while the use of longer TE increases the effect of transversal relaxation (T_2^*), typical of the BOLD contrast [6, 15].

Some previous reports used DE-ASL to evaluate the correlation between CBF time series and the concomitant BOLD (cc-BOLD) signal, either in resting state or with a visual/motor task condition, and analyze the functional connectivity [16–21]. Lu and colleagues showed the influence of BOLD contamination on the temporal dynamics of ASL curve but did not analyze its effects on functional connectivity [17]. Regarding acquisition and analysis, Ghariq and colleagues investigated some specific aspects of the signal and suggested the use of background suppression to reduce BOLD contamination and to increase CBF sensibility [16]. Moreover, Storti and colleagues recently reported the contribution of ASL to understand how CBF is related to functional connectivity [19] and the feasibility of DE-ASL to analyze brain function [20]. However, they did not evaluate the method regarding the direct effect of TE in CBF quantification, cc-BOLD and CBF networks, and functional analysis.

Therefore, we aimed to evaluate the CBF quantification with DE-ASL in comparison with standard ASL acquisition, analyze the similarity of networks between CBF and cc-BOLD and between each TE used, and verify changes in brain connectivity for different TE values.

2. Methods

2.1. Subjects. Twenty healthy participants (age: 32.4 ± 10.2 years, 13 male) were scanned on a 3T Achieva MRI Scanner (Philips Healthcare, Best, Netherlands) equipped with a 32-channel receive head coil. All subjects gave their written informed consent after the ethics committee of the institution approved the study.

2.2. Image Acquisition and Protocol. DE-ASL data were acquired using a 2D echo-planar imaging (EPI) readout and a pseudo-continuous labeling (pCASL) scheme with the following parameters: TR = 4000 ms, $TE_1/TE_2 = 9/28$ ms, labeling duration/postlabeling delay = 1450/1550 ms, 20 slices, slice thickness = 5 mm, spatial resolution = $3.75 \times 3.75 \text{ mm}^2$, FOV = $240 \times 240 \text{ mm}^2$, flip angle = 90° , and total acquisition time of 4.26 min. For conventional single-echo pCASL, the same parameters were used for both TE values (9 and 28 ms). No background suppression was used. In addition, a structural 3D gradient-echo T1-weighted scan was performed with TR = 7 ms, TE = 3.2 ms, FOV = $240 \times 240 \text{ mm}^2$, 180 slices, slice thickness = 1 mm, spatial resolution = $1 \times 1 \text{ mm}^2$, flip angle = 8° .

The experimental protocol was a block design paradigm alternating rest and right-hand finger tapping. Each block had duration of 32 seconds (8 volumes), totaling four blocks of rest and four blocks of motor task. The command to the

subject to start or stop the task was shown in a monitor: red screen during rest blocks and green screen for the task blocks.

2.3. Image Processing. Imaging preprocessing was performed using local scripts in MATLAB (MathWorks, Natick, MA) in combination with Statistical Parametric Mapping (SPM12, <http://www.fil.ion.ucl.ac.uk/spm/software/spm12/>). Structural T1-weighted images were used for segmentation and obtaining the gray matter (GM) and white matter (WM) masks. For ASL images, we adapted scripts from ASLtbx [22] performing the following steps: motion correction, coregistration to anatomical image and masks, temporal filtering, and spatial smoothing through the application of an isotropic Gaussian kernel (FWHM = 4 mm for CBF quantification and FWHM = 6 mm for functional images).

2.4. CBF Quantification. Perfusion maps were generated by the subtraction of control and label images. For basal CBF analysis, we used the sync subtraction, while for functional analysis we performed a running pairwise subtraction to increase the number of perfusion images [23]. Quantification was based on the General Kinetic Model [8] using the following parameters: blood longitudinal relaxation time (T_{1b}) = 1650 ms; labeling efficiency = 0.85; blood/tissue water partition coefficient (GM/WM) = 0.98/0.84 g/mL; tissue T1 (GM/WM) = 1020/770 ms calculated using a Look-Locker sequence [24]. Finally, CBF time series and mean CBF map were normalized to MNI standard space (resolution = $2 \times 2 \times 2 \text{ mm}^3$; matrix size: $79 \times 95 \times 79$).

2.5. General Linear Model. We ran a general linear model (GLM) analysis using FSL (<http://fsl.fmrib.ox.ac.uk/fsl/fslwiki>) to assess the differences regarding CBF and cc-BOLD networks between TE values. Both CBF and cc-BOLD information were obtained using FEAT to preprocess and perform the statistical analysis according to the following steps: subject motion correction (MCFLIRT [25]), brain extraction, spatial smoothing filtering (FWHM = 5 mm), temporal filtering, coregistration to MNI atlas, whitening, GLM analysis according to experimental design, and finally the clustering analysis. The obtained networks were spatially compared by the Dice Similarity Coefficient (DSC) [26] using local scripts in MATLAB.

2.6. Independent Component Analysis Networks. The functional analysis was performed using CONN Toolbox [27], in which CBF time series were detrended and filtered with a low-pass filter ($f < 0.07$). To remove the signal from white matter and cerebrospinal fluid we used principal component analysis (PCA) with the CompCor algorithm. Then, we ran the independent component analysis (ICA) algorithm setting 20 individual components previously.

Next, we selected the motor network that resulted from ICA from CBF maps obtained with each echo to evaluate the difference between them regarding spatial similarity and functional connectivity. For spatial similarity,

TABLE 1: Main anatomical regions activated during the finger-tapping task and the corresponding number of activated voxels.

TE ₁	Number of voxels	TE ₂	Number of voxels
Left Precentral Gyrus	418	Left Precentral Gyrus	431
Left Postcentral Gyrus	407	Left Postcentral Gyrus	500
Right Precentral Gyrus	384	Right Precentral Gyrus	489
Left Superior Parietal Lobule	292	Left Superior Parietal Lobule	281
Right Postcentral Gyrus	265	Right Postcentral Gyrus	176
Right Superior Parietal Lobule	169	Right Superior Parietal Lobule	241

we used the DSC calculated in MATLAB. We also analyzed the difference between groups in Z scores and performed a one-sample t-test using the R Project [28] to obtain a p-value matrix considering only significant differences ($p < 0.05$, corrected for multiple comparisons using Bonferroni-Holm method). Finally we evaluated the differences in functional connectivity between the two CBF time series.

3. Results

3.1. CBF Comparison between Single- and Dual-Echo pCASL. We compared the mean CBF values for gray matter acquired with different sequences and TEs to evaluate how such parameters affected the CBF quantification. Figure 1 shows CBF maps obtained with standard single-echo and dual-echo readouts. No significant difference in gray matter CBF values was observed for different readouts but the same TE. Mean values for TE₁ were 35.50 ± 11.23 mL/100g/min and 36.08 ± 9.45 mL/100 g/min, respectively, for single- and dual-echo acquisitions ($p = 0.95$). For TE₂ mean values were 21.84 ± 8.15 mL/100 g/min and 22.16 ± 6.74 mL/100 g/min, respectively, for single- and dual-echo acquisitions ($p = 0.95$). However, significant differences were observed when comparing CBF for different TE values but the same readout ($p < 0.05$), due to the T2 decay present in images acquired with longer TE value.

Considering only the motor cortex, for TE₁, CBF values were 41.58 ± 12.61 mL/100 g/min and 36.46 ± 14.21 mL/100g/min, respectively, for single- and dual-echo acquisitions ($p = 0.48$). And for TE₂, CBF values were 28.28 ± 8.22 mL/100g/min and 27.38 ± 9.69 mL/100g/min, respectively, for single- and dual-echo acquisitions ($p = 0.88$).

3.2. GLM Analysis. Figure 2 shows the motor network of normalized CBF and cc-BOLD. We only assessed the results obtained with the DE-ASL since they were acquired during the same scan, and no variability resulted due to differences in task performance. The spatial similarity between them was higher for TE₁ (DSC = 0.4, Figure 2(a)) than for TE₂ (Figure 2(b), DSC = 0.25). Moreover, when comparing CBF (Figure 2(c)) or cc-BOLD (Figure 2(d)) network for both TE values, we observed a higher number

of activated voxels for longer TE due to the higher BOLD contamination in the signal. It increases the sensitivity of the method to detect brain activation but decreases its spatial specificity. Such contamination can be seen on CBF time series for the longer TE. Figure 3 shows the mean CBF time series for all voxels of the motor network activated by the finger-tapping task normalized to the mean CBF of first rest condition block, considering all subjects.

3.3. ICA Networks. For both TE values, in a dual-echo acquisition, ICA was able to identify the following networks: motor, auditory, default mode network (DMN), visual and executive control network (ECN). A comparison of the motor network obtained for each TE showed a spatial similarity of 30% (DSC = 0.30). Table 1 shows how that difference in similarity is distributed over the anatomical regions by the different number of activated voxels in the primary motor cortex.

Figure 4 shows the connectivity patterns for the motor network obtained with both TE values of the dual-echo readout. Although for TE₂ (Figure 4(b)) the connectivity within the motor network was stronger than for TE₁ (Figure 4(a)), some connections with other brain regions, such as the precuneus, were not identified for the longer TE. Moreover, the correlation between right precentral and postcentral gyri was statistically significant ($p < 0.05$, FDR corrected) when comparing data of both TE values.

4. Discussion

The acquisition of DE-pCASL is an interesting strategy to acquire quantitative CBF and functional network information simultaneously. To guarantee that CBF is measured with the same precision as in standard pCASL scheme, we compared the results of CBF quantification for both readout schemes, EPI single- and dual-echo. We found that there is no significant difference between the gray matter CBF values obtained for each scheme. The difference in CBF between TE₁ and TE₂ was also nearly the same for single- and dual-echo schemes, in which the CBF values for TE₂ were approximately 60% of the ones for TE₁, due to T2 decay. One could account for such decay, but the lower image SNR for longer TE would

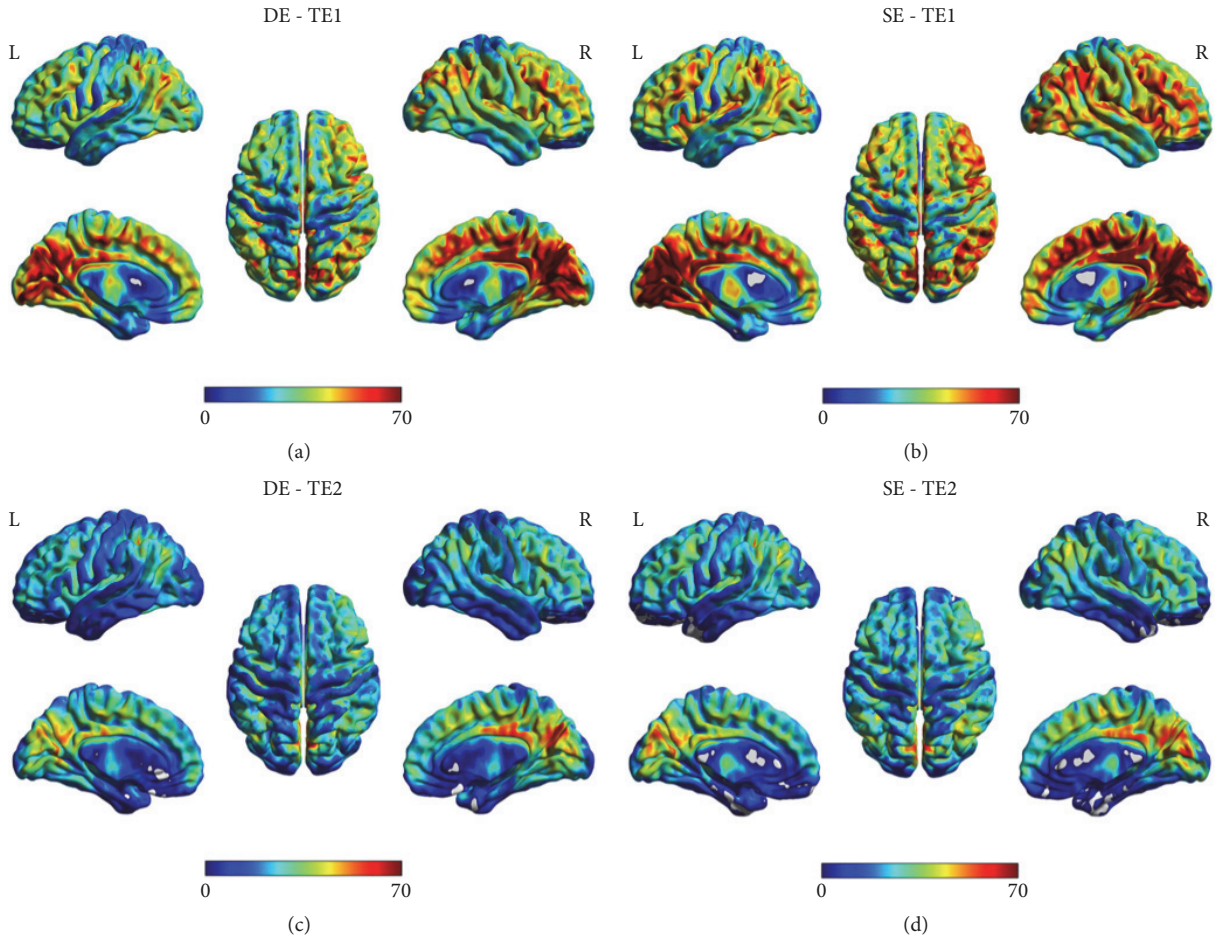


FIGURE 1: CBF maps obtained with different readouts (DE: dual-echo, SE: single-echo) and TE values: (a) DE, $TE_1 = 10$ ms; (b) SE, $TE_1 = 10$ ms; (c) DE, $TE_2 = 28$ ms; (d) SE, $TE_2 = 28$ ms. Color bar shows CBF range in $\text{mL}/100 \text{ g}/\text{min}$.

still be present [29], resulting in a decrease of precision in CBF quantification. Short TE values are preferred for that case. To our knowledge, it is the first study that confirms that it is trustful to quantify CBF with DE-pCASL and short TE.

Although there was considerable spatial overlap between CBF and cc-BOLD activation maps, the similarity coefficient was not high. More activation voxels were observed for cc-BOLD, confirming its higher sensitivity but lower spatial specificity when compared to CBF signal [30, 31]. It is especially observed for the longer TE acquisition where the BOLD contamination was higher (Figure 2). Such contamination may explain the signal variability observed on CBF time series for longer TE (Figure 3). For TE_1 , CBF values followed the experimental design for the finger-tapping task, in which all the four blocks were present. That behavior is not visible for TE_2 due to the lower SNR of the images, so that the effect of outliers had a high impact in the time-series profile.

Those differences in CBF signal for different TE values also reflected changes in functional connectivity. There was a

significant loss of connections among primary motor cortex areas and other regions not primarily associated with motor activation, but important for brain integration, such as the precuneus. Looking specifically to the primary motor cortex, we also found significant differences in the connectivity pattern for the connection between the post- and precentral gyri, two primary anatomical areas related to motor functions.

However, our study has some limitations. First, the number of volumes acquired in each block of the acquisition paradigm was small, which may increase the effects of outliers in the temporal series, especially for the longer TE (Figure 3). However, increasing the number of volumes per block would increase significantly the total acquisition time, so that it must be considered to design the experiment. Second, our sample size may be considered small. However, we performed robust data analysis which is constantly performed in studies with similar sample size.

In conclusion, our study explored a set of information provided by the acquisition of DE-pCASL. Regarding CBF

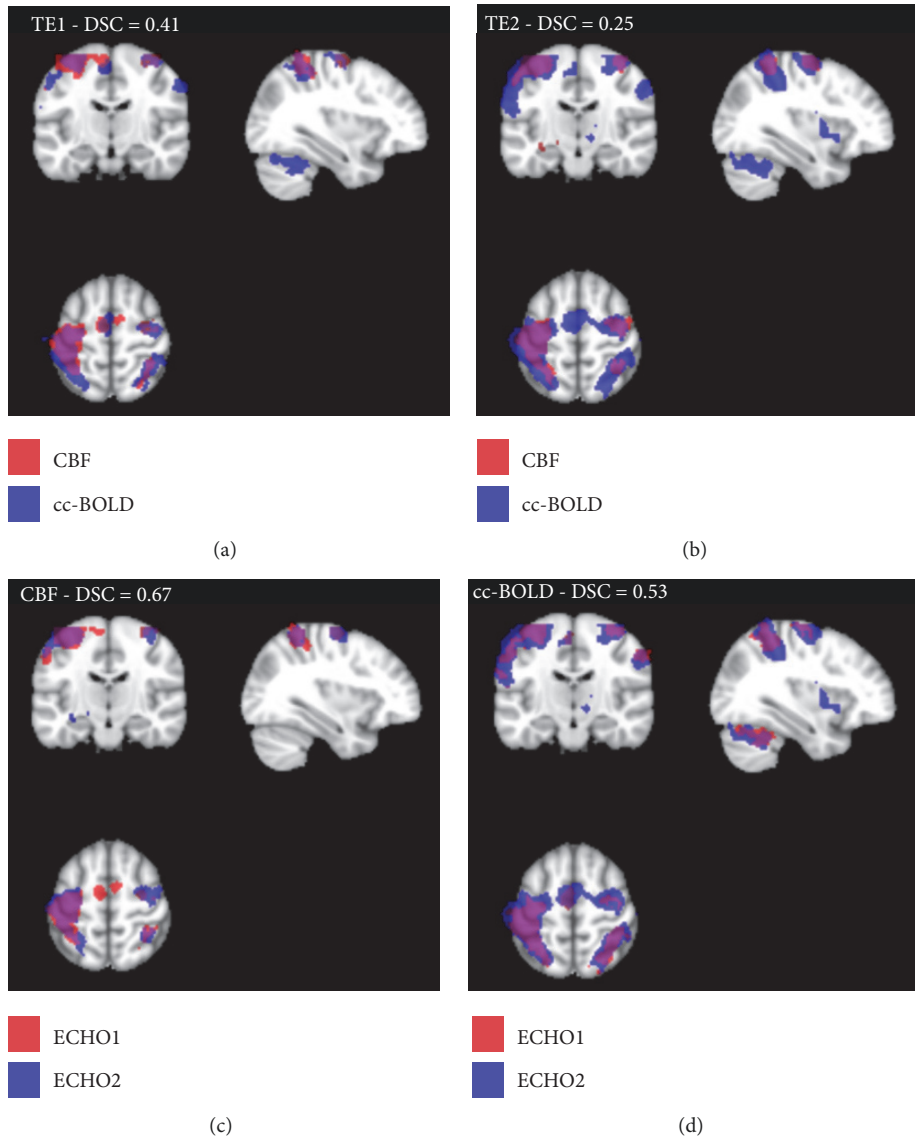


FIGURE 2: Comparisons of GLM results for the motor networks obtained with dual-echo readout: (a) CBF versus cc-BOLD for TE_1 ; (b) CBF versus cc-BOLD for TE_2 ; (c) TE_1 versus TE_2 for CBF networks; and (d) TE_1 versus TE_2 for cc-BOLD networks. DSC: Dice Similarity Coefficient.

quantification, we found that CBF values obtained through DE-pCASL are statistically the same as those obtained with the standard pCASL scheme. Also, for functional analysis, images acquired with short TE were successful in identifying brain networks. Our findings suggest that DE-pCASL results are trustful for both CBF quantification and functional analysis and may be a good alternative to separate acquisitions of ASL and BOLD-fMRI, reducing acquisition time without losing any of that information.

Data Availability

The magnetic resonance images used to support the findings of this study are restricted by the ethics board of the

institution in order to protect the participants' privacy. Data are available from the corresponding author upon request for researchers who meet the criteria for access to confidential data.

Conflicts of Interest

The authors declare that they have no conflicts of interest.

Acknowledgments

This study was supported by CNPq (Conselho Nacional de Desenvolvimento Científico e Tecnológico).

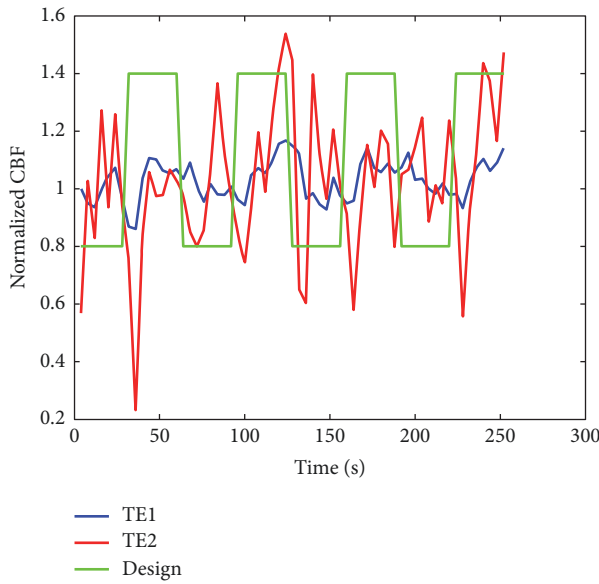


FIGURE 3: CBF time series normalized to the mean CBF of the first rest condition block for TE_1 (blue) and TE_2 (red). The experimental block design is shown in green.

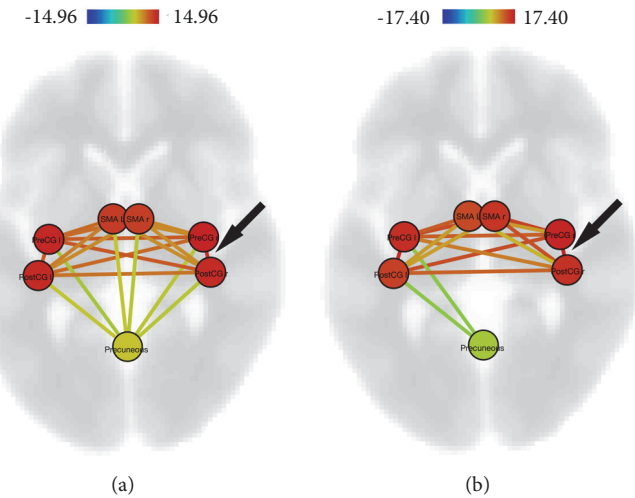
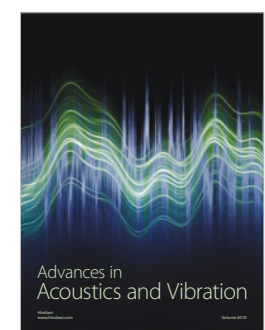
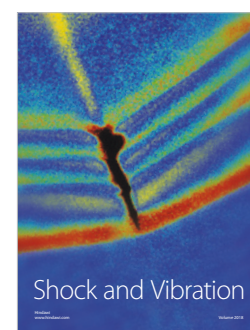
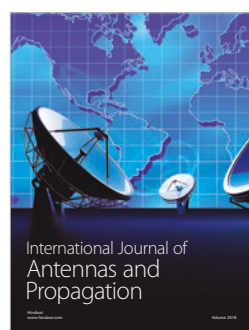
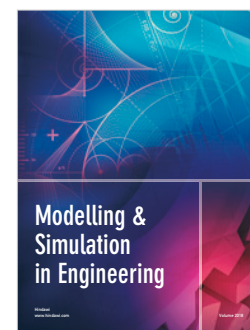
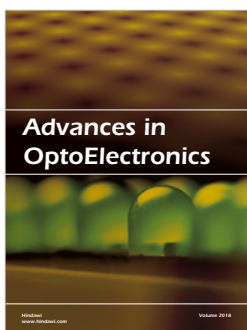
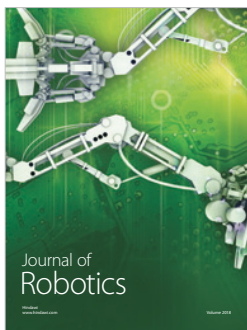
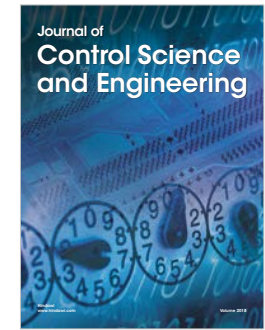
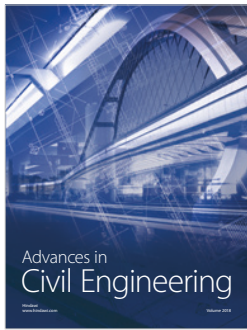
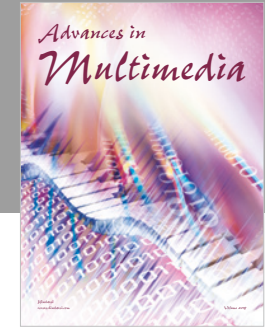
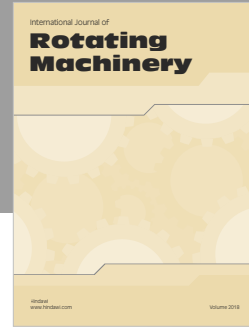


FIGURE 4: Functional connectivity within the motor network for (a) TE_1 and (b) TE_2 . The arrow points to the correlation that shows a significant difference when comparing TE_1 and TE_2 data. PreCG-l: left precentral gyrus; PreCG-r: right precentral gyrus; PostCG-l: left postcentral gyrus; PostCG-r: right postcentral gyrus; SMA-l: left supplementary motor area, SMA-r: right supplementary motor area, precuneus. Color bar refers to the range of T scores.

References

- [1] J. A. Detre, J. S. Leigh, D. S. Williams, and A. P. Koretsky, "Perfusion imaging," *Magnetic Resonance in Medicine*, vol. 23, no. 1, pp. 37–45, 1992.
- [2] J. C. Ferre, E. Bannier, H. Raoult, G. Mineur, B. Carsin-Nicol, and J. Y. Gauvrit, "Arterial spin labeling (ASL) Perfusion: techniques and clinical use," *Journal de Radiologie Diagnostique et Interventionnelle*, vol. 94, no. 12, pp. 1208–1221, 2013.
- [3] E. C. Wong, R. B. Buxton, and L. R. Frank, "Quantitative perfusion imaging using arterial spin labeling," *Neuroimaging Clinics of North America*, vol. 9, no. 2, pp. 333–342, 1999.
- [4] S. L. Talagala and D. C. Noll, "Functional MRI using steady-state arterial water labeling," *Magnetic Resonance in Medicine*, vol. 39, no. 2, pp. 179–183, 1998.
- [5] G. K. Aguirre, J. A. Detre, E. Zarahn, and D. C. Alsop, "Experimental design and the relative sensitivity of BOLD and perfusion fMRI," *Neuroimage*, vol. 15, no. 3, pp. 488–500, 2002.
- [6] E. C. Wong, R. B. Buxton, and L. R. Frank, "Implementation of quantitative perfusion imaging techniques for functional brain mapping using pulsed arterial spin labeling," *NMR in Biomedicine*, vol. 10, no. 4-5, pp. 237–249, 1997.
- [7] R. B. Buxton, "Quantifying CBF with arterial spin labeling," *Journal of Magnetic Resonance Imaging*, vol. 22, no. 6, pp. 723–726, 2005.

- [8] R. B. Buxton, L. R. Frank, E. C. Wong, B. Siewert, S. Warach, and R. R. Edelman, "A general kinetic model for quantitative perfusion imaging with arterial spin labeling," *Magnetic Resonance in Medicine*, vol. 40, no. 3, pp. 383–396, 1998.
- [9] J. A. Detre and J. Wang, "Technical aspects and utility of fMRI using BOLD and ASL," *Clinical Neurophysiology*, vol. 113, no. 5, pp. 621–634, 2002.
- [10] I. Boscolo Galazzo, S. F. Storti, E. Formaggio et al., "Investigation of brain hemodynamic changes induced by active and passive movements: a combined arterial spin labeling-BOLD fMRI study," *Journal of Magnetic Resonance Imaging*, vol. 40, no. 4, pp. 937–948, 2014.
- [11] I. B. Galazzo, S. F. Storti, A. Del Felice et al., "Patient-specific detection of cerebral blood flow alterations as assessed by arterial spin labeling in drug-resistant epileptic patients," *PLoS ONE*, vol. 10, no. 5, 2015.
- [12] W.-M. Luh, E. C. Wong, P. A. Bandettini, B. D. Ward, and J. S. Hyde, "Comparison of simultaneously measured perfusion and BOLD signal increases during brain activation with T1-based tissue identification," *Magnetic Resonance in Medicine*, vol. 44, no. 1, pp. 137–143, 2000.
- [13] M. A. F. Pimentel, P. Vilela, I. Sousa, and P. Figueiredo, "Localization of the hand motor area by arterial spin labeling and blood oxygen level-dependent functional magnetic resonance imaging," *Human Brain Mapping*, vol. 34, no. 1, pp. 96–108, 2013.
- [14] S. Tak, D. J. Wang, J. R. Polimeni, L. Yan, and J. J. Chen, "Dynamic and static contributions of the cerebrovasculature to the resting-state BOLD signal," *NeuroImage*, vol. 84, pp. 672–680, 2014.
- [15] M. W. Woolrich, P. Chiarelli, D. Gallichan, J. Perthen, and T. T. Liu, "Bayesian inference of hemodynamic changes in functional arterial spin labeling data," *Magnetic Resonance in Medicine*, vol. 56, no. 4, pp. 891–906, 2006.
- [16] E. Ghariq, M. A. Chappell, S. Schmid, W. M. Teeuwisse, and M. J. van Osch, "Effects of background suppression on the sensitivity of dual-echo arterial spin labeling MRI for BOLD and CBF signal changes," *NeuroImage*, vol. 103, pp. 316–322, 2014.
- [17] H. Lu, M. J. Donahue, and P. C. van Zijl, "Detrimental effects of BOLD signal in arterial spin labeling fMRI at high field strength," *Magnetic Resonance in Medicine*, vol. 56, no. 3, pp. 546–552, 2006.
- [18] S. F. Storti, I. B. Galazzo, F. B. Pizzini, and G. Menegaz, "Dual-echo ASL based assessment of motor networks: a feasibility study," *Journal of Neural Engineering*, 2017.
- [19] S. F. Storti, I. Boscolo Galazzo, S. Montemezzi, G. Menegaz, and F. B. Pizzini, "Dual-echo ASL contributes to decrypting the link between functional connectivity and cerebral blood flow," *Human Brain Mapping*, vol. 38, no. 12, pp. 5831–5844, 2017.
- [20] S. F. Storti, I. B. Galazzo, F. B. Pizzini, and G. Menegaz, "Dual-echo ASL based assessment of motor networks: a feasibility study," *Journal of Neural Engineering*, vol. 15, no. 2, article 026018, 2018.
- [21] A. D. Cohen, A. S. Nencka, and Y. Wang, "Multiband multi-echo simultaneous ASL/BOLD for task-induced functional MRI," *PLoS ONE*, vol. 13, no. 2, article e0190427, 2018.
- [22] Z. Wang, G. K. Aguirre, H. Rao et al., "Empirical optimization of ASL data analysis using an ASL data processing toolbox: ASLtbx," *Magnetic Resonance Imaging*, vol. 26, no. 2, pp. 261–269, 2008.
- [23] J. P. S. Silva, L. D. M. Mônaco, A. M. Paschoal, I. A. F. Oliveira, and R. F. Leoni, "Effects of global signal regression and subtraction methods on resting-state functional connectivity using arterial spin labeling data," *Magnetic Resonance Imaging*, vol. 51, pp. 151–157, 2018.
- [24] Í. A. Oliveira, T. M. Guimarães, R. M. Souza et al., "Brain functional and perfusional alterations in schizophrenia: an arterial spin labeling study," *Psychiatry Research: Neuroimaging*, vol. 272, pp. 71–78, 2018.
- [25] M. Jenkinson, P. Bannister, M. Brady, and S. Smith, "Improved optimization for the robust and accurate linear registration and motion correction of brain images," *NeuroImage*, vol. 17, no. 2, pp. 825–841, 2002.
- [26] K. Jann, D. G. Gee, E. Kilroy et al., "Functional connectivity in BOLD and CBF data: similarity and reliability of resting brain networks," *NeuroImage*, vol. 106, pp. 111–122, 2015.
- [27] S. Whitfield-Gabrieli and A. Nieto-Castañon, "Conn: a functional connectivity toolbox for correlated and anticorrelated brain networks," *Brain Connectivity*, vol. 2, no. 3, pp. 125–141, 2012.
- [28] R Development Core Team, *Computational Many-Particle Physics*, 2008.
- [29] J. H. Liu and A. Venot, "Design of a computerized system for the retrospective analysis by the physician of his own drug prescriptions," *Studies in Health Technology and Informatics*, vol. 84, no. Pt 2, pp. 1175–1179, 2001.
- [30] M. N. Yongbi, F. Fera, V. S. Mattay, J. A. Frank, and J. H. Duyn, "Simultaneous BOLD/perfusion measurement using dual-echo FAIR and UNFAIR: sequence comparison at 1.5T and 3.0T," *Magnetic Resonance Imaging*, vol. 19, no. 9, pp. 1159–1165, 2001.
- [31] T. T. Liu and E. C. Wong, "A signal processing model for arterial spin labeling functional MRI," *NeuroImage*, vol. 24, no. 1, pp. 207–215, 2005.



Hindawi

Submit your manuscripts at
www.hindawi.com

44 Autoria de artigos completos publicados em jornais e revistas de circulação nacional e internacional na sua área

Esta subseção apresenta o comprovante da autoria do artigo publicado na revista internacional *Magnetic Resonance Materials in Physics, Biology and Medicine* no ano de 2020.



Contrast optimization in arterial spin labeling with multiple post-labeling delays for cerebrovascular assessment

André Monteiro Paschoal^{1,3} · Renata Ferranti Leoni¹ · Bernd Uwe Foerster² · Antonio Carlos dos Santos³ · Octávio Marques Pontes-Neto³ · Fernando Fernandes Paiva²

Received: 2 April 2020 / Revised: 1 July 2020 / Accepted: 25 August 2020
© European Society for Magnetic Resonance in Medicine and Biology (ESMRMB) 2020

Abstract

Objective Improving the readout for arterial spin labeling with multiple post-labeling delays (multi-PLD ASL) through a flip angle (FA) sweep towards increasing contrast-to-noise ratio for long PLD images.

Methods Images were acquired from 20 healthy subjects and 14 patients with severe, asymptomatic carotid artery stenosis (ACAS) in a 3T MRI scanner. Multi-PLD ASL images with conventional and proposed (FA sweep) readouts were acquired. For patients, magnetic resonance angiography was used to validate the multi-PLD ASL results. Perfusion values were calculated for brain regions irrigated by the main cerebral arteries and compared by analysis of variance.

Results For healthy subjects, better contrast was obtained for long PLDs when using the proposed multi-PLD method compared to the conventional. For both methods, no hemispheric difference of perfusion was observed. For patients, the proposed method facilitated the observation of delayed tissue perfusion, which was not visible for long PLD using the conventional multi-PLD ASL.

Conclusion We successfully assessed brain perfusion of patients with asymptomatic CAS using multi-PLD ASL with FA sweep. We were able to show subtle individual differences. Moreover, prolonged arterial transit time in patients was observed, although they were considered asymptomatic, suggesting that it may not be an adequate term to characterize them.

Keywords Arterial spin labeling · Flip angle sweep · Multiphase · Brain · Perfusion

Introduction

Cerebral Blood Flow (CBF) is an important parameter for the investigation of brain hemodynamics, since a variation of blood flow in brain arteries might severely affect tissue perfusion and neurological functions. It is particularly true

in neurovascular disorders, such as stroke [1, 2], which is strongly associated with the carotid artery stenosis (CAS) or occlusion due to arterial embolism and hemodynamic compromise [1]. Patients with CAS may be asymptomatic, i.e., with no incidence of ipsilateral stroke and transient ischemic attack (TIA), but present cognitive decline [3]. Moreover, the patient selection for intervention in these cases is still controversial. Therefore, the ability to properly assess CBF with noninvasive methods is a major determinant for our understanding of the relation between atherosclerotic disease, altered perfusion, and neurological impairment in asymptomatic CAS (ACAS).

Arterial Spin Labeling (ASL) is a noninvasive, perfusion-based magnetic resonance imaging (MRI) method that quantifies CBF in units of mL/min/100 g of tissue [4, 5] and enables prolonged monitoring of cerebral perfusion. The measurement of brain perfusion with ASL requires the acquisition of a labeled image, where arterial blood is tagged with a radiofrequency (RF) pulse, and a control image, where no preparation pulse is used before its acquisition. Therefore, CBF

Electronic supplementary material The online version of this article (<https://doi.org/10.1007/s10334-020-00883-z>) contains

supplementary material, which is available to authorized users.

Fernando Fernandes Paiva
fernando.paiva@usp.br

¹ Inbrain, Faculdade de Filosofia, Ciências e Letras de Ribeirão Preto, Universidade de São Paulo, Ribeirão Preto, SP, Brazil

² Instituto de Física de São Carlos, Universidade de São Paulo, Av. Trabalhador São-Carlense, 400, São Carlos, SP 13566-590, Brazil

³ Faculdade de Medicina de Ribeirão Preto, Universidade de São Paulo, Ribeirão Preto, SP, Brazil

is proportional to the difference between control and label images. An accurate estimation of CBF relies on the acquisition of images at an appropriate time after spins have been tagged, and tagged blood must reach the image plane before data acquisition. The interval between labeling and acquisition is called post-labeling delay (PLD), and its optimization depends on the arterial blood transit time (ATT). Since patients with ACAS may present delayed ATT, an accurate CBF assessment requires an acquisition independent of the PLD choice [6, 7]. The elimination of such dependency is possible with acquisitions at different PLDs. In such a case, each acquisition is a phase, and the method is called multiphase ASL or multi-PLD ASL.

Multi-PLD ASL has been used for different applications, such as measurement of arterial transit time (ATT) [8–10], characterization of cerebral border zones [11], and assessment of water extraction across the blood–brain barrier [11–14]. Different acquisition approaches have been developed to improve the signal-to-noise ratio (SNR) and acquisition time efficiency through the use of Look-Locker readout [15–19] and time-encoded schemes, as the Hadamard [16, 20, 21]. However, the image contrast at later delays is hampered by a repeated application of excitation pulses and longitudinal relaxation, which affect the evaluation of tissue perfusion in regions where the transit time is longer. Therefore, we propose a readout flip angle modulation to the Look-Locker approach for the acquisition of images with good contrast-to-noise ratio (CNR), even for long PLDs, towards overcoming the limitation of conventional Look-Locker methods with a fixed readout flip angle for all the PLDs. We used the method to evaluate cerebral perfusion healthy volunteers and in patients with ACAS. We hypothesize that such patients present delayed ATT and brain hypoperfusion related to the stenosis and that our approach may offer an efficient, but simple tool for such evaluation.

Materials and methods

Flip angle modulation

A multi-PLD ASL acquisition with flip angle α , m phases, an interval τ between two consecutive phases, and longitudinal relaxation time T_1 of the blood was assumed for the calculation of the modulation equation, given by Eq. 1:

$$\Delta M_m = 2M_0 e^{-\left[\frac{T_1+(m-1)\tau}{T_1}\right]} \sin(\alpha_m) \times \begin{cases} 1, & \text{if } m = 1 \\ \prod_{i=1}^{m-1} \cos(\alpha_m), & \text{if } m > 1 \end{cases} \quad (1)$$

The proposed approach calculates the flip angles to keep the magnetization difference constant over the phases. In a

general way, the flip angle for the i th phase for a total of m phases is given by:

$$\alpha_i = \tan^{-1} \left(\frac{\sin(\alpha_m) \exp\left(-\frac{(m-i)\tau}{T_1}\right)}{\sqrt{1 + \sum_{k=1}^{m-i-1} \sin^2(\alpha_m) \exp\left(-\frac{2k\tau}{T_1}\right)}} \right), i = 1 \dots (m-1), \quad (2)$$

where α_m must be defined by the user according to the repetition and relaxation times (detailed description for the FA sweep equation is in supplementary material). The flip angle shown in Eq. 2 is then applied to both control and label images, so that the static tissue will be the same for both conditions. Therefore, after the control-label subtraction, static tissue magnetization will greatly reduce, resulting only in a perfusion signal.

Subjects

Fourteen patients (5 females; mean age \pm standard deviation (SD) = 72 ± 7 , range 56–83) and twenty healthy volunteers (8 females; mean age \pm SD = 26 ± 9 , range 18–47) participated in this cross-sectional study, approved by the Institutional Review Board, after signing informed consent. Patients were recruited at the Clinical Hospital of the institution, and the inclusion criterion was severe ($\geq 70\%$), unilateral CAS, or occlusion, identified by an experienced neuroradiologist using the patient's MR angiography (MRA). The sample size was determined by the number of patients who met the criteria and agreed to participate during the study period (1 year). For all subjects, the exclusion criteria were a history of any cerebrovascular event (stroke, transient ischemic attack); the presence of neurologic disorders, such as epilepsy, multiple sclerosis, amyotrophic lateral sclerosis, brain tumor, and dementia; psychiatric disorders; pregnancy; claustrophobia; contraindications for MRI. The healthy volunteers were recruited to compose a dataset for the evaluation of the quality of the images acquired with the proposed method.

MR system

Data were collected at a 3T MR system (Achieva, Philips Medical Systems, Holland), equipped with gradients of 80 mT/m amplitude and 200 mT/m/ms slew rate. We used a standard transmit body coil and a 32-channel receive-only head coil.

Scanning protocols

The MRI protocol consisted of a whole-brain structural image acquired by a three-dimensional T1-weighted (3DT1) GRE-EPI sequence with $240 \times 240 \text{ mm}^2$ field-of-view

(FOV), 164 1-mm-thick slices and TR/TE = 6.2/2.8 ms. A conventional PULSAR (pulsed STAR labeling of arterial regions) sequence [19] was modified for the use of variable flip angles during the acquisition of the multiple ASL phases. In the same MRI session, two multi-PLD ASL sequences (with and without flip angle modulation) were acquired with the following parameters: TR/TE = 4000/18 ms, FOV = 240 × 240 mm², in-plane resolution = 3.75 mm × 3.75 mm (acquisition matrix = 64 × 64), number of slices = 6, slice thickness = 6 mm, number of phases = 8, and number of repetitions = 35. PLDs varied between 900 and 2825 ms, with a time interval (τ) of 275 ms between each consecutive phase. For the FA sweep method, the flip angle for all the PLDs were 11.01°, 12.96°, 15.38°, 18.49°, 22.65°, 28.74°, 39.19°, and 70°, obtained from Eq. 2. For the conventional method, a flip angle of 30° was used for all PLDs. A 200-mm-wide tagging region was positioned 10 mm below the imaging region. Two time-of-flight (TOF) angiograms were acquired for the visualization of the Internal Carotid Arteries (ICAs) and Vertebral Arteries (VAs).

Data processing

Data were processed using SPM (version 12, Wellcome Trust Center for Neuroimaging, University College London, UK) and custom scripts in Matlab (Mathworks, MA, USA). Raw label and control images were realigned, resliced, and co-registered to anatomical images. Maps of magnetization difference (ΔM) were calculated by subtracting labeled and control images.

ATT maps were estimated by finding the maximum of ASL signal intensity throughout the multiple post-labeling delays. Prior to that, the time interval between the first and the last PLD was linear spaced in 1000 time points, and the linear interpolation of ASL signal value was estimated for every point.

CBF quantification based on the kinetic model [22] was performed using the BASIL toolkit of the Oxford Centre for Functional MRI of the BRAIN (FMRIB)'s software library (FSL) [23, 24], after correcting the ASL signal for Look-Locker effects dividing the ASL images by the sine of FA [18]. Gray matter (GM) and white matter (WM) masks were obtained after running FSL FLIRT [25] to coregister T1-weighted images to the ASL low-resolution space and FSL FAST [25] to segment into the partial volume for GM, WM, and CSF.

Data analysis

The signal evolution of ΔM was analyzed in Regions of Interest (ROI) defined according to the arteries that feed the respective vascular territory, i.e., anterior cerebral artery (ACA), middle cerebral artery (MCA), and posterior

cerebral artery (PCA), for both hemispheres. Mean perfusion values of each ROI were obtained. For healthy subjects, comparisons between regions and phases were made using analysis of variance. Statistical significance was considered for $p < 0.05$. It was also calculated the spatial signal-to-noise ratio (sSNR) of the GM (sSNR = mean GM signal/stand deviation GM signal) as well as the contrast-to-noise ratio (CNR) [CNR = (mean GM signal – mean WM signal)/(standard deviation GM signal + stand deviation WM signal)] to measure the gain of the proposed implementation.

Patients' images were independently reviewed and assessed by two specialists for diagnostic purposes. A neuroradiologist (A.C.S) with 34 year experience analyzed structural images and MRA. A neurologist (O.M.P.N) with 17 year experience in cerebrovascular diseases with no knowledge of previous reports of the patients analyzed the ASL maps (with and without FA sweep). Each patients' dataset was individually analyzed, since patients differed from each other regarding stenosis side and severity. The CNR for each patient was calculated by comparing the GM and WM signal in the ROI indicated by the neurologist. For both control and patients group, differences in sSNR and CNR for each phase were statistically assessed by the application of a paired *t* test using the Bonferroni criteria for correction for multiple comparisons, which considered $p < 0.00625$ for statistical significance.

Results

Method evaluation in healthy volunteers

Data from healthy volunteers were used for the assessment of the FA sweep method. Figure 1 shows perfusion maps from a representative volunteer. Three slices and all eight phases acquired by the proposed FA sweep (Fig. 1a) and the conventional fixed FA (Fig. 1b) are shown. For the initial phases, i.e., shorter PLDs, both methods provided perfusion maps with sufficient contrast for visual inspection. However, the loss of contrast became apparent throughout the later phases for the conventional implementation, which hampered the perfusion analysis for long PLDs. The flip angle modulation circumvented this problem and enabled a precise evaluation of perfusion for all phases acquired. While, for conventional implementation, the signal dropped after reaching its maximum, the use of flip angle sweep led to a sufficient contrast throughout the phases. Furthermore, ATT maps were directly estimated for the FA sweep method by taking the post-labeling delay that had the maximal ASL signal intensity, as exemplified for one healthy subject in Fig. 2.

Considering all regions, we observed differences in signal intensity between phases. For the FA sweep method,

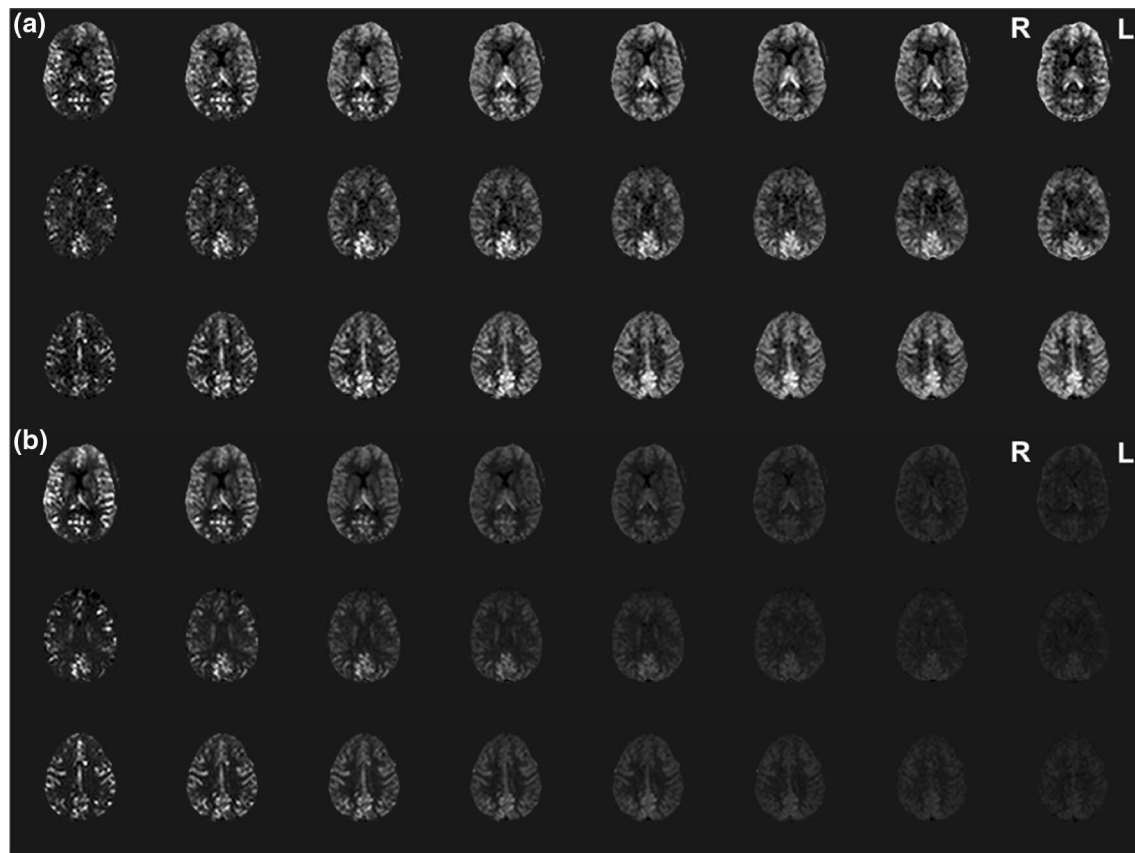


Fig. 1 Perfusion maps of a representative, healthy control. Three slices (rows) for all eight phases (columns) acquired by **a** the proposed multiphase method with flip angle sweep and **b** conventional multiphase arterial spin labeling method. R: right, L: left

signal intensity was significantly lower for phases 1 and 2 ($p < 0.05$). For the conventional map, signal intensity was significantly lower from phase 5 up to the last phase ($p < 0.05$), confirming the visual analysis. This pattern is also quantitatively described through the sSNR measurement, as shown in Fig. 3a, which resulted in increased values when using the FA sweep modulation ($p < 0.00625$ for all phases). Moreover, for both methods, no difference in signal intensity between hemispheres was observed ($p > 0.05$); however, the analysis of variance showed a significant effect of region on such values ($p < 0.05$). Higher values were observed in brain areas irrigated by the posterior circulation, typical of healthy young subjects. For the FA sweep method, this result was observed from phase 4 up to phase 8. However, for the conventional method, it was only observed for phases 4, 5, and 6. The CNR showed in Fig. 3b was significantly higher for the conventional method in the first 4 phases ($p < 0.00625$). For phases 7 and 8, it was significantly higher for the FA sweep method ($p < 0.00625$).

CBF maps were obtained for all healthy volunteers. The average gray matter CBF was 46 ± 11 mL/100 g/min for the FA sweep method and 39 ± 7 mL/100 g/min for the FA fixed method.

Patient analysis

The reports from two specialists are shown in Table 1. For each patient, both reports were considered to determine the performance of multi-PLD ASL with FA sweep in comparison with MRA findings. The overall comparison revealed an agreement of 85%. Additionally, for the conventional method, in 57% of the patients, the neurologist could not give a precise diagnosis, or the diagnosis was incorrect compared to the MRA. All correct diagnoses provided by the conventional method were also correct using the FA sweep approach.

Figure 4 shows data of a patient with an occlusion in the right ICA and a severe stenosis of 90% in the left ICA, as indicated in the TOF image (Fig. 4a, b, Table 1—P05). The analysis of the multi-PLD ASL maps with flip angle modulation (Fig. 4c) revealed an apparent reduction in CBF in the right MCA territory in the initial phases (red arrows). Tissue perfusion started first in the left hemisphere (phases 1, 2, and 3) with delayed transit time (Fig. 5a). For later phases, we observed collateral flow, i.e., blood from arteries in the left hemisphere irrigating regions of the right hemisphere, which resulted in CBF on the right side of the brain. With

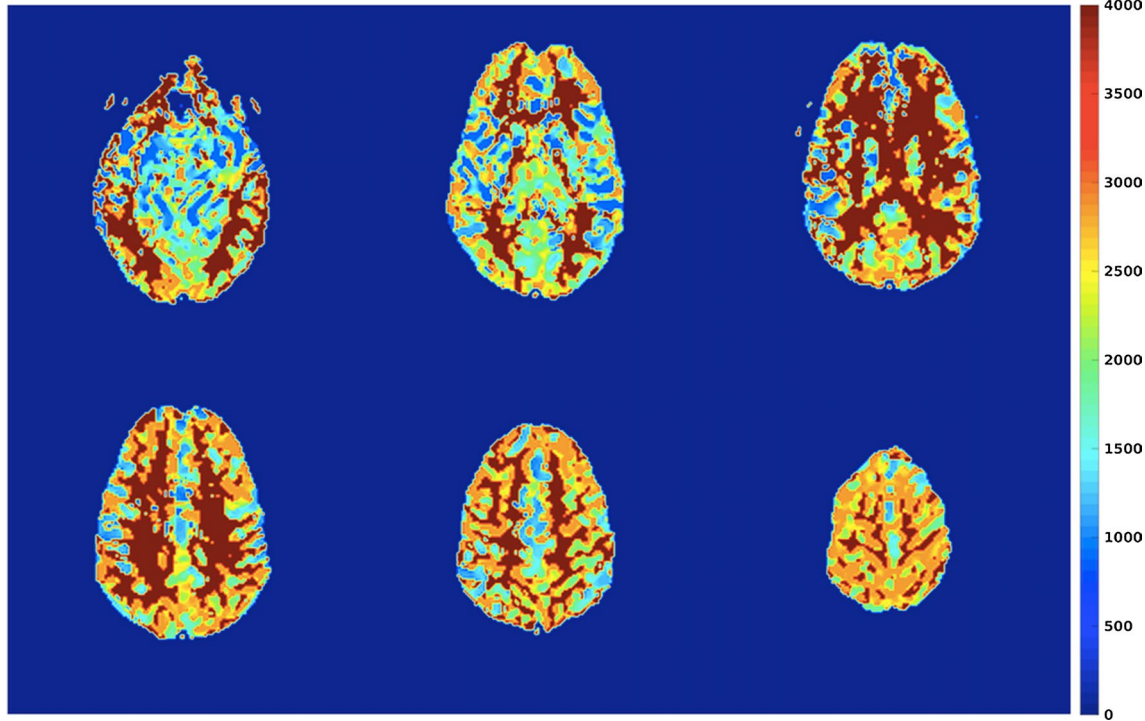


Fig. 2 Arterial transit time (ATT) map for a representative healthy subject. Color scale is in ms

the conventional multi-PLD ASL method (Fig. 4d), such analysis was impaired due to the loss of CNR for long PLDs.

Figure 6 shows the data of a patient with mild stenosis in the right ICA (Table 1—P07). The intracranial angiography revealed blood flow arriving in the intracranial arteries (Fig. 6a, b). Figure 6c displays ASL maps acquired by the FA sweep method, which showed a small increase in the arterial transit time on the right hemisphere (2.96 s for ipsi-PCA vs. 2.90 s for contra-PCA), which resulted in a slight reduction of blood perfusion at the right MCA territory in the first phases (red arrows). With the FA sweep method (Fig. 6c), it was possible to monitor blood perfusion over the phases, which revealed that it reached a similar value at both hemispheres for long PLDs.

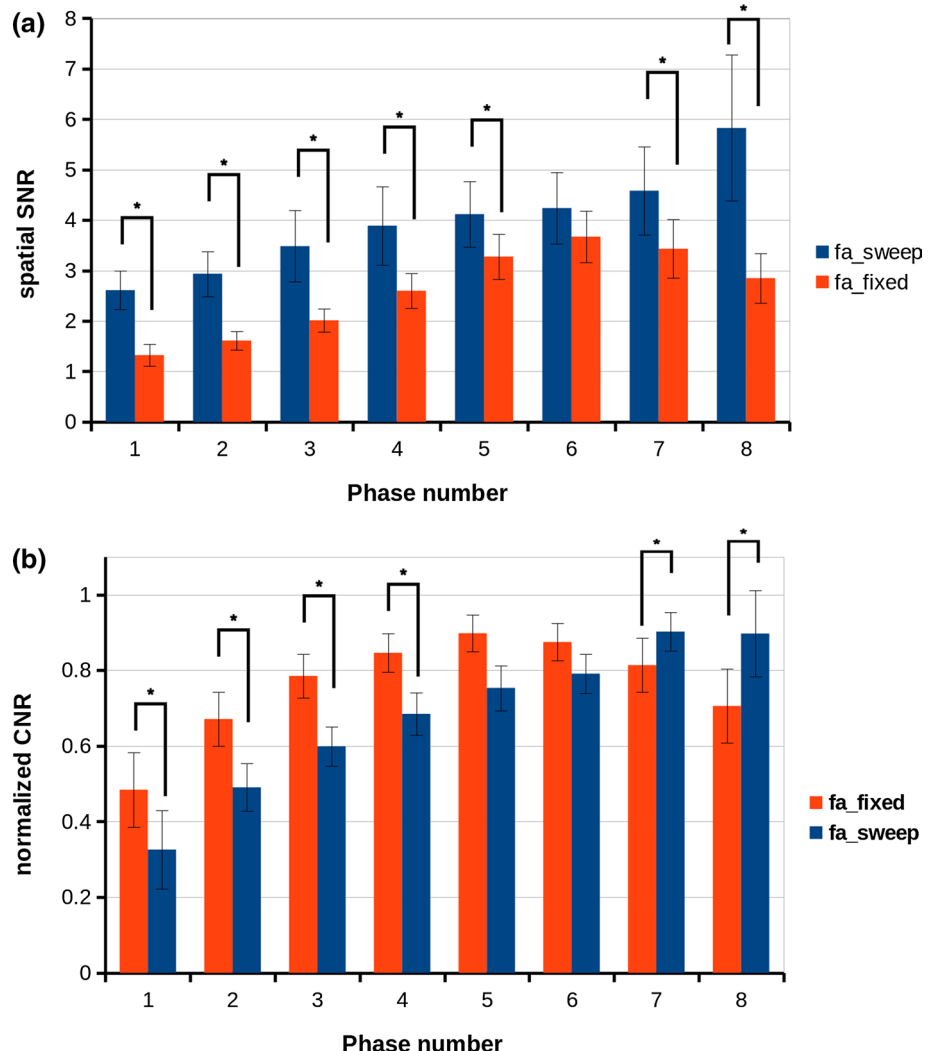
Figure 7 shows data of a patient with severe stenosis of 70% in the left ICA (Table 1—P08), as indicated in the TOF image (Fig. 7a, b). The analysis of the multi-PLD ASL maps with flip angle modulation (Fig. 7c) revealed a slight reduction in CBF in the left MCA territory in initial phases (red arrows). Tissue perfusion has a reduction in the left hemisphere (phases 1, 2, and 3) with delayed transit time, whose average was 3.09 s for ipsi-MCA and 2.86 s for contra-MCA. For later phases, we observed more homogeneous brain perfusion. With the conventional multi-PLD ASL method (Fig. 7d), this behavior could not be seen due to the loss of CNR for long PLDs. CNR evolution for the MCA territory is shown in Fig. 8.

Figure 9 shows data of a patient with an obstruction in the left ICA and moderate (50%) stenosis in the right ICA (Table 1—P13) (Fig. 9a, b). The ASL maps (Fig. 9c) revealed an increase in the arterial transit time on both hemispheres, but more pronounced in the left hemisphere with delayed blood flow (Fig. 5d), especially in the first phases. The entire left hemisphere presented blood perfusion reduction due to reduced flow in the circle of Willis, as verified in the TOF image (Fig. 9b). For longer PLD, there was an increase in blood perfusion due to compensation mechanisms. Such analysis is compromised when data were acquired with the conventional approach (Fig. 9d).

The benefits visually observed in the analysis of the previous examples of patients are enhanced by the CNR measurement in the ROIs of delayed blood flow indicated by the neurologist. The bar plot in Fig. 10 represents the normalized mean CNR for all the 13 patients included in this study, revealing a significant increase in the CNR for the latter two phases ($p < 0.00625$).

The quantitative results of CBF measurements are shown in Fig. 11 for a representative healthy control and for all the exemplified patients. For comparison, CBF maps for both sweep and fixed FA are reported.

Fig. 3 Mean gray matter: **a** spatial signal-to-noise ratio and **b** normalized contrast-to-noise ratio for all 20 healthy subjects (mean \pm standard deviation) for the FA sweep (blue) and FA fixed (red) methods (* p -FWE < 0.00625)



Discussion

We proposed an approach for the multiphase ASL method to guarantee sufficient contrast for perfusion images acquired at long PLDs. First, images were acquired from healthy controls. Perfusion maps showed a better contrast for the proposed method compared to the conventional Look–Locker readout with fixed FA approach for long PLDs, and an increased sSNR for all the PLDs acquired and higher CNR for the last two PLDs. For both methods, no hemispheric difference of perfusion was observed; however, regions irrigated by the posterior cerebral artery showed higher perfusion values, as expected for healthy, young subjects [26]. Furthermore, the ATT map for a representative subject showed a result in agreement with the expected for healthy subjects [27, 28].

Moreover, we investigated the cerebral perfusion of patients with asymptomatic carotid artery stenosis. The visual comparison of images acquired by both methods revealed essential differences between them, mainly for later

phases. The inspection of the perfusion maps obtained for different PLDs was not crucial for healthy controls, in which no alteration in blood transit times is expected, and gray matter is already perfused at first phases. However, patients with arterial stenosis or occlusion may present a delayed transit time. Therefore, the assessment of all phases was necessary for the analysis.

Recent studies have used ASL with at least two PLD values to obtain maps of arterial transit time and quantify CBF with better accuracy [8, 29, 30]. The previous studies have reported methods to improve the CNR of ASL images for long PLDs [31, 32]. Our approach used a maximum PLD of 2825 ms, longer than the ones previously reported [33, 34], and allowed the dynamic assessment of tissue perfusion, including the presence of collateral flow by significantly increasing the sSNR for all the PLDs and especially resulting in significant differences for the CNR of latter phases (Fig. 10). Moreover, it did not require any mathematical models to quantify the arterial transit time (Fig. 5), being more appealing for clinical use.

Table 1 Patients' information and specialists' reports

ID	Gender	Age	Report 1 ^a	Report 2 ^b
P01	Female	56	Critical stenosis on the ICA with flow reduction on the right MCA territory	Flow reduction on the right MCA vascular territory
P02	Female	68	Critical stenosis on the right side of carotid bulb with flow reduction on the right MCA	Flow reduction on the right MCA vascular territory
P03	Male	77	Critical stenosis on the left ICA with flow reduction in the territory of posterior communicant arteries	Flow reduction on the left PCA vascular territory
P04	Male	83	Critical stenosis on the left ICA	Flow reduction on the left MCA vascular territory
P05	Male	77	Occlusion of the right ICA and critical stenosis on left ICA with severe flow reduction in right MCA territory	Flow reduction on the right MCA vascular territory
P06	Female	81	Critical stenosis on the left ICA without a change in flow	No flow reduction
P07	Male	70	Discreet stenosis on the right ICA and severe stenosis on the left external carotid artery	Slight flow reduction on the right MCA vascular territory and left PCA vascular territory
P08	Female	65	Critical stenosis on the left ICA with a slight change in flow	Slight flow reduction on the left MCA vascular territory
P09	Male	70	Critical stenosis on the right ICA with small flow reduction on the right hemisphere	Flow reduction on the right MCA vascular territory
P10	Male	67	Critical stenosis on the right ICA	Flow reduction on the right MCA and left PCA vascular territories
P11	Male	77	Excluded due to motion	Excluded due to motion
P12	Male	67	Occlusion of the left ICA and moderate stenosis on the right ICA	Flow reduction on the left hemisphere
P13	Female	70	Critical stenosis on right ICA with flow reduction at the right side of the circle of Willis	Flow reduction on the right MCA vascular territory
P14	Male	65	Critical stenosis on the right ICA and discreet stenosis on the left ICA	No significant change in flow

ICA internal carotid artery, MCA middle carotid artery, PCA posterior carotid artery

^aFrom MR angiography and Doppler ultrasound

^bFrom multiphase ASL with flip angle sweep

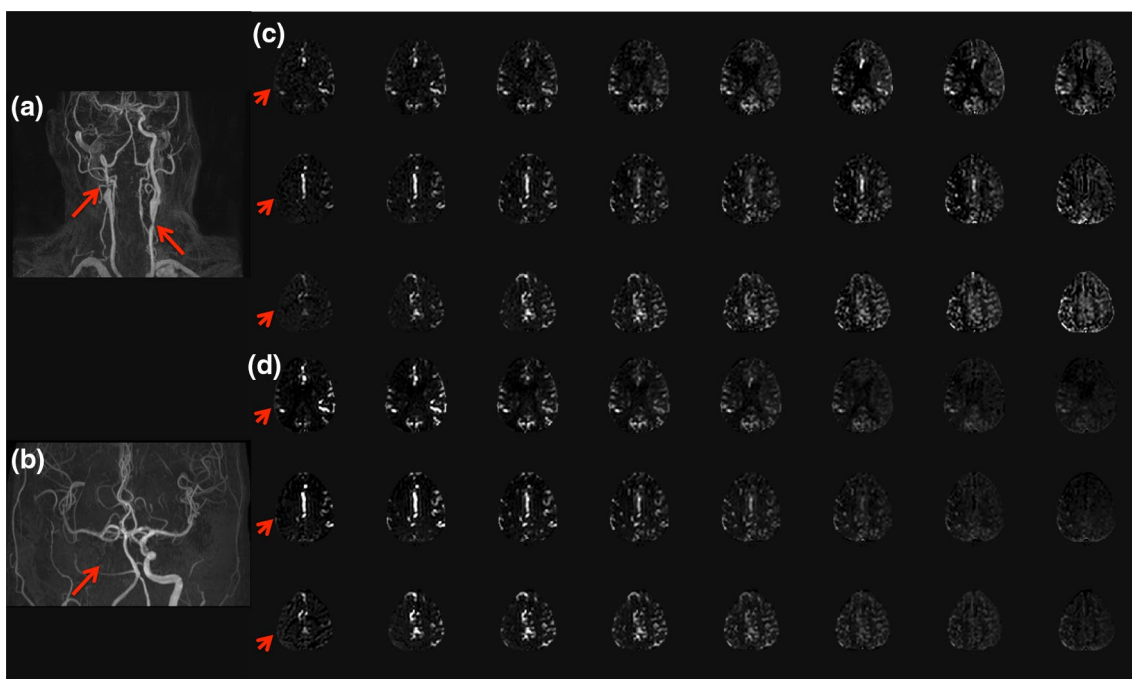


Fig. 4 Data from a patient with an occlusion in the right ICA and a 90% severe stenosis in the left ICA. **a** Carotid and **b** intracranial angiography. Multiphase maps **c** with and **d** without flip angle sweep

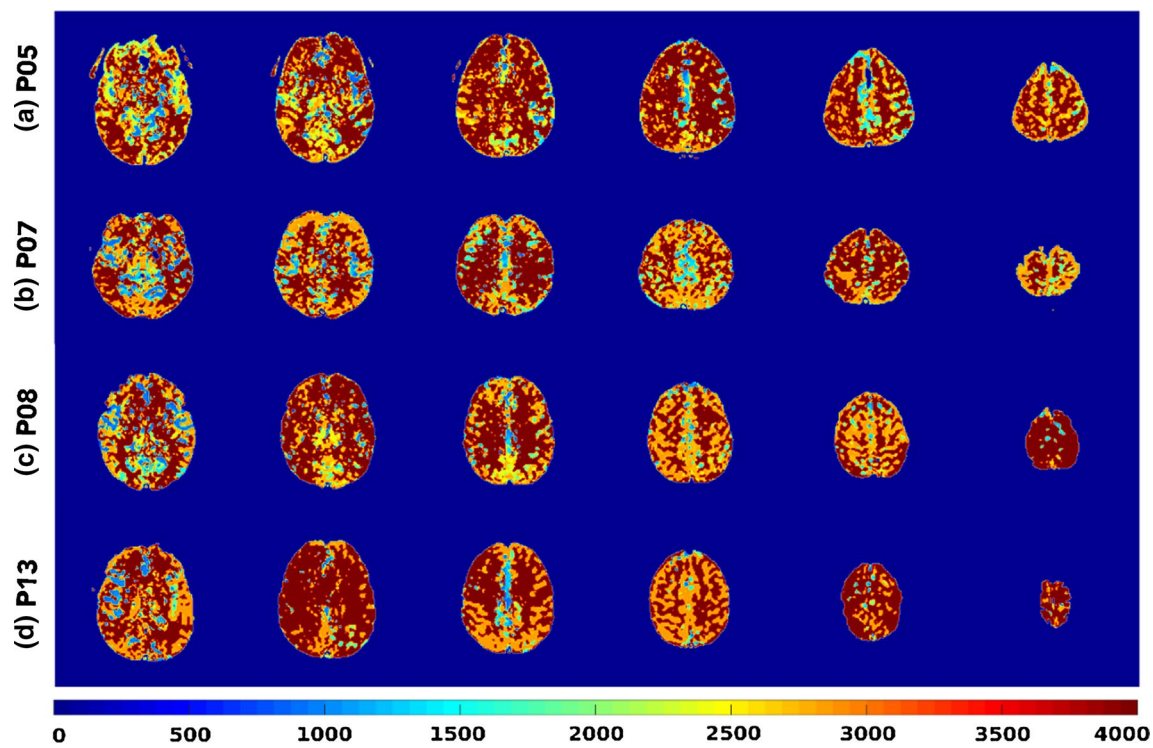


Fig. 5 Arterial transit time (ATT) maps for four patients. Color scale is in ms

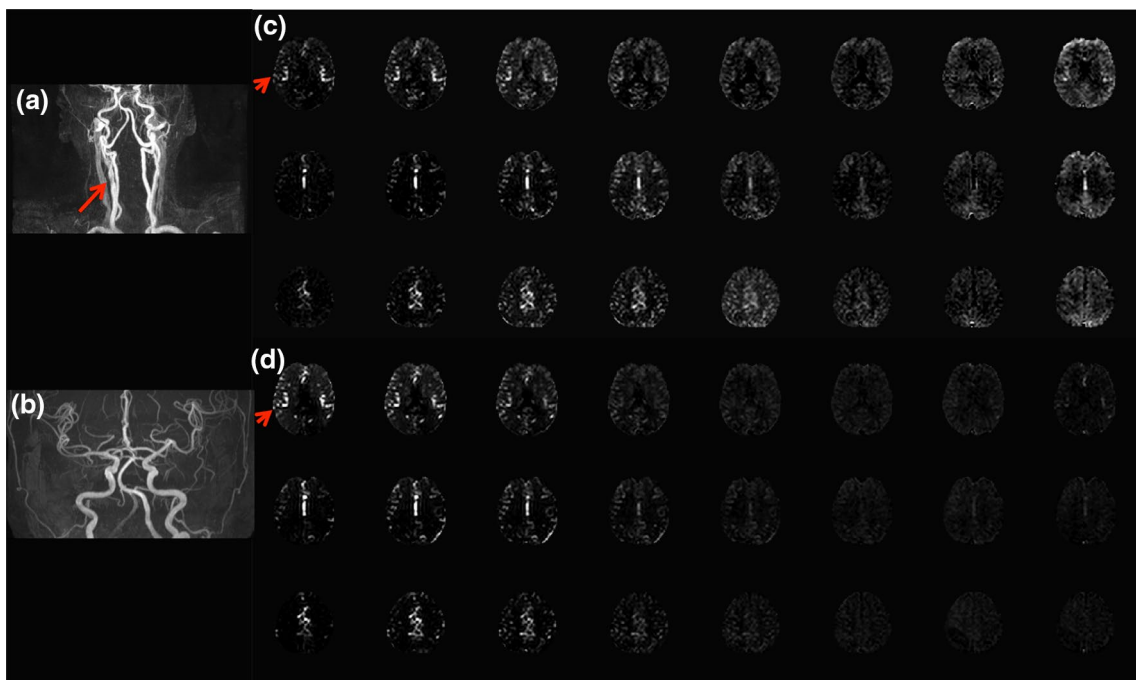


Fig. 6 Data from a patient with mild stenosis in the right ICA. **a** Carotid and **b** intracranial angiography. Multiphase perfusion maps **c** with and **d** without flip angle sweep

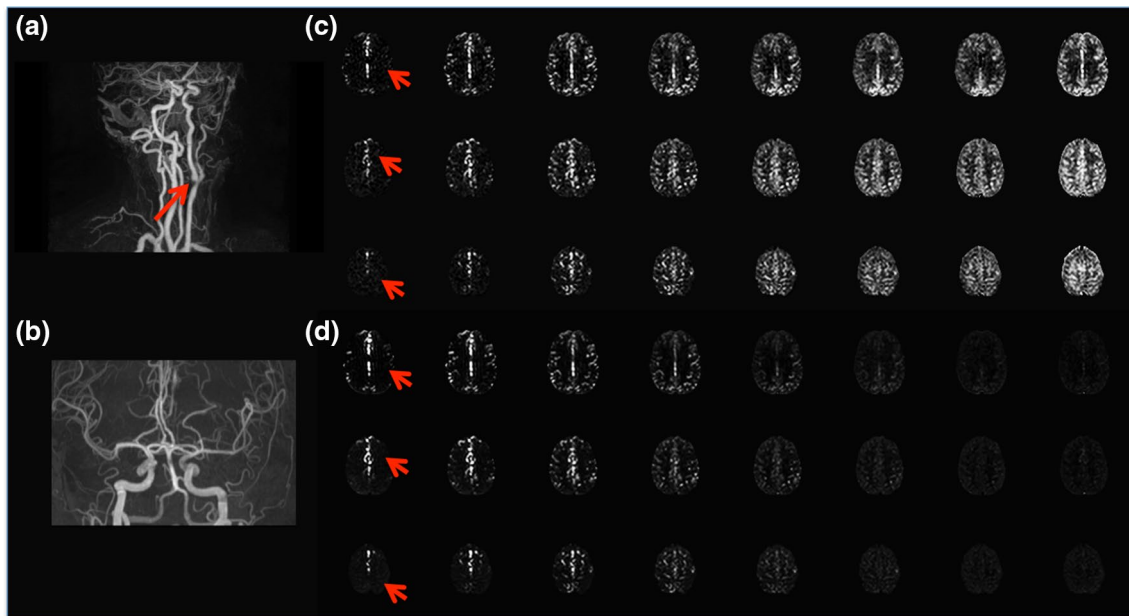
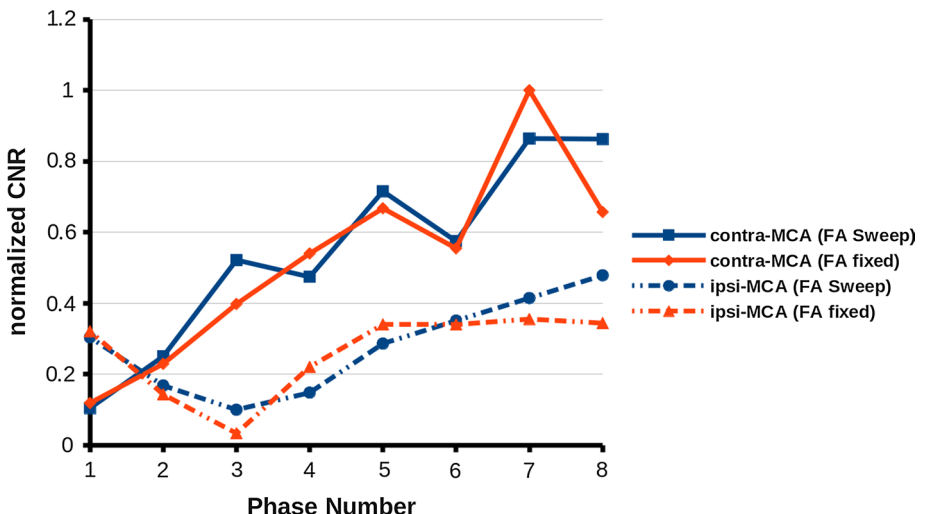


Fig. 7 Data from a patient with severe stenosis in the left ICA. **a** Carotid and **b** intracranial angiography. Multiphase perfusion maps **c** with and **d** without flip angle sweep

Fig. 8 CNR evolution over the phases for the FA sweep method and conventional method for the patient whose maps are shown in Fig. 7. CNR values were calculated for the region irrigated by the middle cerebral artery (MCA), for both hemispheres, ipsi and contralateral to the stenosis



In more than half of the patients with delayed transit time, the neurologist found difficulties in giving an accurate diagnosis due to the loss of information for long PLDs when using the conventional multi-PLD ASL method. The FA sweep approach improved such assessment, whose reports had a higher agreement with the MRA reports. For the critical carotid stenosis example shown in Fig. 4, there is a delayed transit time on both hemispheres, as shown in Fig. 5a. However, a careful analysis of the perfusion maps obtained by FA sweep method enabled the conclusion that the right hemisphere (with a carotid occlusion) is irrigated by the arterial blood coming from the left hemisphere due to vascular regulatory mechanisms, as collateral flow. Such

a conclusion was only possible when analyzing all the phases. The lower CNR of images acquired by the conventional multi-PLD ASL method hampered the assessment of perfusion maps for long PLDs and difficulted the correct diagnosis.

The ability of this method to show perfusion dynamics was confirmed by the neurologist, who could observe subtle differences in patients' perfusion between hemispheres, as shown in Figs. 6 and 7. By evaluating images acquired using the FA sweep method, the neurologist could detect a small difference visible until the sixth PLD, which was hardly seen with the maps obtained by the conventional method. In the critical carotid stenosis example shown in Fig. 9, the TOF

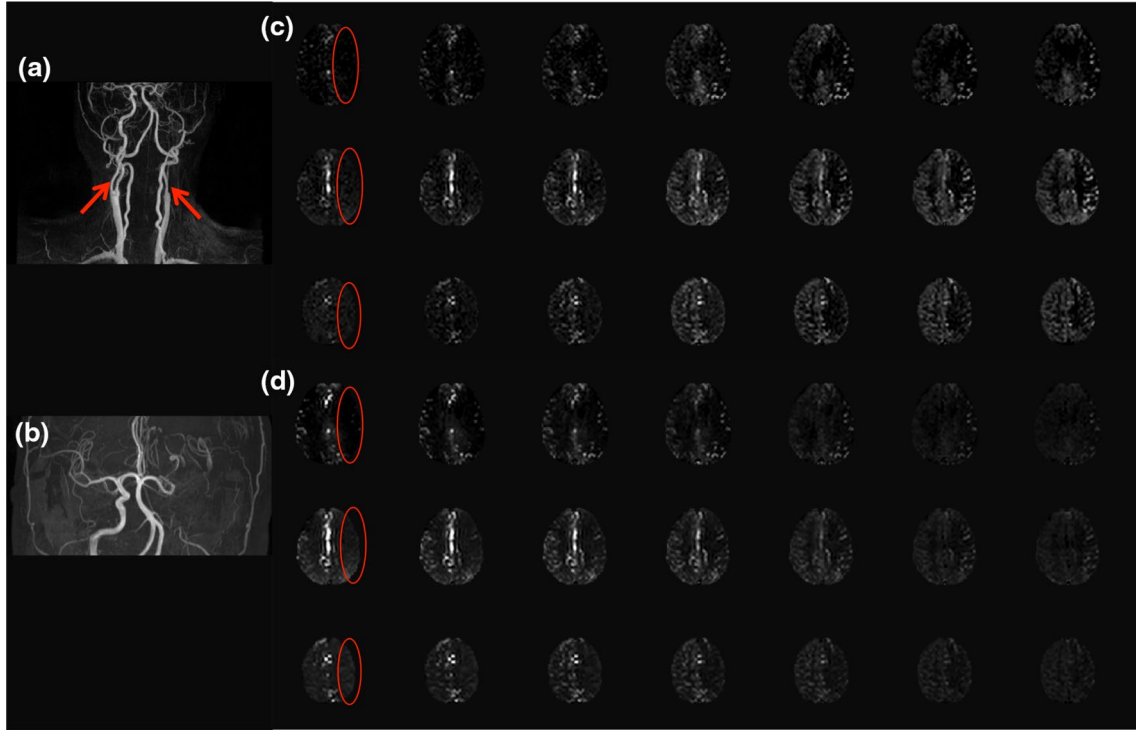


Fig. 9 Data from a patient with an obstruction in the left ICA and 70% stenosis in the right ICA. **a** Carotid and **b** intracranial angiography. Multi-phase maps **c** with and **d** without flip angle sweep

Fig. 10 Mean contrast-to-noise ratio for all 13 patients included in this study (mean \pm standard deviation) for the FA sweep (blue) and FA fixed (red) methods (* p -FWE < 0.00625)

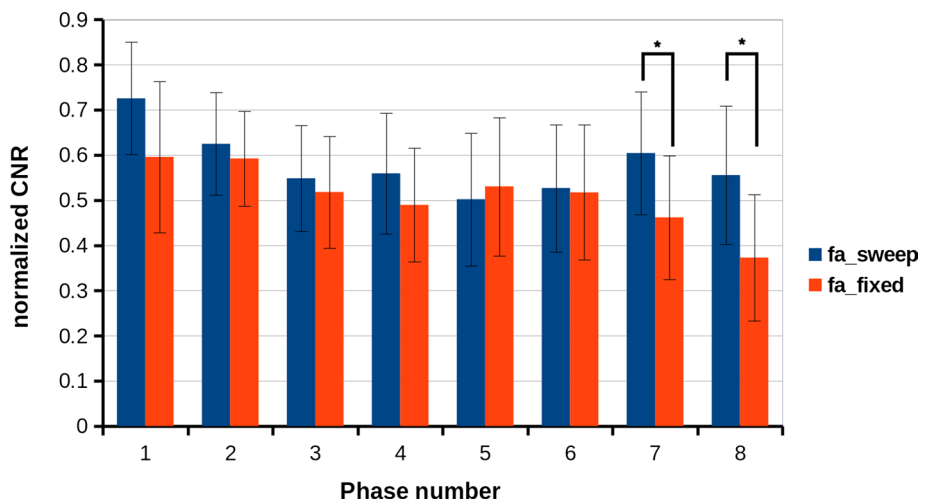
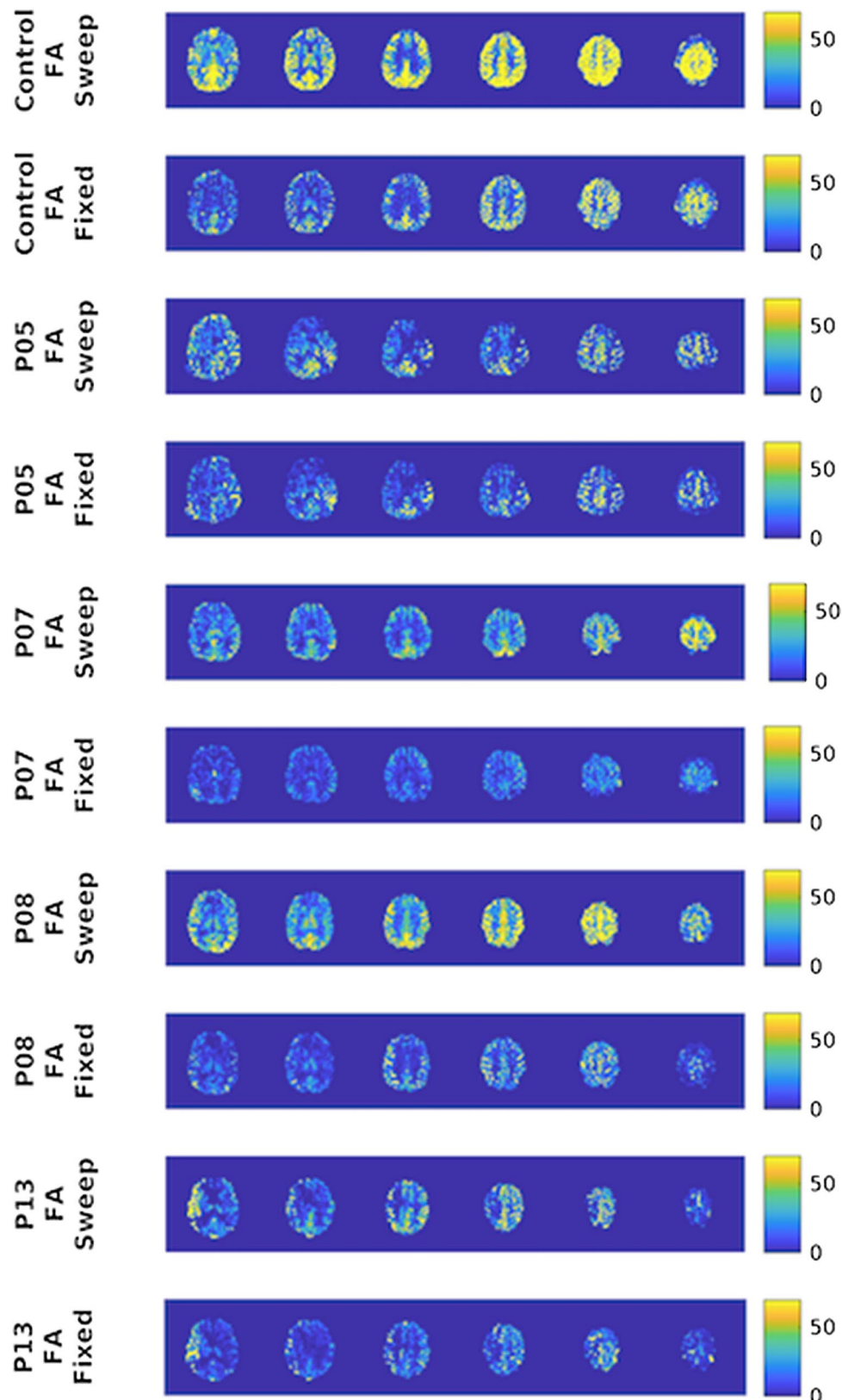


image shows a stenosis higher than 70% on the left side of the internal carotid artery (ICA), which results in prolonged transit time and delayed brain perfusion. The same pattern is observed by the analysis of ASL multi-PLD maps, which shows perfusion reduction in the left MCA in the first phases with prolonged ATT. Over the phases, both sides tend to be the same.

Although the patients were classified as asymptomatic for brain lesions, all of them showed alterations in cerebral

hemodynamics, which may increase their risk for ischemic stroke [35, 36]. Most patients reported flow reduction in MCA vascular territory, which is directly irrigated by ICA. Moreover, delayed transit times were observed, even though the perfusion map for a long PLD was similar for both contralateral and ipsilateral hemispheres. Such results are consistent with the recent literature that reported hemispherical asymmetry of arterial transit time is related to severe ICA stenosis in ACAS patients, even though no

Fig. 11 Quantitative CBF maps for a representative healthy control and four examples of CAS patients for both multi-PLD ASL FA sweep and FA fixed methods. Scales unity are mL/100 g/min



CBF asymmetry was observed [37]. The observed alteration in cerebral hemodynamics of the patients may be related to impaired cognition usually observed in ACAS patients [38, 39]. Therefore, the dynamic investigation of cerebral perfusion is essential to characterize such patients.

Differently from the healthy subjects, the patients' mean CNR of all phases was higher for the FA sweep methods, although the difference was only significant for the last two PLDs. This difference for the first phases can be explained considering the higher sSNR for the FA sweep method as well as the delayed transit time for the patients. Since the blood did not fully arrive in the first PLDs, the mean signal intensity of GM and WM are comparable, equally lowering the CNR for both methods, which highlights the higher sSNR of the FA sweep method.

It is important to mention that even though we used the flip angle for the fixed FA approach within an acceptable range from the previous studies [15, 16], it was not specifically optimized in this study and might not be optimal.

The main benefit of the proposed modification in the Look-Locker readout for multi-PLD ASL is to improve the inspection of latter PLDs for patients with delayed transit time, helping the observation of, e.g., collateral flow (P05—Fig. 4). However, it is also possible to run the analysis under the kinetic model for ASL signal [19, 22] to perform the CBF quantification, taking advantage of higher SNR of the FA sweep approach when compared to the FA fixed.

In conclusion, we successfully assessed brain perfusion of patients with ICA stenosis using the multi-PLD ASL with flip angle sweep. The methodology was able to show subtle individual differences, which may help future studies on the management of the asymptomatic cerebrovascular disease. Moreover, we observed prolonged arterial transit time in patients, although they were considered asymptomatic, suggesting that it is not an adequate term to characterize them.

Acknowledgements The authors would like to acknowledge Angela Cristina Pernolato Giampedro for editing the manuscript for language and style. This work was supported by São Paulo Research Foundation (FAPESP) (Grant # 2013/23740-0), financed in part by the Coordenação de Aperfeiçoamento de Pessoal de Nível Superior—Brasil (CAPES)—Finance Code 001, and by the Conselho Nacional de Desenvolvimento Científico e Tecnológico (CNPq) (Grant # 140110/2016-0).

Author contributions AMP contributed to study conception and design, acquisition of data, analysis, and interpretation of data and drafting of the manuscript. RFL contributed to acquisition of data, analysis, and interpretation of data and critical revision. BUF contributed to study conception and design and acquisition of data. ACS contributed to the analysis and interpretation of data. OMPN contributed to the analysis and interpretation of data. FFP contributed to study conception and design, data acquisition, analysis and interpretation of data, and critical revision.

Compliance with ethical standards

Conflict of interest On behalf of all the authors, the corresponding author states that there is no conflict of interest.

Ethical approval Human in vivo data were acquired in accordance with the guidelines set by the ethics committee of the University of São Paulo and after obtaining written informed consent from the subjects.

References

1. Salinet AS, Haunton VJ, Panerai RB, Robinson TG (2013) A systematic review of cerebral hemodynamic responses to neural activation following stroke. *J Neurol* 260(11):2715–2721
2. Ostergaard L, Jespersen SN, Engedahl T, Gutierrez Jimenez E, Ashkanian M, Hansen MB, Eskildsen S, Mouridsen K (2015) Capillary dysfunction: its detection and causative role in dementias and stroke. *Curr Neurol Neurosci Rep* 15(6):37
3. de Weerd M, Greving JP, Hedblad B, Lorenz MW, Mathiesen EB, O'Leary DH, Rosvall M, Sitzer M, de Borst GJ, Buskens E, Bots ML (2014) Prediction of asymptomatic carotid artery stenosis in the general population: identification of high-risk groups. *Stroke* 45(8):2366–2371
4. Detre JA, Leigh JS, Williams DS, Koretsky AP (1992) Perfusion imaging. *Magnet Reson Med* 23(1):37–45
5. Williams DS, Detre JA, Leigh JS, Koretsky AP (1992) Magnetic resonance imaging of perfusion using spin inversion of arterial water. *Proc Natl Acad Sci USA* 89(1):212–216
6. Lan L, Leng X, Abrigo J, Fang H, Ip VH, Soo YO, Leung TW, Yu SC, Wong LK (2016) Diminished signal intensities distal to intracranial arterial stenosis on time-of-flight MR angiography might indicate delayed cerebral perfusion. *Cerebrovasc Dis* 42(3–4):232–239
7. Grubb RL Jr, Derdeyn CP, Videen TO, Carpenter DA, Powers WJ (2016) Relative mean transit time predicts subsequent stroke in symptomatic carotid occlusion. *J Stroke Cerebrovasc Dis* 25(6):1421–1424
8. Tsujikawa T, Kimura H, Matsuda T, Fujiwara Y, Isozaki M, Kikuta K, Okazawa H (2016) Arterial transit time mapping obtained by pulsed continuous 3D ASL imaging with multiple post-label delay acquisitions: comparative study with PET-CBF in patients with chronic occlusive cerebrovascular disease. *PLoS ONE* 11(6):e0156005
9. Johnston ME, Lu K, Maldjian JA, Jung Y (2015) Multi-TI arterial spin labeling MRI with variable TR and bolus duration for cerebral blood flow and arterial transit time mapping. *IEEE Trans Med Imaging* 34(6):1392–1402
10. Lou X, Yu S, Scalzo F, Starkman S, Ali LK, Kim D, Rao NM, Hinman JD, Vespa PM, Jahan R, Tateshima S, Gonzalez NR, Duckwiler GR, Saver JL, Yoo B, Salamon N, Lyu J, Ma L, Wang DJ, Liebeskind DS (2017) Multi-delay ASL can identify leptomeningeal collateral perfusion in endovascular therapy of ischemic stroke. *Oncotarget* 8(2):2437–2443
11. Schmid S, Teeuwisse WM, Lu H, van Osch MJ (2015) Time-efficient determination of spin compartments by time-encoded pCASL T2-relaxation-under-spin-tagging and its application in hemodynamic characterization of the cerebral border zones. *Neuroimage* 123:72–79
12. Zhang X, Ingo C, Teeuwisse WM, Chen Z, van Osch MJP (2018) Comparison of perfusion signal acquired by arterial spin labeling-prepared intravoxel incoherent motion (IVIM) MRI and conventional IVIM MRI to unravel the origin of the IVIM signal. *Magn Reson Med* 79(2):723–729

13. Lawrence KS, Owen D, Wang DJJ (2012) A two-stage approach for measuring vascular water exchange and arterial transit time by diffusion-weighted perfusion MRI. *Magnet Reson Med* 67(5):1275–1284
14. Hales PW, Clark CA (2013) Combined arterial spin labeling and diffusion-weighted imaging for noninvasive estimation of capillary volume fraction and permeability-surface product in the human brain. *J Cerebr Blood F Met* 33(1):67–75
15. Gunther M, Bock M, Schad LR (2001) Arterial spin labeling in combination with a look-locker sampling strategy: inflow turbo-sampling EPI-FAIR (ITS-FAIR). *Magn Reson Med* 46(5):974–984
16. Varela M, Petersen ET, Golay X, Hajnal JV (2015) Cerebral blood flow measurements in infants using look-locker arterial spin labeling. *J Magn Reson Imaging* 41(6):1591–1600
17. Francis ST, Bowtell R, Gowland PA (2008) Modeling and optimization of Look-Locker spin labeling for measuring perfusion and transit time changes in activation studies taking into account arterial blood volume. *Magn Reson Med* 59(2):316–325
18. van der Plas MCE, Teeuwisse WM, Schmid S, Chappell M, van Osch MJP (2019) High temporal resolution arterial spin labeling MRI with whole-brain coverage by combining time-encoding with Look-Locker and simultaneous multi-slice imaging. *Magn Reson Med* 81(6):3734–3744
19. Golay X, Petersen ET, Hui F (2005) Pulsed star labeling of arterial regions (PULSAR): a robust regional perfusion technique for high field imaging. *Magn Reson Med* 53(1):15–21
20. von Samson-Himmelstjerna F, Madai VI, Sobesky J, Guenther M (2016) Walsh-ordered hadamard time-encoded pseudocontinuous ASL (WH pCASL). *Magn Reson Med* 76(6):1814–1824
21. Wells JA, Lythgoe MF, Gadian DG, Ordidge RJ, Thomas DL (2010) In vivo Hadamard encoded continuous arterial spin labeling (H-CASL). *Magn Reson Med* 63(4):1111–1118
22. Buxton RB, Frank LR, Wong EC, Siewert B, Warach S, Edelman RR (1998) A general kinetic model for quantitative perfusion imaging with arterial spin labeling. *Magn Reson Med* 40(3):383–396
23. Chappell MA, Groves AR, Whitcher B, Woolrich MW (2009) Variational bayesian inference for a nonlinear forward model. *IEEE Trans Signal Process* 57(1):223–236
24. Groves AR, Chappell MA, Woolrich MW (2009) Combined spatial and non-spatial prior for inference on MRI time-series. *Neuroimage* 45(3):795–809
25. Jenkinson M, Beckmann CF, Behrens TE, Woolrich MW, Smith SM (2012) *Fsl. Neuroimage* 62(2):782–790
26. Pfefferbaum A, Chanraud S, Pitel AL, Shankaranarayanan A, Alsop DC, Rohlfing T, Sullivan EV (2010) Volumetric cerebral perfusion imaging in healthy adults: regional distribution, laterality, and repeatability of pulsed continuous arterial spin labeling (PCASL). *Psychiatry Res* 182(3):266–273
27. Qin Q, Huang AJ, Hua J, Desmond JE, Stevens RD, van Zijl PC (2014) Three-dimensional whole-brain perfusion quantification using pseudo-continuous arterial spin labeling MRI at multiple post-labeling delays: accounting for both arterial transit time and impulse response function. *NMR Biomed* 27(2):116–128
28. Chen Y, Wang DJ, Detre JA (2012) Comparison of arterial transit times estimated using arterial spin labeling. *MAGMA* 25(2):135–144
29. Hara S, Tanaka Y, Ueda Y, Hayashi S, Inaji M, Ishiwata K, Ishii K, Maehara T, Nariai T (2017) Noninvasive evaluation of CBF and perfusion delay of moyamoya disease using arterial spin-labeling MRI with Multiple postlabeling delays: comparison with AJNR Am J Neuroradiol 38(4):696–702
30. Haga S, Morioka T, Shimogawa T, Akiyama T, Murao K, Kanazawa Y, Sayama T, Arakawa S (2016) Arterial spin labeling perfusion magnetic resonance image with dual postlabeling delay: a correlative study with acetazolamide loading (123)I-iodoamphetamine Single-Photon emission computed tomography. *J Stroke Cerebrovasc Dis* 25(1):1–6
31. Paschoal AM, Leoni RF, Santos AC, Foerster BU, Paiva FF (2015) ASL contrast optimization in multiphase STAR labeling using variable flip angle. In: 21st annual meeting of the organization for human brain mapping, Honolulu, p 1857
32. Paschoal AM, Leoni RF, Santos AC, Foerster BU, Paiva FF (2017) Improving arterial spin labeling acquisition to reduce the effect of delayed arrival time. In: ISMRM 25th annual meeting & exhibition, Honolulu, p 1496
33. MacIntosh BJ, Filippini N, Chappell MA, Woolrich MW, Mackay CE, Jezzard P (2010) Assessment of arterial arrival times derived from multiple inversion time pulsed arterial spin labeling MRI. *Magn Reson Med* 63(3):641–647
34. MacIntosh BJ, Lindsay AC, Kylington I, Kuker W, Günther M, Robson MD, Kennedy J, Choudhury RP, Jezzard P (2010) Multiple inflow pulsed arterial spin-labeling reveals delays in the arterial arrival time in minor stroke and transient ischemic attack. *AJNR Am J Neuroradiol* 31(10):1892–1894
35. Wang T, Xiao F, Wu G, Fang J, Sun Z, Feng H, Zhang J, Xu H (2017) Impairments in brain perfusion, metabolites, functional connectivity, and cognition in severe asymptomatic carotid stenosis patients: an integrated MRI study. *Neural Plast* 2017:8738714
36. Camargo AP, Silva P, Rodrigues G, Camilo M, Paschoal A, Barreira C, Abud D, Leoni R, Pontes-Neto OM (2018) Cerebral perfusion, functional connectivity and cognitive profile of patients with asymptomatic carotid stenosis. *Stroke* 49:ATP422
37. Chen YF, Tang SC, Wu WC, Kao HL, Kuo YS, Yang SC (2017) Alterations of cerebral perfusion in asymptomatic internal carotid artery steno-occlusive disease. *Sci Rep* 7(1):1841
38. Xiang J, Zhang T, Yang QW, Liu J, Chen Y, Cui M, Yin ZG, Li L, Wang YJ, Li J, Zhou HD (2013) Carotid artery atherosclerosis is correlated with cognitive impairment in an elderly urban Chinese non-stroke population. *J Clin Neurosci* 20(11):1571–1575
39. Wang T, Mei B, Zhang J (2016) Atherosclerotic carotid stenosis and cognitive function. *Clin Neurol Neurosurg* 146:64–70

Publisher's Note Springer Nature remains neutral with regard to jurisdictional claims in published maps and institutional affiliations.

45 Autoria de artigos completos publicados em jornais e revistas de circulação nacional e internacional na sua área

Esta subseção apresenta o comprovante da autoria do artigo publicado na revista internacional *Magnetic Resonance in Medicine* no ano de 2021.

Three-dimensional gradient and spin-echo readout for time-encoded pseudo-continuous arterial spin labeling: Influence of segmentation factor and flow compensation

Andre M. Paschoal^{1,2,3,4}  | Renata F. Leoni²  | Bruno F. Pastorello³ |
Matthias J. P. van Osch⁴ 

¹Medical School of Ribeirao Preto, University of Sao Paulo, Ribeirao Preto, SP, Brazil

²InBrain Lab, Department of Physics - FFCLRP, University of Sao Paulo, Ribeirao Preto, SP, Brazil

³LIM44 - Instituto e Departamento de Radiologia, Faculdade de Medicina - Universidade de São Paulo, São Paulo, SP, Brazil

⁴C.J. Gorter Center for High Field MRI, Department of Radiology, Leiden University Medical Center, Leiden, The Netherlands

Correspondence

Andre M. Paschoal, LIM44, Instituto e Departamento de Radiologia, Faculdade de Medicina, Universidade de São Paulo, São Paulo, SP 05403-010, Brazil.

Email: andre.paschoal@usp.br

Twitter: @paschoal_am

Funding information

Coordenação de Aperfeiçoamento de Pessoal de Nível Superior - Brasil (CAPES) - PDSE, Grant/Award Number: 88881.188976/2018-01; Conselho Nacional de Desenvolvimento Científico e Tecnológico (CNPq), Grant/Award Number: 140110/2016-0; Research program in Applied and Engineering Sciences - Netherlands Organization for Scientific Research (NWO), Grant/Award Number: VIC: 016.160.351

Purpose: To monitor the complete passage of the labeled blood through the vascular tree into tissue and improve the quantification of ASL maps, we evaluated the effect of 3D gradient and spin-echo (GRASE) readout segments on temporal SNR (tSNR) and image blurriness for time-encoded pseudo-continuous arterial spin labeling and the effect of flow-compensation gradients on the presence of intravascular signal.

Methods: Fifteen volunteers were scanned using time-encoded pCASL with 2D EPI and single-segment, two-segments, and three-segments 3D-GRASE readouts with first-order flow compensation (FC) gradients. Two-segments 3D-GRASE scans were acquired with 25%, 50%, 75%, and 100% of full first-order FC. Temporal SNR was assessed, and cerebral blood flow and arterial blood volume were quantified for all readout strategies.

Results: For single-segment 3D GRASE, tSNR was comparable to 2D EPI for perfusion signal but worse for the arterial signal. Two-segments and three-segments 3D GRASE resulted in higher tSNR than 2D EPI for perfusion and arterial signal. The arterial signal was not well visualized for 3D-GRASE data without FC. Visualization of the intravascular signal at postlabeling delays of 660 ms and 1060 ms was restored with FC. Adequate visualization of the intravascular signal was achieved from 75% of FC gradient strength at a postlabeling delay of 660 ms. For a postlabeling delay of 1060 ms, full-FC gradients were the best option to depict intravascular signal.

Conclusion: Segmented GRASE provided higher effective tSNR compared with 2D-EPI and single-segment GRASE. Flow compensation with GRASE readout should be carefully controlled when applying for time-encoded pCASL to visualize intravascular signal.

This is an open access article under the terms of the Creative Commons Attribution-NonCommercial License, which permits use, distribution and reproduction in any medium, provided the original work is properly cited and is not used for commercial purposes.

© 2021 The Authors. *Magnetic Resonance in Medicine* published by Wiley Periodicals LLC on behalf of International Society for Magnetic Resonance in Medicine

KEY WORDS

3D GRASE, flow compensation, time-encoded pCASL, tSNR

1 | INTRODUCTION

Arterial spin labeling (ASL) is a noninvasive perfusion-weighted imaging technique that exploits arterial blood as an endogenous tracer. A bolus of arterial blood is magnetically labeled through inversion in a slab proximal to the imaging plane, from which it will flow through the arterial tree until crossing the blood-brain barrier and reaching the brain-tissue compartment. After labeling the blood through the application of RF pulses has stopped, the image is acquired after a time interval called postlabeling delay (PLD). A single PLD is considered adequate to measure cerebral blood flow (CBF).¹ However, when the subject suffers from prolonged arterial transit time (ATT), CBF will be underestimated, which can be corrected by acquiring a multiple-timepoint ASL (multi-PLD ASL).

Moreover, multi-PLD ASL allows monitoring the labeled arterial blood within the intravascular space at short PLDs, until finally perfusing the brain tissue at the later PLDs. By using, for example, Bayesian inference under the appropriate kinetic model, all PLDs are used to estimate quantitative ASL maps, which include the CBF, arterial blood volume (aBV), and ATT. In such a model, all PLDs acquired are important for the final CBF maps to be corrected for arrival-time artifacts and intravascular signal.

In 2015, a consensus paper set the recommended implementation of ASL for clinical applications,¹ to help with standardization and dissemination of the technique. In summary, a segmented 3D gradient and spin-echo (GRASE) readout^{2,4} was recommended in combination with pseudo-continuous arterial spin labeling (pCASL), as it can be optimally combined with background suppression using a single excitation pulse per TR, resulting in higher SNR compared with 2D EPI.^{5,6} However, choosing the number of segments for 3D GRASE requires fine-tuning to balance SNR, blurring in z-direction, and vulnerability to motion. Segmented 3D sequences fill less k-space lines per excitation pulse, thereby reducing signal losses due to T_2^* and consequently providing less blurring at boundaries between tissues, especially where a significant signal difference exists (eg, between CSF and gray matter). Therefore, segmented acquisitions are less suited in situations in which many different conditions need to be measured, such as in multi-postlabeling delays (PLD) ASL. Although single-segment 3D GRASE provides a more time-efficient acquisition, it results in significant blurring in z-direction, so it has been scarcely used.

There are three main approaches for multi-PLD ASL. First, traditional pCASL scans can be repeated with different PLDs and labeling duration. Recently, Woods et al⁷ proposed optimal settings for such an acquisition. Second,

a Look-Locker readout can be used as, for example, in the inflow turbo-sampling EPI-flow-sensitive alternating inversion recovery and QUASAR (Modus QA, London, ON, Canada) sequences.^{8,9} This approach has the advantage that all PLDs are acquired simultaneously, albeit with lower SNR resulting in similar total scan times. Finally, Hadamard-encoded pCASL or time-encoded pCASL (te-pCASL) was demonstrated, which achieves multiple PLDs by the temporal encoding of the labeled blood following a Hadamard matrix.¹⁰⁻¹³ When designing a 3D readout sequence for multi-PLD acquisitions, the criteria are different compared with single-PLD perfusion imaging. Special attention is needed when considering the use of flow compensation (FC) gradients that compensate for first-order dephasing effects.¹⁴ Use of FC can increase TE and readout times, but its absence will crush vascular ASL signal, which is an essential part of the information conveyed in early PLDs by showing the passage of label through the arterial system.

The appropriate readout setup and use of FC gradients provide the promise of images with higher temporal SNR (tSNR) and improved delineation of the angiographic phase, respectively, as an input for the quantitative model, which would lead to more accurate CBF, aBV, and ATT maps. Therefore, we aimed to evaluate the effect of the number of segments of 3D-GRASE readout on tSNR, comparing its performance with the 2D-EPI readout, and analyze the effect of FC gradients in delineating the presence of vascular signal.

2 | METHODS

2.1 | Hadamard-encoded pCASL

Time-encoded pCASL is a time-efficient strategy to acquire multi-PLD pCASL, providing the opportunity to monitor the dynamic inflow of blood into brain tissue, improving CBF quantification, and allowing the measurements of ATT and aBV. In a time-encoded acquisition, the labeling module is divided into small subboli, encoded according to a Hadamard matrix to be either control or label. In this study, a Hadamard-8 matrix was chosen for the labeling module, with a total labeling duration of 3500 ms split into seven blocks of 1800, 800, 400, 2 × 150, and 2 × 100 ms (ie, the free-lunch approach).¹³ After the labeling module, there was a PLD of 160 ms until starting the readout module (Figure 1B). Two background suppression pulses were applied at 1831 ms and 3135 ms.

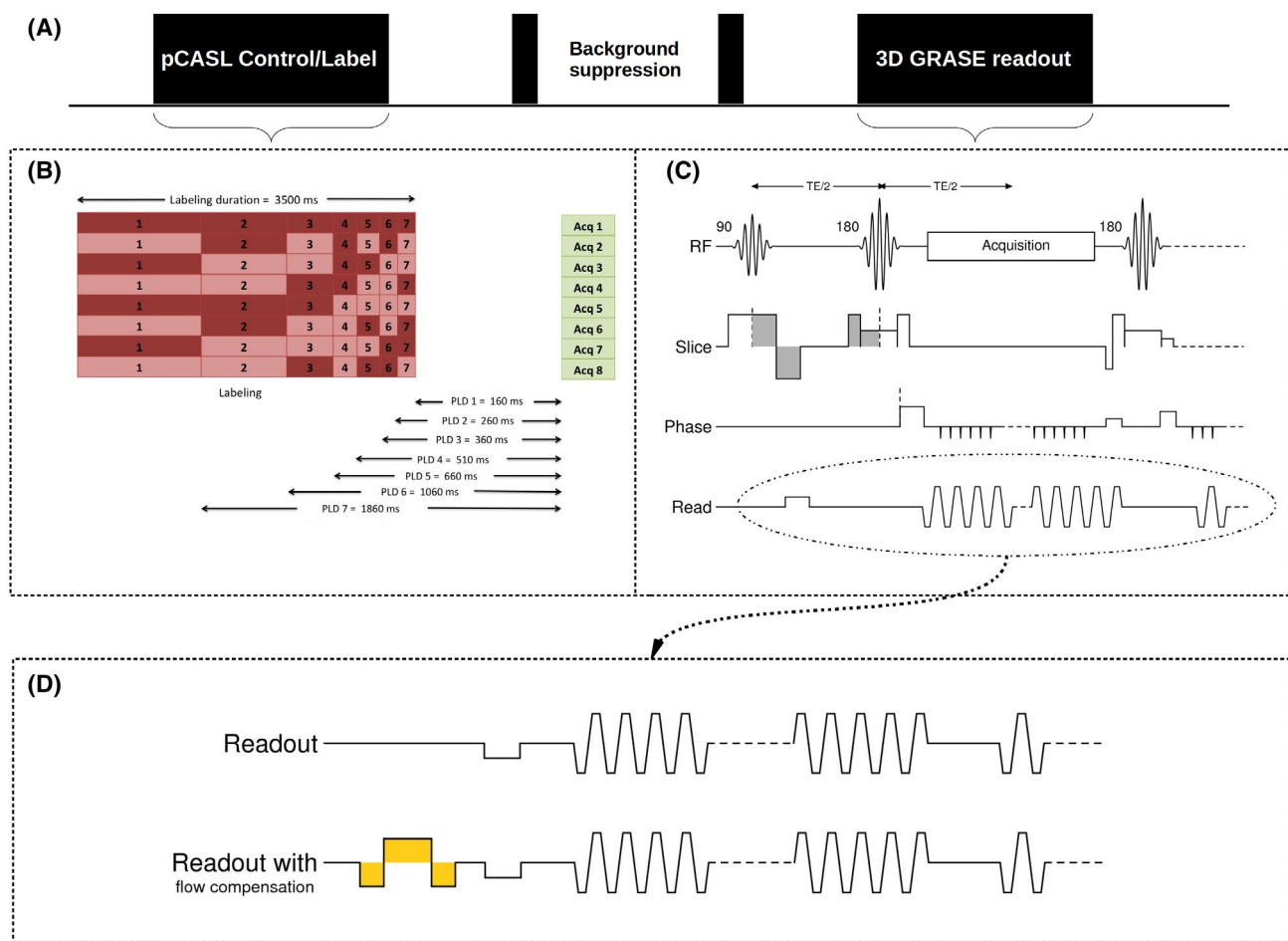


FIGURE 1 A, Pulse sequence diagram of 3D time-encoded pseudo-continuous arterial spin labeling (te-pCASL). B, Eight Hadamard matrix for pCASL labeling encoding, followed by the even postlabeling delay (PLD) intervals (in which the background suppression pulses are applied) until reaching the readout module for acquisitions 1 to 8. C, Three-dimensional gradient and spin-echo (GRASE) readout module. When the image is acquired with a single segment, the whole-brain acquisition is achieved with only one 90° RF excitation pulse, whereas for two-segments and three-segments images, the readout module is repeated two and three times, respectively, (two and three 90° RF excitation pulses) to acquire a whole-brain volume. D, When flow compensation is desired, bipolar gradient lobes are applied in the readout direction just before the acquisition

2.2 | Three-dimensional GRASE readout: Number of segments

The 3D-GRASE readout combines the time efficiency of EPI with higher SNR of 3D imaging by exploiting the rapid imaging with refocused echoes readout¹⁵ technique in the z-direction (Figure 1C). When an entire volume is acquired using only a single excitation pulse, the approach is called single-segment 3D GRASE. When more than one segment is required to fill the 3D k-space, the approach is referred to as multisegmented or segmented 3D GRASE. Because T₂ signal decreases over the readout train result in blurring on the kz-axis, GRASE segmentation is recommended. In this study, we evaluated how the number of segments in 3D-GRASE readout influences the te-pCASL acquisition performance concerning time efficiency, blurring in the z-direction, and SNR. Moreover, the results were compared with a 2D multislice EPI readout.

2.3 | Three-dimensional GRASE readout: FC

The purpose of using FC gradients is to correct for flow-induced dephasing. It can be achieved using additional bipolar gradient lobes before the signal readout (Figure 1D). As the area under the positive and negative lobes are the same, the added mean gradient is zero, but the timing of each gradient lobe is chosen, so that the spins flowing with constant velocity end up with zero phase accumulation over the total readout (ie, no dephasing). For first-order FC, the dephasing is only circumvented for constant velocity (ie, acceleration [deceleration] of blood can still lead to dephasing). Due to the added gradients, flow compensation will increase TE value and lengthen the total readout time. Nonetheless, especially when using a 3D readout, visualization of intravascular signal of dynamic ASL signal can be considered critical, especially during the inflow phase. Therefore, we analyzed the

effect of FC gradients scaling for two-segments 3D-GRASE readout on the resulting images, for both the angiographic and the perfusion phase of multi-PLD time-encoded ASL.

2.4 | Magnetic resonance imaging experiments details

Fifteen volunteers (8 females, age 26.3 ± 5.2 years) were scanned on a 3T Philips MRI scanner (Amsterdam, Netherlands), from which 10 were scanned for the readout segmentation experiment and five for the FC experiment. All volunteers agreed to participate after signing informed consent, and the study was in agreement with local internal review board policies. We used a time-encoded Hadamard-8 pCASL labeling sequence with single-segment, two-segments, and three-segments 3D GRASE and a multislice 2D-EPI readout. Table 1 lists the acquisition parameters.

For the FC experiment, two-segments 3D-GRASE scans were acquired with the FC gradient strengths of 0%, 25%, 50%, 75%, and 100% of full first-order strength to analyze the effect of FC on the visualization of the vascular ASL signal.

2.5 | Data analysis

Hadamard matrix decoding for ASL subtraction was performed in *MATLAB* (MathWorks, Natick, MA) to obtain multi-PLD ASL maps (note that labeling duration is also different among the multi-PLD maps). Further processing of

ASL data and quantification of CBF and aBV were performed using the BASIL toolkit (Oxford Center for Functional MRI of the Brain's software library [FSL]),^{16,17} considering all PLDs acquired. Scans were corrected for motion using the MCFLIRT tool (FSL), and the structural images were segmented and transformed into the ASL space to create whole-brain, gray-matter, and white-matter masks using FAST and FLIRT tools (FSL).

Perfusion images were deblurred using the oxasl-deblur toolkit of the Quantitative Biomedical Inference Group, Oxford Institute of Biomedical Engineering (<https://oxasl.readthedocs.io/en/latest/download.html>), which uses a fast Fourier transform filter in the frequency space to reduce the blurring in z-direction for 3D-GRASE data. Furthermore, both blurred and deblurred ASL perfusion maps were compared with the gray-matter region of interest of the T₁-weighted structural images transformed to the ASL space (reference image). The blurring estimation in z-direction was done in *MATLAB* using a method that compares the desired image with a reference image and outputs the blurring of the input image.¹⁸

Postprocessing and calculation of tSNR was done in *MATLAB* according to:

$$tSNR = \frac{S}{\sigma} * \sqrt{\frac{\text{Number of averages in 6 min}}{\text{Total averages acquired}}}, \quad (1)$$

where S is the mean signal of a voxel over the different averages, and σ is the SD. The perfusion tSNR was voxel-wise calculated within the region of interest of the gray-matter mask

TABLE 1 Acquisition parameters

Scan parameter	2D EPI	3D GRASE Single segment	3D GRASE Two segments	3D GRASE Three segments
FOV (mm)	240 × 240	240 × 240 × 102	240 × 240 × 102	240 × 240 × 102
Voxel size (mm)	3.75 × 3.75 × 6	3.75 × 3.75 × 6	3.75 × 3.75 × 6	3.75 × 3.75 × 6
Acquisition matrix	64 × 64 × 17	64 × 64 × 31	64 × 64 × 31	64 × 64 × 31
Reconstructed slices	17	17	17	17
Oversampling factor	–	1.8	1.8	1.8
Slice thickness (mm)	6	6	6	6
TR (ms)	4100	4100	3900	3900
TE (ms)	9.2	9.2	13.9	10.5
No. of repetitions	6	6	3	2
EPI factor	25	25	13	5
TSE factor	–	16	16	16
Bandwidth (Hz) (frequency direction)	3136	3160	3160	3160
SENSE factor (AP direction)	2.5	2.5	2.5	2.5
Total scan duration (minutes)	6:03	6:15	7:56	12:10
FC	No	Yes	Yes	Yes

Abbreviations: AP, anterior-posterior; TSE, turbo spin echo.

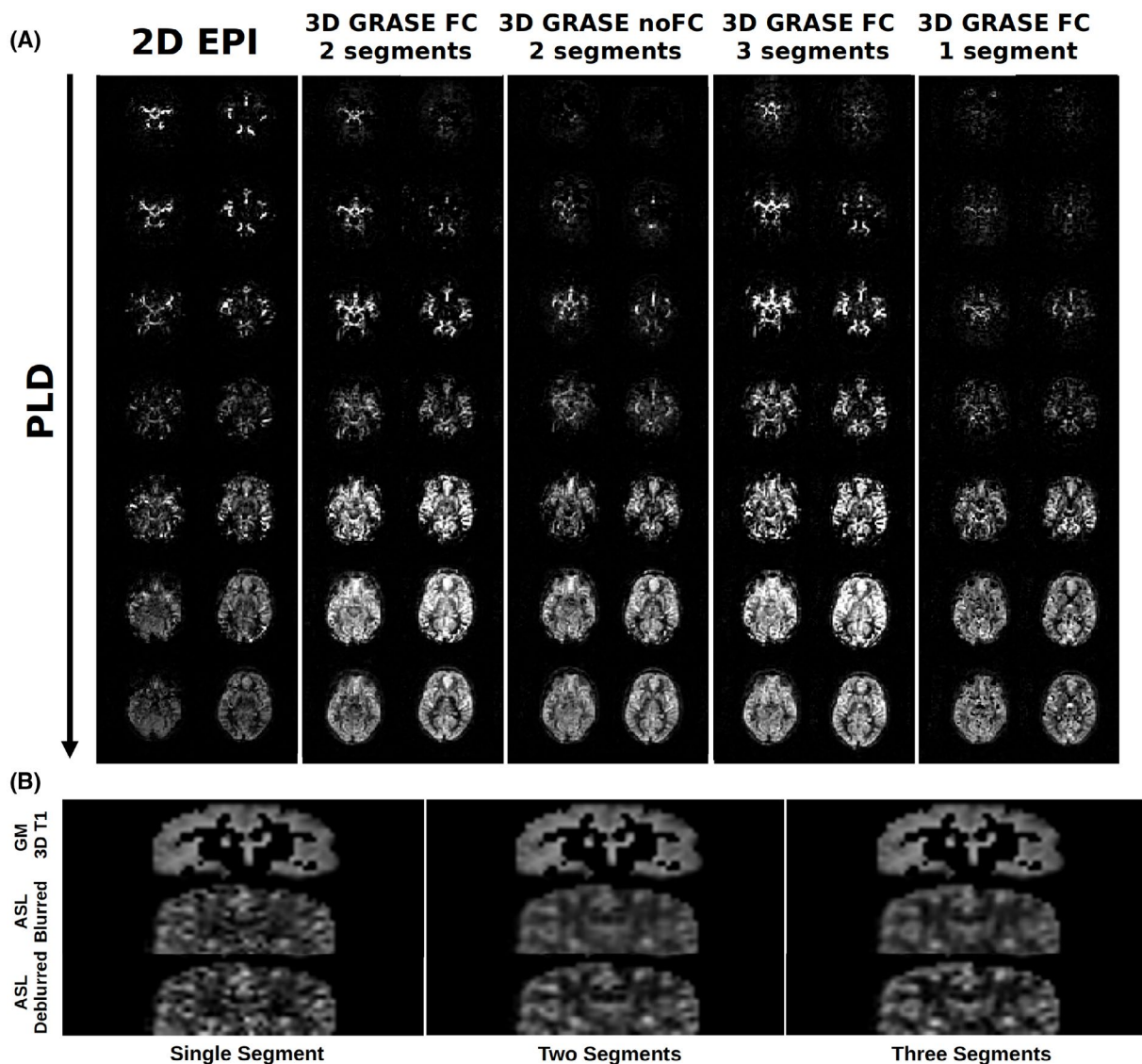


FIGURE 2 A, Two representative slices for all PLDs and readout schemes. B, Comparison of gray matter (GM) of 3D T₁ images transformed to ASL space with blurred and deblurred ASL images for each of the 3D-GRASE readouts acquired. Abbreviation: FC, flow compensation

transformed to the ASL images space, whereas for the vascular tSNR analysis, we used the aBV outputs from the two-segments 3D GRASE thresholded at 1 mL/100 g/min. The contrast-to-noise ratio (CNR) was calculated for the perfusion block (PLD of 1860 ms) for all readouts, according to:

$$CNR = \frac{\text{mean}(GM) - \text{mean}(WM)}{\sigma_s}, \quad (2)$$

where mean(GM) and mean(WM) are the mean signal over the gray-matter and white-matter masks, and σ_s is the spatial SD of the whole-brain ASL images.

The statistical analysis was performed in R.¹⁹ A one-way ANOVA was used to compare tSNR among different numbers of segments and FC levels. We also performed the two-way ANOVA to compare CNR and blurring levels. In such cases, the factors were the number of segments and the use or

not of deblurring. Results were adjusted for multiple comparisons using the Tukey's method.

3 | RESULTS

3.1 | Effects of segmentation number

Two representative slices of ASL maps at multiple PLDs are shown in Figure 2A for axial view and in Supporting Information Figure S1 for sagittal views for the 3D-GRASE readout with different numbers of segments and the 2D multislice scan. The sagittal maps are shown to assess blurring in z-direction, which is especially apparent in the single-segment GRASE scan. Figure 3 shows the tSNR maps in axial directions for two representative PLDs that focus on the intravascular (left) and the perfusion signal (right panel). For

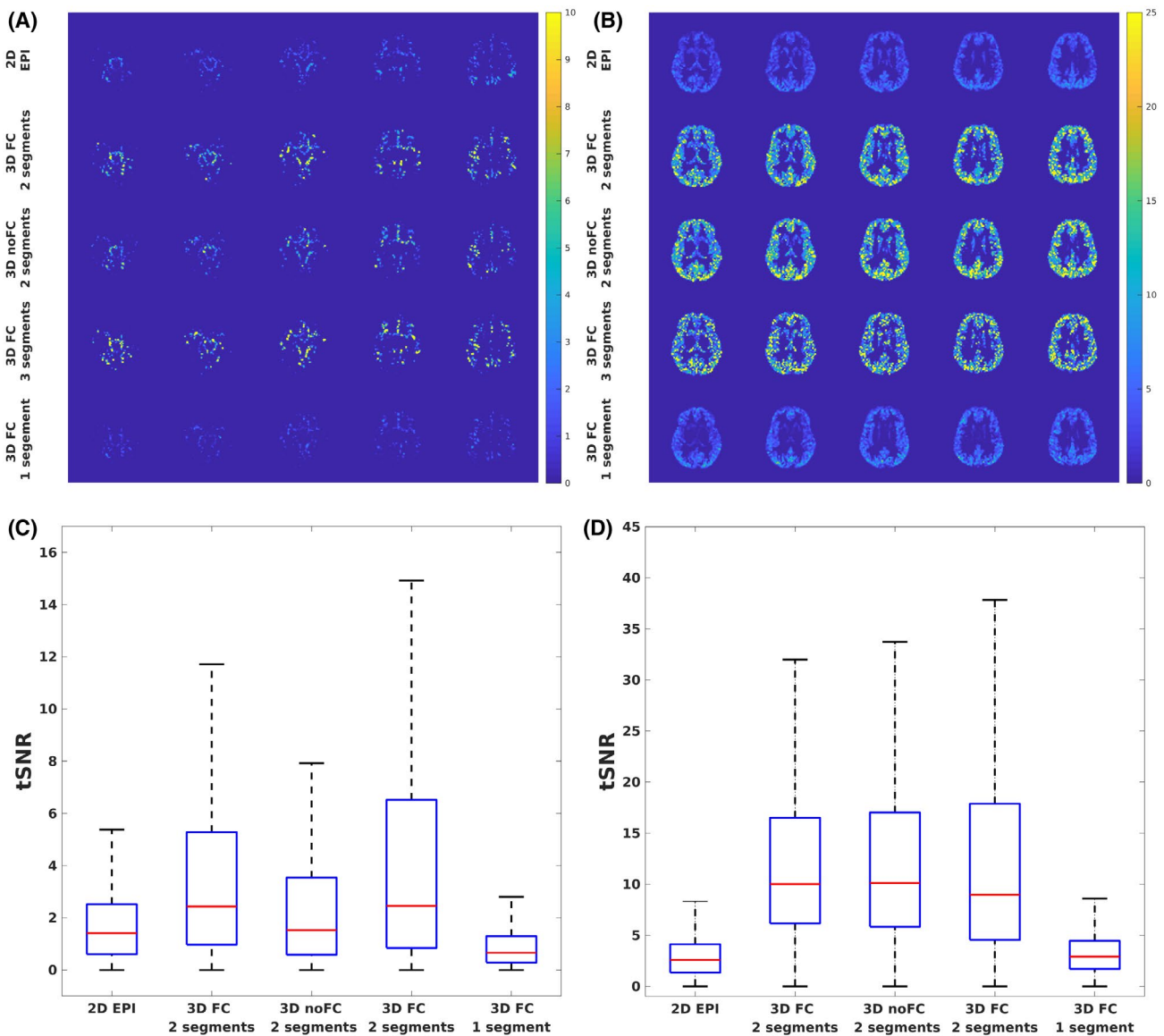


FIGURE 3 Temporal SNR (tSNR) calculated for all readouts at a PLD of 660 ms (A,C) and 1860 ms (B,D)

the PLD of 660 ms, the EPI readout had significantly higher tSNR (0.85 ± 1.01 , $P < .01$) than the single-segment 3D GRASE (0.54 ± 0.60), whereas the tSNR for both the two-segments and three-segments 3D GRASE (tSNR = 2.17 ± 3.90 and 3.10 ± 7.39 , respectively), were significantly higher than the single-segment 3D GRASE and the 2D-EPI readout ($P < .01$). For the perfusion signal measured at a PLD of 1860 ms, all 3D-GRASE acquisitions showed higher tSNR than the 2D-EPI readout (tSNR = 2.94 ± 2.12 , $P < .01$), and the two-segments and three-segments 3D GRASE (tSNR = 13.60 ± 12.55 and 14.88 ± 17.12 , respectively) exhibited significantly higher tSNR than single-segment 3D GRASE (tSNR = 3.33 ± 2.33 , $P < .01$).

The comparisons between blurred and deblurred images for single, two, and three segments are shown in Figure 2B (coronal view). The comparison between the two-segments

and three-segments images did not show significant differences (blurring = $42.20 \pm 5.42\%$ vs $34.86 \pm 7.46\%$, $P > .05$) for blurred images. For deblurred images, the three-segments images showed significantly lower blurring (blurring = $5.19 \pm 4.20\%$, $P < .05$) than the two-segments ($11.82 \pm 8.47\%$) and single-segment images ($10.09 \pm 4.97\%$). The CNR measurements revealed significantly higher values ($P < .01$) for two-segments and three-segments 3D GRASE (CNR = 0.32 ± 0.03 and 0.33 ± 0.02 , respectively), compared with single-segment 3D GRASE (0.201 ± 0.037) and 2D EPI (0.204 ± 0.023).

For a better analysis of the vascular signal, aBV maps were calculated from the multi-PLD images for different numbers of segments (see Supporting Information Figure S2A). The CBF maps were also quantified for different numbers of segments, taking all PLDs into account (see Supporting Information Figure S3A).

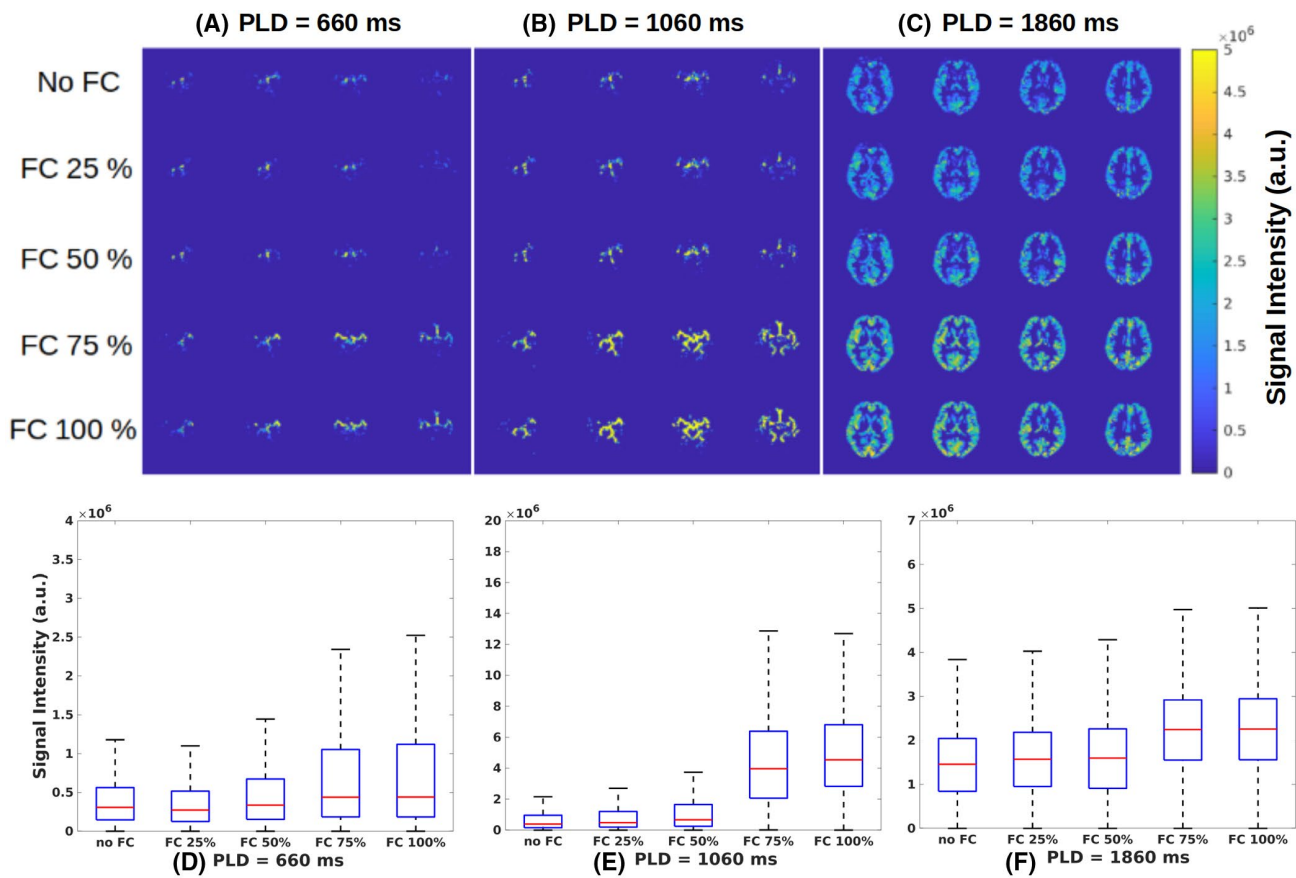


FIGURE 4 Signal intensity calculated for different levels of FC at a PLD of 660 ms (A,D), 1060 ms (B,E), and 1860 ms (C,F). For the PLD of 660 ms, the comparison between the FC of 25% and no FC and between FC of 50% and no FC did not show statistical difference ($P < .01$). For the PLD of 1060 ms, the only comparison that did not show statistical difference ($P < .01$) was between the FC of 25% and FC of 50%, whereas for the PLD of 1860 ms, the only comparison that did not result in significant difference was between FC of 75% and FC of 100%.

3.2 | Effects of FC

Finally, the intensity of FC gradients was varied (Figure 1D), and the effect of the vascular signal on the visualization was evaluated. The FC gradient scaling was performed for two-segments 3D-GRASE te-pCASL, and the results are found in Supporting Information Figure S4 for two representative slices at multiple PLDs. The signal intensity maps for three representative PLDs are shown in Figure 4. We compared the signal intensities for different FC scales two by two. All comparisons were significant for a PLD of 660 ms ($P < .01$) except for no FC versus FC of 25%, and FC of 75% versus FC of 100%. No significant differences were observed between FC of 25% and FC of 50% for a PLD of 1060 ms, and between FC of 75% and FC of 100% for a PLD of 1860 ms. Finally, aBV and CBF maps from the respective FC scaling are shown in Supporting Information Figures S3B and S4B, respectively.

4 | DISCUSSION

In this study, the number of segmentations in 3D-GRASE readout and the use of FC gradients were evaluated for

te-pCASL. Optimal settings of 3D-GRASE readout for traditional pCASL imaging for perfusion measurements (ie, measured at a PLD of approximately 1.8 seconds) cannot be assumed optimal for te-pCASL due to two important differences: In te-pCASL, the angiographic phase of ASL is also captured, and the temporal footprint of te-pCASL (eight Hadamard encodings) is longer than for traditional pCASL (two conditions: label and control). The main findings of this study are 2-fold. First, segmented 3D GRASE outperforms single-segment 3D GRASE and multislice 2D EPI. Second, the use of proper FC is advised, to allow correct visualization of the angiographic phase.

The 2D-EPI readout showed good results for te-pCASL, allowing the visualization of both arterial and perfusion signal (Figure 2A). However, a more careful analysis revealed lower tSNR than segmented 3D GRASE (Figure 3). For perfusion signal, the tSNR of 2D EPI was lower than the one for single-segment 3D GRASE; for the angiographic phase, 2D EPI had a higher SNR than single-segment 3D GRASE. For two-segmented and three-segmented 3D-GRASE images, the tSNR values were significantly higher for both perfusion and arterial signal when compared with the 2D EPI (Figure 2A). When comparing the two-segments and three-segments 3D

GRASE, the latter produced the best results. Similar results were reported by Feinberg et al,⁴ who analyzed the effects of the number of segments on single-PLD 3D-GRASE pulsed ASL data.

The blurring effects on 3D-GRASE data were also assessed. Previous studies reported a higher amount of blurring when using single-segment readout for 3D-GRASE ASL than a segmented acquisition.^{4,20} However, they did not quantify the blurring, and the conclusion was based on visual inspection. We also observed a higher amount of blurring for single-segment 3D GRASE following visual inspection, but a quantitative analysis did not confirm this. This is probably because the tSNR and the spatial CNR are significantly lower than for segmented 3D GRASE. For segmented data, two-segments and three-segments images showed a comparable amount of blurring before applying a deblurring algorithm. After deblurring, the three-segments data were significantly less blurred than the two-segments 3D-GRASE images.

The aBV maps from data with first-order FC better delineated arterial signal. Similarly, two-segments and three-segments GRASE provided better aBV maps than single-segment GRASE (Supporting Information Figure S2A). As shown in the experiment in which the flow compensation was varied, FC use plays a big role in depicting the vascular signal.²¹⁻²⁴ The present results revealed that the intravascular signal visualization at PLDs of 660 ms and 1060 ms is hampered without FC (Figure 4A,B), with FC being especially essential at the PLD of 1060 ms (Figure 4B). At this PLD, and opposed to the PLD of 660 ms, most of the labeled blood already filled the large arteries within the imaging volume, while still flowing fast. For the even longer PLD of 1800 ms, the blood will have slowed down, resulting in a weaker influence of FC on image quality, although FC of 75% and 100% still provided slightly higher signal than lower FC levels. The smaller dependency on FC when the label arrives within the microvasculature and exchanges with tissue magnetization explains why FC has not been recognized earlier as an important sequence-design parameter. With the introduction of efficient multi-PLD ASL sequences, this effect becomes more prominent, as these sequences also focus on the more angiographic phase. The fact that still higher signal was observed with FC at a PLD of 1800 ms points to the fact that not all labels arrive at the capillary exchange site. Inclusion of a macrovascular component during postprocessing would correct for the label that did not arrive yet at the voxel of their final destination, similar to what Chappell et al has shown in a macrovascular component that still identifies a vascular signal in vascular crushed ASL data.²⁵ When the label would already have arrived in the final destination voxel, the signal should be included in quantification to provide the best estimate of perfusion.

The main limitation of this study is the investigation of FC gradients only in the readout direction. Future studies may explore their application in other directions. Another

limitation is that we did not analyze the influence of motion, as segmented 3D GRASE results in a longer temporal footprint, making the acquisition more prone to motion artifacts.

5 | CONCLUSIONS

This study showed higher effective tSNR and CNR for two-segments and three-segments GRASE compared with 2D EPI and single-segment GRASE. Therefore, its use is recommended for te-pCASL. Moreover, FC properties of the GRASE readout should be carefully controlled when applying it to te-pCASL. The use of full FC is essential to visualize the inflow of blood through the arterial system, whereas without FC the vascular signal can be considerably dephased, hampering the assessment of the passage of the blood from the intravascular space to the brain tissue. With the complete passage, data modeling can be considered optimal, providing more accurate CBF, aBV, and ATT maps. When a single-segment readout is required, 3D GRASE and multislice EPI provide similar results regarding tSNR, although the tSNR for 2D EPI is higher for the angiographic phase.

CONFLICT OF INTEREST

MJP van Osch receives research support from Philips, the Netherlands.

ORCID

Andre M. Paschoal  <https://orcid.org/0000-0001-8269-711X>

Renata F. Leoni  <https://orcid.org/0000-0002-4568-0746>

Matthias J. P. van Osch  <https://orcid.org/0000-0001-7034-8959>

REFERENCES

1. Alsop DC, Detre JA, Golay X, et al. Recommended implementation of arterial spin-labeled perfusion MRI for clinical applications: a consensus of the ISMRM perfusion study group and the European consortium for ASL in dementia. *Magn Reson Med.* 2015;73:102-116.
2. Oshio K, Feinberg DA. GRASE (gradient-and spin-echo) imaging: a novel fast MRI technique. *Magn Reson Med.* 1991;20:344-349.
3. Gunther M, Oshio K, Feinberg DA. Single-shot 3D imaging techniques improve arterial spin labeling perfusion measurements. *Magn Reson Med.* 2005;54:491-498.
4. Feinberg D, Ramann S, Gunther M. Evaluation of new ASL 3D GRASE sequences using parallel imaging, segmented and interleaved k-space at 3T with 12- and 32-channel coils. In: Proceedings of the 17th Annual Meeting of ISMRM, Honolulu, Hawaii, 2009. Abstract #622.
5. Ye FQ, Frank JA, Weinberger DR, McLaughlin AC. Noise reduction in 3D perfusion imaging by attenuating the static signal in arterial spin tagging (ASSIST). *Magn Reson Med.* 2000;44: 92-100.

6. Garcia DM, Duhamel G, Alsop DC. Efficiency of inversion pulses for background suppressed arterial spin labeling. *Magn Reson Med.* 2005;54:366-372.
7. Woods JG, Chappell MA, Okell TW. A general framework for optimizing arterial spin labeling MRI experiments. *Magn Reson Med.* 2019;81:2474-2488.
8. Gunther M, Bock M, Schad LR. Arterial spin labeling in combination with a look-locker sampling strategy: inflow turbo-sampling EPI-FAIR (ITS-FAIR). *Magn Reson Med.* 2001;46:974-984.
9. Varela M, Petersen ET, Golay X, Hajnal JV. Cerebral blood flow measurements in infants using Look-Locker arterial spin labeling. *J Magn Reson Imaging.* 2015;41:1591-1600.
10. Gunther M. Encoded continuous arterial spin labeling. In: Proceedings of the ISMRM Workshop on Cerebral Perfusion and Brain Function: Novel Techniques and Applications, Salvador, Bahia, 2007.
11. Wells JA, Lythgoe MF, Gadian DG, Ordidge RJ, Thomas DL. In vivo Hadamard encoded continuous arterial spin labeling (H-CASL). *Magn Reson Med.* 2010;63:1111-1118.
12. Dai W, Shankaranarayanan A, Alsop DC. Volumetric measurement of perfusion and arterial transit delay using Hadamard encoded continuous arterial spin labeling. *Magn Reson Med.* 2013;69:1014-1022.
13. Teeuwisse WM, Schmid S, Ghariq E, Veer IM, Van Osch MJP. Time-encoded pseudocontinuous arterial spin labeling: basic properties and timing strategies for human applications. *Magn Reson Med.* 2014;72:1712-1722.
14. Parker DL, Goodrich KC, Roberts JA, et al. The need for phase-encoding flow compensation in high-resolution intracranial magnetic resonance angiography. *J Magn Reson Imaging.* 2003;18:121-127.
15. Hennig J, Nauerth A, Friedburg H. RARE imaging: a fast imaging method for clinical MR. *Magn Reson Med.* 1986;3:823-833.
16. Chappell MA, Groves AR, Whitcher B, Woolrich MW. Variational Bayesian inference for a nonlinear forward model. *IEEE Trans Signal Process.* 2009;57:223-236.
17. Groves AR, Chappell MA, Woolrich MW. Combined spatial and non-spatial prior for inference on MRI time-series. *Neuroimage.* 2009;45:795-809.
18. Elsayed M, Sammani F, Hamdi A, Al-Baser A, Babalghoom H. A new method for full reference image blur measure. *Int J Simul Syst Sci Technol.* 2018;19:4.
19. R Core Team. *R: A Language and Environment for Statistical Computing. Foundation for Statistical Computing.* Vienna, Austria: R Foundation for Statistical Computing; 2020. <https://www.R-project.org/>. Accessed March 12, 2021.
20. Vidorreta M, Wang Z, Rodriguez I, Pastor MA, Detre JA, Fernández-Seara MA. Comparison of 2D and 3D single-shot ASL perfusion fMRI sequences. *Neuroimage.* 2013;66:662-671.
21. Wang J, Alsop DC, Song HK, et al. Arterial transit time imaging with flow encoding arterial spin tagging (FEAST). *Magn Reson Med.* 2003;50:599-607.
22. Le TT, Fischbein NJ, André JB, Wijman C, Rosenberg J, Zaharchuk G. Identification of venous signal on arterial spin labeling improves diagnosis of dural arteriovenous fistulas and small arteriovenous malformations. *Am J Neuroradiol.* 2012;33:61-68.
23. Wolf RL, Wang J, Detre JA, Zager EL, Hurst RW. Arteriovenous shunt visualization in arteriovenous malformations with arterial spin-labeling MR imaging. *Am J Neuroradiol.* 2008;29:681-687.
24. van Osch MJP, Teeuwisse WM, Chen Z, Suzuki Y, Helle M, Schmid S. Advances in arterial spin labelling MRI methods for measuring perfusion and collateral flow. *J Cereb Blood Flow Metab.* 2018;38:1461-1480.
25. Chappell MA, MacIntosh BJ, Donahue MJ, Günther M, Jezzard P, Woolrich MW. Separation of macrovascular signal in multi-inversion time arterial spin labelling MRI. *Magn Reson Med.* 2010;63:1357-1365.

SUPPORTING INFORMATION

Additional Supporting Information may be found online in the Supporting Information section.

FIGURE S1 Two representative slices for all postlabeling delays (PLDs) and readout schemes in sagittal view

FIGURE S2 A, Arterial blood volume (aBV) maps quantified from the time-encoded pseudo-continuous arterial spin labeling (pCASL) data in a representative subject. Color bar shows aBV range in mL/100 g. B, The aBV maps quantified from the time-encoded pCASL data for each different flow compensation (FC) level. Color bar shows aBV range in mL/100 g

FIGURE S3 A, Cerebral blood flow (CBF) maps quantified from the time-encoded pCASL data in a representative subject for the different readouts. Color bar shows CBF range in mL/100 g/min. B, The CBF maps quantified from the time-encoded pCASL data for each different FC level. Color bar shows the CBF range in mL/100 g

FIGURE S4 Two representative slices for all PLDs and each FC level acquired

How to cite this article: Paschoal AM, Leoni RF, Pastorello BF, van Osch MJP. Three-dimensional gradient and spin-echo readout for time-encoded pseudo-continuous arterial spin labeling: Influence of segmentation factor and flow compensation. *Magn Reson Med.* 2021;00:1-9. <https://doi.org/10.1002/mrm.28807>

46 Autoria de artigos completos publicados em jornais e revistas de circulação nacional e internacional na sua área

Esta subseção apresenta o comprovante da autoria do artigo publicado na revista internacional *Journal of Neural Engineering* no ano de 2021.

Journal of Neural Engineering



PAPER

RECEIVED
26 November 2019

REVISED
28 May 2021

ACCEPTED FOR PUBLICATION
4 June 2021

PUBLISHED
22 June 2021

Semantic verbal fluency brain network: delineating a physiological basis for the functional hubs using dual-echo ASL and graph theory approach

André Monteiro Paschoal^{1,2,*} , Pedro Henrique Rodrigues da Silva², Carlo Rondinoni², Isabella Velloso Arrigo², Fernando Fernandes Paiva³ and Renata Ferranti Leoni²

¹ LIM44, Instituto e Departamento de Radiologia, Faculdade de Medicina, Universidade de São Paulo, São Paulo, Brazil

² Inbrain Lab, Department of Physics, FFCLRP, University of São Paulo, Ribeirão Preto, Brazil

³ Institute of Physics of São Carlos, University of São Paulo, São Carlos, Brazil

* Author to whom any correspondence should be addressed.

E-mail: andre.paschoal@usp.br

Keywords: brain connectivity, cerebral blood flow, dual-echo readout, functional ASL, language network

Supplementary material for this article is available [online](#)

Abstract

Objective. Semantic verbal fluency (SVF) is a cognitive process that engages and modulates specific brain areas related to language comprehension and production, decision making, response inhibition, and memory retrieval. The impairment of the brain network responsible for these functions is related to various neurological conditions, and different strategies have been proposed to assess SVF-related deficits in such diseases. In the present study, the concomitant changes of brain perfusion and functional connectivity were investigated during the resting state and SVF task performance. **Approach.** Arterial spin labeling (ASL), a perfusion-based magnetic resonance imaging (MRI) method, was used with a pseudocontinuous labeling approach and dual-echo readout in 28 healthy right-handed Brazilian Portuguese speakers. The acquisition was performed in a resting state condition and during the performance of a SVF task. **Main results.** During task performance, a significant increase in cerebral blood flow (CBF) was observed in language-related regions of the frontal lobe, including Brodmann's areas 6, 9, 45, and 47, associated with semantic processing, word retrieval, and speech motor programming. Such regions, along with the posterior cingulate, showed a crucial role in the SVF functional network, assessed by seed-to-voxel and graph analysis. Our approach successfully overcame the generalization problem regarding functional MRI (fMRI) graph analysis with cognitive, task-based paradigms. Moreover, the CBF maps enabled the functional assessment of orbital frontal and temporal regions commonly affected by magnetic susceptibility artifacts in conventional T2*-weighted fMRI approaches. **Significance.** Our results demonstrated the capability of ASL to evaluate perfusion alterations and functional patterns simultaneously regarding the SVF network providing a quantitative physiological basis to functional hubs in this network, which may support future clinical studies.

1. Introduction

Verbal fluency (VF) is a cognitive function that allows retrieving specific semantic or phonemic information within restricted searching parameters [1, 2]. More specifically, semantic verbal fluency (SVF) typically involves generating words belonging to a given category. The cognitive processing associated with the SVF is supposed to engage and modulate

specific brain areas related to language comprehension and production, decision making, response inhibition, and memory retrieval [3]. The impairment of the brain network responsible for these functions is related to several neurological conditions, such as Alzheimer's disease [4], Parkinson's disease [5], attention-deficit/hyperactivity disorder [6], epilepsy [7], and schizophrenia [8]. Therefore, different strategies have been employed to assess SVF-related

deficits related to them. They include the applications of neuropsychological tests [9] and neuroimaging techniques [3] in both clinical and investigational domains.

Functional neuroimaging studies have demonstrated the specialization of brain areas, mainly in frontal, parietal, and temporal lobes, for SVF processing [10, 11]. A recent meta-analysis reported left frontal areas along with left anterior cingulate (AC), thalamus, and precuneus as the central regions involved with word production, attentional demands, and working memory [3]. Other studies have also discussed the role of the temporal cortex, which is believed to mediate semantic-based word retrieval [11, 12]. A recent study confirmed its involvement with SFV in investigating the effects of cortical excitability modulation with transcranial direct current stimulation [13]. However, more than locating SFV-related regions, it is desirable to investigate how they are integrated. A dual-stream model consisted of ventral and dorsal pathways for language proposed that the dorsal route, which connects regions of the frontal lobe, is restricted to sensory-motor mapping of sound to articulation. In contrast, the ventral pathway, connecting the middle temporal lobe and the prefrontal cortex, subserves linguistic processing of sound to meaning [14]. The ventral regions are also highly connected during resting-state, representing a semantic network and facilitating neuronal activation during semantic-based tasks [15].

Moreover, recent studies have used graph theory analysis (GTA) to assess the topology of brain networks. They have reported that semantic, phonological, and orthographic networks have small-world characteristics defined by short average path lengths between nodes and high local clustering [16]. Regions of the anterior temporal lobe and inferior frontal cortex, including Broca's area, were reported as hubs in functional brain networks related to language processing [17, 18]. Also, graph analysis seems likely to become clinically relevant in neurology and psychiatry. It was useful to differentiate between mild cognitive impairment and Alzheimer's disease and assess atypical hemispheric dominance in brain tumors, evaluating functional connections in the language-related network [19, 20].

Many SVF studies have used functional magnetic resonance imaging (fMRI) based on the blood oxygen level-dependent (BOLD) contrast, given its fair compromise between spatial and temporal resolution and high sensitivity to neuronal-related hemodynamic changes [21]. However, BOLD contrast depends on a complex combination of blood oxygenation, cerebral blood volume, cerebral blood flow (CBF), and metabolic rate of oxygen, which may hinder the analysis of different diseases. On the other hand, assessing a single physiological parameter such as CBF, which is tightly coupled with glucose metabolism [22], is

an appealing alternative for providing a novel perspective on the physiological basis underlying functional connectivity changes in the healthy and damaged brain.

Arterial spin labeling (ASL) has shown its advantages as a magnetic resonance (MR) perfusion-weighted technique. Besides being noninvasive, ASL shows tissue specificity [23] and, to some degree, is insensitive to susceptibility artifacts [24]. Perfusion-weighted images are achieved using the arterial blood as an endogenous tracer, magnetically labeled by the application of radiofrequency pulses. The pulses are applied in a strategic position (labeling plane), so the magnetization in the region of interest (ROI) is altered compared to a non-labeled condition [25, 26]. CBF is then estimated from the subtraction between unlabeled images (ASL control images) and labeled images. Due to the ASL intrinsic low signal-to-noise ratio, multiple unlabeled-label pairs are acquired and averaged to quantify CBF [27]. Moreover, the temporal series of ASL images allows the evaluation of CBF fluctuations over time, from which functional information can be estimated [21, 27, 28].

The investigation of the functional organization through ASL has two main advantages over BOLD-fMRI. First, ASL provides quantitative information about a single physiologic parameter (CBF) [29, 30]. Second, ASL has a better spatial specificity to neuronal activity because its signal originates in the capillary bed [31–35]. However, it is not as sensitive to hemodynamic alterations as BOLD-fMRI. Therefore, simultaneous BOLD and ASL sequences have been proposed [36–38]. In this context, ASL, combined with a dual-echo readout (DE-ASL), is an emerging approach to optimize the acquisition aiming at both CBF quantification and functional analysis [39]. Acquisition using short echo time (TE) provides perfusion-weighted images, while the use of longer TE increases the effect of transversal relaxation ($T2^*$), typical of the BOLD contrast [27, 40]. The BOLD signal measured from ASL images is called the concurrent BOLD (ccBOLD).

Therefore, a simultaneous BOLD-CBF analysis was performed to assess the brain functional connectivity of the SVF-related network in healthy participants. Both cognitive and resting-state runs were used to evaluate brain connectivity changes, as evidenced by CBF and ccBOLD signals. A single perfusion-based ASL acquisition with dual-echo readout was used to ensure the same state during task engagement for BOLD and CBF responses. No similar study was previously reported for a cognitive task. Therefore, our objectives were to demonstrate the feasibility and advantages of performing this method to investigate the physiological basis underlying the functional organization of the SVF network; and investigate the alterations in the SVF network from resting-state to task performance. We

Table 1. Data acquisition parameters.

	3D T1W	DE-pCASL	M0	3D TOF	3D FLAIR
FOV (mm ²)	240 × 240	240 × 240	240 × 240	200 × 180	240 × 240
Spatial resolution (mm ²)	1 × 1	3.75 × 3.75	3.75 × 3.75	0.45 × 0.63	1 × 1
Slice thickness (mm)	1	5	5	1.1	3
Number of slices	180	20	20	96	180
TR (ms)	7	4000	4000	20	5000
TE (ms)	3.2	(TE1/TE2) 9/28	14	3.45	324.21
FA (degrees)	8	90	90	20	90
Labeling duration (ms)	—	1550	—	—	—
Post-labeling delay (ms)	—	1600	—	—	—
Total scan time (min)	5.98	(RS/task) 4.4/6.8	1.5	3.58	3.45

hypothesize that CBF and frontal cortex (FC) changes will mainly involve the classical word production SVF-related regions, such as the left frontal and temporal regions.

2. Material and methods

2.1. Subjects

Twenty-eight healthy right-handed Brazilian Portuguese speakers were recruited. Exclusion criteria included: abuse of alcohol or illicit drugs, verified by the CAGE questionnaire (O'Brien 2008); previous experience with the cognitive test within less than 6 months; language other than Portuguese; psychiatric disorders; the presence of partial or total carotid artery stenosis, unilateral or bilateral; the presence of brain injury from stroke or tumor; the presence of pacemaker or prosthesis incompatible with the MR environment; claustrophobia; visual deficits; and pregnancy. Gender, age, and education years were obtained from a demographic questionnaire. Cognitive status was assessed by the Mini-Mental State Examination—Expanded Version (MMSE-2EV) [41]. Participants showed no cognitive impairment (MMSE-2EV: 60 ± 6). The Ethics Committee of the institution approved the study, and all participants gave their written informed consent before participating in the study.

2.2. Image acquisition and protocol

Images were acquired on a 3T MRI scanner (Philips Healthcare, Best, Netherlands) equipped with a 32-channel receive head coil. The complete protocol consisted of 3D T1-weighted TFE images, DE-ASL images under resting state and task performance. Proton-density-weighted images (M0) and 3D-TOF (time of flight), and axial FLAIR (fluid-attenuated inversion recovery), which were acquired with clinical protocols of the institution to confirm the absence of arterial occlusions and brain lesions, respectively. The acquisition parameters for all the sequences are reported in table 1.

The experimental protocol was divided into two runs: one consisting of a block-designed paradigm alternating a SVF task and a control condition, and

another consisting of a 6 min run at resting-state. For the task-based experiment [42], one category (among animals, colors, sports, and foods) was presented for each task block, and the participants were asked to think about words related to that category. During the control condition, participants were asked to read the months of the year presented randomly on a screen. Each block lasted 32 s (eight image volumes), totaling four blocks of rest and four blocks of tasks. Commands were developed in PsychoPy software [43] and presented on a monitor positioned in front of the MR scanner. Participants viewed the monitor through a mirror system placed on the head coil. During the resting-state run, participants were asked to stay still with their eyes open in the absence of any specific thought or intention. Instead of including a rest condition between the task and control blocks, we chose to run a separate resting-state sequence to compare the task condition with the classical resting-state fMRI.

2.3. Image preprocessing

Imaging preprocessing was performed using customized scripts in MATLAB (MathWorks, Natick, MA), SPM12 (www.fil.ion.ucl.ac.uk/spm), and an open-source toolbox for ASL images (ASLtbx) [44]. Preprocessing steps were applied to each participant's data separately. First, raw ASL images were head-motion corrected, considering the middle image of the time series as reference. No image dataset was excluded because of the incorrigible motion artifact. Then, ASL images were coregistered to M0 and T1-weighted anatomical images, followed by a temporal filtering (high pass > 0.04 Hz) and spatial smoothing using an isotropic Gaussian kernel (FWHM = 4 mm for CBF quantification and FWHM = 6 mm for functional analysis). Furthermore, T1-weighted anatomical images were segmented into gray matter, white matter, and cerebrospinal fluid (CSF).

2.4. CBF quantification

Perfusion maps were generated by subtracting unlabeled and label images acquired with the short TE (= 9 ms). Quantification was performed using the sinc subtraction for regional CBF

mapping, while a running pairwise subtraction was performed for functional analysis to increase the number of perfusion-weighted images in the time series [45]. Quantification was based on the General Kinetic Model [29] using the following parameters: blood longitudinal relaxation time ($T1b$) = 1650 ms; labeling efficiency = 0.85; blood-/tissue water partition coefficient (gray matter/white matter) = 0.98/0.84 g ml⁻¹; tissue $T1$ (gray matter/white matter) = 1020/770 ms [46]. Finally, CBF time series and mean CBF map were normalized to the MNI standard space (resolution = $2 \times 2 \times 2$ mm³; matrix size: $79 \times 95 \times 79$).

2.5. Functional localization analysis

Functional analysis for resting-state and task conditions was performed using the time series of CBF and ccBOLD. The latter was obtained from the residual $T2^*$ weighting of the ASL images acquired with long TE (= 28 ms), regressing out the paradigm of the labeling and unlabeled $[-1, 1, \dots, -1, 1]$ from the label/unlabeled image series [47]. CBF and ccBOLD time series were detrended and band-pass filtered (0.01–0.07 Hz for CBF; 0.0078–0.1 Hz for ccBOLD) [37]. A standard principal component analysis was used together with the CompCor algorithm [48] to remove the signal of white matter and CSF.

A general linear model analysis using the FSL (<http://fsl.fmrib.ox.ac.uk/fsl/fslwiki>) was performed on each participant's data to check the activation map obtained from CBF and ccBOLD ($p\text{-FDR} < 0.05$). The resulting maps were then compared with an anatomical template derived from the meta-analysis of different language tasks and fMRI [3]. After overlapping the activated regions of our GLM maps and the template from the meta-analysis, six anatomical brain regions in the left hemisphere were coincident: superior frontal gyrus (SFG)—Brodmann area (BA) 6 and BA8; medial frontal gyrus (MFG)—BA6; inferior frontal gyrus (IFG)—BA9, BA45 and BA47. They were selected for further analysis along with the posterior division of the left middle temporal gyrus (pMTG)—BA21 and the posterior division of the left superior temporal gyrus (pSTG)—BA22. These regions are called SVF-related in the remaining of the text. Additionally, four nodes of the default mode network (DMN) and the cingulate gyrus (anterior and posterior divisions) were assessed (supplementary material—table 1 (available online at stacks.iop.org/JNE/18/046089/mmedia)). The additional regions were included due to the recent literature on SVF tasks [49].

The mean CBF value of each region was obtained for three conditions: resting-state, control, and SVF. A two-way ANOVA with repeated measures was performed to assess the effects of region and condition on CBF, considering significance at $p < 0.05$. A Tukey posthoc analysis was performed to evaluate

CBF changes among conditions for each ROI, considering multiple comparisons and significance at $p < 0.05$. This statistical analysis was performed in R software [50].

A seed-to-voxel analysis was performed using CONN Toolbox [51], considering the SVF-related regions (supplementary material—table 1, regions 1–8) as seeds for the task-based data. First, CBF and ccBOLD were considered separately, and then the main effects of each one were analyzed to obtain a single map from both imaging modalities. For the three cases, a bivariate Pearson's correlation on r -values transformed to z -scores was performed. Significant correlations after correction for multiple comparisons and a cluster size cut-off (two-sided $p\text{-FDR} < 10^{-11}$, $k \geq 10$ for CBF and ccBOLD separately; two-sided $p\text{-FDR} < 10^{-13}$, $k \geq 10$ for CBF and ccBOLD main effects) were shown in a spatial map. Surface maps were plotted using the standard template of CONN toolbox, the Freesurfer fsaverage surfaces.

The laterality index to verify the hemispheric dominance of SVF function and the degree of clustering to assess the spatial layout of the obtained maps were calculated since meaningful processes tend to exhibit a well-defined spatial structure [52]. The laterality index was defined as $LI = (VLH - VRH)/(VLH + VRH)$, where VLH and VRH are the numbers of significant voxels in the left and right hemispheres of the obtained spatial maps, respectively. Left ($LI > LITH$) and right ($LI < -LITH$) dominances were assessed considering an LI threshold ($LITH$) of 0.2 [53]. The degree of clustering was defined as $DCi = Nclu/Ntot$ for each obtained cluster i , where $Nclu$ is the number of significant voxels of cluster i , and $Ntot$ is the total number of significant voxels in the spatial map [54].

2.6. Functional integration analysis

First, an ROI-to-ROI analysis was performed considering the CBF and ccBOLD data separately for both SVF task and resting-state conditions. Then, for a combined analysis of CBF and ccBOLD, the ROI-to-ROI analysis was performed considering both data ($p\text{-FDR} = 0.05$, two-sided). For all cases, a bivariate Pearson's correlation on r -values transformed to z -scores was performed and checked the significance correcting for multiple comparisons.

2.7. Inter-subject variability

The inter-subject variability was assessed for each condition (i.e. CBF-rest, ccBOLD-rest, CBF-task, and ccBOLD-task) in all activated regions. To calculate the variability, a correlation was performed between the time-series of each eight SVF-related ROIs and the seven remaining ROIs, which resulted in a vector of correlations for every ROI. Next, for all the ROIs, another correlation was done among the 28 subjects for all the conditions [55]. A two-way

ANOVA with repeated measurements was employed to assess the difference between the inter-subject variability in the different conditions. The significance level was considered $p < 0.05$ corrected for multiple comparisons using Tukey's method.

2.8. GTA

Graph analysis was performed using the Graph toolbox implemented in CONN [51]. The topological structure of the functional brain network organization during the performance of the SVF task was analyzed to verify whether a small-world topology was satisfied for CBF, ccBOLD, and combined CBF and ccBOLD data. The determination of the cut-off threshold was performed based on the approach of a previously reported study [56], as well as the analysis was run in two different templates separately.

Template 1: ROIs previously used for functional integration analysis (supplementary material—table 1).

Template 2: Functional templates of the resting-state networks available in CONN toolbox and composed by the DMN, sensory-motor network (SMN), visual network, salience network (SAN), dorsal attention network, frontal-parietal network, language network (LAN), cerebellar network, and their subdivisions, totaling 32 nodes (supplementary material—table 2). This template comprised a whole-brain network and was used for exploratory analysis of the brain organization during the SVF task.

The next step was constructing a weighted adjacency matrix for each template and thresholding them over a range of r -values in steps of 0.01. Since there is no consensus on the most accurate approach for such thresholding [57], the following criteria to define the r -value range [56] were considered. First, the experimental network should be fully connected, i.e. every node should be integrated into the network by at least one edge [58]. Second, the experimental network should meet the criteria for a small-world network, as expected from a group of young participants [59]. Finally, the experimental network should be as cost-efficient as possible, i.e. it should have the lowest connection density while keeping the same efficiency. Therefore, its wiring cost should not exceed the value of 0.5 [60].

The small-world network considering two main criteria was also analyzed. First, the range in which the global efficiency of the experimental network approximates the global efficiency of an equivalent random network and, second, when its local efficiency surpasses that of an equivalent random network [61]. The analysis considering all criteria described above was used to find the range of r -values (Fisher transformed) for thresholding. The following parameters were calculated over the obtained range: clustering coefficient, local efficiency, characteristic path length, global efficiency, degree, and betweenness centrality

(BC) [61–63]. Nodes with degree and BC values at least one standard deviation above the average values for the network were considered hubs.

All graph metrics were compared to assess the differences between the resting-state and SVF task. First, variable homoscedasticity was tested with the Shapiro-Wilk normality test (two-sided $p < 0.05$). For normal variables, a parametric t -test for two independent means was used. For non-normal variables, it was used non-parametric Mann-Whitney U -test (two-sided $p < 0.05$).

3. Results

3.1. CBF changes

Figure 1 shows the mean CBF values for all ROIs comparing resting-state, control condition, and SVF task performance. No region showed CBF differences when comparing the control condition with the other two conditions (SVF and resting-state). CBF differences were significant between SVF and resting-state conditions for the SFG (SFG—BA8, $p = 0.0134$; BA6, $p = 0.0067$), MFG (MFG—BA6; $p = 0.0214$), and IFG (IFG—BA45, $p = 0.0061$; BA9, $p = 0.0256$; BA47, $p = 0.0025$).

3.2. Seed-to-voxel analysis

Functional maps obtained from ccBOLD (figure 2(a)) and CBF (figure 2(b)) showed responses mostly in the left hemisphere during the SVF task, confirming the lateralization of this function. Responses were more lateralized for ccBOLD ($LI = 0.65$) compared to CBF ($LI = 0.46$), but no difference was observed regarding degree of clustering ($CBF - DC = 0.017$, $ccBOLD - DC = 0.022$; $p > 0.05$). Moreover, ccBOLD map showed a more extended response in the parietal lobule, while the CBF map showed a more extended response in the middle temporal gyrus, Heschl's gyrus, planum temporale, and insular cortex. When considering CBF and ccBOLD information simultaneously (figure 2(c)), it resulted in left lateralization ($LI = 0.47$) and degree of clustering similar to the other maps ($DC = 0.018$).

3.3. ROI-to-ROI analysis

Figure 3 shows the functional connectivity patterns for the SVF network compared to the resting-state (SVF task $>$ resting-state). Results from ccBOLD (figure 3(a)) showed the IFG (BA9) connected to the Broca's area (IFG—BA47) and the posterior portion of the superior temporal gyrus. Moreover, connections among DMN regions were observed. Functional connectivity obtained from CBF (figure 3(b)) showed the AC connected to pMTG and PC. Finally, the SVF-related network, when considering the main effects of CBF and ccBOLD together (figure 4), showed the IFG-BA9 as an essential node, connecting

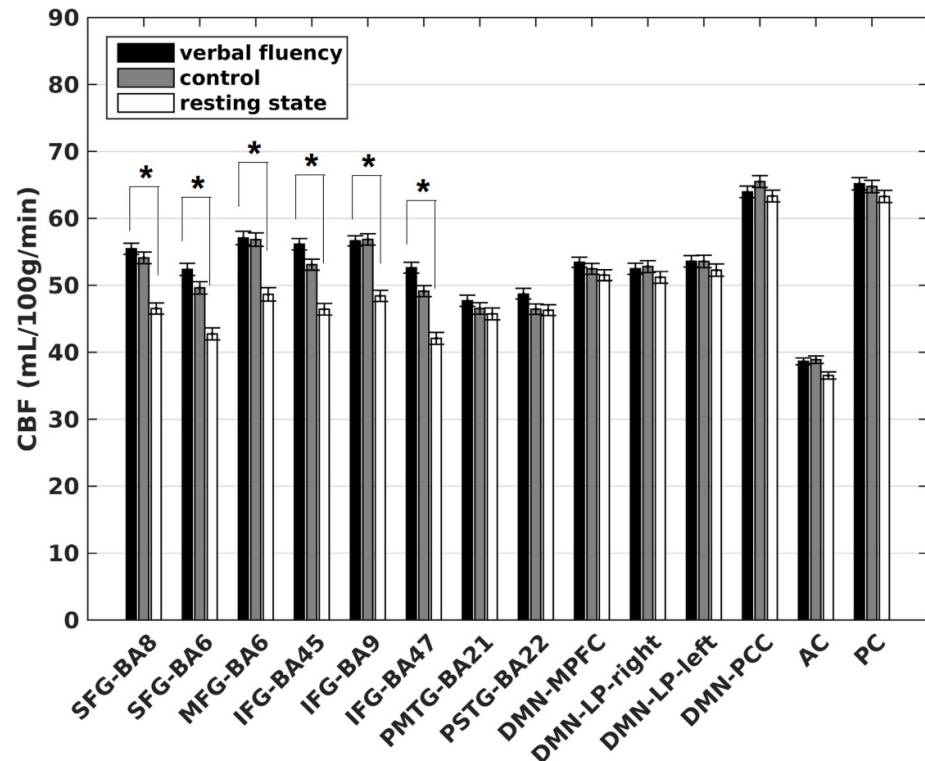


Figure 1. Regional CBF. Mean CBF values ($\text{ml}/100 \text{ g min}^{-1}$) of each ROI for SVF (black), control (gray), and resting-state (white) conditions. A two-way ANOVA with repeated measures was performed to assess the effects of region and condition on CBF. A Tukey posthoc analysis was performed to assess CBF changes among conditions for each ROI. * $p < 0.05$, corrected for multiple comparisons. SFG: superior frontal gyrus, MFG: medial frontal gyrus, IFG: inferior frontal gyrus, pMTG: middle temporal gyrus—posterior division, pSTG: superior temporal gyrus—posterior division, DMN: default mode network. MPFC: medial prefrontal cortex, LP: lateral parietal, PCC: posterior cingulate cortex, AC: anterior cingulate, PC: posterior cingulate.

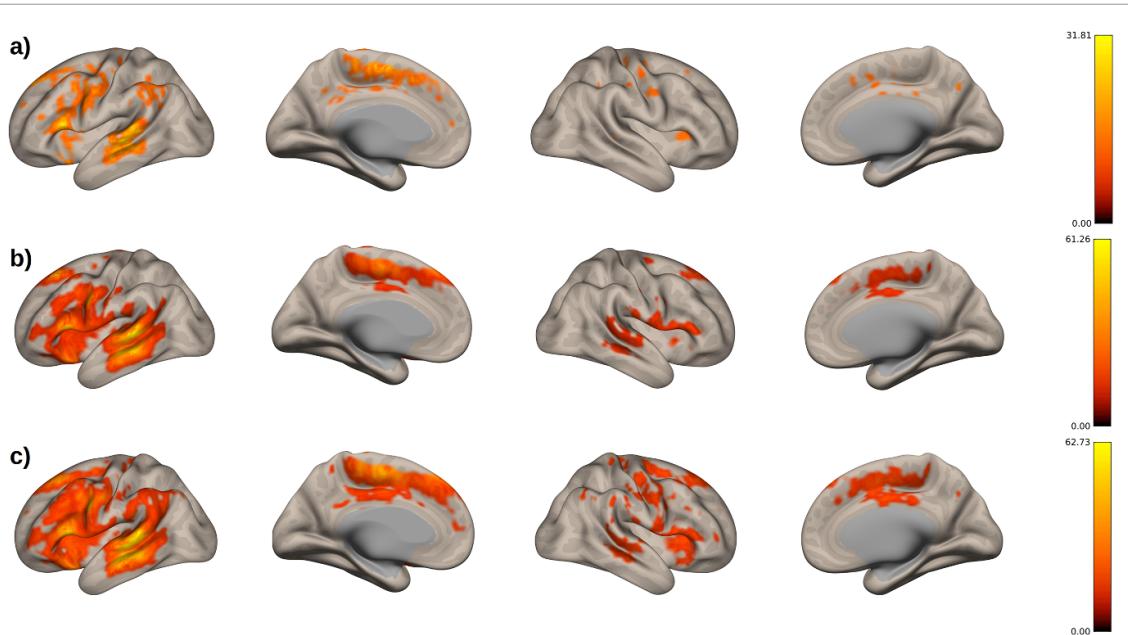


Figure 2. Functional localization. Functional maps of the SVF task for (a) ccBOLD ($p\text{-FDR} < 10^{-11}, k \geq 10$), (b) CBF ($p\text{-FDR} < 10^{-11}, k \geq 10$) and (c) combined CBF and ccBOLD time series ($p\text{-FDR} < 10^{-13}, k \geq 10$). Color bars represent F -values.

inferior frontal and temporal regions and the connections among DMN regions. This conjunction analysis showed a more integrated network when compared to the findings depicted in figure 3.

3.4. Inter-subject variability

Figure 5 shows the mean inter-subject variability values for all SVF-related ROIs comparing the CBF and ccBOLD time-series for task and resting-state

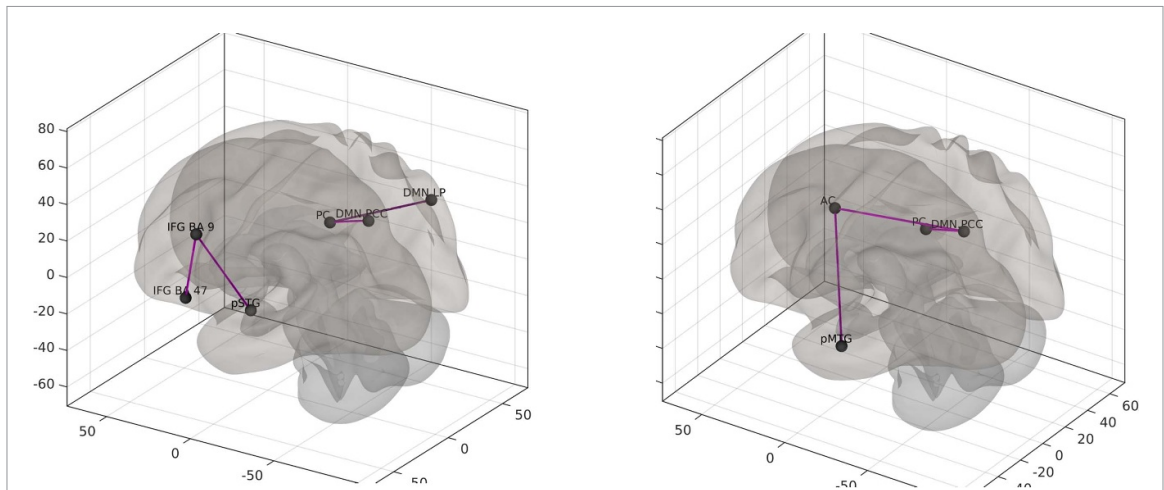


Figure 3. Functional connectivity. ROI-to-ROI functional connectivity patterns for (a) ccBOLD, and (b) CBF. Significance was set to $p < 0.05$, FDR-corrected (two-sided for ccBOLD and one sided for CBF).

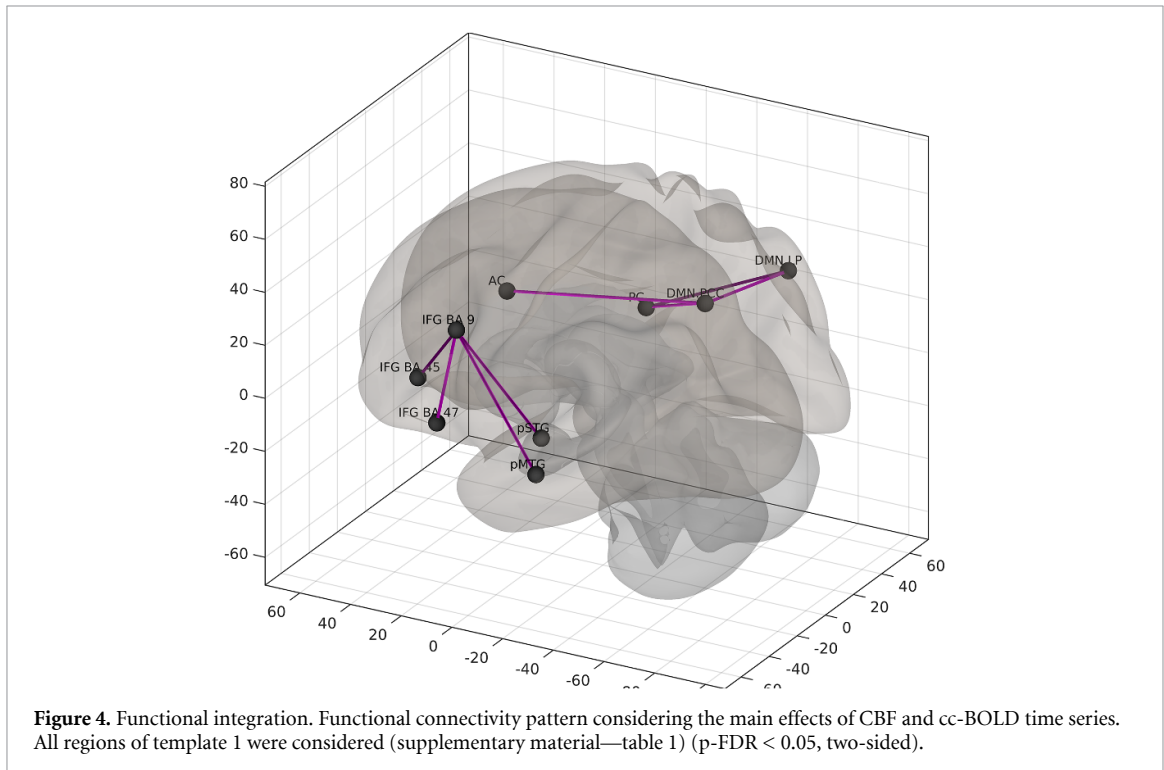


Figure 4. Functional integration. Functional connectivity pattern considering the main effects of CBF and cc-BOLD time series. All regions of template 1 were considered (supplementary material—table 1) (p -FDR < 0.05 , two-sided).

conditions. Differences in the variability were significant between CBF-task and all other conditions for SFG—BA8; ccBOLD-task and all other conditions for MFG—BA6; between CBF-task and CBF-rest and ccBOLD-task for IFG—BA45; CBF-rest and CBF-task for IFG—BA47; and between ccBOLD-rest and CBF-rest and ccBOLD-task.

4. Graph analysis

4.1. Small-world networks

During resting-state and SVF tasks, our empirical data network met all criteria for small-worldness when considering CBF, ccBOLD, and CBF-ccBOLD time series for both templates. Table 2 presents the

respective r -value ranges for such cases. For illustration, figure 6 shows the obtained graphs for combined CBF-ccBOLD data, indicating the intervals of costs where the networks present small-world characteristics when template 2 was used.

4.2. Graph metrics

Table 3 presents the graph metrics calculated from data obtained with CBF, ccBOLD, and the combination of CBF and ccBOLD information for both resting-state and task conditions, using templates 1 and 2, and the respective r -value ranges obtained for small-wordness criteria (table 2).

For template 1, local and global efficiency, degree and cost decreased significantly when considering

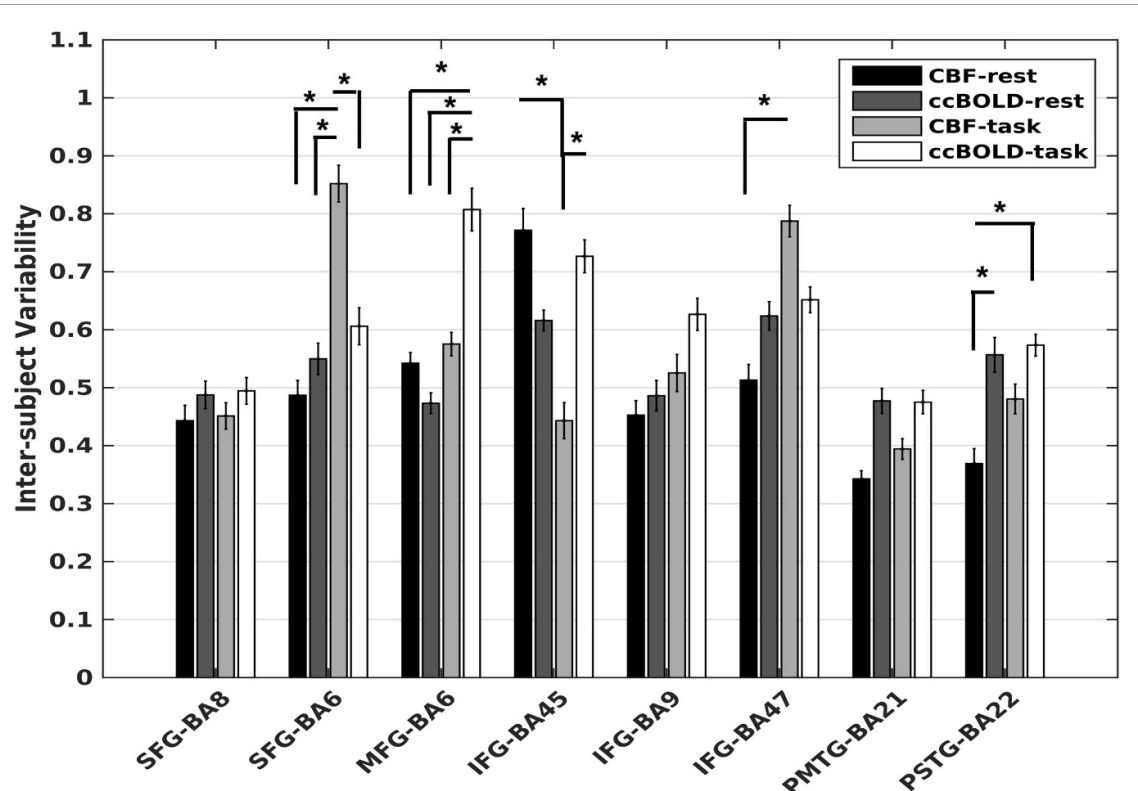


Figure 5. Inter-subject variability. Mean inter-subject variability of each ROI for CBF-rest (black), ccBOLD-rest (dark gray), CBF-task (light gray) and ccBOLD-task (white) conditions. A two-way ANOVA with repeated measures was performed to assess the effects of region and condition on inter-subject variability. A Tukey posthoc analysis was performed to assess CBF changes among conditions for each ROI. * $p < 0.05$, corrected for multiple comparisons.

Table 2. R -value ranges, where the empirical data shows small-world characteristics.

	Resting-state condition				SVF task			
	Template 1		Template 2		Template 1		Template 2	
	r_{\min}	r_{\max}	r_{\min}	r_{\max}	r_{\min}	r_{\max}	r_{\min}	r_{\max}
ccBOLD	0.35	0.52	0.31	0.50	0.41	0.52	0.37	0.58
CBF	0.32	0.35	0.26	0.46	0.34	0.40	0.31	0.56
CBF-ccBOLD	0.32	0.39	0.29	0.46	0.38	0.46	0.35	0.56

r_{\min} : minimum r -value; r_{\max} : maximum r -value.

the CBF time-series, while all graph metrics showed statistically significant differences when considering CBF-ccBOLD time-series conjointly. For template 2, when combining both imaging categories, the global efficiency, BC, and cost decreased significantly, while the average path length and degree increased when comparing the resting-state condition and the SVF task performance.

Moreover, for template 2, regions that constitute the SMN, LAN established hubs during the resting-state condition, while regions of the DMN, SAN, LAN were hubs during task performance (table 4). The left IFG portion of LAN englobes part of the IFG-BA47 node, while both the superior node of SMN overlap with part of the SFG-BA6. In contrast, no functional hubs were found for template 1 when using the three time series (CBF, ccBOLD, and the combination of both) (figure 7).

5. Discussion

In the present study, the SVF network in healthy controls was evaluated using a dual-echo ASL acquisition, allowing the quantification of CBF and functional connectivity assessment concomitantly, which provided a physiological basis to our functional findings.

When comparing task performance with the resting-state condition, an increase in CBF was observed in language-associated regions in the frontal lobe, mainly in the inferior (BA 9, 45, and 47) and superior (BA 6 and 9) frontal gyri. These areas are associated with semantic [46, 47, 64] and phonological processing [51] and encoding [37, 48]. Broca's area (IFG—BA45) is involved in generating words and working memory during tasks similar to ours [27, 29, 30]. Moreover, a PET study reported that SFG

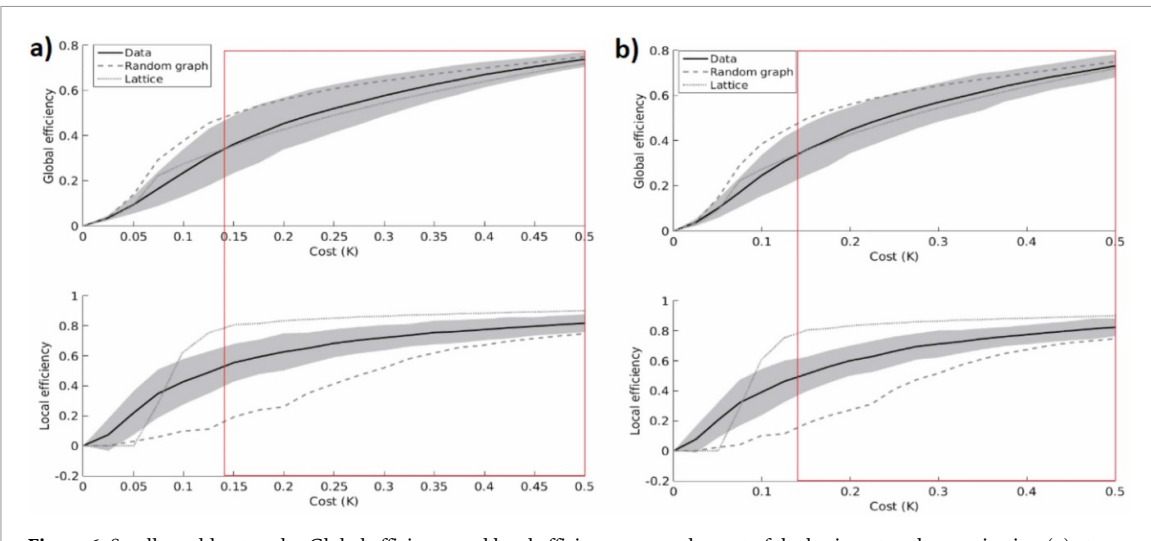


Figure 6. Small-world networks. Global efficiency and local efficiency versus the cost of the brain network organization (a) at resting-state and (b) task performance using template 2. Combined CBF-ccBOLD data was considered. Red rectangles indicate the regions where the networks present small-world characteristics.

is related to word retrieval [65], while a previous BOLD study reported its activation during an overt speech [66]. The significant CBF change in such a region during our covert word production task seems to be associated with word retrieval and speech motor programming. However, these areas did not show CBF increase when comparing the SVF task with the control condition, probably because these regions are also related to word reading, aloud or silently, as in our control task (reading the months of the year) [67, 68].

The functional connectivity maps obtained with the seed-to-voxel analysis showed similar spatial patterns when comparing CBF and ccBOLD data regarding left lateralization and response of the central SVF-related regions. However, the ccBOLD map showed response in a greater area of the superior frontal lobe and parietal lobule. These regions, associated with language processing and speech motor programming, were also found in CBF maps but in smaller clusters. On the other hand, the CBF map showed an extended response in the orbital part of the IFG and in the temporal gyrus, which encloses part of the LAN for comprehension and production, as identified in PET studies [58, 69]. Such areas are mostly affected by the signal loss at the interface of tissue and fluid/air due to local differences of magnetic susceptibility in conventional T2*-weighted fMRI approaches [17, 70]. The results obtained by DE-ASL overcame this issue, which suggests this method an appealing alternative to combine brain physiology and functionality in a non-invasive approach.

Additional connectivity findings include the anterior and posterior parts of the cingulate gyrus and parietal regions associated with transferring visual information to Wernicke's area and lexico-semantic processing of familiar words [71]. Moreover, the AC

is activated during word generation and related to the task attentional demands. It was recently reported that this region is critical in reducing distraction from irrelevant stimuli and driving attention toward specific sites [72].

An ROI-to-ROI analysis evaluated the changes in brain temporal functional connectivity patterns between resting-state and SVF conditions. For ccBOLD, the IFG-BA9 appeared as a connecting region, as previously reported [9]. On the other hand, although CBF can represent a more spatial specific localization of activation sites [73, 74], there were fewer significant connections and nodes, which did not include the SFV-related regions in the inferior and superior frontal gyri. Such a feature reinforced the lower sensitivity of CBF for such measurements, presenting a limitation of using only CBF for ROI functional connectivity analysis during a cognitive task.

Moreover, the combined CBF-ccBOLD analysis presented two separate networks. One is composed of classical language-related regions, including Wernicke's area, where the information from the stimulus is comprehended, and phonological retrieval happens [74], then transferred to frontal areas words are generated [75]. The other network includes the posterior nodes of the DMN and the anterior and posterior portions of the cingulate cortex. Such a network may be related to aspects of memory retrieval [76] in mnemonical conditions. SVF functional organization presented small-world characteristics, i.e. high local and global efficiencies. It reflects highly clustered networks with a small average path length, allowing rapid communication between any two network regions [59]. As expected, the most probable functional hubs were found in regions of the language and sensorimotor networks when considering the whole brain (template 2).

Table 3. Graph metrics (mean \pm SD) of the overall network for CBF, ccBOLD, and combined CBF-ccBOLD data.

Template 1											
CBF					ccBOLD						
	RS	Task	Statistics		RS	Task	Statistics		RS	Task	Statistics
Clustering coefficient	0.67 \pm 0.19	0.63 \pm 0.20	$U = 282, z = -1.79,$ $\dagger p = 0.07$	0.67 \pm 0.15	0.69 \pm 0.13	$t = 1.08, *p = 0.28$	0.68 \pm 0.18	0.62 \pm 0.11	$U = 1059, z = -2.96,$ $\dagger p = \mathbf{0.0031}$		
Local efficiency	0.75 \pm 0.21	0.70 \pm 0.22	$U = 267, z = -2.04,$ $\dagger p = \mathbf{0.041}$	0.75 \pm 0.16	0.78 \pm 0.13	$U = 351, z = 0.66,$ $\dagger p = 0.51$	0.76 \pm 0.19	0.73 \pm 0.11	$U = 1123, z = -2.59,$ $\dagger p = \mathbf{0.0096}$		
Global efficiency	0.645 \pm 0.19	0.48 \pm 0.24	$t = -2.85, *p = \mathbf{0.006}$	0.58 \pm 0.21	0.61 \pm 0.22	$t = 0.54, *p = 0.59$	0.64 \pm 0.21	0.51 \pm 0.13	$U = 887, z = -3.96,$ $\dagger p = \mathbf{0.0008}$		
Average path length	1.79 \pm 0.52	1.64 \pm 0.26	$U = 357, z = -0.56,$ $\dagger p = 0.57$	1.73 \pm 0.34	1.69 \pm 0.36	$t = -0.45, *p = 0.65$	1.67 \pm 0.37	2.08 \pm 0.32	$U = 647, z = 5.36,$ $\dagger p = \mathbf{0.00001}$		
BC	0.06 \pm 0.04	0.04 \pm 0.02	$U = 295, z = -1.58,$ $\dagger p = 0.11$	0.05 \pm 0.02	0.05 \pm 0.02	$t = -0.35, *p = 0.73$	0.05 \pm 0.02	0.03 \pm 0.01	$t = -5.66,$ $*p < \mathbf{0.00001}$		
Degree	5.89 \pm 2.78	4.41 \pm 2.83	$U = 268, z = -2.02,$ $\dagger p = \mathbf{0.043}$	5.09 \pm 2.57	5.55 \pm 2.82	$t = 0.64, *p = 0.52$	5.99 \pm 2.84	8.86 \pm 3.74	$t = 4.56,$ $*p = \mathbf{0.000013}$		
Cost	0.45 \pm 0.21	0.34 \pm 0.22	$U = 268, z = -2.02,$ $\dagger p = \mathbf{0.043}$	0.39 \pm 0.20	0.43 \pm 0.22	$t = 0.64, *p = 0.52$	0.46 \pm 0.22	0.29 \pm 0.12	$t = -5.25,$ $*p < \mathbf{0.00001}$		
Template 2											
CBF					ccBOLD					CBF-ccBOLD	
	RS	Task	Statistics		RS	Task	Statistics		RS	Task	Statistics
Clustering coefficient	0.65 \pm 0.10	0.63 \pm 0.12	$t = -0.44, *p = 0.66$	0.65 \pm 0.10	0.66 \pm 0.13	$t = 0.12, *p = 0.91$	0.67 \pm 0.20	0.64 \pm 0.13	$U = 1316, z = -1.46,$ $\dagger p = 0.14$		
Local efficiency	0.76 \pm 0.09	0.74 \pm 0.12	$U = 359, z = -0.53,$ $\dagger p = 0.59$	0.77 \pm 0.09	0.77 \pm 0.13	$U = 374, z = 0.29,$ $\dagger p = 0.77$	0.74 \pm 0.22	0.75 \pm 0.13	$U = 1412, z = -0.90,$ $\dagger p = 0.37$		
Global efficiency	0.59 \pm 0.11	0.54 \pm 0.11	$t = -1.73, *p = 0.089$	0.59 \pm 0.12	0.56 \pm 0.16	$t = -0.92, *p = 0.36$	0.63 \pm 0.22	0.55 \pm 0.14	$U = 1113, z = -2.64,$ $\dagger p = \mathbf{0.0083}$		
Average path length	1.97 \pm 0.35	2.01 \pm 0.32	$t = 0.45, *p = 0.65$	2.00 \pm 0.45	1.91 \pm 0.41	$U = 359, z = 1.51,$ $\dagger p = 0.13$	1.67 \pm 0.39	1.97 \pm 0.39	$U = 908, z = 3.84,$ $\dagger p = \mathbf{0.00012}$		

(Continued.)

Table 3. (Continued.)

	Template 2						CBF-ccBOLD		
	CBF		ccBOLD		Task		RS	Task	Statistics
	RS	Task	Statistics	RS	Task	Statistics			
BC	0.03 ± 0.01	0.03 ± 0.01	$U = 377, z = -0.24,$ $\dagger p = 0.81$	0.03 ± 0.01	0.02 ± 0.01	$U = 299, z = -0.53,$ $\dagger p = 0.60$	0.05 ± 0.03	0.03 ± 0.01	$U = 907, z = -3.84,$ $\dagger p = 0.00012$
Degree	10.6 ± 3.76	9.68 ± 3.91	$t = -0.95, * p = 0.35$	10.78 ± 4.35	10.72 ± 5.40	$t = -0.05, * p = 0.96$	5.92 ± 3.06	10.17 ± 4.92	$U = 757, z = 4.72,$ $\dagger p < 0.00001$
Cost	0.34 ± 0.12	0.31 ± 0.13	$t = -0.95, * p = 0.35$	0.35 ± 0.14	0.35 ± 0.17	$t = -0.05, * p = 0.96$	0.46 ± 0.23	0.33 ± 0.16	$U = 1074, z = -2.87,$ $\dagger p = 0.0041$

RS: resting-state; SD: standard deviation.

Compared to resting-state: * p calculated using the t -test for two independent means; $\dagger p$ calculated using Mann Whitney U -test. Significant differences in bold.

Table 4. Functional hubs obtained for template 2.

	Resting-state			Task		
	Region	BC	Degree	Region	BC	Degree
CBF	Left lateral (SMN)	0.050	16.30	Left Lateral (SMN)	0.043	14.63
	Right lateral (SMN)	0.047	16.00	Left SMG (SAN)	0.042	13.86
	Left pSTG (LAN)	0.053	16.35	Left pSTG (LAN)	0.051	15.17
ccBOLD + CBF	Left lateral (SMN)	0.048	13.50	Left pSTG (LAN)	0.049	15.13
	Right lateral (SMN)	0.046	13.19	—	—	—
	Left pSTG (LAN)	0.057	13.32	—	—	—

BC: betweenness centrality, SMN: sensory-motor network, LAN: language network, SAN: salience network. pSTG: posterior superior temporal gyrus, SMG: supramarginal gyrus.



Figure 7. Graphs metrics. Panels (A)–(G) illustrate the averaged graph metrics of the SVF network considering the combined CBF-ccBOLD information (r -value range: 0.38–0.46) during task condition. Red: the network mean values; blue: regions with a mean value higher than the average value for the network; light green: regions with equal or smaller values than the average value for the network. Error bars represent the standard error. SFG: superior frontal gyrus, MFG: medial frontal gyrus, IFG: inferior frontal gyrus, pMTG: middle temporal gyrus—posterior division, pSTG: superior temporal gyrus—posterior division, DMN: default mode network. MPFC: medial prefrontal cortex, LP: lateral parietal, PCC: posterior cingulate cortex, AC: anterior cingulate, PC: posterior cingulate.

The analysis of inter-subject variability revealed noteworthy findings when comparing CBF and ccBOLD functional connectivity results. First, the classical language areas, namely Broca (BA45) and Wernicke (BA22), showed differences in variability between subjects across conditions, which probably

points to the fact that under a language task, these key regions are engaged at most during processing. Furthermore, a lower inter-subject variability was found for CBF under task condition, pointing to a homogenous activity across the subjects. The variability can be justified considering that language can

be influenced by sex, education, cognitive strategy, or even physiological noise. Secondly, the regions whose CBF variation coincided with functional hubs (SFG-BA6 and IFG47), as observed in graph analysis results, also showed differences in variability across subjects. Beyond providing a physiological basis for SVF task-related functional hubs, the quantitative nature of the analysis and its lower inter-subject variability would make CBF fMRI a good technique for group comparisons.

Another approach used to verify the alterations in the whole-brain network from resting-state to task performance was the graph metrics. For this analysis, increases in the average path length and degree and decreases in the BC, global efficiency, and cost were observed when analyzing the combined CBF-ccBOLD. Previous resting-state fMRI studies pointed towards small-world topology [77], which is considered a characteristic of healthy subjects. However, graph analysis in task-based fMRI suffers from limited validity and generalization [41]. Therefore, we applied the criteria used in a previous GTA of language in the brain at rest [56] and found similar and consistent results.

In summary, the graph analysis using the CBF and BOLD information concomitantly and a whole-brain template for the nodes allowed us to assess the changes in the SVF functional network when comparing the resting-state condition with the task performance. Our results suggest that the used methodology may overcome the generalization problem regarding fMRI graph analysis with cognitive paradigms. Therefore, the graph theory approach can be used as a tool in future studies to assess functional markers between healthy and clinical groups in both rest and task-based fMRI if one carefully selects the regions of interest.

The joint CBF-ccBOLD analysis presented a more interconnected network with every node integrated with the network by at least one edge than ccBOLD and CBF individual findings. Interestingly, it meets the first criteria considered in this study to perform graph analysis [58]. It suggests that joint CBF-ccBOLD is useful to apply graph theory approaches. Additionally, it was possible to delineate a physiological basis for functional hubs in the SVF network once significant CBF changes in SFG-BA6 and IFG-47 nodes match areas of functional hubs of the SVF network namely the SMN and LAN networks. It suggests that dual-echo acquisition providing CBF and ccBOLD conjunction analysis helps determine functional hubs in task performance and its related physiological basis using a whole-brain parcellation template.

Limitations of our study include the relatively small number of participants, and the SVF task performed silently. Currently, VF fMRI studies have used loud articulation of words since silent articulation may produce non-linguistic activation, resulting from

response inhibition within the motor speech system. However, we chose the silent performance of the SVF task to avoid motor and movement artifacts. Regarding the sample size, although small, it is similar to the number of participants of other task-based fMRI studies. Moreover, the results were consistent between subjects and were following what we expected based on the literature.

In conclusion, our study demonstrated the potential of the ASL technique to assess an important brain function by evidence of a quantitative physiological parameter. Through a single MRI acquisition, our results suggested the effectiveness of ASL to detect CBF changes under an SVF task and are comparable to other imaging techniques. Moreover, our CBF/ccBOLD results for network delineation, functional connectivity, and graph analysis provided a complete evaluation of the functional brain connectivity in agreement with classical literature results. The advantage of spatial specificity and quantitative physiological information makes ASL an appealing method to investigate neurological disorders that affect the cognitive processing of language-associated brain function.

Data availability statement

The data that support the findings of this study are available upon reasonable request from the authors.

Acknowledgments

This study was financed in part by the Coordenação de Aperfeiçoamento de Pessoal de Nível Superior—Brasil (CAPES)—Finance Code 001, and Conselho Nacional de Desenvolvimento Científico e Tecnológico—Process Number 140110/2016-0.

Author contributions

All authors designed the study, analyzed the results, and wrote the paper. A M P acquired all MRI data and performed the imaging pre- and post-processing and functional connectivity analysis. P H R S participated in the imaging post-processing and functional connectivity analysis and performed the graph analysis.

Conflict of interest

The authors declare no competing interests.

ORCID iDs

André Monteiro Paschoal  <https://orcid.org/0000-0001-8269-711X>

Renata Ferranti Leoni  <https://orcid.org/0002-4568-0746>

References

- [1] Lezak M D, Loring D W and Howieson D B 2004 *Neuropsychological Assessment* 5th (Oxford: Oxford University Press) 1200
- [2] Mascali D, DiNuzzo M, Serra L, Mangia S, Maraviglia B, Bozzali M and Giove F 2018 Disruption of semantic network in mild Alzheimer's disease revealed by resting-state fMRI *Neuroscience* **371** 38–48
- [3] Wagner S, Sebastian A, Lieb K, Tuscher O and Tadic A 2014 A coordinate-based ALE functional MRI meta-analysis of brain activation during verbal fluency tasks in healthy control subjects *BMC Neurosci.* **15** 19
- [4] Zhao Q, Guo Q and Hong Z 2013 Clustering and switching during a semantic verbal fluency test contribute to differential diagnosis of cognitive impairment *Neurosci. Bull.* **29** 75–82
- [5] Pettit L, McCarthy M, Davenport R and Abrahams S 2013 Heterogeneity of letter fluency impairment and executive dysfunction in Parkinson's disease *J. Int. Neuropsychol. Soc.* **19** 986–94
- [6] Andreou G and Trott K 2013 Verbal fluency in adults diagnosed with attention-deficit hyperactivity disorder (ADHD) in childhood *Atten. Defic. Hyperact. Disord.* **5** 343–51
- [7] Metternich B, Buschmann F, Wagner K, Schulze-Bonhage A and Kriston L 2014 Verbal fluency in focal epilepsy: a systematic review and meta-analysis *Neuropsychol. Rev.* **24** 200–18
- [8] Tyburski E, Sokolowski A, Chec M, Pelka-Wysiecka J and Samochowiec A 2015 Neuropsychological characteristics of verbal and non-verbal fluency in schizophrenia patients *Arch. Psychiatr. Nurs.* **29** 33–38
- [9] Piskunowicz M, Bielinski M, Zglinski A and Borkowska A 2013 Verbal fluency tests—application in neuropsychological assessment *Psychiatr. Pol.* **47** 475–85
- [10] Glikmann-Johnston Y, Oren N, Handler T and Shapira-Lichter I 2015 Distinct functional connectivity of the hippocampus during semantic and phonemic fluency *Neuropsychologia* **69** 39–49
- [11] Price C J 2010 The anatomy of language: a review of 100 fMRI studies published in 2009 *Ann. New York Acad. Sci.* **1191** 62–88
- [12] Baldo J V, Schwartz S, Wilkins D and Dronkers N F 2006 Role of frontal versus temporal cortex in verbal fluency as revealed by voxel-based lesion symptom mapping *J. Int. Neuropsychol. Soc.* **12** 896–900
- [13] Ghanavati E, Salehinejad M A, Nejati V and Nitsche M A 2019 Differential role of prefrontal, temporal and parietal cortices in verbal and figural fluency: implications for the supramodal contribution of executive functions *Sci. Rep.* **9** 3700
- [14] Saur D et al 2008 Ventral and dorsal pathways for language *Proc. Natl Acad. Sci.* **105** 18035–40
- [15] Wawrzyniak M, Hoffstaedter F, Klingbeil J, Stockert A, Wrede K, Hartwigsen G, Eickhoff S B, Classen J, Saur D and Stamatakis E A 2017 Fronto-temporal interactions are functionally relevant for semantic control in language processing *PLoS One* **12** e0177753
- [16] Trautwein J and Schroeder S 2018 Orthographic networks in the developing mental lexicon. insights from graph theory and implications for the study of language processing *Front. Psychol.* **9** 2252
- [17] Visser M, Jefferies E and Lambon Ralph M A 2010 Semantic processing in the anterior temporal lobes: a meta-analysis of the functional neuroimaging literature *J. Cogn. Neurosci.* **22** 1083–94
- [18] Elmer S 2016 Broca pars triangularis constitutes a 'Hub' of the language-control network during simultaneous language translation *Front. Hum. Neurosci.* **10** 491
- [19] Bertola L, Mota N B, Copelli M, Rivero T, Diniz B S, Romano-Silva M A, Ribeiro S and Malloy-Diniz L F 2014 Graph analysis of verbal fluency test discriminate between patients with Alzheimer's disease, mild cognitive impairment and normal elderly controls *Front. Aging Neurosci.* **6** 185
- [20] Li Q, Dong J W, Del Ferraro G, Petrovich Brennan N, Peck K K, Tabar V, Makse H A and Holodny A I 2019 Functional translocation of Broca's area in a low-grade left frontal glioma: graph theory reveals the novel, adaptive network connectivity *Front. Neurol.* **10** 702
- [21] Aguirre G K, Detre J A, Zarahn E and Alsop D C 2002 Experimental design and the relative sensitivity of BOLD and perfusion fMRI *Neuroimage* **15** 488–500
- [22] Liang X, Zou Q, He Y and Yang Y 2013 Coupling of functional connectivity and regional cerebral blood flow reveals a physiological basis for network hubs of the human brain *Proc. Natl Acad. Sci.* **110** 1929–34
- [23] Detre J A, Zhang W, Roberts D A, Silva A C, Williams D S, Grandis D J, Koretsky A P and Leigh J S 1994 Tissue specific perfusion imaging using arterial spin labeling *NMR Biomed.* **7** 75–82
- [24] Petcharunpaisan S 2010 Arterial spin labeling in neuroimaging *World J. Radiol.* **2** 384–98
- [25] Detre J A, Leigh J S, Williams D S and Koretsky A P 1992 Perfusion imaging *Magn. Reson. Med.* **23** 37–45
- [26] Ferre J-C, Bannier E, Raoult H, Mineura G, Carsin-Nicol B and Gauvrit J-Y 2013 Perfusion par arterial spin labeling (ASL): technique et mise en œuvre clinique *J. Radiol. Diagn. Int.* **94** 1208–21
- [27] Wong E C, Buxton R B and Frank L R 1997 Implementation of quantitative perfusion imaging techniques for functional brain mapping using pulsed arterial spin labeling *NMR Biomed.* **10** 237–49
- [28] Talagala S L and Noll D C 1998 Functional MRI using steady-state arterial water labeling *Magn. Reson. Med.* **39** 179–83
- [29] Buxton R B, Frank L R, Wong E C, Siewert B, Warach S and Edelman R R 1998 A general kinetic model for quantitative perfusion imaging with arterial spin labeling *Magn. Reson. Med.* **40** 383–96
- [30] Buxton R B 2005 Quantifying CBF with arterial spin labeling *J. Magn. Reson. Imaging* **22** 723–6
- [31] Detre J A and Wang J J 2002 Technical aspects and utility of fMRI using BOLD and ASL *Clin. Neurophysiol.* **113** 621–34
- [32] Galazzo I B, Storti S F, Formaggio E, Pizzini F B, Fiaschi A, Beltramello A, Bertoldo A and Manganotti P 2014 Investigation of brain hemodynamic changes induced by active and passive movements: a combined arterial spin labeling–BOLD fMRI study *J. Magn. Reson. Imaging* **40** 937–48
- [33] Galazzo I B, Storti S F, Del Felice A, Pizzini F B, Arcaro C, Formaggio E, Mai R, Chappell M, Beltramello A and Manganotti P 2015 Patient-specific detection of cerebral blood flow alterations as assessed by arterial spin labeling in drug-resistant epileptic patients *PLoS One* **10** 1–24
- [34] Lu H Z, Donahue M J and van Zijl P C M 2006 Detrimental effects of BOLD signal in arterial spin labeling fMRI at high field strength *Magn. Reson. Med.* **56** 546–52
- [35] Pimentel M A F, Vilera P, Sousa I and Figueiredo P 2013 Localization of the hand motor area by arterial spin labeling and blood oxygen level-dependent functional magnetic resonance imaging *Hum. Brain Mapp.* **34** 96–108
- [36] Storti S F, Boscolo Galazzo I, Montemezzi S, Menegaz G and Pizzini F B 2017 Dual-echo ASL contributes to decrypting the link between functional connectivity and cerebral blood flow *Hum. Brain Mapp.* **38** 5831–44
- [37] Storti S F, Galazzo I B, Pizzini F B and Menegaz G 2018 Dual-echo ASL based assessment of motor networks: a feasibility study *J. Neural. Eng.* **15** 26018
- [38] Cohen A D, Nencka A S, Wang Y and Pillai J 2018 Multiband multi-echo simultaneous ASL/BOLD for task-induced functional MRI *PLoS One* **13** e0190427
- [39] Tak S, Wang D J J, Polimeni J R, Yan L and Chen J J 2014 Dynamic and static contributions of the cerebrovasculature to the resting-state BOLD signal *Neuroimage* **84** 672–80

- [40] Woolrich M W, Chiarelli P, Gallichan D, Perthen J and Liu T T 2006 Bayesian inference of hemodynamic changes in functional arterial spin labeling data *Magn. Reson. Med.* **56** 891–906
- [41] Folstein M F 2010 *Mini-Mental State Examination MMSE-2; User's Manual* (Lutz, FL: PAR)
- [42] Li Y T, Cercueil J-P, Yuan J, Chen W, Loffroy R and Wang Y X J 2017 Liver intravoxel incoherent motion (IVIM) magnetic resonance imaging: a comprehensive review of published data on normal values and applications for fibrosis and tumor evaluation *Quant. Imaging Med. Surg.* **7** 59–78
- [43] Peirce J W 2007 PsychoPy—Psychophysics software in Python *J. Neurosci. Methods* **162** 8–13
- [44] Wang J J, Fernandez-Seara M A, Wang S M and St Lawrence K S S 2007 When perfusion meets diffusion: *in vivo* measurement of water permeability in human brain *J. Cereb. Blood Flow Metab.* **27** 839–49
- [45] Silva J P S, Mônaco L D M, Paschoal A M, Oliveira Í A F D and Leoni R F 2018 Effects of global signal regression and subtraction methods on resting-state functional connectivity using arterial spin labeling data *Magn. Reson. Imaging* **51** 151–7
- [46] Oliveira Í A F, Guimaraes T M, Souza R M, dos Santos A C, Machado-de-Sousa J P, Hallak J E C and Leoni R F 2018 Brain functional and perfusional alterations in schizophrenia: an arterial spin labeling study *Psychiatry Res. Neuroimaging* **272** 71–78
- [47] Wang Z 2012 Improving cerebral blood flow quantification for arterial spin labeled perfusion MRI by removing residual motion artifacts and global signal fluctuations *Magn. Reson. Imaging* **30** 1409–15
- [48] Behzadi Y, Restom K, Liau J and Liu T T 2007 A component based noise correction method (CompCor) for BOLD and perfusion based fMRI *Neuroimage* **37** 90–101
- [49] Bzdok D, Heeger A, Langner R, Laird A R, Fox P T, Palomero-Gallagher N, Vogt B A, Zilles K and Eickhoff S B 2015 Subspecialization in the human posterior medial cortex *Neuroimage* **106** 55–71
- [50] RCoreTeam 2020 *R: A Language and Environment for Statistical Computing. Foundation for Statistical Computing* (available at: www.r-project.org/)
- [51] Whitfield-Gabrieli S and Nieto-Castanon A 2012 Conn: a functional connectivity toolbox for correlated and anticorrelated brain networks *Brain Connect.* **2** 125–41
- [52] Esposito F, Formisano E, Seifritz E, Goebel R, Morrone R, Tedeschi G and Di Salle F 2002 Spatial independent component analysis of functional MRI time-series: to what extent do results depend on the algorithm used? *Hum. Brain Mapp.* **16** 146–57
- [53] Seghier M L 2008 Laterality index in functional MRI: methodological issues *Magn. Reson. Imaging* **26** 594–601
- [54] de Martino F, Gentile F, Esposito F, Balsi M, Di Salle F, Goebel R and Formisano E 2007 Classification of fMRI independent components using IC-fingerprints and support vector machine classifiers *Neuroimage* **34** 177–94
- [55] Ren Y, Nguyen V T, Guo L and Guo C C 2017 Inter-subject functional correlation reveal a hierarchical organization of extrinsic and intrinsic systems in the brain *Sci. Rep.* **7** 10876
- [56] Muller A M and Meyer M 2014 Language in the brain at rest: new insights from resting state data and graph theoretical analysis *Front. Hum. Neurosci.* **8** 228
- [57] Bassett D S and Bullmore E 2006 Small-world brain networks *Neuroscientist* **12** 512–23
- [58] Mueller P A and Oppenheimer D M 2014 The pen is mightier than the keyboard: advantages of longhand over laptop note taking *Psychol. Sci.* **25** 1159–68
- [59] Alaerts K, Geerlings F, Herremans L, Swinnen S P, Verhoeven J, Sunaert S, Wenderoth N and Zuo X-N 2015 Functional organization of the action observation network in autism: a graph theory approach *PLoS One* **10** e0137020
- [60] Sporns O 2011 The non-random brain: efficiency, economy, and complex dynamics *Front. Comput. Neurosci.* **5** 5
- [61] Rubinov M and Sporns O 2010 Complex network measures of brain connectivity: uses and interpretations *Neuroimage* **52** 1059–69
- [62] Latora V and Marchiori M 2001 Efficient behavior of small-world networks *Phys. Rev. Lett.* **87** 198701
- [63] Wang J, Zuo X and He Y 2010 Graph-based network analysis of resting-state functional MRI *Front. Syst. Neurosci.* **4** 16
- [64] Wang Z, Aguirre G K, Rao H, Wang J, Fernandez-Seara M A, Childress A R and Detre J A 2008 Empirical optimization of ASL data analysis using an ASL data processing toolbox: ASLtbx *Magn. Reson. Imaging* **26** 261–9
- [65] Warburton E, Wise R J S, Price C J, Weiller C, Hadar U, Ramsay S and Frackowiak R S J 1996 Noun and verb retrieval by normal subjects studies with PET *Brain* **119** 159–79
- [66] Shuster L I and Lemieux S K 2005 An fMRI investigation of covertly and overtly produced mono- and multi-syllabic words *Brain Lang.* **93** 20–31
- [67] Cutting L E, Clements A M, Courtney S, Rimrodt S L, Schafer J G, Bisesi J, Pekar J J and Pugh K R 2006 Differential components of sentence comprehension: beyond single word reading and memory *Neuroimage* **29** 429–38
- [68] Dietz N A E, Jones K M, Gareau L, Zeffiro T A and Eden G F 2005 Phonological decoding involves left posterior fusiform gyrus *Hum. Brain Mapp.* **26** 81–93
- [69] Papathanassiou D, Etard O, Mellet E, Zago L, Mazoyer B and Tzourio-Mazoyer N 2000 A common language network for comprehension and production: a contribution to the definition of language epicenters with PET *Neuroimage* **11** 347–57
- [70] Olman C A, Davachi L, Inati S and García A V 2009 Distortion and signal loss in medial temporal lobe *PLoS One* **4** e8160
- [71] Ischebeck A, Indefrey P, Usui N, Nose I, Hellwig F and Taira M 2004 Reading in a regular orthography: an fMRI study investigating the role of visual familiarity *J. Cogn. Neurosci.* **16** 727–41
- [72] Kim J, Wasserman E A, Castro L and Freeman J H 2016 Anterior cingulate cortex inactivation impairs rodent visual selective attention and prospective memory *Behav. Neurosci.* **130** 75–90
- [73] Paschoal A M, Paiva F F and Leoni R F 2019 Dual-echo arterial spin labeling for brain perfusion quantification and functional analysis *Concepts Magn. Reson. A* **2019** 5040465
- [74] Liu T T and Wong E C 2005 A signal processing model for arterial spin labeling functional MRI *Neuroimage* **24** 207–15
- [75] Costafreda S G, Fu C H Y, Lee L, Everitt B, Brammer M J and David A S 2006 A systematic review and quantitative appraisal of fMRI studies of verbal fluency: role of the left inferior frontal gyrus *Hum. Brain Mapp.* **27** 799–810
- [76] Shapira-Lichter I, Oren N, Jacob Y, Gruberger M and Handler T 2013 Portraying the unique contribution of the default mode network to internally driven mnemonic processes *Proc. Natl Acad. Sci. USA* **110** 4950–5
- [77] O'Brien C P 2008 The CAGE questionnaire for detection of alcoholism: a remarkably useful but simple tool *JAMA* **300** 2054–6

47 Autoria de artigos completos publicados em jornais e revistas de circulação nacional e internacional na sua área

Esta subseção apresenta o comprovante da autoria do artigo publicado na revista internacional *Journal of Magnetic Resonance Imaging* no ano de 2021.

Editorial for “Diffusion Tensor Imaging Reveals Altered Topological Efficiency of Structural Networks in Type-2 Diabetes Patients With and Without Mild Cognitive Impairment”

Type 2 diabetes mellitus (T2DM) is the most frequent category of diabetes, consisting of a chronic metabolic disease in a response for the deficit in insulin secretion and/or action, which results in hyperglycemia¹ and in long term is associated with the dysfunction of several organs such as kidney, heart, eyes, and the vascular system. These dysfunctions and failures are enhanced by coexisting comorbidities, including obesity, hypertension, and dyslipidemia.² The severity of T2DM increases when it affects the vascular system, with the flow reaching its final target in the cerebrovascular and brain tissues.

While hyperglycemia and glucose intolerance are the main manifestation for T2DM patients, the neurological impact of type 2 diabetes, whose main outcome is the cognitive impairment,³ is also an important condition for these patients. Although evaluating the direct impact of T2DM in the occurrence of cognitive impairment is hampered due to the coexisting cerebrovascular diseases, emerging evidence are being carried out to elucidate the relationship between T2DM and cognitive impairment, which may increase the risk of developing dementia.⁴

Neuroimaging studies arise as an important field in the understanding of the pathways, mechanisms, and the preferred target regions in the brain that are related to the development of cognitive impairment. In especial, magnetic resonance imaging provides a set of tools to investigate the alterations in the T2DM patient’s brain. Among all the methods available, structural analysis of volumetry and cortical thickness,⁵ functional integration,⁶ and metabolic evaluation⁷ has already resulted in alterations when compared to healthy subjects. Furthermore, diffusion-weighted imaging has been well explored to evaluate the macro and microstructural integrity of white matter (WM) for specific regions and brain topology.^{8,9} However, there is still lacking a deeper understanding on the specific

brain organization in T2DM that differs from patients with and without cognitive impairment.

In this issue of *JMRI*, Xiong et al assessed the differences between T2DM patients with and without mild cognitive impairment (MCI) regarding the alterations in WM network topology at global and nodal levels.¹⁰ The network topological study was based on the use of diffusion-weighted images to perform a deterministic tractography and graph theory analysis followed by the appropriate statistical analysis to identify the differences between the two target groups of T2DM patients. For the regions that resulted in differences between the groups, they performed a correlation analysis to investigate the relationship between topological brain networks and traditional markers for diabetes severity.

Xiong et al revealed that T2DM-MCI patients presented more damaged global topological organization of WM than T2DM patients without MCI when compared to healthy subjects and decreased network efficiency when straight compared to T2DM without MCI. It was also reported that despite decreased nodal efficiency was found for both MCI and not-MCI T2DM patients in the frontal, parietal, temporal, and occipital cortices than in healthy controls, other regions showed decreased efficiency only for MCI-T2DM patients in comparison to healthy subjects, suggesting advanced disease stages for this group. In that sense, the outcomes of this study included the correlation of the severity of diabetes and reduced cognitive capacity to the alterations in several network parameters.

Finally, the authors suggested a possible early biomarker of cognitive impairment for T2DM patients by reporting reduced nodal efficiency in brain regions straight related to cognitive functions (posterior cingulate, insula, and the orbital part of the inferior frontal gyrus) for the group of diabetes patients with normal cognition

than the healthy control group. Although it represents promising results, there is still the need for a deeper investigation of these findings. Other limitation of the study is the comparison of MCI patients with and without T2DM, which might enlighten the cause/consequence relationship between cognitive impairment and severity of T2DM.

André M. Paschoal, PhD  

LIM44, Instituto e Departamento de Radiologia, Faculdade de Medicina
Universidade de São Paulo
São Paulo, Brazil
E-mail: andre.paschoal@usp.br
Twitter: @paschoal_am

References

1. Gavin JR, Alberti KGMM, Davidson MB, et al. Report of the expert committee on the diagnosis and classification of diabetes mellitus. *Diabetes Care* 2002;25(Suppl. 1):5-20.
2. McCrimmon RJ, Ryan CM, Frier BM. Diabetes and cognitive dysfunction. *Lancet* 2012;379:2291-2299.
3. Kodl CT, Seaquist ER. Cognitive dysfunction and diabetes mellitus. *Endocr Rev* 2008;29:494-511.
4. Kloppenborg RP, van den Berg E, Kappelle LJ, Biessels GJ. Diabetes and other vascular risk factors for dementia: Which factor matters most? A systematic review. *Eur J Pharmacol* 2008;585:97-108.
5. Wu G, Lin L, Zhang Q, Wu J. Brain gray matter changes in type 2 diabetes mellitus: A meta-analysis of whole-brain voxel-based morphometry study. *J Diabetes Complications* 2017;31:1698-1703.
6. Yang SQ, Xu ZP, Xiong Y, et al. Altered intranetwork and internetwork functional connectivity in type 2 diabetes mellitus with and without cognitive impairment. *Sci Rep* 2016;6(December 2015):1-11.
7. Del Coco L, Vergara D, De Matteis S, et al. NMR-based metabolomic approach tracks potential serum biomarkers of disease progression in patients with type 2 diabetes mellitus. *J Clin Med* 2019;8:720.
8. Zhang J, Wang Y, Wang J, et al. White matter integrity disruptions associated with cognitive impairments in type 2 diabetic patients. *Diabetes* 2014;63:3596-3605.
9. Xiong Y, Sui Y, Zhang S, et al. Brain microstructural alterations in type 2 diabetes: Diffusion kurtosis imaging provides added value to diffusion tensor imaging. *Eur Radiol* 2019;29:1997-2008.
10. Xiong Y, Tian T, Fan Y, Yang S, Xiong X, Zhang Q, Zhu W. Diffusion tensor imaging reveals altered topological efficiency of structural networks in type-2 diabetes patients with and without mild cognitive impairment. *J Magn Reson Imaging*. 2021.

DOI: 10.1002/jmri.27899

Level of Evidence: 5

Technical Efficacy: Stage 2

48 Autoria de artigos completos publicados em jornais e revistas de circulação nacional e internacional na sua área

Esta subseção apresenta o comprovante da autoria do artigo publicado na revista internacional *Magnetic Resonance Materials in Physics, Biology and Medicine* no ano de 2021.



Feasibility of intravoxel incoherent motion in the assessment of tumor microvasculature and blood–brain barrier integrity: a case-based evaluation of gliomas

Andre Monteiro Paschoal^{1,2,3} · Maria Clara Zanon Zotin^{2,4} · Lucas Murilo da Costa³ · Antonio Carlos dos Santos² · Renata Ferranti Leoni³

Received: 30 June 2021 / Revised: 5 December 2021 / Accepted: 6 December 2021 / Published online: 15 December 2021
© The Author(s), under exclusive licence to European Society for Magnetic Resonance in Medicine and Biology (ESMRMB) 2021

Abstract

Objective To evaluate the feasibility of intravoxel incoherent motion (IVIM) in assessing blood–brain barrier (BBB) integrity and microvasculature in tumoral tissue of glioma patients.

Methods Images from 8 high-grade and 4 low-grade glioma patients were acquired on a 3 T MRI scanner. Acquisition protocol included pre- and post-contrast T1- and T2-weighted imaging, FLAIR, dynamic susceptibility contrast (DSC), and susceptibility-weighted imaging (SWI). In addition, IVIM was acquired with 15 b-values and fitted under the non-negative least square (NNLS) model to output the diffusion (D) and pseudo-diffusion (D^*) coefficients, perfusion fraction (f), and f times D^* (fD^*) maps.

Results IVIM perfusion-related maps were sensitive to (1) blood flow and perfusion alterations within the microvasculature of brain tumors, in agreement with intra-tumoral susceptibility signal (ITSS); (2) enhancing areas of BBB breakdown in agreement with DSC maps as well as areas of BBB abnormality that was not detected on DSC maps; (3) enhancing perfusion changes within edemas; (4) detecting early foci of increased perfusion within low-grade gliomas.

Conclusion The results suggest IVIM may be a promising approach to delineate tumor extension and progression in size, and to predict histological grade, which are clinically relevant information that characterize tumors and guide therapeutic decisions in patients with glioma.

Keywords Intravoxel incoherent motion · Gliomas · Microvasculature · Blood–brain barrier

Introduction

Gliomas are a critical and heterogeneous class of primary brain tumors originating from the glial cells, representing about 50% of all cerebral neoplasm [1]. The WHO

classification system subdivides gliomas according to histopathological grade and molecular profile [1]. For example, it is well known that glioblastomas (GBMs, grade 4) and isocitrate dehydrogenase (IDH) wild type tumors are typically aggressive, with poor prognosis. In contrast, low-grade gliomas (LGG, grades 1 and 2) encompass a more heterogeneous group of tumors with variable clinical prognosis [1].

Histopathological analysis with molecular phenotyping is the gold-standard approach for tumor classification, but the quest for noninvasive alternatives capable of offering relevant diagnostic and prognostic information remains. In that sense, several magnetic resonance imaging (MRI) techniques have been increasingly used to enhance brain tumors characterization and predict histopathological grade and biological behavior. Among the many promising MRI techniques in neuro-oncology, contrast-free perfusion imaging has gained increased attention. Performed alongside contrast-enhanced sequences, it allows for better characterization of

✉ Andre Monteiro Paschoal
andre.paschoal@hc.fm.usp.br

¹ LIM44, Instituto e Departamento de Radiologia, Faculdade de Medicina, Universidade de São Paulo, São Paulo, SP 05403-010, Brazil

² Medical School of Ribeirão Preto, University of São Paulo, Ribeirão Preto, SP 14040-900, Brazil

³ InBrain Lab, FFCLRP, University of São Paulo, Ribeirão Preto, SP 14040-900, Brazil

⁴ Department of Neurology, Massachusetts General Hospital, Harvard Medical School, Boston, MA, USA

tumor hemodynamics, which directly reflects tumor aggressiveness [2–4]. Specifically, contrast-free perfusion imaging evaluates tumor microvasculature and offers several advantages over gadolinium-based techniques. It does not require a precise knowledge of the injection parameters and does not expose the patient to eventual gadolinium collateral effects, or to potential tissue retention effects. Susceptibility-weighted imaging (SWI) is also useful to analyze glioma's microvasculature. Intratumoral susceptibility signal (ITSS) has been related to intralesional hemorrhage, calcification, and neovascularity, contributing to glioma histopathological characterization [5, 6].

Among the contrast-free perfusion imaging approaches alternatives, intravoxel incoherent motion (IVIM) is an MRI method that explores a scaling in diffusion weighting to infer diffusion and perfusion information simultaneously by separating each contribution of the total signal measured [4, 7]. In contrast, arterial spin labeling (ASL) uses the arterial blood as an endogenous tracer magnetically labeled through the application of radiofrequency (RF) pulses [8, 9]. Although ASL is well established in the literature with a broad range of clinical applications [10], it suffers from limitations related to signal intensity decays with the longitudinal relaxation time (T_1), hampering the analysis for patients with very long arterial transit time, which is the case for the perfusion in white matter. On the other hand, since IVIM explores the diffusion movement of water molecules, it is not dependent on the arterial transit time. Also, like ASL [11], IVIM allows for the characterization of microvascular perfusion within the tumor. Previous studies have already reported the success of IVIM in glioma grading [12–18].

Though the categorization of gliomas in different grades contributes to harmonizing diagnosis and therapeutic approaches, the genetic, metabolic, and morphological abnormalities that underlie tumor progression occur instead as a continuum and help explain how tumors of similar grades may present heterogeneous evolution patterns. Identifying early signs of tumor progression through neuroimaging biomarkers can guide appropriate and prompt therapeutics and has become a research priority. It is especially important for LGG, in which MRI markers can predict evolution to HGG, demanding a more aggressive treatment. It is well known that high-grade gliomas (HGG, grades 3 and 4) develop an extensive microvascular tree, with BBB disruption [19]. Accordingly, MRI techniques able to capture such perfusion and permeability abnormalities may serve as biomarkers, predicting prognosis and evolution of gliomas.

In this case series, we aimed to evaluate how IVIM findings in HGG can be associated with increased microvascular perfusion and BBB damage by comparing such findings against more established markers (perfusion maps extracted from dynamic susceptibility contrast (DSC), microvascular signal of ITSS obtained from SWI, and hyperintensities in

post-contrast FLAIR) and assessing whether they offer complementary information. Furthermore, we assessed whether IVIM findings in LGG could capture microvasculature changes predictive of earlier evolution to HGG.

Methods

Subjects

Twelve patients (8 HGG, 4 LGG; mean age \pm standard deviation (SD) = 56.11 ± 19.14) participated in this cross-sectional study, approved by the Institutional Review Board, after signing the informed consent agreement. Patients were recruited at the Clinical Hospital of the Institution, and the inclusion criteria were presence of glioma compatible findings in the MR images, confirmed and characterized through histopathological analysis. Exclusion criteria were previous surgical intervention, non-glioma final diagnosis (e.g., germline neoplasms, colorectal metastasis, infectious lesions), pregnancy, claustrophobia, and contraindications for MRI. The sample size was determined by the number of patients who met the criteria and agreed to participate in the study.

MR system

Data were acquired at a 3 T MR system (Achieva, Philips Medical System, The Netherlands), equipped with gradients of 80 mT/m amplitude and 200 mT/m/ms slew rate. A vendor standard transmit body coil, and a 32-channel receive-only head coil were used to measure the signal.

Scanning protocols

Patients were scanned under the Institution clinical protocol for tumors, which consists of whole-brain three-dimensional T1-weighted images (3D-T1W GRE) acquired pre- and post-gadolinium injection, three-dimensional fluid-attenuated inversion recovery (FLAIR), axial T2-weighted images, MR spectroscopy (MRS), dynamic susceptibility contrast (DSC) T_2^* -weighted perfusion images, high-resolution diffusion-weighted images (DWI) and high-resolution susceptibility-weighted images (SWI), and the addition of IVIM images using 15 b-values (0, 4, 8, 16, 30, 60, 120, 250, 500, 1000, 1200, 1400, 1600, 1800 and 2000s/mm 2). Table 1 shows the description of the complete parameters of the whole protocol.

Data processing

IVIM and DSC data preprocessing were performed in SPM12 (Wellcome Trust Center for Neuroimaging, University College London, UK). For IVIM data, the preprocessing

Table 1 Data acquisition parameters

	3D T1W	AXIAL T2W	3D FLAIR	MRS	DSC	HR DWI	HR SWI	IVIM
FOV (mm ²)	240×240	240×240	240×240	200×180	240×240	240×240	240×240	240×240
Spatial resolution (mm ²)	1×1	0.39×0.39	0.6×0.6	0.45×0.63	1.44×1.44	2×2	0.43×0.43	2×2
Slice thickness (mm)	1	3	1	1.1	5	4	4	5
Number of slices	180	50	180	96	24	150	150	20
TR (ms)	7	6620	5000	20	17	2900	15.8	3000
TE (ms)	3.2	80	334.21	3.45	25	68	22.4	102
TI (ms)	–	–	1600	–	–	–	–	–
FA (degrees)	8	90	90	20	90	90	15	90
Number of repetitions	1	1	1	1	70	1	1	1
Number of b-values	–	–	–	–	–	2	–	15
Total scan time (min)	5.98	3.09	3.83	3.58	1.86	1.17	2.17	4.20

included motion correction, while correction for eddy current and susceptibility artifacts were performed through the ACID toolbox for SPM12 [20, 21]. The preprocessing of DSC images consisted of motion correction and realignment of the time-series using the middle image as reference.

The IVIM fitting was performed in local python scripts (<https://github.com/inbrainlab/IVIMKurtosis>) using bi-exponential model [22] corrected for high b-values including the kurtosis contribution (K), which is described in Eq. 1. The kurtosis maps were obtained using the DTIFIT tool of FSL [23].

$$y(b_i) = \left\{ \left[fe^{-bD^*} + (1-f)e^{-bD+(bD)^2 \frac{K}{6}} \right]^2 + NCF \right\}^{1/2} \quad (1)$$

where $y(b_i)$ is the measured signal, D is the diffusion coefficient, D^* represents the pseudo-diffusion coefficient and f is the perfusion fraction. NCF represents the noise correction factor. After performing the fitting, fD^* maps were obtained by multiplying f and D^* maps. The robustness of the fitting was estimated by calculating the RMSE.

The DSC outputs as cerebral blood flow (CBF), cerebral blood volume (CBV), and mean transit time (MTT) maps were obtained with the Dynamic Susceptibility Contrast MRI toolbox for Matlab (<https://github.com/marcocasteillaro/dsc-mri-toolbox>) by performing the semi-automatic arterial input function (AIF) selection [24] and the deconvolution of DSC curve [25].

Data analysis

Patients' images were independently reviewed and assessed by two neuroradiologists (M.C.Z.Z and A.C.S) for diagnosis purposes. The neuroradiologists also selected the appropriate slices to assess IVIM-derived maps and the corresponding slices for other imaging modalities. The specialists' reports were further confirmed with the results of the biopsies.

Quantitative measurements were performed in R [26] by extracting the voxelwise values of normalized DSC-CBF, diffusion coefficient, normalized fD^* and perfusion fraction maps within the ROIs of tumor border, tumor interior and edema (when present). The ROIs were manually drawn using the FSLeyes tool of FSL [23] considering multiple images modalities, as post-contrast T1w, post-contrast FLAIR and IVIM perfusion fraction to delineate regions of tumors' border, interior/necrosis and adjacent regions of edema. Contralateral ROIs were also selected in normal-appearing, contralateral regions. An illustrative example of the ROIs is shown in Supplementary Figure 9. Voxelwise correlations between normalized DSC-CBF and normalized fD^* and perfusion fraction for the same ROIs were performed.

Results

Figure 1 shows the fitting result of IVIM signal decay of a tumoral region for an illustrative patient, including the value of RMSE measurement. Table 2 shows the reports from two neuroradiologists based on all the acquired sequences except the IVIM images, analyzed separately. The histological reports and tumor grades are provided.

Next, we describe in detail relevant examples of microvascular and BBB tumoral alterations detected through IVIM (Figs. 2, 4 and 5). Images of the other patients are shown in the supplementary material. The quantitative measurements of IVIM outputs and normalized DSC-CBF are shown in Table 3 for all patients.

Figure 2 shows the images for patient 4 (Table 2) with a high-grade glioma. In this case, there is evidence of BBB disruption in the tumor borders (pointed by the red arrows), which is enhanced in the T1 post-contrast images (Fig. 2a). The same region also shows ITSS in SWI, indicating increased vascularization, also captured in DSC perfusion. In addition, IVIM f and fD^* maps displayed increased values

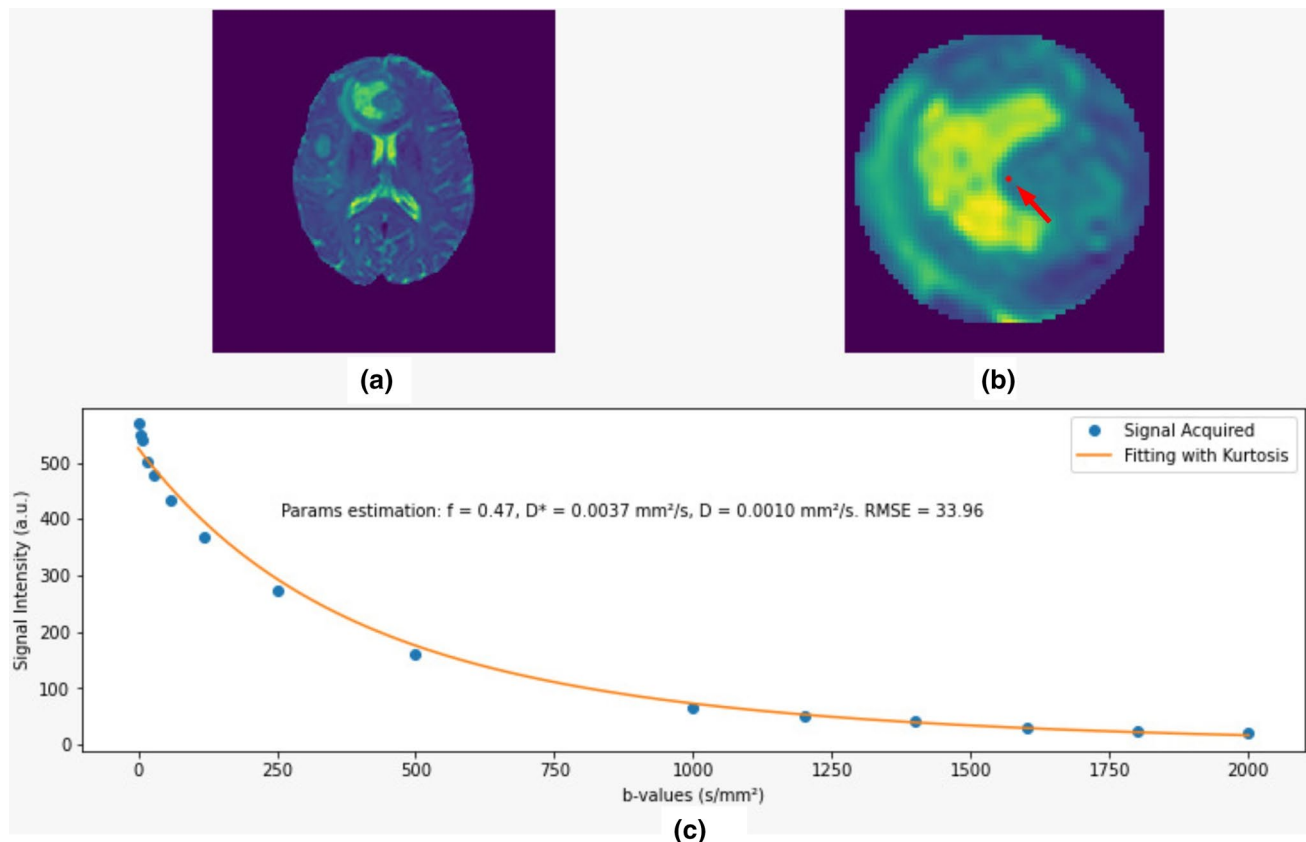


Fig. 1 **a** Raw IVIM data with $b=0$. **b** Zoomed tumor ROI. **c** The results of a bi-exponential fitting model for IVIM data signal decay corrected with the kurtosis contribution including the measure of RMSE for an illustrative voxel within the region shown in (b)

for these regions, suggesting sensitivity to BBB breakdown and neovascularity. Interestingly, in regions pointed by the yellow arrows, there is no clear evidence of BBB disruption according to T1 post-contrast images, but there are linear foci of increased f and fD^* values, suggesting increased local perfusion and BBB damage, also captured in the post-contrast FLAIR. Of importance, it was also possible to capture increased IVIM perfusion fraction in the extensive areas of abnormal FLAIR signal around and posterior to the tumor (pink arrow), which was not detectable through DSC-CBF or SWI. The same areas also did not show any pathological enhancement on post-contrast T1. The analysis of the quantitative measurements for patient 4 in the boxplots of Fig. 3 shows that increase in perfusion-related parameters are more evident for IVIM outputs in comparison to DSC-CBF. The diffusion coefficient maps in Fig. 2d show increased diffusion in regions with increased perfusion and decreased diffusion in regions of high cellularity, according to the expected in the literature of diffusion imaging for tumors [27].

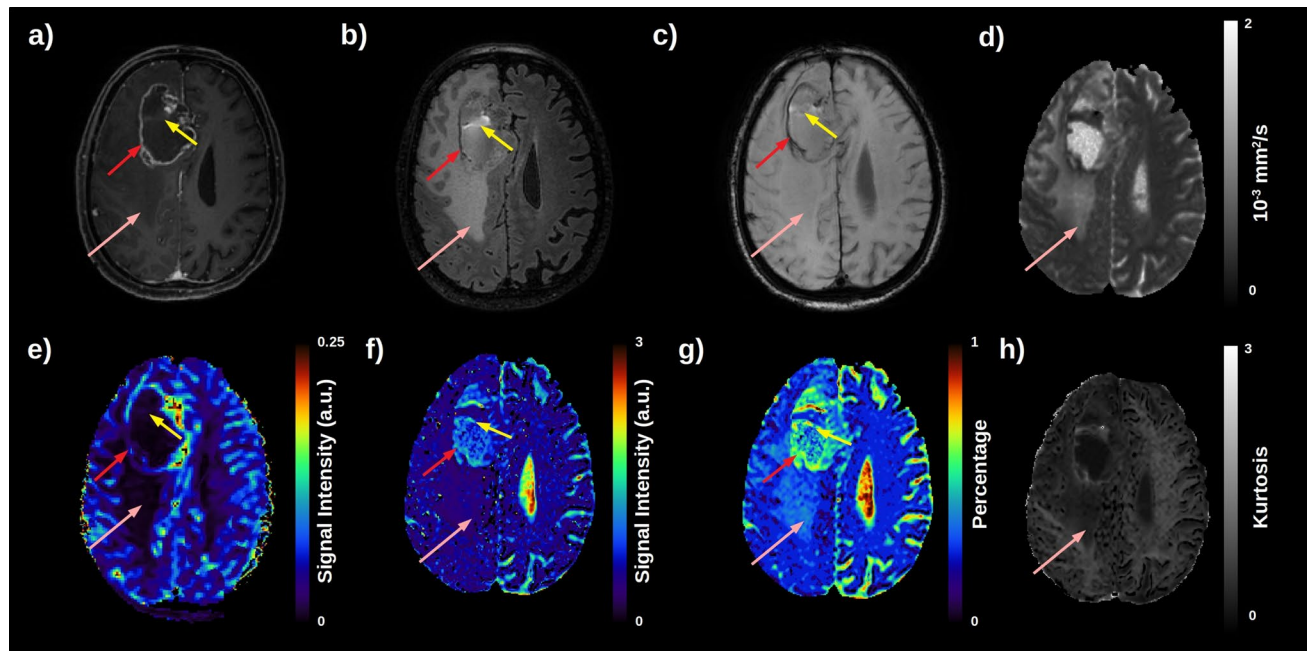
The glioblastoma case in Fig. 4 clearly displays BBB breakdown, evident in areas of post-contrast enhancement on T1W images (Fig. 4a, yellow arrows). The red arrow in Fig. 4 indicates an area of low signal on SWI, high signal on FLAIR,

and absence of enhancement on post-contrast T1, interpreted as an area of necrosis, probably with a hemorrhagic component. While regions with viable tumoral tissue presented subtle increased perfusion on IVIM maps, the necrotic area did not (Fig. 4f and g). In areas of increased signal intensity on FLAIR located adjacent and posterior to the core of the tumor (pink arrow), we could detect increased perfusion fraction on IVIM maps. For regions where there is no BBB disruption, DSC-CBF could not capture increased blood flow.

For the LGG patient shown in Fig. 5, no evident disruption of BBB was detectable on post-contrast T1-weighted images. The subtle medial foci of apparent enhancement on the post-contrast T1 (yellow arrow), also visible on DSC CBF map, represents a vessel within the tumor, confirmed on reformatting images. The regions of ITSS in the SWI map (red arrows) are compatible with the increase IVIM perfusion signal intensity, suggesting neovascularization. Moreover, increased IVIM perfusion was also detected in the posterior areas of the tumor, which showed only increased signal on FLAIR (pink arrow), without corresponding ITSS or increased CBF. The quantitative measurements in the boxplots of Fig. 6 depict the sensibility of IVIM f and fD^* maps in detecting early changes in tumor's hemodynamic. Both the tumor's periphery

Table 2 Patients' information and specialists' reports based on MR imaging and histopathology

ID	Gende	Age	MRI report	Histological report	Grade
P01	Male	69	Right frontal and nucleocapsular expansive formation, compatible with high-grade primary neoplasm	Glioma grade 3 or 4	HGG
P02	Female	67	Findings compatible with neoplasm; central area suggestive of necrosis, multicentric, with increased perfusion and very high choline peaks. Glioblastoma	Glioma grade 3 or 4	HGG
P03	Female	71	Multiple lesions suggestive of neoplasia, with high cellularity and necrosis, with distribution in the edge of the ventricles, suggesting primary lymphoma of the CNS	Glioma grade 4 – GBM – IDH-wildtype	HGG
P04	Male	76	Expansive brain lesion suggestive of high-grade neoplasm	Glioma grade 3 or 4	HGG
P05	Male	59	Expansive lesion in the corpus callosum, compatible with high-grade glioma	Glioma grade 4 – GBM	HGG
P06	Female	38	Frontal expansive formation on the right compatible with high-grade glioma	Glioma grade 4 – GBM – IDH-wildtype	HGG
P07	Male	71	Expansive brain lesion suggestive of high-grade neoplasm	Glioma grade 4 – GBM	HGG
P08	Male	77	Left temporal expansive lesion with signs of aggressiveness, compatible with neoplasia and suggestive of high-grade glioma	Glioma grade 3 or 4	HGG
P09	Male	28	Left frontal intra-axial expansive lesion suggestive of low-grade glioma	Astrocytoma grade 2 – IDH-mutant (R132H)	LGG
P10	Male	33	Expansive left parietal lesion, compatible with the clinical hypothesis of low-grade glioma	Astrocytoma grade 2 – IDH-mutant	LGG
P11	Male	39	Temporoparietal expansive cortico-subcortical lesion on the left compatible with diffuse glioma	Oligodendrogioma grade 2	LGG
P12	Male	56	Expansive lesion, compatible with the clinical hypothesis of low-grade glioma	Glioma grade 2	LGG

**Fig. 2** High-grade glioma patient. **a** post-contrast T1-weighted image; **b** post-contrast FLAIR image; **c** susceptibility-weighted image; **d** Diffusion coefficient map **e** DSC CBF map; **f** IVIM fD^* map; **g** IVIM perfusion fraction map and **h** Map of diffusion kurtosis. The red arrow shows the tumor border in which there is BBB disruption. For the region pointed by the yellow arrow, there is no clear evidence

of increased perfusion or BBB damage in DSC or post-contrast T1 images, but findings from the SWI, post-contrast FLAIR, and IVIM suggested high neovascularity and possible BBB damage. The pink arrow displays increased IVIM perfusion in the more infiltrative, edema-like, posterior regions

Table 3 Quantitative measurements for normalized DSC-CBF (a.u.) and the IVIM outputs, diffusion coefficient (D) in mm²/s, perfusion fraction (f) and fD* (a.u.) maps for the ROIs of tumor border, tumor interior and the respective contra-lateral regions

	HGG1	HGG2	HGG3	HGG4	HGG5	HGG6	HGG7	HGG8	LGG1	LGG2	LGG3	LGG4
<i>Tumor border</i>												
CBF	0.66±0.14	0.45±0.19	0.5±0.17	0.24±0.15	0.6±0.18	0.64±0.2	0.32±0.28	0.41±0.2	0.59±0.14	0.19±0.17	0.59±0.15	0.65±0.14
D	0.73±0.06	0.93±0.09	1.19±0.29	2.24±0.27	0.72±0.09	0.77±0.23	0.94±0.39	1.11±0.37	1.39±0.24	1.44±0.18	0.85±0.09	1.11±0.31
f	0.17±0.05	0.35±0.09	0.52±0.13	0.35±0.09	0.24±0.06	0.17±0.07	0.22±0.06	0.41±0.16	0.19±0.08	0.3±0.06	0.19±0.09	0.3±0.05
fD*	0.047±0.137	0.049±0.09	0.521±0.2	0.022±0.092	0.038±0.11	0.074±0.165	0.049±0.155	0.595±0.267	0.584±0.184	0.017±0.098	0.144±0.202	0.46±0.19
<i>Contra-lateral region of tumor border</i>												
CBF	0.65±0.23	0.68±0.16	0.38±0.14	0.24±0.12	0.68±0.16	0.39±0.22	0.33±0.23	0.37±0.24	0.49±0.26	0.43±0.18	0.55±0.15	0.5±0.2
D	0.64±0.05	0.66±0.06	0.55±0.19	0.76±0.1	0.77±0.16	0.56±0.14	0.69±0.12	0.59±0.1	0.57±0.14	0.69±0.18	0.71±0.08	0.61±0.13
f	0.2±0.09	0.2±0.04	0.2±0.09	0.24±0.06	0.27±0.1	0.23±0.15	0.29±0.11	0.19±0.07	0.26±0.13	0.3±0.2	0.21±0.13	0.21±0.1
fD*	0.052±0.110	0.071±0.134	0.023±0.104	0.014±0.073	0.036±0.139	0.025±0.106	0.031±0.103	0.016±0.111	0.012±0.085	0.053±0.157	0.047±0.138	0.03±0.09
<i>Tumor interior</i>												
CBF	0.61±0.2	0.09±0.05	0.38±0.19	0.14±0.08	0.79±0.12	0.42±0.23	0.09±0.09	0.31±0.27	0.43±0.14	0.39±0.18	0.53±0.17	0.5±0.14
D	0.92±0.13	0.76±0.09	0.61±0.11	1.13±0.17	0.89±0.14	1.58±0.51	0.72±0.17	1.16±0.17	1.37±0.14	1.54±0.18	1.19±0.14	1.07±0.16
f	0.19±0.09	0.46±0.11	0.06±0.14	0.27±0.09	0.36±0.08	0.36±0.07	0.4±0.05	0.33±0.07	0.18±0.05	0.25±0.08	0.33±0.04	0.3±0.04
fD*	0.073±0.169	0.532±0.272	0.029±0.157	0.521±0.082	0.092±0.101	0.598±0.194	0.649±0.151	0.345±0.118	0.115±0.052	0.093±0.242	0.582±0.148	0.01±0.05
<i>Contra-lateral region of tumor interior</i>												
CBF	0.76±0.14	0.36±0.23	0.56±0.14	0.25±0.16	0.59±0.1	0.62±0.16	0.18±0.19	0.43±0.13	0.27±0.22	0.51±0.17	0.59±0.16	0.49±0.2
D	0.8±0.14	0.8±0.1	1.75±0.33	0.63±0.26	1.22±0.07	0.51±0.04	0.98±0.16	0.88±0.2	0.56±0.09	0.68±0.08	0.65±0.17	0.71±0.21
f	0.2±0.06	0.05±0.18	0.63±0.09	0.24±0.12	0.23±0.03	0.2±0.02	0.21±0.09	0.4±0.19	0.23±0.1	0.04±0.07	0.2±0.15	0.21±0.13
fD*	0.153±0.201	0.081±0.199	0.025±0.092	0.015±0.082	0.566±0.144	0.015±0.09	0.029±0.097	0.04±0.079	0.049±0.161	0.187±0.132	0.022±0.079	0.03±0.1

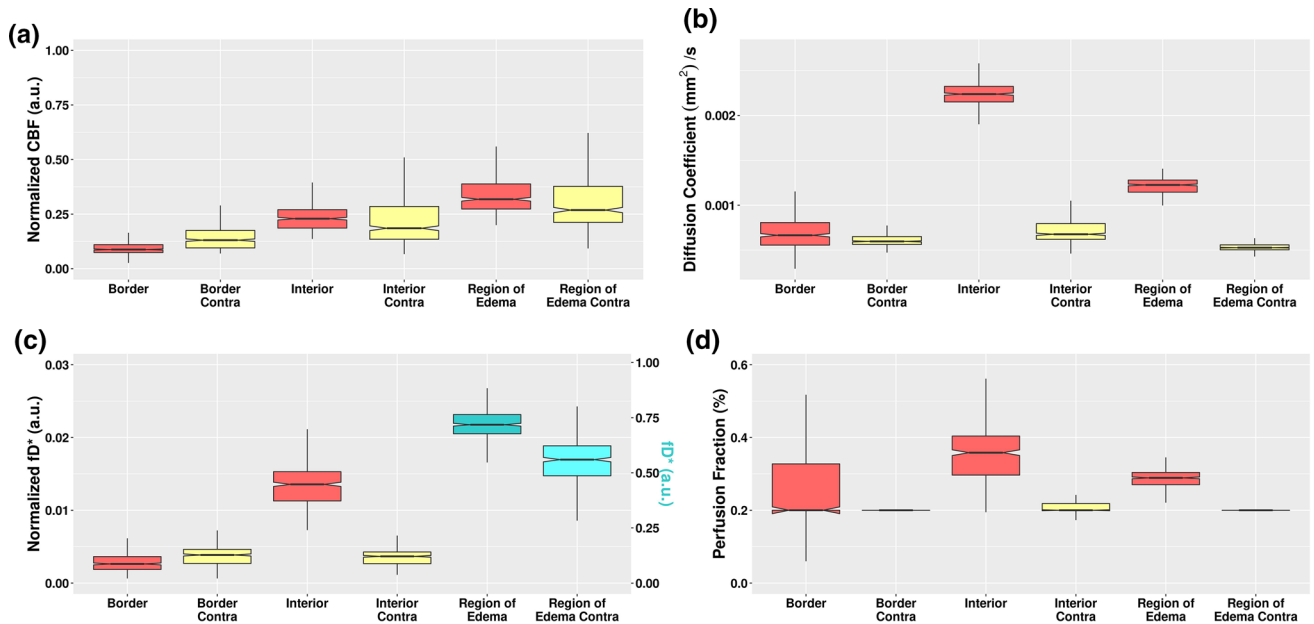
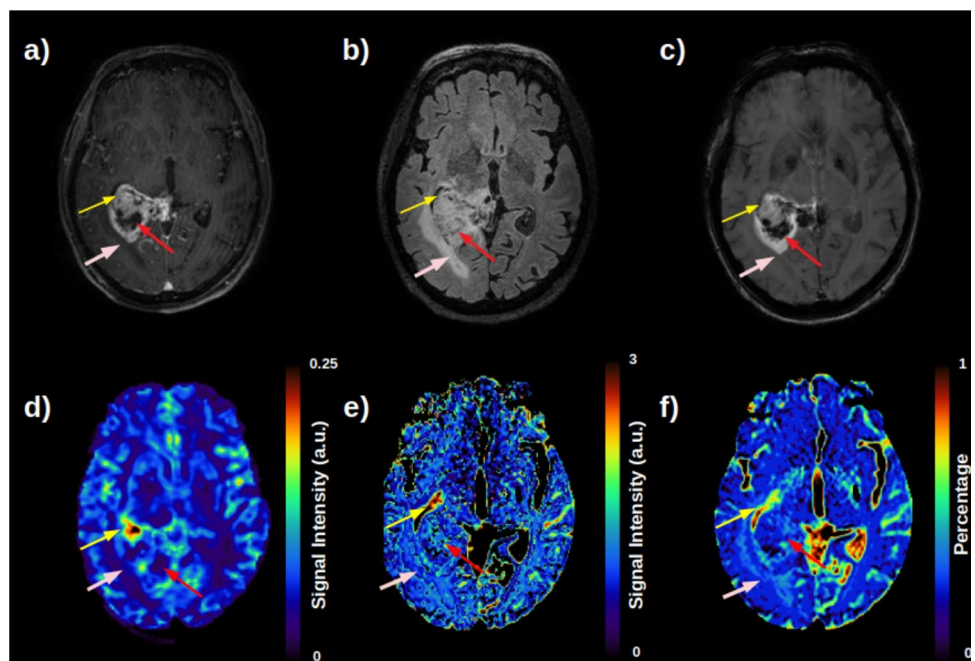


Fig. 3 Boxplots of quantitative measurements for **a** Normalized DSC-CBF, and the IVIM output maps of **b** Diffusion coefficient, **c** fD^* maps and **d** Perfusion fraction f for the ROIs of tumor border, tumor

interior and edema of the HGG patient of Fig. 2. For fD^* maps, the scale for regions of edema were higher than for Tumor border and interior, and therefore it was plotted in a secondary y axis in blue

Fig. 4 Glioblastoma patient. **a** post-contrast T1-weighted image; **b** post-contrast FLAIR image; **c** susceptibility-weighted image; **d** DSC CBF map; **e** IVIM fD^* map; **f** IVIM perfusion fraction map. The yellow arrow shows areas of BBB disruption within the tumor. The red arrow points to areas of necrosis. The pink arrow shows region of increased perfusion fraction within areas of edema-like



and central regions show a great increase in f and fD^* values, compared to normal-appearing contra-lateral regions.

The correlation analysis between DSC-CBF and IVIM perfusion-related maps in Table 4 showed no significant correlation for almost all the patients. For most of them, the correlation coefficients were close to zero or slightly negative.

Discussion

In general, for high-grade glioma patients, IVIM maps were able to detect regions with BBB breakdown, in agreement with post-contrast T1W images, and demonstrated increased perfusion in regions that also showed increased

Fig. 5 Low-grade glioma patient. **a** post-contrast T1-weighted image; **b** post-contrast FLAIR image; **c** susceptibility-weighted image; **d** DSC CBF map; **e** IVIM fD* map; **f** IVIM perfusion fraction map. No evidence of BBB damage in post-contrast T1-weighted images. IVIM maps showed increase perfusion in regions of high ITSS in the susceptibility-weighted image, compared to the normal contralateral hemisphere

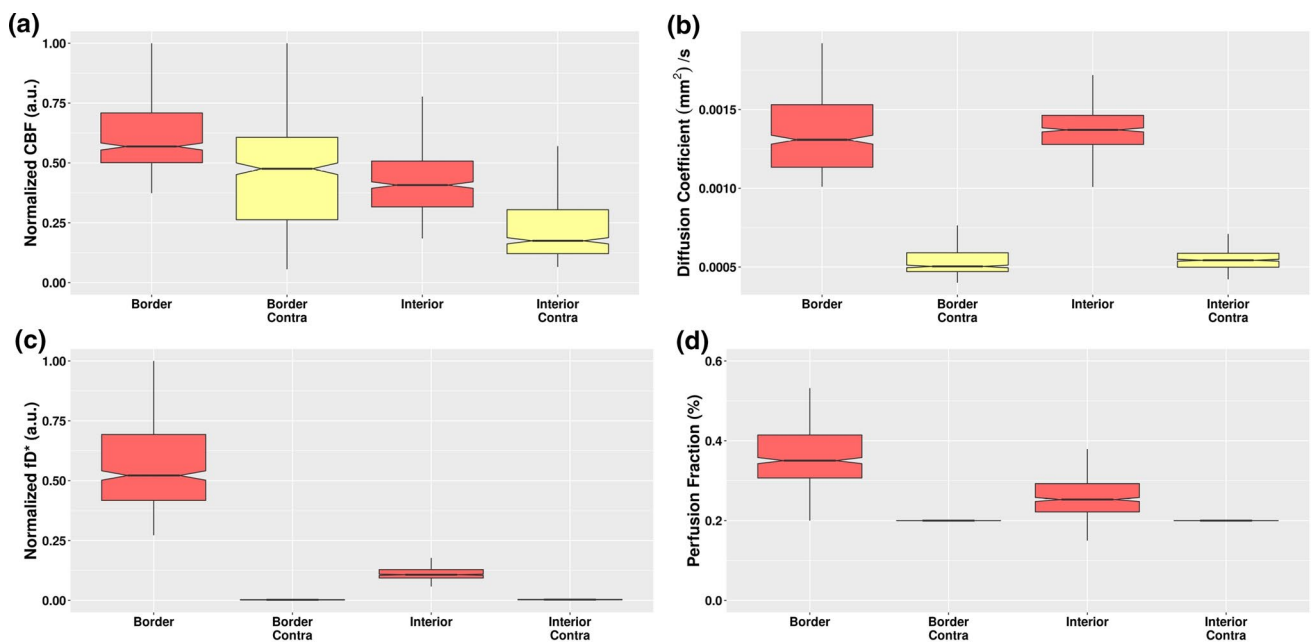
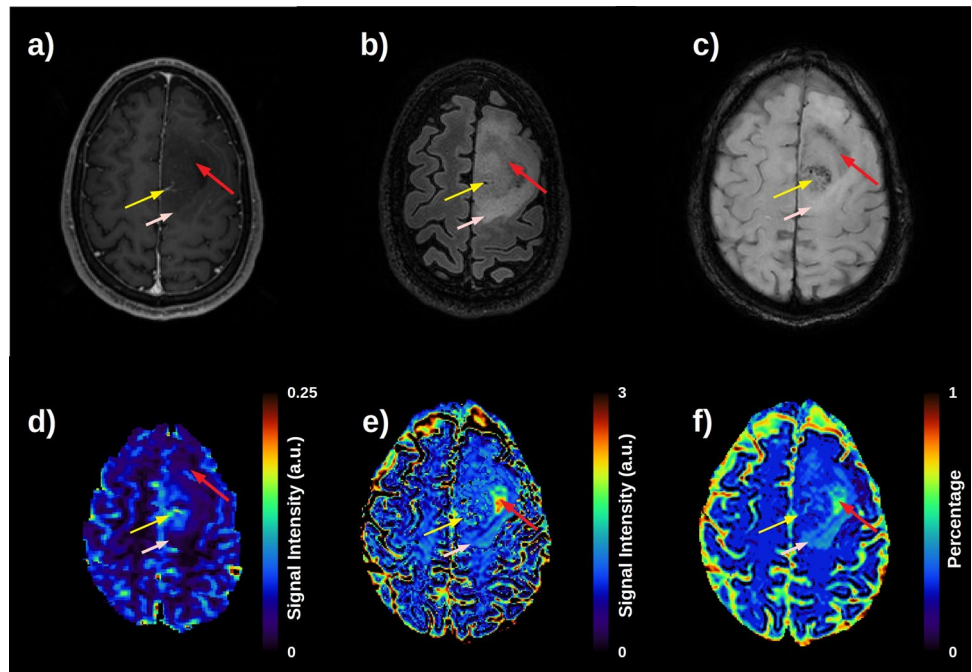


Fig. 6 Boxplots of quantitative measurements for **a** Normalized DSC-CBF, and the IVIM output maps of **b** Diffusion coefficient, **c** fD* and **d** Perfusion fraction f for the ROIs of tumor border and tumor interior of the LGG patient of Fig. 5

ITSS on SWI, therefore interpreted as neovascularity. Moreover, IVIM perfusion fraction and fD* maps showed hyperintensity within edema-like areas, not apparent in DSC CBF maps. In LGG patients, IVIM perfusion-related maps were sensitive to detect perfusion changes due to neovascularity, in agreement with ITSS changes on SWI.

BBB breakdown and increased vascular demand with intratumoral neovascularization are common features in HGG, detectable through different MRI techniques. This study focused on investigating how these changes manifest in IVIM f and fD* maps. We further investigated whether this novel technique could detect hemodynamic changes typical of HGG within LGG, indicating a potential role in

Table 4 Results for the correlation between normalized DSC-CBF and IVIM f and fD* maps in their ROIs of tumor interior and tumor border

	Tumor border		Tumor interior	
	CBF x f	CBF x fD*	CBF x f	CBF x fD*
HGG1	0.30	-0.28	-0.65	0.40
HGG2	0.12	0.01	-0.76	-0.68
HGG3	0.10	0.05	0.27	-0.04
HGG4	0.20	0.06	0.23	0.01
HGG5	0.18	0.19	0.61	0.05
HGG6	0.22	-0.13	0.01	0.30
HGG7	-0.17	0.21	0.09	0.10
HGG8	-0.61	-0.64	-0.32	-0.23
LGG1	-0.39	-0.47	-0.08	0.06
LGG2	-0.02	0.10	-0.02	-0.16
LGG3	-0.38	-0.03	0.01	0.19
LGG4	-0.13	0.41	-0.03	0.31

predicting more aggressive behavior and possibly worse prognosis. Several key findings emerge from the present study. First, IVIM maps are sensitive to increased microvascular density in regions with corresponding ITSS. Second, IVIM maps detected increased perfusion in areas of BBB disruption, characterized as foci of contrast enhancement in T1-weighted images. Third, IVIM was sensitive to areas of abnormal perfusion within LGG. Finally, IVIM was the only MRI modality showing abnormalities in peritumoral areas, where only increased FLAIR signal was evident.

Starting with HGG patients' analysis, the first finding is the increased IVIM perfusion in the tumor border (Fig. 2, red arrow). In this region, an enhanced signal in post-contrast T1-weighted images represents a viable hyperproliferative tumor whose increased demand for blood supply led to neovascularization and BBB breakdown. BBB disruption becomes evident by the extravasation of gadolinium from the intravascular compartment into tumoral tissues, perceived as areas of contrast enhancement [28]. In such regions, DSC-CBF was sensitive to increased perfusion, as well as IVIM maps, which agrees with previous studies [12, 14]. In that sense, increased perfusion fraction f maps reflected the increased blood content within the tumor even in regions with intact BBB function. Increased values in fD* maps suggest increased regional neovascularization, which is confirmed by analyses of susceptibility-weighted images that exhibit ITSS in the same regions of increased signal in IVIM perfusion-related maps. In the boxplots of Fig. 3, the perfusion fraction f was the most sensitive perfusion measurement to detect increase in blood flow in the tumor border, and both f and fD* maps showed higher vascularization in the tumor's core.

Another interesting contribution of IVIM maps in HGG cases is the analysis of adjacent regions with abnormal T2

signals in FLAIR. For example, in patient 4, shown in Fig. 2, areas of hyperintensity in FLAIR extend over a large portion of the right hemisphere. Moreover, in the T2 hyperintense areas surrounding the necrotic lesion in Fig. 2b, there was also no evidence of BBB breakdown in post-contrast T1, nor of increased CBF in DSC maps or ITSS in SWI. However, IVIM f and fD* maps showed increased signal in those areas. In such cases, f and fD* maps could either be capturing subtle perfusional changes of underlying viable tissue or could be capturing remnants of edema, secondary to IVIM imperfect fitting. When planning surgical approaches in these cases, an important question lies in distinguishing areas that harbor viable neoplastic tissue that should be removed, responsible for future progression/recurrence, from areas representing just vasogenic edema. In this context, histopathological studies are necessary to investigate what tissue abnormalities underlie the increased perfusional fraction detected through IVIM on edema-like peritumoral regions. If viable tumoral tissue is detected in those regions, then IVIM probably offers an added value in delineating tumoral extent, outperforming other MRI techniques in detecting vascular changes that precede BBB leakage. In addition, among other HGG cases (supplementary material), foci of increased IVIM perfusion were found in regions of necrosis, which could also potentially represent remnant microvasculature and viable tumoral tissue [29].

Since IVIM was able to detect BBB damage and increased neovascularization in HGGs from our sample, we sought to analyze its performance in LGGs. The example in Fig. 5 refers to an IDH-mutant LGG case, in which post-contrast T1W images show no BBB breakdown, and the DSC-CBF map did show a subtle increase in perfusion within the tumor. IVIM f and fD* maps showed increased signal in the tumor's borders, in agreement to regions of ITSS on SWI and inside the tumor, reflecting hemodynamic changes considered atypical for slow-growing tumors and more in line with HGG. This finding exemplifies how IVIM might be useful in identifying more aggressive LGGs, with potential for early progression and a worse prognosis.

The analysis of the correlation between DSC-CBF and IVIM perfusion maps showed no significant correlation for most of the patients for both tumor interior and tumor borders. This lack of correlation points toward to the conclusion that the perfusion measurements of DSC and IVIM are not the same, reinforcing complementary microvascular information provided by the IVIM acquisition.

Our study has several limitations, mostly related to our small sample size, which precluded statistical analyses. Regarding the IVIM protocol, b0 images with the blips of phase-encoding in both anterior-posterior and posterior-anterior directions were not acquired, and hence the top up correction for susceptibility artifacts could not be performed [30, 31]. Moreover, slice thickness of 5 mm may result in partial

voluming, and can be pointed out as another methodological limitation. Importantly, we interpreted the regional IVIM perfusional changes observed within the gliomas based on how they correlate with neuroimaging findings from other MRI techniques. However, the current understanding of IVIM's biological meaning is still limited. Studies using MRI-guided histopathology sampling would be particularly useful to assess which pathological changes underlie the perfusional alterations detected through IVIM. Longitudinal studies confirming progression of suspicious areas could also be useful in understanding the meaning of early IVIM perfusional changes. Therefore, our results should be regarded as preliminary and warrant confirmation in larger and longitudinal samples, ideally with MRI-guided histopathological correlation.

Nonetheless, our study examined a well-characterized and pathologically confirmed cohort, comparing IVIM's findings against other, more established, MRI techniques, allowing for comparisons and biological inferences.

In conclusion, our initial findings suggest that IVIM maps may offer clinically relevant information that could potentially help guide therapeutic decisions in patients with gliomas. By detecting microvascular perfusion changes in areas displaying nonspecific signal abnormalities, IVIM could help better delineate the extent of the underlying tumor tissue and monitor its progression in size and histological grade. Future studies are needed to confirm our observations and to further assess the potential role of IVIM maps as neuroimaging biomarkers in the field of neuro-oncology.

Supplementary Information The online version contains supplementary material available at <https://doi.org/10.1007/s10334-021-00987-0>.

Acknowledgements This work was supported by São Paulo Research Foundation (FAPESP) (process number: 2019/06148-6) and by the Conselho Nacional de Desenvolvimento Científico e Tecnológico (CNPq) (process number: 151245/2019-3).

Author contributions AMP, ACS and RFL contributed to the study conception and design. Material preparation, data collection was performed by AMP. Data processing was performed by AMP and LMC. Data analysis was performed by AMP, MCZZ, ACS and RFL. The first draft of the manuscript was written by AMP, critical revision was performed by MCZZ and all authors commented on previous versions of the manuscript. All authors read and approved the final manuscript.

Declarations

Conflict of interest The authors declare no competing interests.

Ethical statement Twelve patients (8 HGG, 4 LGG; mean age \pm standard deviation (SD) = 56.11 ± 19.14) participated in this cross-sectional study, approved by the Institutional Review Board, after signing the informed consent agreement

References

- Louis DN, Perry A, Reifenberger G, von Deimling A, Figarella-Branger D, Cavenee WK, Ohgaki H, Wiestler OD, Kleihues P, Ellison DW (2016) The 2016 World Health Organization classification of tumors of the central nervous system: a summary. *Acta Neuropathol* 131:803–820
- Wang X, Cao M, Chen H, Ge J, Suo S, Zhou Y (2020) Simplified perfusion fraction from diffusion-weighted imaging in preoperative prediction of IDH1 mutation in WHO grade II–III gliomas: Comparison with dynamic contrast-enhanced and intravoxel incoherent motion MRI. *Radiol Oncol* 54:301–310
- Wang C, Dong H (2020) Ki-67 labeling index and the grading of cerebral gliomas by using intravoxel incoherent motion diffusion-weighted imaging and three-dimensional arterial spin labeling magnetic resonance imaging. *Acta radiol* 61:1057–1063
- Paschoal AM, Leoni RF, dos Santos AC, Paiva FF (2018) Intravoxel incoherent motion MRI in neurological and cerebrovascular diseases. *NeuroImage Clin*. <https://doi.org/10.1016/j.nicl.2018.08.030>
- Hsu CCT, Watkins TW, Kwan GNC, Haacke EM (2016) Susceptibility-weighted imaging of glioma: update on current imaging status and future directions. *J Neuroimaging* 26:383–390
- Su CQ, Lu SS, Han QY, Zhou MD, Hong XN (2019) Integrating conventional MRI, texture analysis of dynamic contrast-enhanced MRI, and susceptibility weighted imaging for glioma grading. *Acta radiol* 60:777–787
- Le Bihan D, Breton E, Lallemand D, Grenier P, Cabanis E, Laval-Jeantet M (1986) MR imaging of intravoxel incoherent motions: application to diffusion and perfusion in neurologic disorders. *Radiology* 161:401–407
- Detre JA, Leigh JS, Williams DS, Koretsky AP (1992) Perfusion imaging. *Magn Reson Med* 23:37–45
- Alsop DC, Detre JA, Golay X, Gunther M, Hendrikse J, Hernandez-Garcia L, Lu H, MacIntosh BJ, Parkes LM, Smits M, van Osch MJ, Wang DJ, Wong EC, Zaharchuk G (2015) Recommended implementation of arterial spin-labeled perfusion MRI for clinical applications: A consensus of the ISMRM perfusion study group and the European consortium for ASL in dementia. *Magn Reson Med* 73:102–116
- Detre JA, Rao H, Wang DJ, Chen YF, Wang Z (2012) Applications of arterial spin labeled MRI in the brain. *J Magn Reson Imaging* 35:1026–1037
- Wolf RL, Wang J, Wang S, Melhem ER, O'Rourke DM, Judy KD, Detre JA (2005) Grading of CNS neoplasms using continuous arterial spin labeled perfusion MR imaging at 3 Tesla. *J Magn Reson Imaging* 22:475–482
- Bisdas S, Koh TS, Roder C, Braun C, Schittenhelm J, Ernemann U, Klose U (2013) Intravoxel incoherent motion diffusion-weighted MR imaging of gliomas: feasibility of the method and initial results. *Neuroradiology* 55:1189–1196
- Federau C, O'Brien K, Meuli R, Hagmann P, Maeder P (2014) Measuring brain perfusion with intravoxel incoherent motion (IVIM): initial clinical experience. *J Magn Reson Imaging* 39:624–632
- Federau C, Meuli R, O'Brien K, Maeder P, Hagmann P (2014) Perfusion Measurement in Brain Gliomas with Intravoxel Incoherent Motion MRI. *Am J Neuroradiol* 35:256–262
- Shen N, Zhao L, Jiang J, Jiang R, Su C, Zhang S, Tang X, Zhu W (2016) Intravoxel incoherent motion diffusion-weighted imaging analysis of diffusion and microperfusion in grading gliomas and comparison with arterial spin labeling for evaluation of tumor perfusion. *J Magn Reson Imaging* 44:620–632
- Li WF, Niu C, Shakir TM, Chen T, Zhang M, Wang Z (2018) An evidence-based approach to assess the accuracy of intravoxel

- incoherent motion imaging for the grading of brain tumors. *Med (United States)*. <https://doi.org/10.1097/MD.00000000000013217>
- 17. Yan LF, Sun YZ, Zhao SS, Hu YC, Han Y, Li G, Zhang X, Tian Q, Liu ZC, Yang Y, Nan HY, Yu Y, Sun Q, Zhang J, Chen P, Hu B, Li F, Han TH, Wang W, Bin CG (2019) Perfusion, diffusion, or brain tumor barrier integrity: Which represents the glioma features best? *Cancer Manag Res* 11:9989–10000
 - 18. Gu T, Yang T, Huang J, Yu J, Ying H, Xiao X (2021) Evaluation of gliomas peritumoral diffusion and prediction of IDH1 mutation by IVIM-DWI. *Aging (Albany NY)* 13:9948–9959
 - 19. Dubois LG, Campanati L, Righy C, D'Andrea-Meira I, e Spohr TCL de S, Porto-Carreiro I, Pereira CM, Balça-Silva J, Kahn SA, DosSantos MF, Oliveira M de AR, Ximenes-da-Silva A, Lopes MC, Faveret E, Gasparetto EL, Moura-Neto V (2014) Gliomas and the vascular fragility of the blood brain barrier. *Front Cell Neurosci* 8:1–13
 - 20. Mohammadi S, Möller HE, Kugel H, Müller DK, Deppe M (2010) Correcting eddy current and motion effects by affine whole-brain registrations: Evaluation of three-dimensional distortions and comparison with slicewise correction. *Magn Reson Med*. <https://doi.org/10.1002/mrm.22501>
 - 21. Ruthotto L, Kugel H, Olesch J, Fischer B, Modersitzki J, Burger M, Wolters CH (2012) Diffeomorphic susceptibility artifact correction of diffusion-weighted magnetic resonance images. *Phys Med Biol* 57:5715–5731
 - 22. Le Bihan D (2019) What can we see with IVIM MRI? *Neuroimage*. <https://doi.org/10.1016/j.neuroimage.2017.12.062>
 - 23. Jenkinson M, Beckmann CF, Behrens TEJ, Woolrich MW, Smith SM (2012) FSL. *Neuroimage* 62:782–790
 - 24. Peruzzo D, Bertoldo A, Zanderigo F, Cobelli C (2011) Automatic selection of arterial input function on dynamic contrast-enhanced MR images. *Comput Methods Programs Biomed* 104:e148–e157
 - 25. Zanderigo F, Bertoldo A, Pillonetto G, Cobelli C (2009) Nonlinear stochastic regularization to characterize tissue residue function in bolus-tracking MRI: Assessment and comparison with SVD, block-circulant SVD, and tikhonov. *IEEE Trans Biomed Eng* 56:1287–1297
 - 26. Team R core (2021) R: A Language and Environment for Statistical Computing
 - 27. Kang Y, Choi SH, Kim YJ, Kim KG, Sohn C-H, Kim J-H, Yun TJ, Chang K-H (2011) Gliomas : Histogram analysis of apparent diffusion coefficient maps purpose : methods : results. *Radiology* 261:882–890
 - 28. Kiviniemi A, Gardberg M, Ek P, Frantzén J, Bobacka J, Minn H (2019) Gadolinium retention in gliomas and adjacent normal brain tissue: association with tumor contrast enhancement and linear/macrocyclic agents. *Neuroradiology* 61:535–544
 - 29. Brat DJ, Van Meir EG (2004) Vaso-occlusive and prothrombotic mechanisms associated with tumor hypoxia, necrosis, and accelerated growth in glioblastoma. *Lab Investig* 84:397–405
 - 30. Andersson JLR, Skare S, Ashburner J (2003) How to correct susceptibility distortions in spin-echo echo-planar images: Application to diffusion tensor imaging. *Neuroimage* 20:870–888
 - 31. Smith SM, Jenkinson M, Woolrich MW, Beckmann CF, Behrens TEJ, Johansen-Berg H, Bannister PR, De Luca M, Drobniak I, Flitney DE, Niazy RK, Saunders J, Vickers J, Zhang Y, De Stefano N, Brady JM, Matthews PM (2004) Advances in functional and structural MR image analysis and implementation as FSL. *Neuroimage* 23:208–219

Publisher's Note Springer Nature remains neutral with regard to jurisdictional claims in published maps and institutional affiliations.

49 Monitorias para disciplinas de graduação

Esta subseção apresenta o comprovante de Monitoria para alunos de graduação.

CERTIFICADO DE MONITORIA

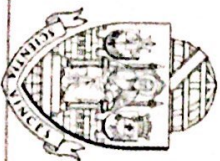
Certifico que o(a) aluno(a) ANDRÉ MONTEIRO PASCHOAL, nº USP 6418299, foi monitor(a) junto à disciplina de graduação FF10181 Laboratório de Física Geral II, sob a supervisão da Profa. Dra. Betti Hartmann e Prof. Dr. José Pedro Donoso Gonzalez, no período de 17/08 a 09/12/2015, com carga horária de 06 (seis) horas semanais.

São Carlos, 02 de fevereiro de 2016.



Prof. Dr. Luís Gustavo Marcassa

Presidente da Comissão de Graduação
Instituto de Física de São Carlos
Universidade de São Paulo



50 Monitorias para disciplinas de graduação

Esta subseção apresenta o comprovante de Monitoria para alunos de graduação.



Universidade de São Paulo

Faculdade de Filosofia, Ciências e Letras de Ribeirão Preto
Campus de Ribeirão Preto
Comissão de Graduação



DECLARAÇÃO

DECLARO, que o(a) Sr(ta). **ANDRÉ MONTEIRO PASCHOAL** foi aluno(a) monitor(a) voluntário(a) na disciplina **5910173 - Princípios de Imagens Médicas**, durante o 1º semestre de 2017, junto ao Departamento de Física da Faculdade de Filosofia, Ciências e Letras de Ribeirão Preto da Universidade de São Paulo.

Ribeirão Preto, 27 de outubro de 2020.

A handwritten signature in blue ink, appearing to read "Eder Rezende Moraes".

Prof. Dr. Eder Rezende Moraes
Presidente da Comissão de Graduação/FFCLRP

Processo: 2017.1.544.59.9

51 Monitorias para disciplinas de graduação

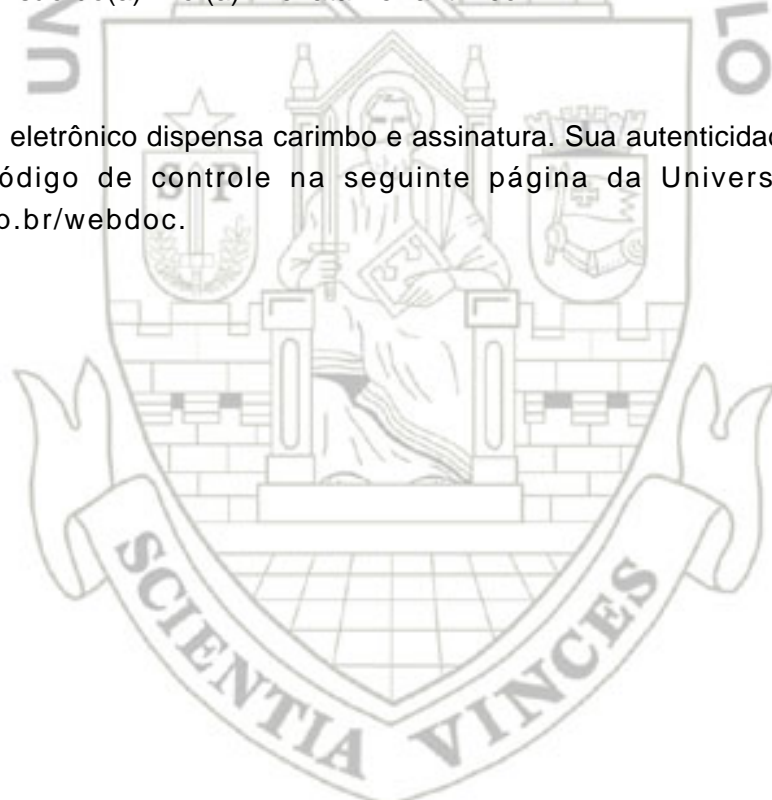
Esta subseção apresenta o comprovante de Monitoria para alunos de graduação.

PROGRAMA DE APERFEIÇOAMENTO DE ENSINO

ATESTADO

A Comissão Central do Programa de Aperfeiçoamento de Ensino atesta que o(a) Sr(a). ANDRÉ MONTEIRO PASCHOAL aluno(a) de pós-graduação, nível Doutorado, na área Física Aplicada à Medicina e Biologia, do(a) Faculdade de Filosofia, Ciências e Letras de Ribeirão Preto, foi estagiário(a) do Programa de Aperfeiçoamento de Ensino, com carga horária total de 120 horas-atividade, de Julho à Novembro de 2017, tendo desenvolvido atividades didáticas junto à disciplina 5910142 - Imagens Por Ressonância Magnética Nuclear em Biomedicina do(a) Faculdade de Filosofia, Ciências e Letras de Ribeirão Preto, aos alunos de graduação, sob supervisão do(a) Prof(a). Renata Ferranti Leoni.

Este é um documento eletrônico dispensa carimbo e assinatura. Sua autenticidade pode ser comprovada fornecendo-se o código de controle na seguinte página da Universidade de São Paulo:
<http://uspdigital.usp.br/webdoc>.



52 Monitorias para disciplinas de graduação

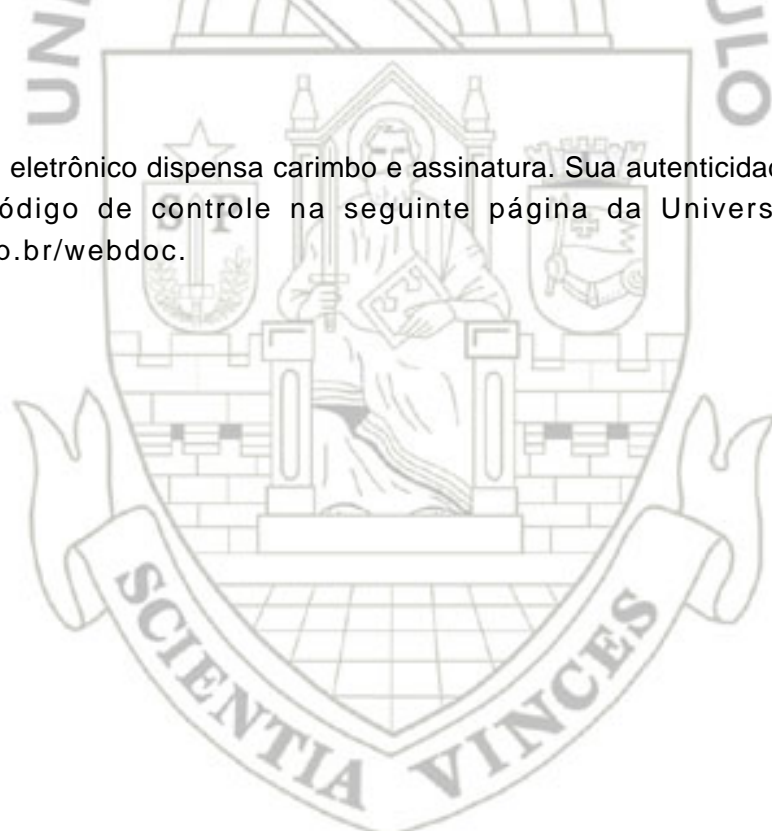
Esta subseção apresenta o comprovante de Monitoria para alunos de graduação.

PROGRAMA DE APERFEIÇOAMENTO DE ENSINO

ATESTADO

A Comissão Central do Programa de Aperfeiçoamento de Ensino atesta que o(a) Sr(a). ANDRÉ MONTEIRO PASCHOAL aluno(a) de pós-graduação, nível Doutorado, na área Física Aplicada à Medicina e Biologia, do(a) Faculdade de Filosofia, Ciências e Letras de Ribeirão Preto, foi estagiário(a) do Programa de Aperfeiçoamento de Ensino, com carga horária total de 120 horas-atividade, de Julho à Novembro de 2019, tendo desenvolvido atividades didáticas junto à disciplina 5910235 - Física I do(a) Faculdade de Filosofia, Ciências e Letras de Ribeirão Preto, aos alunos de graduação, sob supervisão do(a) Prof(a). Renata Ferranti Leoni.

Este é um documento eletrônico dispensa carimbo e assinatura. Sua autenticidade pode ser comprovada fornecendo-se o código de controle na seguinte página da Universidade de São Paulo:
<http://uspdigital.usp.br/webdoc>.



53 Membro de Comissão Avaliadora

Esta subseção apresenta o comprovante de participação em comissão avaliadora de eventos.

27º SIICUSP - Simpósio Internacional de Iniciação Científica e Tecnológica da Universidade de São Paulo

Declaração de Participação

Declaro para os devidos fins que **André Monteiro Paschoal** participou como Avaliador(a) do **27º Simpósio Internacional de Iniciação Científica e Tecnológica da USP - SIICUSP**



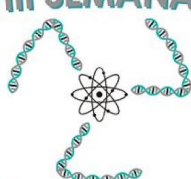
Documento emitido às **15:24:21** horas do dia **03/10/2019** (hora e data de Brasília).

Código de controle: **FWB4-IASK-5HF4-7WY1**

A autenticidade deste documento pode ser verificada na página da Universidade de São Paulo
<http://uspdigital.usp.br/webdoc>

54 Membro de Comissão Avaliadora

Esta subseção apresenta o comprovante de participação em comissão avaliadora de eventos.

XVIII SEMANA DA

Física Médica

Certificamos que **André Monteiro Paschoal** atuou como avaliador de pôster durante a **XVIII Semana da Física Médica**, que ocorreu de 4 a 8 de Novembro de 2019 no Departamento de Física da Faculdade de Filosofia, Ciências e Letras de Ribeirão Preto da Universidade de São Paulo.



Profº Dr. Antônio José da Costa Filho



Profº Dr. Ubiraci Pereira da Costa Neves

55 Comissão Organizadora de Eventos Internacional, Nacional, Regional ou Local

Esta subseção apresenta o comprovante de Participação de Comissão Organizadora de Eventos Nacionais e Internacionais.

INBRAIN WORKSHOP

Advanced  Imaging

• 2 0 2 0 •

The **InBrain Lab** hereby certifies that **André Monteiro Paschoal**, composed the *organizing committee* of the **InBrain Workshop: Advanced Brain Imaging 2020**, held at Ribeirão Preto - São Paulo, Brazil, from February 13th to 15th, 2020.



Carlos Ernesto Garrido Salmon
Organizing Committee



Renata Ferranti Leoni
Organizing Committee



FFCLRP - University of São Paulo
Building B3 - Room 103
Bandeirantes Avenue, 3900
Ribeirão Preto, SP

E-mail: inbrain@usp.br
Tel: +55 16 3315-3721

56 Comissão Organizadora de Eventos Internacional, Nacional, Regional ou Local

Esta subseção apresenta o comprovante de Participação de Comissão Organizadora de Eventos Nacionais e Internacionais.



EIFAMB 2018

III ESCOLA DE INVERNO EM FÍSICA
FÍSICA APLICADA À MEDICINA E BIOLOGIA



Certificamos que

André Monteiro Paschoal

participou da Comissão Organizadora da III Escola de Inverno em Física Aplicada à Medicina e Biologia, com duração de 30 horas, realizada pelo Programa de Pós-graduação em Física Aplicada à Medicina e Biologia do Departamento de Física da Faculdade de Filosofia Ciências e Letras de Ribeirão Preto da Universidade de São Paulo, de 16 a 20 de Julho de 2018 na cidade de Ribeirão Preto, São Paulo, Brasil.

Prof. Dr. Antonio José da Costa Filho
Coordenador do Programa de
Pós-graduação em Física Aplicada à
Medicina e Biologia

Profa. Dra. Patrícia Nicolucci
Professora Chefe da Comissão
Organizadora da III Escola de Inverno de
Física Aplicada à Medicina e Biologia